ADAM15/PTK6/cMET interplay: Promotors of prostate cancer progression

Melanie Hurtz, MSc.

September 2017

School of Medicine

Cardiff University

Cardiff, CF14 4XN

Cardiff, United Kingdom

A thesis submitted in partial fulfilment of the requirements of the degree of

Doctor of Philosophy (PhD)

DECLARATION

This work has not been submitted in substance for any other degree or award at this or any other university or place of learning, nor is being submitted concurrently in candidature for any degree or other award.

Signed …… (candidate) Date ……

STATEMENT 1

This thesis is being submitted in partial fulfilment of the requirements for the degree of PhD

Signed ……(candidate) Date ……

STATEMENT 2

This thesis is the result of my own independent work/investigation, except where otherwise stated. Other sources are acknowledged by explicit references. The views expressed are my own.

Signed ……(candidate) Date ……

STATEMENT 3

I hereby give consent for my thesis, if accepted, to be available for photocopying and for inter-library loan, and for the title and summary to be made available to outside organisations.

Signed ……(candidate) Date ……

STATEMENT 4: PREVIOUSLY APPROVED BAR ON ACCESS

I hereby give consent for my thesis, if accepted, to be available for photocopying and for inter-library loans after expiry of a bar on access previously approved by the Academic Standards & Quality Committee.

Signed ……(candidate) Date ……

Σε αυτό που βρήκα εδώ στο καρντιφ, και το μικρό μπόνους

Für Joko, und all die guten Tage zum Fliegen

Für Mama und Papa

Acknowledgments

This thesis would have been impossible without the support of my supervisor's

Dr Zara Poghosyan and Dr Vera Knäuper.

…. and also without the support and great organization from the people behind the scene, Julia, Trish, Marie and AJ.

I would like to say thank you to Dr Lisa Spary from the Wales Cancer Bank, for the great sample coordination.

I would like to say thank you to my sponsor, Cancer Research Wales, for supporting this project.

A special thank you also to all unknown patients, that were willing to support prostate cancer research, only with you we can try to find a way to beat cancer.

Abstract

ADAM15 is a transmembrane metalloproteinase involved in disease progression and aggressiveness in prostate cancer (PCa). ADAM15 is composed of an extracellular domain, a transmembrane region and an intracellular domain, the latter being subject to splicing due to alternative use of exons 19 to 21. The splice variants that will be subject in this study are ADAM15-A, ADAM15-B, ADAM15-C, ADAM15-D and ADAM15-E. Previously, ADAM15 splice variant A and B were reported to associate with the PCa promotor PTK6 and the cMET adaptor protein Grb2.

In order to understand the underlying mechanisms for the contribution of ADAM15 to disease progression in PCa, ADAM15 A-E splice variants, overexpressed in LNCaP and PC3 PCa cells, were biochemically and functionally characterized.

Overexpression of ADAM15-A in PC3 led to enhanced invasion upon HGF treatment, which could be reverted by cMET inhibitor treatment. In addition, ADAM15-induced invasion was dependent on its proteolytic activity. Moreover, PC3 cells expressing proteolytically active ADAM15 showed more MMP2 activity compared to cells with the proteolytically inactive ADAM15 mutant in cell supernatants. In contrast to the aggressive, androgen independent PC3, androgen dependent LNCaP cells did not show any response to HGF treatment upon ADAM15 A-E overexpression. All ADAM15 splice variants were found in a complex with PTK6, which could be disrupted upon cMET inhibition in PC3.

Strikingly, ADAM15 was found in a complex with cMET/Gab1/Grb2/PTK6. cMET inhibition led to complex loss of cMET/Gab1/PTK6, however, Grb2 remained in complex with ADAM15 regardless of treatment. Unlike cMET, PTK6 activity was not needed for formation of the ADAM15 complex.

Analysis of the ADAM15 splice profile in prostate cancer patients and comparison with healthy prostate tissue revealed a significant overexpression of all ADAM15 splice variants.

In summary, we show for the first time that ADAM15 is found in a complex with cMET/Gab1/Grb2/PTK6, and importantly, that, this complex formation is dependent on the cMET/HGF axis in PC3 PCa cells. Moreover, we found that proteolytically active ADAM15 resulted in enhanced invasion upon HGF treatment in PC3s. Our data suggest an important role for ADAM15 in prostate cancer disease progression.

Table of contents

Overview of Figures and Tables

List of abbreviations

(T_m)	Melting Temperature
AA	Amino acids
Abl	Abelson murine leukemia
ADAMs	A disintegrin and metalloproteinases
AR-V7	AR splice variant 7
AS	alternative splice
ATP	adenosine triphosphate
Aβ	amyloid β peptide
BCA	Bicinchoninic acid assay
BRK	Breast tumor kinase
BSA	Bovine serum albumin
Cbl	casitas B-lineage lymphoma
CDK4	cyclin-dependent kinase 4

CDKs	cyclin-dependent kinases
cDNA	complementary deoxyribonucleic acid
cMET	HGF receptor
CO_2	carbon dioxide
CRMPC	castration resistance metastatic prostate cancer
CRPC	castration-resistance PC
CTD	c-terminal domain
DBD	DNA-binding domain
DHT	Dihydrotestosterone
DRE	digital rectal examination
ECD	extracellular domain
ECM	extra cellular matrix
EGF	epidermal growth factor
EGFR	epidermal growth factor receptor
ESS	exonic splice enhancer
FGFR2iiib	fibroblast growth factor receptor 2iiib
FISH	Fluorescence in situ hybridization
FSH	Follicle stimulating hormone
Gab1	Grb2-associated adaptor protein
GI	Gastrointestinal
GnRH	gonadotropin-releasing hormone
Grb2	growth factor receptor-bound protein 2
h	Hour
H&E	hematoxylin and eosin
HGF-like	hepatocyte growth factor receptor-like
HGFR	hepatocyte growth factor receptor
HIF1α	hypoxia inducible factor 1α
hnRNP	heterogenous nuclear ribonucleproteins
ICD	intracellular domain
IGF-IR	insulin-like growth factor I-recepor
IL-6R	interleukin-6 receptor

IPT	Ig-like also found in plexins, semaphorins and transcriptional factors
IR	insulin-receptor
IRR	insulin receptor-related receptor
ISUP	International Society of Urology and pathology
K219	Lysine 219
kDa	Kilodalton
LH	luteinizing hormone
LNCaP	Lymph Node carcinoma of the Prostate
MBP	myelin basic protein
min	Minute
MMP	matrix metalloproteinase
MP	Metalloproteinase
MPD	membrane-proximal domain
MTS	[3-(4,5-dimethylthiazol-2-yl)-5-(3-carboxymethoxyphenyl)-2-(4-sulfophenyl)-2H-tetrazolium
NCF1 (I)	Neutrophil cytosolic factor 1
NF-κB	nuclear factor kappa-light-chain-enhancer of activated B cells
NTC	No-Template-Control
NTD	NH_2-Terminal domain
OSF1	Osteoclast-Stimulating Factor 1
PBS	Phosphate-buffered saline
PC3	Prostate Cancer Cell Line
PCa	prostate cancer
PI3K	phosphatidylinositol-3-kinase
PIA	proliferative inflammatory atropy
PIN	prostatic intraepithelial neoplasia
PKCα	protein kinase Cα
PLCO	The Prostate, Lung, Colorectal and Ovarian Cancer Screening Randomized Controlled Trial

pPTK6	phospho-PTK6
pro-HB-EGF	pro-heparin-binding EGF-like growth factor
PSA	prostate specific antigen
PSI	plexin-sema-integrin
PTB	phosphotyrosine binding sites
PTK6	Protein tyrosine kinase 6
PTP	phosphatase tyrosine proteins
PVDF	Polyvinylidene difluoride
PZ	peripheral zone
qPCR	quantitative PCR
RGD-motif	Arginine-Glycine-Aspartic Acid – motif
RIN	RNA integrity number
RIPA	Radioimmunoprecipitation assay buffer
RNA	Ribonucleic acid
RON	recepteur d'origine Nantais
rpm	revolutions per minute
RTK	receptor tyrosine kinases
RX6DLPEF	Arginine-X-6-Aspartic Acid-Leucine-Proline-Glutamic Acid-Phenylalanine
SDS-PAGE	Sodium dodecyl sulfate polyacrylamide gel electrophoresis
Sema	Semaphoring
SH1	Src Homology-1
SH2	Src homology-2
SH3	Src-homology-3
SH4	Src-homology-4
Ship1	SH2 domain containing inositol phosphatase-1
Shp2	Src homology protein tyrosine phosphatase 2
SLM-1	Sam68-like mammalian protein 1
SNBs	small nuclear bodies

SOS	son of sevenless
SPH	serine protease homology
Src	Sarcoma-family kinase
STAT3	signal transducer and activator of transcription 3
TACE	tumour necrosis factors –α converting enzyme
TBST	Tris-buffered saline Tween
TEMED	Tetramethylethylenediamine
TGF	transforming growth factor
TK	Tyrosine kinases
TKIs	tyrosine kinase inhibitors
TRP	translocating promotor region
TRUS	transrectal ultra sound
V	Volt
WHO	World Health Organisation
Y342	Tyrosine 342
Y447	Tyrosine 447
ΔG	Gibbs Free Engery G

1 Introduction

The human body consists of approximately 37.2 trillion cells, which all have a distinct task depending on the tissue they belong to. They all divide and die in a strictly controlled and regulated manner. If this strict regulation is disrupted cell growth is out of control, which in most cases is the onset of cancer. Cancer cells possess two distinct characteristics, namely, they are able to reproduce independent from the body's own restrains, and they are able to colonize and invade other tissues.

Cancer has become a leading cause of death in the western world, with 14,1 million new identified cases only in 2014[1]. It is multifactorial and does not depend on age or sex, although 1/3 of all cancer cases are found in patients above 60, whereas only 50% of all diagnosed cases survive for 10 years or more. In 2012, 8.2 million cancer related deaths were reported from which 50% were linked to lung, breast and liver cancer. Looking at cancer on a geographical level, it turns out that organ specific cancers like thyroid cancer or liver cancer are predominantly found in South Korea and Laos, whereas breast and prostate cancer are not elevated in these countries[2].

The disease burden is tremendous for patients and for their families. Even though the patient will undergo a successful first treatment, the chance of a disease relapse is never eliminated.

1.1 Cancer

The name cancer, in greek, karkinos (καρκινος), goes back to Hippocrates (460-370BC). He used this word to describe the structure of cancerous tissue that he observed, which reminded him of the arms of a moving crab, the translation of the word cancer[3]. Cancer is classified due to its origin, i.e. cell type and the organ from which it originated. There are five classes to be mentioned, carcinomas, sarcomas, leukaemia, myelomas and lymphomas.

According to Cancer Research UK, carcinomas make up 85% of all cancers diagnosed in the UK, and are of epithelial origin. Sarcomas, are cancers which originate from the bone, cartilage, muscles, fat and blood vessels. Myelomas and lymphomas are cancers originating and affecting the immune system; approximately 6% of cancer diagnosis are related to these categories of cancer. 3% of cancer patients are diagnosed with leukaemia. Brain and spinal cord cancer are classified as cancers of the nervous system and affect less than 3% of all patients. The most common form of brain cancer is called glioma, arising from the glial cells. One out of

100 diagnosed cancer cases are classified as sarcomas. Leukaemia develops from blood forming tissues, such as bone marrow.

Once classified, cancer types can be described based on their developmental stage, as in situ, namely, a still isolated accumulation of tumour cells, or as invasive, which means the cancer cells start to invade the surrounding tissue. Cells have found a way to escape the primary tumour and spread through the body to initiate the formation of new tumours, known as metastasis.

1.2 Prostate Cancer

The World Health Organisation (WHO) cancer statistic from 2014 for the UK shows that from 557,000 deaths within the UK, in men, 86,300 can be assigned to prostate cancer (PCa). It is the second leading cause of death in men, with 14.0% of all cancer related deaths. PCa affects one out of eight men, and in 2014, 45,406 cases only in the UK have been registered[4]. PCa has multiple faces, from slow growing with good treatment chances, to highly invasive and metastatic. When diagnosed at an early stage, the chances of complete recovery are almost 100%, however, there are no clinical symptoms associated with early disease onset. In a US study, 1/3 of autopsy samples from men above 50, a PCa incidence was identified histologically, although the patients were non-symptomatic[5].

The most common form of prostate tumours are adenocarcinomas, which show similarities with epithelial malignancies such as breast and colon cancers[6,7]. Established risk factors such as ethnicity, family history, age and hormones are linked to PCa onset, however they do not give a satisfying explanation of disease onset[1,4,8–10].

One hypothesis for PCa onset is that it arises from a lesion within the prostate epithelium, which progresses over decades, leading to proliferative inflammatory atropy (PIA), which is characterized as the precursor of PCa. PIA can be stimulated by chronic inflammation, infection or even the exposure to carcinogens, and is characterized by an increased epithelial proliferation, which can progress to prostatic intraepithelial neoplasia (PIN), which is characterized as low to high-grade prostate cancer (HGPIN) [11].

In contrast to this, Maitland *et al.* postulate the theory of prostate cancer stem cells. Prostate cancer appears as heterogenic disease, although most therapies aim to eliminate the tumour mass, the disease progresses and reaches an incurable stage, raising the question about the origin of resistance [12].

1.2.1 The Prostate

The prostate is a walnut shaped, exocrine gland. It is located underneath the bladder and surrounds via its peripheral zone (PZ) the urethra. It is connected via ducts to the urethra and composed of approximately 50 single tubuloalveolar glands, regulated via testosterone[13](Figure 1.1).

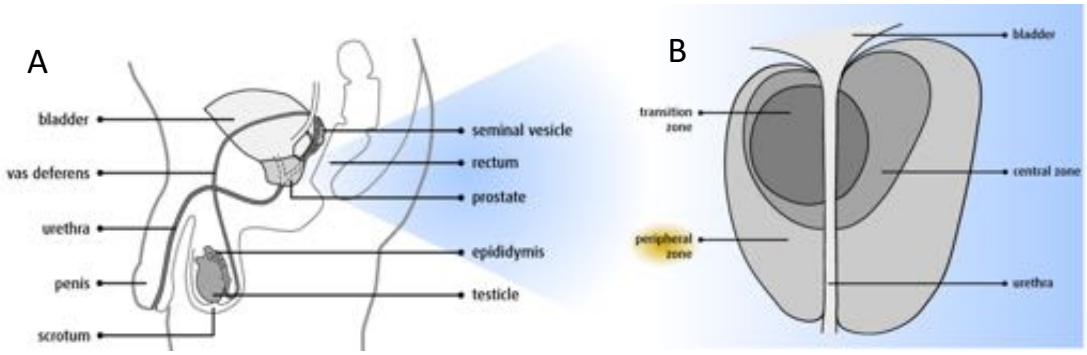

Figure 1.1 The anatomy of the human prostate.

(A) Overview of the male prostate and its location within the reproductive system. The prostate is located underneath the bladder and surrounds the peripheral zone and the urethra. (B) A closer look to the prostate anatomy, three different prostate zones surround the urethra starting from the internal transition zone, which is surrounded by the central zone and the outer peripheral zone, the most prominent site of prostate tumours. Adapted from the Canadian Cancer Society.

During ejaculation, the prostate epithelial cells produce an alkaline secretion (pH 6.4), which makes up 30% of the male seminal plasma. This seminal plasma contains prostate specific antigen (PSA), a kallikrein-like serine protease, which liquefies the seminal plasma due to degradation of semenogelin and fibronectin[14]. PSA is found in the blood when changes in the prostate epithelial architecture occur[15], and these PSA levels are a prognostic tool for prostate malfunction and for prostate cancer screening[16].

1.2.2 PCa screening

The purpose of any cancer related screening program is to identify the cancer in a curable, early stage, as an early diagnosis is associated with a complete recovery for the patient[17]. For PCa detection, three techniques are commonly used, such as digital rectal examination (DRE), transrectal ultra sound (TRUS) and biomarker screening for prostate specific antigen (PSA)[18]. As an early prognostic tool PSA testing is used in men to evaluate risk[19,20]. From an epidemiological point of view, age is the most outstanding factor to define men at risk. The chances of being diagnosed with PCa at an age below 40 is 1 in 10,000, from 40 to 60 the chances are 1 in 103 and from 60

to 80, 1 in 8[5]. Independent studies from the European Union, The Randomised study of Screening for Prostate Cancer (ERSPC) and the United States, The Prostate, Lung, Colorectal and Ovarian Cancer Screening Randomized Controlled Trial (PLCO), showed that PSA screening is able to reduce prostate cancer mortality. However, PCa screening is debatable due to the high risk of over-diagnosis, which affects up to 50% of all cases [21].

1.2.3 Prostate cancer grading, the Gleason Score

Prostate cancers are in most cases adenocarcinomas. A key histological grading system on which prognosis and therapy is based, is the Gleason score. This scoring system was developed in 1966 by Dr Donald F. Gleason and is based on hematoxylin and eosin (H&E) staining of tumour structures from initially 270 patients[22,23]. The system was refined by Gleason and Mellinger from 1974-1977 by including samples of 1032 patients [24]. It was updated to common modern practice during The 2005 International Society of Urology and Pathology (ISUP) Consensus Conference on Gleason Grading of Prostate Carcinoma[25]. The tumour grading for the Gleason score is divided into 5 classes, each representing a morphological progression in PCa. Grade 1 to 3 tumours show high similarity with the normal prostatic tissue, whereas tumours graded with 4 and 5 show abnormal morphological pattern. During the 1960s, two biopsy samples were taken directly from the area showing the abnormality, via a thick-gauge needle. During the 1980s this was replaced via an 18-gauge needle[23,26,27]. Nowadays, 6-8 different core samples from areas of the prostate are taken. The Gleason score is an average measure of the most common primary and most common secondary patterns within the biopsied sample. The two most prominent Gleason grades (i.e. 1-5), present in the prostate core samples, are combined to the Gleason score, i.e. 3+4 =7. An overview of the histological grades by Gleason is given in Figure 1.2.

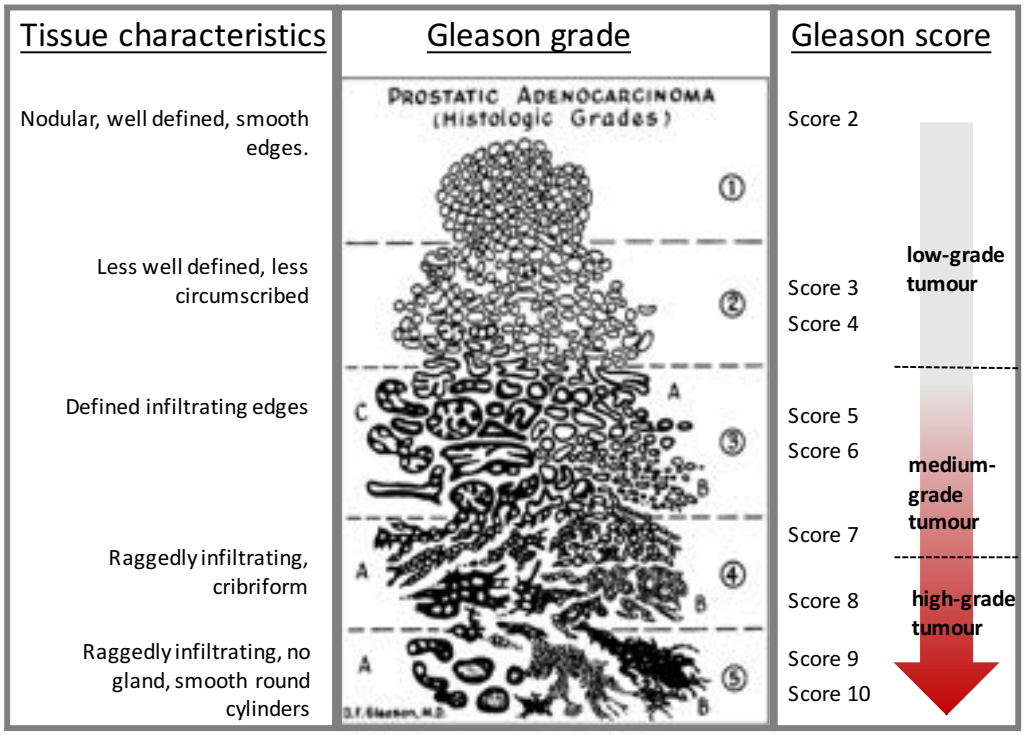

Figure 1.2 Prostate cancer grading by the Gleason score and its pathological pattern.

The Gleason score is the grading system developed by Gleason and Mellinger in 1977, including 1032 patient samples. The original system is divided into 5 classes with respect to abnormalities in morphology. Gleason score 1 to 3 show high morphological similarity with normal prostate tissue, whereas scores 4 to 5 show abnormal morphologies. For each score stage tumour shape, invasion, tumour cell arrangement and gland size are described. Adapted from Gleason *et al.*

1.2.4 Androgen dependent PCa development

Androgens and the signalling via the androgen receptor (AR) play a crucial role in the development of the prostate, and the growth of prostate epithelium[28]. Morphological changes of the prostate are induced during puberty via increasing androgen levels. The result is an encapsulated glandular structure at a mature age. This encapsulated structure of the prostate needs constant supply and control of androgens. The production of androgen is regulated via luteinizing hormone (LH), which underlies the levels of gonadotropin-releasing hormone (GnRH) within the adrenal glands, the peripheral tissues and the prostate. In more the detail, GnRH is released from the hypothalamus and stimulates the anterior pituitary gland leading to the production and release of LH and follicle stimulating hormone (FSH). FSH stimulates the sertoli cells facilitating spermatogenesis. The LH stimulates the Leydig cells within the testis leading to the production of testosterone. The testosterone further stimulates the sertoli cells, inducting spermatogenesis, and moreover, it acts as inhibitor on the

pituitary gland and the hypothalamus, regulating the production and release of GnRH and FSH[29,30]. As much as androgens are needed for development and maintenance, at a later stage in life, androgens can become the main drivers of pathological damage within the prostate leading to cancer[31].

Upon entering the prostate cell, the androgen testosterone is converted to dihydrotestosterone (DHT), by 5-α-reductase. The AR is bound to heat-shock proteins (HSP) within the cytoplasm, which dissociate upon DHT binding. The AR-DHT complex dimerizes and becomes phosphorylated, leading to receptor translocation to the nucleus. The AR-DHT complex allows the association with androgen responsive elements (ARE) in the promoter region of target genes, such as PSA, Cdk1 and Cdk2, or TMPRSS2[32] (Figure 1.3). Co-activators and co-repressors, for instance ARA70, are recruited to the promoter region, initiating or preventing transcription. Under physiological conditions, this complex maintains the homeostasis between proliferation, growth and survival. During cancer these genes induce enhanced proliferation and prevent apoptosis[33]. At an early stage PCa is highly dependent on the stimulation by androgens.

Androgen depletion therapy (ADT) is an outstanding treatment for an early stage PCa. The aim of ADT is to reduce androgen levels in a therapeutic way, as they have also a major impact on development, maturation and differentiation of the male reproductive system[34]. Two target sites are used for ADT, first, gonadotropin-hormone analogues, leading to suppression of testosterone production and chemical castration, or androgen-analogues, binding directly to the AR, impairing androgens to bind to the receptor[35]. However, in most cases the cancer progresses within 2-3 years after ADT start, and overcomes the androgen-deprivation. Disease recurrence is termed castration-resistant PCa (CRPC)[36].

1.2.5 Androgen independent PCa

During the first stage of PCa the AR signalling is predominant, however, as soon as it progresses, the signalling pathways that are involved become more diverse, although androgen signalling is still involved. For example, although CRPC is resistant to androgen deprivation therapy it still involves gene amplification and increased AR expression, or splice variants of the AR which allow not only androgens to bind but also steroids, estrogens or tyrosine kinases (TKs) [34,36]. Until today, the development from androgen dependent to androgen independent prostate cancer remained unclear. In 2001, Feldman *et al.* published five hypothetic mechanisms,

indicating possible reasons for prostate cancer to progress from androgen dependent to androgen independent and becoming resistant to ADT[32] (Figure 1.3).

The first mechanism how prostate cancer cells are able to overcome ADT is the hypersensitivity to androgens, by gene amplification of the AR, by hypersensitivity towards DHT, or local production of androgens. Visakorpi *et al.* showed that 30% of patient tumours with normal AR expression levels prior to ADT, had AR amplification after ADT, indicating a specific selection of those cells[32,37]. Gregory *et al.* confirmed that androgen hypersensitivity of tumours was related not only to AR amplification but further to enhanced DHT binding, AR-DHT complex stability, and enhanced nuclear localization of the complex[38]. Within this context the local production of androgens would be another way to overcome ADT, which is described by Labrie *et al*.. Although circulating androgen levels remain low due to ADT, the peripheral prostate tissue is able to produce androgens locally, maintaining the AR signalling[39].

The second mechanism of PCa progression is the promiscuous pathway, extending the ligands for the AR due to mutations in the binding site. Veldscholte *et al.* first published a change in the AR-ligand binding site from alanine to threonine at Amino Acid position 877, leading to androgen insensitivity and response to different ligands, i.e. corticosteroids of the receptor[40]. Flutamide, an androgen analogue used for ADT, caused a rapid increased in PSA-levels in patients, who had the A877T mutation. The antagonistic effect of Flutamide is changed to an agonistic, AR-stimulating effect in those patients[41].

In the outlaw pathway, receptor tyrosine kinases (RTK) phosphorylate and activate the AR via the MAPK or Akt signalling pathway, leading to an 'outlaw-AR' signalling. One RTK which is overexpressed in patients is the HER-2/neu. The MAPK-pathway is activated via Her-2/neu induced phosphorylation leading to a ligand independent activation of the AR[42]. Loss of the tumour suppressor *PTEN* can also induce AR-outlaw-signalling via activation of PI3K/Akt. Moreover, the PI3K/Akt pathway is downstream of other RTKs, such as cMET and EGFR[43].

The bypass pathway introduces a parallel signalling pathway, avoiding AR signalling, while maintaining the survival of prostate cancer cells. The *BCL2* gene is overexpressed in patients with prostatic intraepithelial neoplasia (PIN), but also in patients with CRPC, and is linked to apoptosis inhibition[44]. Gleave *et al.* showed, that upon *BCL-2* antisense oligonucleotide treatment of castrated mice, the progression of androgen-independent PCa could be delayed[45].

The fifth mechanism of prostate cancer progression is the lurker cell pathway, which involved the take-over of prostate cancer stem cells, which are androgen independent. Craft *et al.* showed that upon androgen deprivation LAPC-9 cells went to a dormant stage for approximately 6 months, however after this period cells could escape and showed androgen independent growth[46]. Maitland *et al.* followed the idea and identified a subpopulation of $CD133^{+}/\alpha_1\beta_2$ expressing cells as tumour initiating and as possible targets in prostate cancer therapy[47].

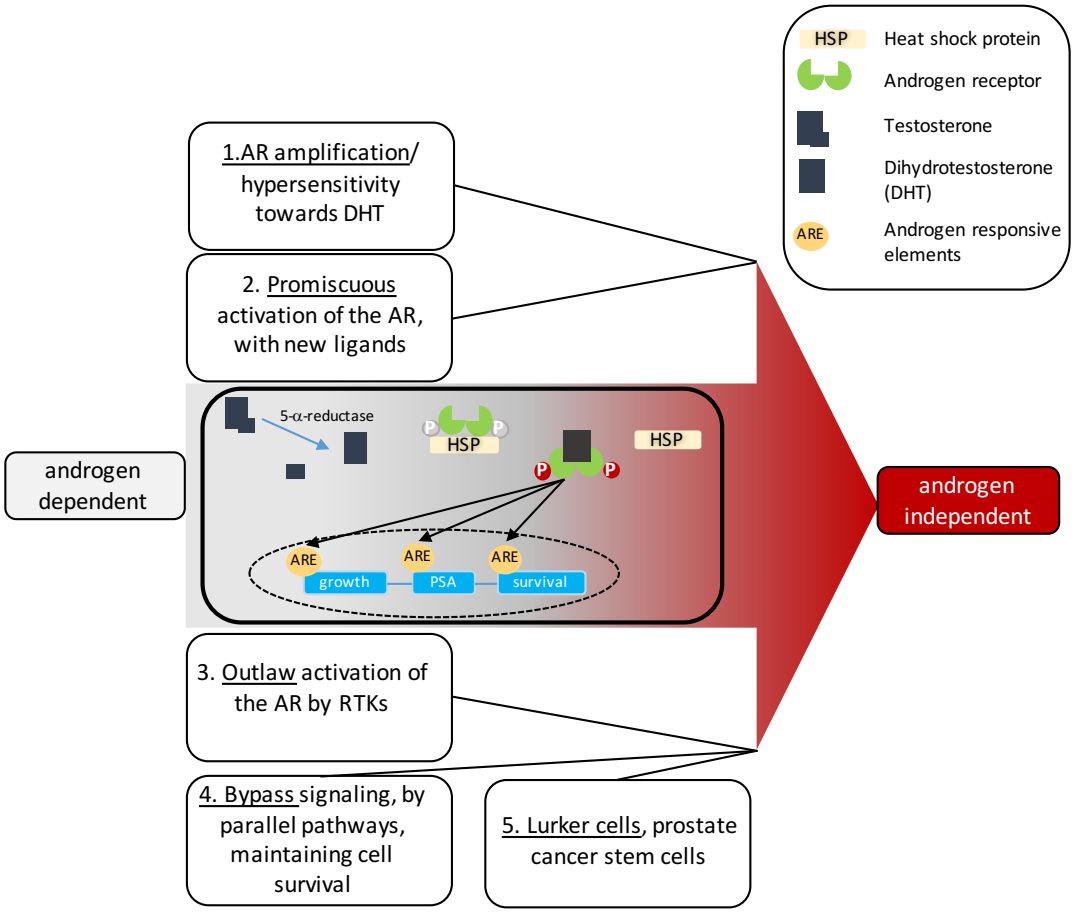

Figure 1.3 From androgen dependent to androgen independent prostate cancer

At an early stage, when prostate cancer is androgen dependent, upon entering the prostate tissue, testosterone is converted into DHT by 5-α-reductase. Once bound to the androgen receptor, HSP detaches and the active DHT-androgen-receptor complex can translocate to the nucleus, where it actives the ARE, leading to promotion of growth, upregulation of PSA and survival. Enhanced androgen dependent signalling can be inhibited via androgen ablation therapy; however, 5 mechanisms are postulated, which might lead to the androgen independent progression of prostate cancer. The mechanisms are as follows: 1) AR upregulation, causing DHT hypersensitivity, 2) activation of the AR by new ligands, 3) activation of the AR via RTKs, 4) activation growth and survival via independent mechanisms, and 5) prostate cancer stem cells which are androgen independent.

1.2.6 Alternative splicing, a promotor of prostate cancer?

To elucidate the molecular steps that contribute to the change in therapy susceptibility and identify new biomarkers, mRNA expression analysis of alternative splice (AS) variants were performed in two independent studies. Zhang *et al.* and Li *et al.* were able to identify 1532 mRNA splice variants form 364 prostate cancer related genes in 38 patients. In both studies it was possible via the alternative splice profile to distinguish normal from cancerous prostate tissue[48–50]. Two examples for AS in prostate cancer are discussed as new therapeutic targets, the *AR* gene, and the *CCND1* gene.

The AR is a transcription factor, activated via its ligand binding domain[51]. It is located at position Xq11-12, and men only possess one copy. The AR belongs to the steroid receptor transcription factor family, involved in regulation of testosterone and DHT. The AR shows a modular design consisting of a N-Terminal domain (NTD), encoded by exon 1, a DNA-binding domain (DBD), encoded by exons 2 and 3, and the C-terminal domain (CTD), encoded by exons 5-8. The NTD makes 60% of the AR cDNA, which is 10.6kb (Figure 1.4). One naturally occurring splice variant is known, AR45, arising from an exon within exon 1, termed exon 1a[52] (Figure 1.4). The AR CTD contains the ligand binding domain, which is subject to alternative splicing leading to PCa disease progression. The AR splice variants lack the ligand binding domain and become independent of androgens, which might be a reason for the shift from androgen dependent to androgen independent PCa[53]. Dehm *et al*., further identified AR splice variants which show duplication of exon 3 within the DBD, and a new exon 2a, which is attached to the 3' end. Especially, exon 2a variant led to androgen independent AR signalling in a xenograft-based model of androgen resistance therapy[54]. Another splice variant of the AR is AR-V7, lacking the CTD (Figure 1.4). This splice variant has been linked to treatment failures of patients with androgen resistant tumours. Enzalutamide, a non-steroid androgen, is used in the clinic with high efficacy in treatment of castration resistance metastatic prostate cancer (CRMPC) [55]. Abiraterone, an androgen synthesis inhibitor, is also used to treat patients with CRMPC[56]. However, although both drugs show high efficiency in first instance, there is also a high failure rate. Antonarakis *et al.* linked the AR splice variant 7 (AR-V7) to treatment resistance and failure in patients, which showed high abundance of this splice variant in clinical samples[57,58]. Currently, clinical trials are investigating new drugs, for instance Galeterone, targeting the AR-V7 in patients, showing efficacy in CRMPC patients in early clinical trials (ARMOR2)[59].

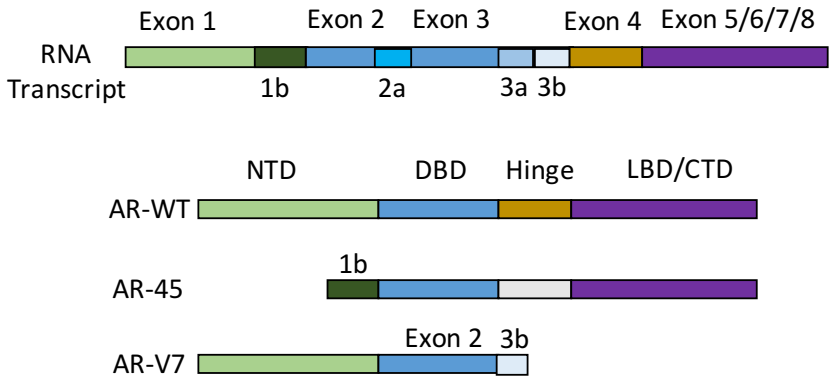

Figure 1.4 Overview of the Androgen receptor splice variants

The AR is subject to alternative splicing. An example of AR splicing is shown for the splice variants AR-45 and AR-V7 compared to the AR-wild type (WT).

The *CCND1* is classified as a proto-oncogene and used as a biomarker for disease progression in cancer[60]. It encodes cyclin D1, which is involved in cell cycle progression. During the cell cycle, cyclin D1 binds to cyclin-dependent kinase 4 (CDK4) triggering the G1 phase of the cell cycle. Two distinct splice variants of cyclin D have been identified in prostate cancer, cyclin D1a and cyclin D1b. Expression of cyclin D1b was linked to poor patient prognosis in prostate cancer[61]. One splice factor that was identified promoting cyclin D1b expression in prostate cancer is Sam68. The binding site for Sam68 was identified by Paronetto *et al.* in intron 4 leading to a transcription failure at the exon4/intron4 boundary and the stop codon present in intron 4 leads to a translation termination. They suggested that Sam68 is a splice factor of *CCND1* leading to alternative splicing. They assumed that increasing expression of Sam68 leads to enhanced expression of the cyclin D1b splice variant[61,62]. Cyclin D1 is suggested as potential therapeutic target in cancer therapy, however patients need to be carefully selected based on tumour genetics and proteomic signature to ensure treatment efficacy[60].

1.3 Zinc Metalloproteinases

Metalloproteases, which are mostly zinc dependent, are able to cleave peptide bonds and maintain many physiological and pathophysiological processes[63]. The super family of zinc metalloproteinases contains a conserved Met-turn and a zinc binding

motif, which contains a glutamic acid (E), flanked by two histidines (H), HEXXH. The histidines are required for zinc binding, whereas the glutamic acid deprotonates H_2O to OH^-, which is able to act as nucleophile during peptide bond cleavage [64,65]. This family can be further subdivided into three distinct subfamiles; gluzincin, aspzincin and metzincin. The metzincin family shows an elongated zinc binding motif, HEXXHXXGXXH , and the metzincin family will be the focus of this work. Due to structural conservation, Bode *et al.* suggested the subdivision of this family into different classes; serralysin, pappalysin, the matrix metalloproteinases, astacins and the A Distintegrin and Metalloproteinase (ADAMs) family[64,66,67].

1.3.1 Matrix metalloproteinases

Matrix metalloproteinases (MMPs), or matrixins, contribute to remodelling and maintenance of tissue due to their ability to degrade extracellular matrix components. The extracellular matrix is the main regulator for cellular function due to cell-matrix interactions. Extracellular matrix degradation regulates cell growth, morphology, apoptosis, invasion and migration, and it is mainly regulated by MMPs and serine proteases. Changes in regulation of this important function leads to cell invasion of surrounding tissue as seen in metastasis formation[68].

The first MMP discovered was the collagenase by Gross and Lapiere in 1962[65]. There are 23 MMPs have been identified in humans[69]. The conserved structures throughout the MMP family are the cysteine switch motif that regulates MMP activity, as it maintains the zymogen form, and the zinc-binding motif in the catalytic domain, a hinge region and some members contain a hemopexin domain. The only exception lacking the zinc-binding domain is MMP-23.

Since the first discovery in 1962, MMPs became more important as they are key players in diseases such as rheumatoid arthritis and cancer.

1.3.2 ADAMs

The ADAMs are a family of multi-domain transmembrane glycoproteins that are essential regulators of cell surface events such as cell adhesion, shedding, migration and fertilization. They also belong to the metzincins family (Figure 1.5). Their name summarizes the conserved structures, as they all contain a Met residue within the active site and require zinc ions for the catalytic enzymatic reaction[70]. The human genome comprises 21 ADAM genes and five pseudogenes[71], all of which contain a metalloproteinase (MP) domain, however, only 13 ADAMs are proteolytically active. They further contain a modular conserved domain structure consisting of the N-terminal extracellular domain, the transmembrane region and the C-terminal

intracellular domain. They were identified during an analysis of proteolytic processing of fertilin (PH-30) involved in sperm-egg fusion, and were first described by Wolfsberg *et al.* and later by Blobel *et al.* [72–74].

Most ADAM family members are type I transmembrane proteins, which are located at the cell surface, however, soluble splice variants for ADAM12 and ADAM33 exist[75,76].

1.3.2.1 ADAMs modular protein structure and function

ADAMs are synthesised as inactive precursor proteins, as zymogens. The inactive state of the ADAMs is maintained via the interaction of a cysteine residue in the pro-domain and the zinc ion in the MP-domain. The activation of the protease occurs either via furin-like convertases or via autocatalysis[77]. The activation mechanism is known as cysteine switch[78]. The pro-domain is further important in its function as intramolecular chaperon, enabling proper protein folding[79]. The protease domain comprises the catalytic conserved sequence, HEXXH. Only those ADAMs containing the HEXXH motif in their protease domain are catalytically active[70] (Figure 1.5). Substrates that are target sites of the protease function are growth factors, adhesion molecules, cytokines, and cytokine receptors[77]. The disintegrin-domain, downstream of the protease domain, is conserved in all 21 ADAM family members. It contains a 14-amino acid sequence known as the disintegrin loop, allowing association with integrins. Most integrin ligand binding occurs via an Arginine-Glycine-Aspartic Acid – motif, RGD-motif, which is only present in ADAM15, which enables specific binding to $\alpha_v\beta_3$ and $\alpha_5\beta_1$ integrins[80]. The conserved sequence, Arginine-X-6-Aspartic Acid-Leucine-Proline-Glutamic Acid-Phenylalanine (RX6DLPEF), enables other ADAM family members to associate with integrins. Downstream of the disintegrin domain is the cysteine-rich region, which is involved in cell adhesion and substrate recognition. The transmembrane region or linker region connects the N-terminal extracellular domain (ECD) and C-terminal intracellular domain (ICD) (Figure 1.5). The ICD is highly variable within the ADAM family and differs in sequence and size, with common proline-rich regions enable interaction with Src homology 3 – domain (SH3) containing proteins. ADAM specific interaction partners, such as Src, Grb2, growth factor receptor binding protein 2 (GFRBP2), phosphatidylinositol 3-kinase (PI-3K), protein tyrosine kinase 6 (PTK6) have been identified[79,81].

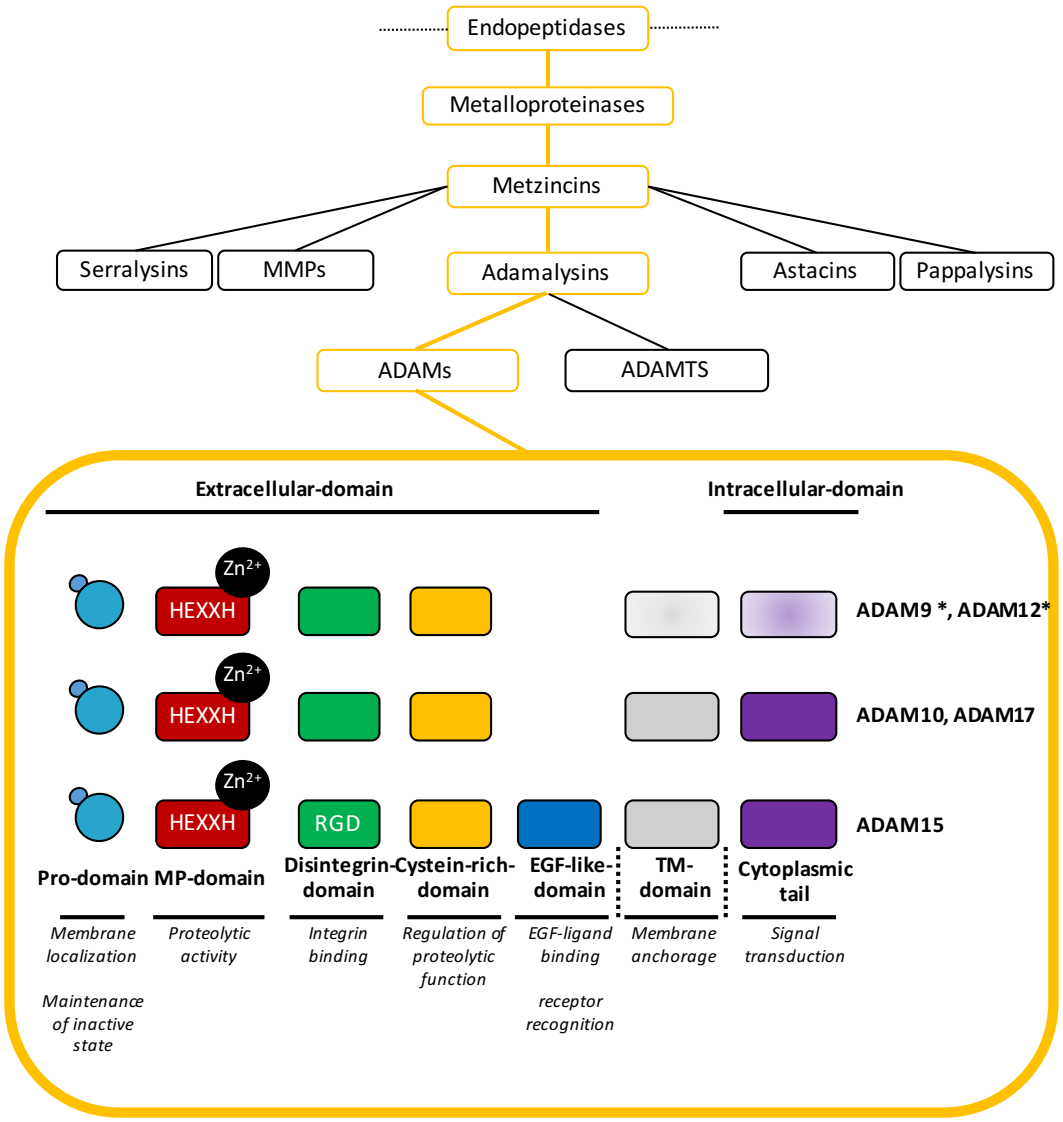

Figure 1.5 ADAMs modular protein structure and their functions.

The ADAMs family belongs to the family of endopeptidases and is further classified as metalloproteinase, due to the metalloproteinase domain, which is conserved in the proteolytically active ADAMs. Metalloproteinases are further classified as metzincins and Adamlysis, leading to the ADAM family. Proteolytically active ADAMs, such as ADAM9, ADAM12, ADAM10, ADAM17 and ADAM15, all contain the zinc binding metalloproteinase domain. Further they exhibit a disintegrin and cysteine-rich domain. ADAM15, has a RGD motif within the Disintegrin-domain, which enables association with the integrins $\alpha_v\beta_3$ and $\alpha_5\beta_3$. Compared to the others, ADAM15 further has a EGF-domain. ADAM9 and ADAM12 can be present as membrane anchored or as soluble (indicated by the asterisk), i.e. not membrane anchored. The soluble variants lack the cytoplasmic domain, important for intracellular signalling.

1.3.2.2 The physiological and pathological roles of ADAMs

The ADAMs family is essential during fertilization, development of the central nervous system, the heart, the lung and the epithelium. The first ADAMs to be identified were ADAM1 and 2 which were found to be involved in sperm-egg fusion, an essential process in human development[82]. ADAM3 was also linked to sperm-egg fusion and membrane adhesion. Yuan *et al.* found upon comparison with ADAM2, that ADAM3 is involved in the adhesion of sperm and egg, leading to the fusion of both[83]. The Phenotype of knock out mice showed a prenatal lethality for ADAM10[84] and ADAM17[85] knock out models. For ADAM17 faulty EGFR signalling could be identified leading to prenatal lethality[86]. ADAM12 knock-outs had a 30% prenatal death rate[87], and ADAM19 knock out models were up to 80% lethal postnatally due to defects in cardiac morphology [88].

Although ADAMs are linked to disease progression in cancer, they are also known to be involved in non-cancer diseases such as rheumatoid arthritis, chronic renal diseases, asthma and Crohn disease[70]. ADAM8 is commonly expressed on leukocytes, neurons and osteoclasts. It has been identified to be involved in neurogenerative processes and osteoclastogenesis, however its function is not yet fully understood. Gomez-Gaviro *et al.* identified a higher amount of expressed ADAM8 on neutrophils isolated from the synovial fluid of rheumatoid arthritis patients. The level of ADAM8 expression correlated with the degree of joint inflammation in those patients[89]. ADAM10 on the other hand has been identified to shed the APP, a key protein in Alzheimer's plaque formation. ADAM33 overexpression is linked to asthma susceptibility. The ADAMs 11, 22 and 23 are predominantly expressed in the central nervous system (CNS) [90,91]. ADAM11 has been linked to pain transmission due to its expression in the CNS. In neuropathic animal pain models such as Von Frey or Hot-plate, ADAM11 showed a role in pain transmission and perception. The role in neuropathic pain maintenance, caused by inflammation, was suggested to be mediated by adhesion to β_1 integrin[92], as ADAM11 is able to bind to $\alpha_6\beta_1$ and $\alpha_9\beta_1$[93]. ADAM17 is a key player in rheumatoid arthritis and inflammatory diseases, as it is known to produce soluble TNF-α[94]. With regard to its major role in inflammatory diseases, ADAM17 is also thought to be a mediator of inflammation-related cancer[77,95].

Most of the ADAMs are reported to be upregulated during disease progression, for instance, cancer or rheumatoid arthritis. Mochizuki *et al.* concluded that the upregulation in cancer might be linked to the multiple function of the ADAMs in cancer

biology. They described five distinct functional interactions: 1) The zymogen transition to the active, functional state of ADAMs, via furin or MMPs, which are also upregulated during cancer[96], 2) the proteolytic cleavage of growth factors and their receptors, and further the downstream activation via the intracellular domain of PKC or MAPK pathway, inducing cell proliferation and increased survival, 3) the interaction via their disintegrin-like and cysteine-rich domain with integrin and syndecans, leading to impaired cell-cell or cell-matrix interaction, 4) the proteolytic disruption via the metalloproteinase domain of the extracellular matrix, 5) the proteolytic cleavage of membrane bound cytokines or chemokines leading to cancer progression and proliferation.[97] ADAM10 and ADAM17 are extensively investigated in relation to cancer, which might be due to their shedding of the epidermal growth factor receptor (EGFR) ligands EGF and TGF-α[98]. ADAM8, ADAM15 and ADAM19 on the other hand are linked to invasion of cancer cells[99,100].

1.3.2.3 Prostate cancer and ADAMs

ADAMs are considered as promotors of metastasis in prostate cancer due to two key features. Their ability to degrade the extracellular matrix (ECM) via their metalloproteinase domain and their ability to induce cell migration. ADAMs are known to degrade a variety of ECM components such as collagen IV, laminin, vitronectin, fibronectin and gelatin[101]. To be able to metastasise, cells further need to migrate through the degraded matrix. ADAMs are able to bind integrins leading to formation of cell-cell or cell-ECM interactions. Enabeling the cell to move through the ECM.

McCulloch *et al*. identified ADAM9, ADAM10, ADAM11, ADAM15 and ADAM17 to be present in the LNCaP, ALVA-41, DU-145 and PC3 human prostate cancer cell lines[102]. They further revealed the androgen-dependent regulation of ADAM9, 10 and -17 expression in the LNCaP cell line. Arima *et al*. showed that in benign prostate cancer ADAM10 is localized to the plasma membrane. During disease progression, localization of ADAM10 is shifted form the membrane to the nucleus[103]. ADAM9 is described as an independent prognostic marker in prostate cancer by Fritzsche *et al*. [104]. In addition, Najy *et al.* identified ADAM15 as a metastatic promotor in prostate cancer. Downregulation of ADAM15 in a PC3 cell model reduced adhesion and migration and further weakened the bone-homing effect of those cells in a SCID mouse model[105].

Although ADAMs play a role in prostate cancer progression and are a promising target due to their involvement in pathways such as EFGR or MAPK, they have so far not been considered as key target site for prostate cancer[66].

1.3.3 ADAM9

ADAM9, Meltrin-γ was first identified as a myoblast fusion protein by Yagami-Hiromasa *et al.*[106]. It was characterized as a membrane-anchored glycoprotein with a molecular weight of 84kDa. Weskamp *et al.*, proposed a role in cell-cell interaction[107]. Although most of the ADAM9 structure is conserved when compared to the ADAMs family, it contains a Threonine-Serine-Glutamic acid-Cysteine motif (TSEC) within the disintegrin domain[107]. To identify the physiological role of ADAM9 in development, knock out mice were created and they developed normally, suggesting that ADAM9 itself is not essential for development[108]. Proteolytic substrates that have been identified for ADAM9 are the EGFR ligand HB-EGF[109], the extracellular matrix protein laminin[110], and the epithelial adhesion molecule collagen XVII [111]. Recently Moss *et al.*, identified the family member ADAM10 as substrate for ADAM9[112].

Like most ADAMs, ADAM9 is upregulated in various types of cancer to the extent that the ADAM9 levels correlate with cancer progression. In prostate cancer ADAM9 has been validated as a prognostic marker. By characterization of 198 patient immunohistostainings, Fritzsche *et al.* found that ADAM9 expression can be used as independent marker for disease relapse. They showed high levels of ADAM9 in prostate cancer samples from patients which had undergone prostatectomy correlated with relapse free survival. High expression levels of ADAM9 and aggressive disease progression, were identified in younger patients diagnosed with prostate cancer[104]. In general, ADAM9 is found in several prostate cancer cell lines which are androgen independent or dependent[113]. Overexpression of ADAM9 in the androgen dependent prostate cancer cell line LNCaP leads to increased cell survival, and knock down of ADAM9 resulted in higher cell death[114]. Martin *et al.* identified the recombinant disintegrin domain of ADAM9 as anti-adhesive molecule inhibiting cell adhesion, migration and invasion via interaction with the integrin $\alpha_6\beta_1$. Furthermore, they suggested ADAM9 as key to reduce metastatic spread, when adding an artificial ADAM9 disintegrin domain to cells[115].

1.3.4 ADAM10

ADAM10 is a 748 amino acid type I transmembrane glycoprotein. It was identified by Chantry *et al.* in bovine brain myelin membrane as myelin basic protein (MBP) degrading protein[116]. Lammich *et al.* identified the amyloid precursor protein (APP) as a substrate for ADAM10. Cleaved fragments of the APP, such as amyloid β peptide (Aβ), are major components of amyloid plaques in Alzheimer's disease[117].

ADAM10 was shown to have an important role in Alzheimer's disease and is also an important promotor in prostate cancer. McCulloch *et al.* showed ADAM10 overexpression in the androgen dependent prostate cancer cell line LNCaP, and they linked increased DHT levels to increased ADAM10 expression[118]. Importantly, they were able to show a translocation of ADAM10 from the plasma membrane in benign prostate cancer to the nucleus in advanced prostate cancer[102]. Notably Arima *et al.* identified ADAM10 as a factor regulating cell proliferation in LNCaPs due to nuclear translocation. This translocation from the membrane to the nucleus is androgen dependent and is important for tumour progression[103]. ADAM10 was identified to shed E-cadherin, important for cell-cell adhesion, migration, differentiation and tissue development, when overexpressed in ADAM10$^{-/-}$ fibroblasts, and HaCaT epithelial cells. Shedding of E-cadherin further modulated β-catenin translocation. β-catenin is involved in controlling cell proliferation by binding to transcription factors, such as lymphocyte enhancer-binding factor 1, regulating c-myc and cyclin D1. Translocation of β-catenin leads to enhanced cell proliferation[119]. In the nasopharyngeal carcinoma cell line CNE-2, epithelial-mesenchymal transition (EMT), proliferation and migration was significantly reduced upon ADAM10 siRNA knock down[120] (Figure 1.6).

The molecular mechanism leading to cMET shedding upon treatment with the anti-cMET antibody DN30, inhibiting anchorage independent growth and HGF dependent invasion, remained unclear for a long time. Schelter *et al.* identified that ADAM10 is necessary to induce DN30 mediated cMET shedding. Previously, Kopitz *et al.* identified that down-regulation of ADAM10 prevents shedding of cMET in patient liver tumour samples with elevated tissue inhibitor of metalloproteinases-1 (TIMP1) levels, a known ADAM10 inhibitor[121]. Shedding of cell surface receptors such as NOTCH and Axl, overexpressed in aggressive cancers like glioblastoma or triple negative breast cancer, was also identified to be caused by ADAM10. Shedding of NOTCH by ADAM10 leads to receptor activation, and results in a remaining transmembrane NOTCH fragment. The NOTCH intracellular domain (NICD) is processed by γ-secretase, leading to its translocation to the nucleus, and upregulation of gene transcription containing recombinant binding protein suppressor of hairless (RBP-J) binding sits[84,122]. Miller *et al.*, showed that down regulation of ADAM10 by siRNA in MDA-MB-231 breast cancer cells, results in reduced soluble Axl in the medium, and enhanced surface level. Combined Axl inhibition and ADAM10 knock down results in decreased cell growth and proliferation[123] (Figure 1.6).

1.3.5 ADAM17

The tumour necrosis factor (TNF) –α converting enzyme (TACE), ADAM17, was identified by Moss *et al.* in 1997. Compared to the structural domains of the ADAM family, ADAM17 does not contain the EGF-like and the cysteine-rich domain. Instead, it possesses a disulfide-regulated membrane-proximal domain (MPD) and a stalk region, the conserved ADAM17 Dynamic Interaction Sequence (CANDIS). Both mentioned domains, are important for ADAM17 substrate recognition and binding, and further regulate the protease activity via interaction with the plasma membrane[124]. pro-TNF-α is a 26kDa membrane bound precursor form of TNF-α. ADAM17 cleaves pro-TNF-α between Alanine at position 76 and Valine at position 77, resulting in a 17kDa active form[125]. TNF-α is involved in inflammatory diseases and ADAM17 cleavage of pro-TNF-α is thought to be a key initiator of inflamation[126]. ADAM17 is further characterized as regulator of immune responses ,due to its function to cleave ErbB ligands and their receptors interleukin-6 receptor (IL-6R) and the cell adhesion molecules L-selectin and ICAM-1[95].

In prostate cancer, ADAM17 was identified as regulator for cell proliferation by Lin *et al.*[127]. Via shedding of epidermal growth factor receptor (EGFR) - pro ligands, such as transforming growth factor – α (TGF-α), it regulates the EGFR/PI3K/AKT signalling cascade. Upon EGFR signalling cascade activation, cancer cell proliferation is enhanced due to downstream activation of cell cycle coordinators, such as cyclin-dependent kinases (CDKs). As a result Lin *et al.* postulated ADAM17 as a promotor of prostate cancer progression[127]. Different from the effect on cell proliferation, overexpression of ADAM17 enables cell invasion in androgen independent prostate cancer cell lines, DU-145 and PC3. ADAM17 is able to upregulate matrix metalloproteinase (MMP)-2 and MMP-9, involved in tumour metastasis. Enhanced EGFR-MEK-Erk activation due to ADAM17 overexpression, leads to upregulation of MMP-2 and MMP9, enhanced TGF-α media levels, and increased cell invasion of DU-145 and PC3 prostate cancer cells[128] (Figure 1.6).

ADAM17 was also identified as a sheddase of RTKs such as Axl and cMET, which are highly overexpressed in primary tumours and metatstatsis[129,130]. Van Schaeybroeck *et al.* identified that inhibition of MEK in *KRAS*-mutant colorectal cancer, caused increased cMET signalling, due to inhibition of ADAM17. Combined treatment, including cMET inhibitors, leads to increased apoptosis and decreased tumour growth *in-vivo*[131].

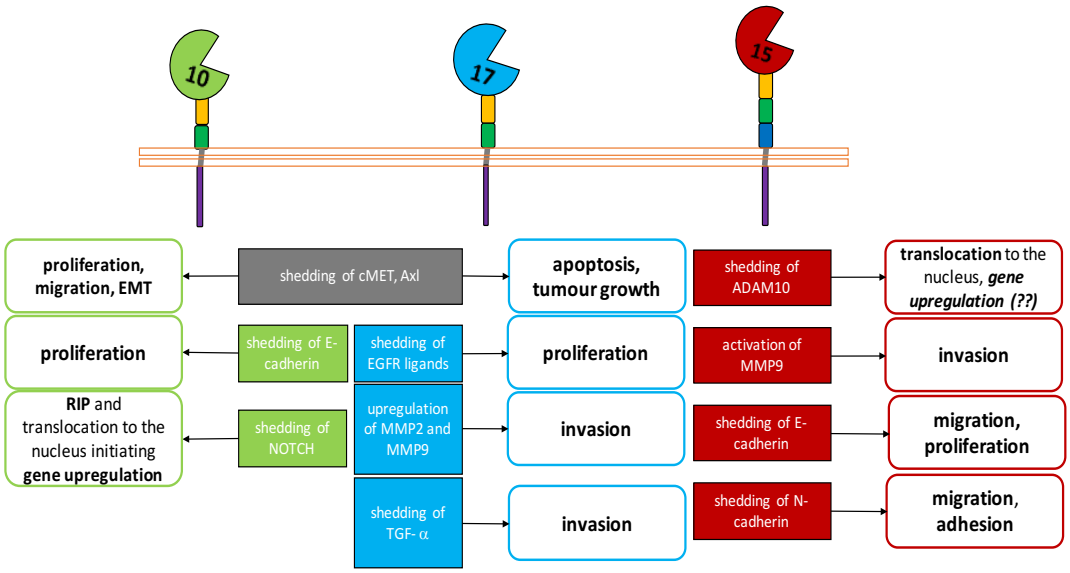

Figure 1.6 Overview of ADAM10, ADAM17 and ADAM15 functions and their consequences in cancer

Overexpression of ADAM10 (green), ADAM17 (blue) or ADAM15 (red) is linked to disease progression in cancer. The proteolytic activity is required and leads to shedding of receptors such as cMET, Axl or NOTCH, or ligands such as TGF-α, or cell-adhesion proteins like E-cadherin or N-cadherin, which all lead to enhanced invasion, migration, proliferation and tumour growth. ADAM10 is shed by ADAM15, leading to the translocation of the ICD to the nucleus and might be linked to upregulation of gene expression.

1.4 ADAM15

ADAM15 is a transmembrane multi-domain, multi-functional metalloprotease and is upregulated in many cancers. During prostate cancer, the upregulation of ADAM15 correlates with disease progression[132] which is linked to ADAM15s multi-functional domain structure[81]. ADAM15 is involved in reduction of tumour cell adhesion, reduction of cell-cell adhesion and further promotes metastatic spread of cells via its disintegrin and metalloproteinase domain[100]. In its function as protease, it is able to influence cell signalling via growth factor shedding, which leads to receptor activation[100]. ADAM15 is therefore considered as key player in cancer progression and could be an important therapeutic target.

1.4.1 ADAM15 discovery

ADAM15 was first described and biochemically analysed by Kraetzschmar *et al.* in 1996[133]. A 2740bp cDNA for *ADAM15* was identified with an open reading frame encoding a 814 amino acid protein with a calculated molecular weight of 85kDa.

1.4.2 ADAM15 gene structure

ADAM15 is localized on chromosome 1q21.3, a region that is often rearranged in prostate and breast cancer[134]. From translation initiation to the polyadenylation

signal, the *ADAM15* gene spans a region of 11.4kb. It includes 23 exons and 22 introns. The exon size varies between 63 to 316bp, whereas the intron size varies from 79bp to 1283bp. Exons 19 to 21 encoding the intracellular domain (ICD) of ADAM15, are alternatively used and the resulting splice variants have varying expression levels in different tissues[135]. So far, 13 different splice variants have been identified[135].

1.4.3 The modular structure of ADAM15

1.4.3.1 Pro-domain

The N-terminal pro-domain of ADAM15 consists of the signal peptide, which is 17 amino acids in length and the pro-peptide consisting of 189 amino acids (Figure 1.7). The signal peptide targets ADAM15 to the plasma membrane[136]. At position 179 of the pro-domain, ADAM15 contains a cysteine, which is conserved within the metzincin family. The cysteine binds the catalytic zinc ion and due to this, the inactive state as a zymogen is maintained. Furin-like endopeptidases, cleave within the pro-domain causing a structural destabilization, known as the cysteine-switch-mechanism, and leading to the activation of ADAM15[66,78].

1.4.3.2 Metalloproteinase domain

The active site of ADAM15 is downstream of the pro-domain and is comprised of 210 amino acids in total. Within this domain, the zinc-binding motif, the Met-turn, is important for metalloproteinase activity of ADAM15 (Figure 1.7). The Met-turn of ADAM15 starts from position 376 to 382 with the following one-letter amino acid code: CIMEAST[137]. Tallant *et al.* reveal the importance of the Met-turn via crystallography, which is found in all metzincins metalloproteases[138]. In a 3D-model the Met-turn is directly found below the zinc-binding motif. The Met-turn seems to be important for folding as when it was replaced, proteolytic activity was reduced up to 50%[138]. Tallant *et al.* concluded that the structure of the Met-turn itself maintains the architecture of the zinc-binding site due to hydrogen bonds that are formed via the Met-turn. The zinc-binding domain of ADAM15 is upstream of the Met-turn and starts at position 348 to 359 with the following amino acid sequence: HELGHSLGLDHD. The underlined structures are conserved within the metzincin family. The histidines (H) starting from position 348 enable zinc binding. In more detail, the 3 histidines within this domain show a tetrahedral molecular arrangement, an additional H_2O molecule guides the zinc towards the binding domain. Glutamic acid (E) at position 349 initiates catalysis[139].

1.4.3.3 Disintegrin domain

The disintegrin domain of ADAM15 spans 90 amino acids. Within the disintegrin domain, 15 cysteines are present which are conserved with other ADAMs of the metzincin family[139]. Further, the domain contains an arginine-glycine-aspartic acid (RGD) binding motif at position 484-486 (Figure 1.7). This RGD motif is a unique motif of ADAM15 among ADAMs, which is also found in snake venom disintegrins and in most disintegrin-like proteins[139]. The disintegrin domain enables ADAM15 to interact with intergrins, a family of heterodimeric transmembrane glycoproteins. The binding occurs via the disintegrin loop which is conserved in all ADAMs. The disintegrin loop ADAM15 starts from position 480 and ends at 493: CRPT**RGD**CDLPEFC, the underlined amino acids are the conserved ones. The RGD-motif within the extracellular disintegrin domain enables ADAM15 to specifically bind to αvβ3 and α5β3 integrins as Zhang et al. described[80], and more over leads to the proposed name as metargidin i.e. metalloprotease-RGD-disintegrin protein[136]. Trochon-Joseph *et al*. showed the importance of the RGD domain of ADAM15, as melanoma cells with impaired ADAM15 RGD-motif showed reduced migration and metastasis[140].

1.4.3.4 Cysteine-rich domain

Within the metzincin family the cysteine-rich domain is linked to membrane fusion and regulation of protease function[73]. However, little is known and published about the ADAM15 cysteine-rich domain and its' function. It starts downstream of the disintegrin domain (Figure 1.7) and it comprises in total 12 cysteine-residues. Due to the lack of a hydrophobic region within this domain (e.g. ASRPVIGTNAVSIETNIPLQQGGRIL for i.e ADAM12[141]), which is essential for ADAM dependent membrane fusion, it is debatable whether this domain is linked to membrane fusion[142].

1.4.3.5 EGF-like domain

The EGF-like domain of ADAM15 is the last functional domain of the ADAM15 ECD. The name EGF-like derives from its sequence similarity with epidermal growth factors (EGF). It starts with a cysteine (C), contains 29 amino acids and is the shortest of all functional domains of ADAM15 (Figure 1.7). The domain is structurally stabilized by three disulphide bonds, and shows a β-sheet fold[143].

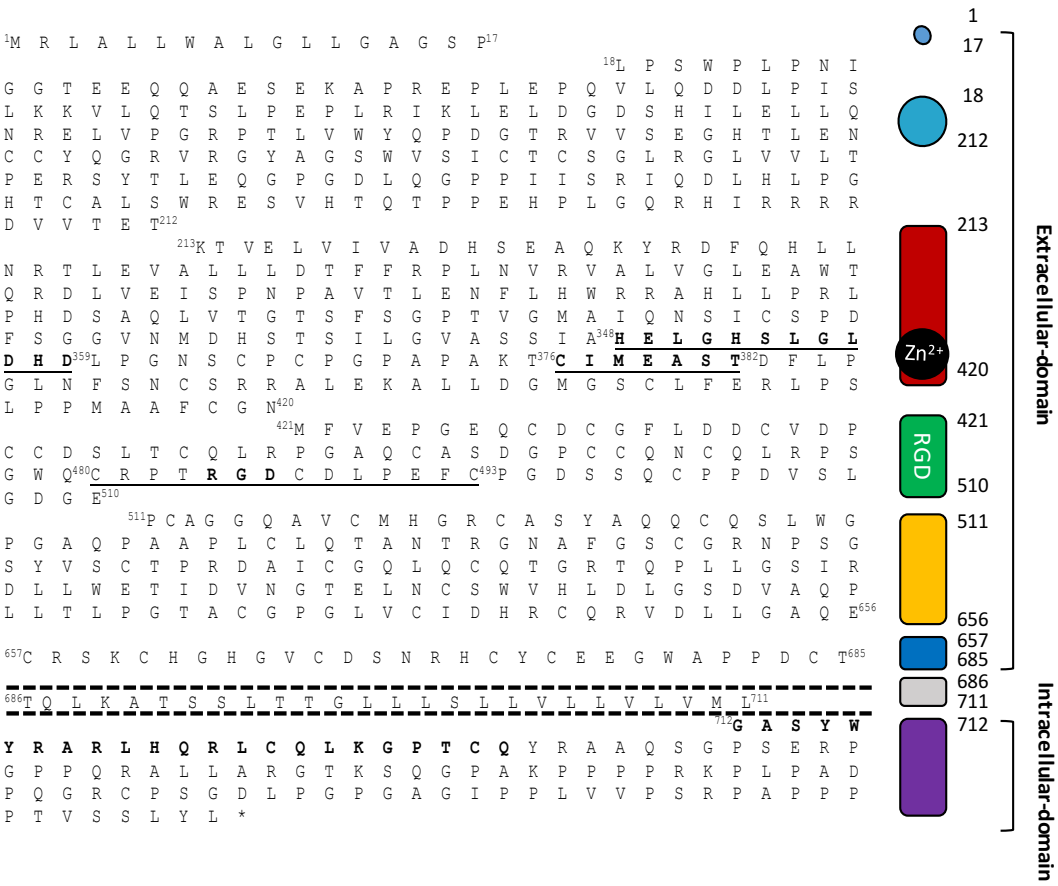

Figure 1.7 Overview of the ADAM15 amino acid domain structure

ADAM15 has a modular structure and is composed of five ECDs, a transmembrane region and the ICD. The ECD starts with the signal peptide (amino acid 1-17), targeting ADAM15 to the membrane and the pro-domain (amino acid 18-212), keeping ADAM15 in an inactive state. Downstream (amino acid 213-420), the proteolytic domain, the metalloproteinase domain is located. The zinc-binding motif is located within the metalloproteinase domain from position 348-359. The Met-turn, upstream of the metalloproteinase domain, is responsible for maintaining zinc-binding. The disintegrin domain (amino acid 421-510) contains the integrin binding motif RGD (amino acid 480-491), enabling ADAM15 to bind αvβ3 and α5β3 integrins. The cysteine rich domain follows form position (amino acid 511 to 656), however little is known about its function. The last domain of the ECD is the EGF-like domain (amino acid 657 - 685) enabling ADAM15 to contribute to NOTCH-signalling. The transmembrane region (amino acid 686- 711), links ECD and ICD. The ICD of ADAM15 is subject to alternative splicing. This example shows the amino acid structure of ADAM15-A, starting from amino acid position 712 and exhibiting proline-rich regions, which enable SH3-domain containing proteins to associate.

1.4.3.6 The intracellular domain (ICD)

The extracellular domain (ECD) of ADAM15 is connected via the transmembrane region to the intracellular domain (ICD) (Figure 1.7). The ADAM15 ICD is subject to alternative splicing, with 13 splice variants identified, spanning amino acid sequences between 772 and 863[144]. The main difference within the splice variants is the number of proline rich regions, which enable ADAM15 to associate with SH3 containing

signalling molecules, such as Src-family kinases[145]. A detailed overview of identified ADAM15 interaction partners will be given in section 1.4.5. Tyrosines within the ADAM15 ICD are subject to phosphorylation and enable binding with SH2 domain containing proteins[145].

Although 13 ICD splice variants have been identified, the focus of this study will be on splice variant 2, 4a, 6a, 1 and 5[135]. These splice variants are from high interest in our study as these are the only splice variants which show proline rich binding motif within the ICD[144], they are expressed within cancerous tissue[146], they have been linked to functional consequences when overexpressed in breast cancer cells and further have have been linked to different disease outcome in patients[81]. The terminology which will be used here, is ADAM15-A (2), ADAM15-B (4a), ADAM15-C (6a), ADAM15-D (1) and ADAM15-E (5). All of them differ in their number of proline-rich regions due to the alternative use of exons 19 to 21. ADAM15-D lacks proline rich binding motifs because a frameshift mutation in exon 18 leads to the insertion of a premature stop codon resulting in the lack of proline rich regions. ADAM15-C is the longest variant, with 863 amino acid and the highest number of proline-rich regions, containing exon 19,20a and 21. ADAM15-B and E consist of 839 amino acid and differ in the alternative exon use of 20a for B and 21 for E. ADAM15 splice variant A consists of 814 amino acid, the alternative exon present is 19[81,135]. A schematic overview of the ADAM15 ICD splice variants is shown in Figure 1.9.

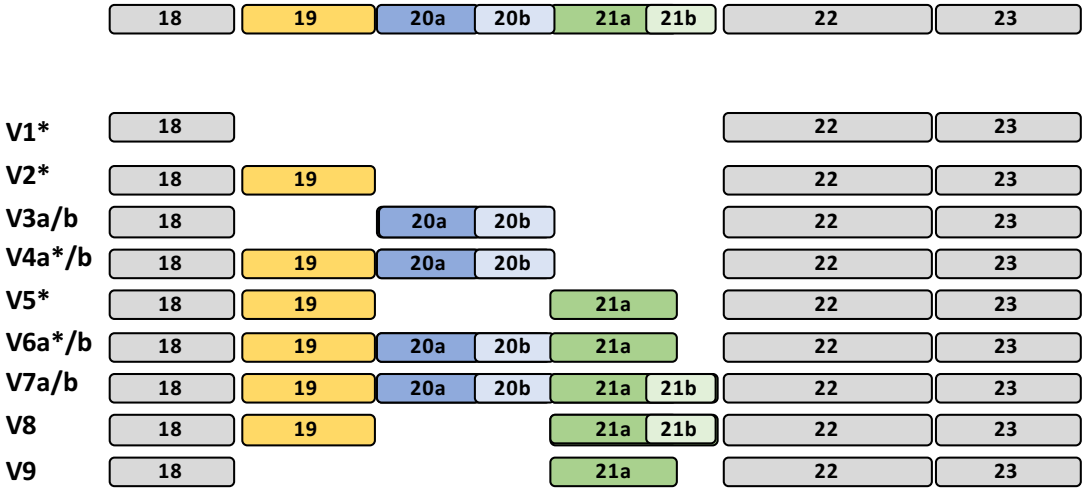

Figure 1.8 Overview of the 13 *ADAM15* splice variants

Alternative exon use of the ADAM15 ICD leading to the presence of 13 splice variants. Splice varaints highlighted with the asterisk are the splice variants which are subject in this study.

1.4.4 ADAM15 alternative exon use of the ICD

13 different variants of the ICD of ADAM15 have been identified which is due to an alternative exon use of 19 to 21[135] (Figure 1.9). Kleino *et al.*, described the alternative exon use as physiological post-transcriptional mechanism which regulates the expression of ADAM15 splice variants in human tissue. The mechanism leading to the different splice variants is unknown, however, as splice variants from human, and mouse match, it is likely that a common factor regulates the splicing of ADAM15[135] (Figure 1.9).

As indicated before, the mechanism that gives rise to the 13 different splice variants is unknown, however Kleino *et al.* discussed possible factors that might lead to the alternative exon use. They suggested that ADAM15 splicing might be controlled via the exonic splice enhancer (ESS) motifs which are flanking exons 19, 20a/b and 21a. Kleino *et al.* postulated a looping out mechanism that regulated the alternative exon use, and they based their hypothesis on the presence of heterogenous nuclear ribonucleoproteins (hnRNP) binding motifs within exon 19, 20 and 21[135]. HnRNPs are a family of RNA-binding proteins that recognize specific sequences of RNA. They are involved in RNA processing and can further act as a factor regulating gene expression[147]. The introns which are next to the exons contain even more ESS motifs compared to the exons. The introns further show a number of alternative splicing-elements, such as FOX, Nova1/2, CELF/BrunoL, MBNL1 and ESACG[135]. Warzecha *et al.* found that ESRP1 and ESRP2 are also involved in ADAM15 splicing, as they regulate enhanced use of exon 20 and 21[148]. Kleino *et al*. showed that introns 18, 19 and 21 contain ESACG binding motifs. ESACG is known to recognize C- and G-rich motifs which are found in high numbers in introns 18, 19 and 21 and this is linked to exon skipping[135].

Although some splice related elements and regions have been found in the introns and exons of the ICD of ADAM15, no potential regulator has been identified. The identification of an ADAM15 ICD splice regulator would be helpful as only a few of the ADAM15 ICD splice variants are associated with aggressive disease progression in cancer.

A

Splice variant	Kleino *et al.*	DNA variant sequence	Protein sequence	Gene Bank variant	Proline- rich regions	Amino acids
A	2	NM003815.4	NP003806.3	2	3	814
B	4a	NM 207194.2	NP 997077.1	3	4	839
C	6a	NM 207196.2	NP 997079.1	5	5	862
D	1	NM 207191.2	NP 997074.1	1	0	772
E	5	NM 207195.2	NP 997078.1	4	4	838

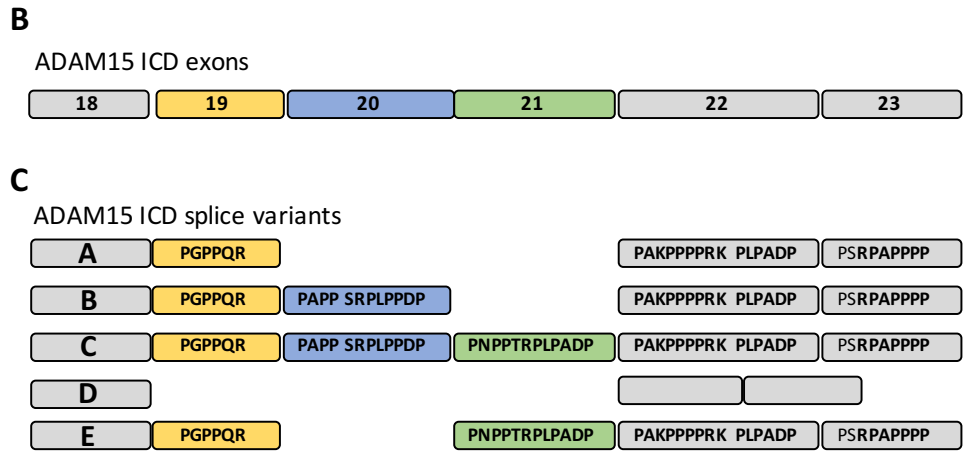

Figure 1.9 Overview of the ADAM15 ICD splice variants.

(A)Splice variants are shown as used throughout the thesis, with their name, DNA and protein sequence number, gene bank variant nomenclature, number of proline rich regions and the number of amino acids. (B) The ADAM15 ICD with the corresponding exons 18 to 23 is shown, from which exons 19 to 21 are alternatively used. (C) The alternative used of exons 19 to 21 give rise to the 5 different splice variants, subject of this study, all varying in their number of proline-rich regions. ADAM15 splice variant D lacks proline rich regions, due to a premature stop codon, upstream exon 19.

1.4.5 Identified interaction partners of the ADAM15 ICD

The proline-rich regions of the ICD enable the binding of Src homology-3 (SH3) – domain containing proteins. The different number of proline-rich regions, impact protein binding and might contribute to intracellular signalling, protein regulation and cellular function[144]. Out of the 13 splice variants, ADAM15 ICD splice variants A, B and C have been extensively characterized for different association partners, with the aim to identify splice variant specific protein/protein complexes.

Zhong *et al.* identified equal association of the adaptor proteins Grb2 and Tks5/Fish and the serine/threonine kinase ERK to ADAM15 A, B and C. Splice variant specific interaction was shown for the adaptor protein NcK, which associates with ADAM15- B

and C but not with A. Src associates strongly with B and C but shows only weak interaction with ADAM15 A. Another tyrosine kinase, PTK6, was found to associate with A and B but not with C[81]. Poghosyan *et al*. identified the association of ADAM15-A with Src family kinases Lck and Hck. Here, the binding via the SH3 domains for Lck is the main factor leading to the association, however phosphorylation of ADAM15 seems to be required. Next to the SH3-domains, Hck possesses an SH2-domain, allowing binding to phosphorylated tyrosines. Upon ADAM15 phosphorylation Hck showed enhanced binding[145]. This finding was also confirmed by Yasui *et al.*, which validated the phosphorylation dependent interaction between ADAM15 and Lck and further showed that ADAM15-C binds Lck and Hck upon ADAM15 phosphorylation[149]. To enable the screening of more association partners for ADAM15 ICD splice variants, Kleino *et al.* used the yeast two hybrid approach and identified the sorting nexins SNX33 and SNX9 as strong interaction partners for ADAM15-A and C. For ADAM15-C they also identified Nephrocystin and the Src family kinase member Lyn[144]. They also identified Neutrophil cytosolic factor 1 (NCF1) (I), Osteoclast-Stimulating Factor 1 (OSTF1) and the adaptor protein p85α [150]. An overview of published, identified interaction partners of the ADAM15 ICD is shown below (Table 1).

Table 1 Overview of identified ADAM15 ICD interaction partners

Src Family kinases		Sorting Nexin		Tyrosine kinases		Serine/ Threonine kinases		Adaptor Proteins		other	
Lck	*Poghosyan (2002), Yasui (2004)*	SNX9	*Kleino (2009)*	PTK6	Zhong (2008)	Erk	*Zhong (2008)*	Grb2	*Poghosyan (2002)*	Nephrocystin	*Kleino (2009)*
Fyn	*Poghosyan (2002)*	SNX18 (SH3PX1)	*Howard (1999)*	Btk	Kleino (2015)			Tsk5/ Fish	*Zhong (2008)*	Endophilin 1	*Howard (1999)*
Abl	*Poghosyan (2002)*	SNX33 (SNX30)	*Kleino (2009)*					Nck	*Zhong (2008)*	Intersectin 1 (III)	*Kleino (2015)*
Src	*Poghosyan (2002)*							Tks5 (V)	*Kleino (2015)*	NCF1	*Kleino (2009)*
Hck*	*Yasui (2004)*							Tks5 (I)	*Kleino (2015)*	OSTF1	*Kleino (2015)*
Yes	*Karkkainen (2006)*							p85α (PIK3R1)	*Kleino (2009)*		

*association via SH2

1.4.6 Substrates for ADAM15

Via its metalloproteinase domain ADAM15 is able to proteolytically process cytokines, growth factors and membrane bound receptors[151,152].

Until now 11 substrates for ADAM15 have been identified (Table 2). The first ADAM15 substrate was identified by Martin *et al.* in 2002. They identified collagen IV as ADAM15 substrate in human mesangial cells. They showed that ADAM15 is able to proteolytically process collagen IV in a dose dependent manner, and this effect could only be inhibited with EDTA. They concluded that ADAM15 might have a significant role in mesangial cell migration due to processing of collagen IV[153]. To further identify ADAM15 specific substrates Fourie *et al.* screened a library of synthetic peptides and found the CD23 receptor as a substrate. Soluble CD23 is a ligand for the IgE receptor, which is known to be involved in inflammatory diseases when overexpressed[154]. However, the tissue distribution of ADAM15 and CD23 do not correspond to each other. They concluded that although CD23 is an ADAM15 substrate, it is more likely to be processed by other ADAMs[151]. Maretzky *et al.* identified fibroblast growth factor receptor 2iiib (FGFR2iiib) as a substrate for ADAM15, although the physiological role in this proteolytic event is unclear[155]. ADAM15-B contains an additional Src-binding domain in contrast to A and interaction enhances the proteolytic activity of ADAM15-B which could be inhibited by Src-inhibitors such as PP1, PP2 and dasatinib[156]. They concluded, that Src inhibition could be used in patients who display overexpression

of ADAM15-B[81,156]. They further investigated possible substrates, such as the membrane bound EGFR ligands ampiregulin, betacellulin, TGF-α, and TNF-α. However, ADAM15 was unable to cleave these substrates[155]. Dong *et al.* found that ADAM15 is able to enhance lung cancer cell invasion. The presence of ADAM15 induced MMP9 overexpression via activation of the MEK-ERK pathway. ADAM15 cleaved pro-MMP9 to the active form MMP9, thus enhancing cell invasion and metastasis. Thus, ADAM15 is able to induce cell migration in lung cancer via MMP9 activation [157] (Figure 1.6).

Although Maretzky *et al.* showed that ADAM15 cannot cleave amphiregulin or TGF-α and TNF-α, Schäfer *et al.* showed that ADAM15 is involved in EGFR signalling via cleavage of pro-amphiregulin and pro-TGFα enabling EGFR signalling[158]. Hart *et al.* showed that ADAM15 is able to shed pro-heparin-binding EGF-like growth factor (pro-HB-EGF) which induced thrombin related EGFR phosphorylation. Upon ADAM15 knock down, they showed that the EGFR phosphorylation is reduced[159].

Najy *et al.* described that ADAM15 is involved in processing of the adhesion molecule CD44 and the integrin α_v, as ADAM15 expression correlated with less detectable amount of both molecules[105]. They further showed that the expression of α_v integrin was reduced in cells expressing ADAM15, which might indicate a role of ADAM15 in reducing cell interactions with the extracellular matrix leading to disease progression and metastatic spread.

Duan *et al.* identified major histocompatibility complex class I polypeptide-related sequence B (MICB) as an ADAM15 substrate. Upregulation of MICB is observed in lung, prostate, breast and kidney cancer, although it is usually restricted to the gastrointestinal tract[160].

ADAM15 is not only able to cleave growth factors or receptors, but also other ADAMs. One ADAM that is an ADAM15 substrate is ADAM10. Tousseyn *et al.* published that ADAM15 mediates ectodomain shedding of ADAM10. ADAM15 cleaves ADAM10 from the membrane and ADAM10 ectodomain is released, thus modifying cell signalling events that require cell surface associated ADAM10, such as NOTCH, APP, cMET and Axl[161] (Figure 1.6).

Although substrates have been identified up until recently no selective ADAM15 metalloproteinase inhibitor was available. In 2016 Hiles *et al.* showed that after administration of the selective inhibitor for the ADAM15 metalloproteinase function,

adamastat, cell viability was reduced in bladder cancer[162]. They further showed, that via administration of adamastat, bladder tumour growth was reduced in mice.

Table 2 Overview of identified ADAM15 substrates

Substrate	
Collagen IV	Martin (2002)
E-cadherin	Najy (2008)
Pro-Amphiregulin, Pro-TGFa	Schafer (2004)
Pro-HB-EGF	Hart (2005)
CD23	Fourie (2003)
FGFR2IIIb	Maretzky (2009)
ADAM10	Tousseyn (2009)
Pro-MMP9	Dong (2015)
MCIB	Duan (2013)

1.4.7 ADAM15 splice variants as biomarkers

Alternative use of exons can be used as prognostic marker in cancer, as alternative splice variants are linked to oncogenic function[163].

In 48 breast cancer patients, Zhong *et al.*, compared the expression level of ADAM15-A, B, C and D, against healthy control tissue. A significant increase was found for mRNA levels of ADAM15-B and C, however not for A and D. In a follow up study, they investigated expression levels of ADAM15-A, B and C, in 229 breast cancer patients. Upon correlation of expression levels with age, tumour size and grade, menopausal status, hormone receptor expression and node status, ADAM15 expression levels could not be linked to any of those. However, when patients were grouped based on mRNA expression for ADAM15, overexpression of ADAM15-A and B were linked to poor prognosis for patients, without lymph node metastasis. However, lymph node metastasis and overexpression of ADAM15-C, patients' prognosis was positive[81]. Zhong *et al.* concluded, that ADAM15 splice variant expression levels could affect disease outcome in breast cancer patients.

Maretzky *et al.*, showed that the additional proline-rich region present in ADAM15-B allows Src to bind leading to enhanced proteolytic activity of ADAM15-B compared to A[156].

Therefore, ADAM15-B overexpression in breast cancer could be treated by Src inhibitor to reduce FGFR2iib shedding in these patients, which might provide a new therapeutic approach.

1.5 Protein Tyrosine kinases

Intra- and extracellular phosphorylation of protein tyrosines is a strictly regulated post-translational process, and is used as signal transduction within eukaryotes. Proteins that execute phosphoryl-transfer, i.e. the transfer of a phosphate group to a tyrosine, by using phosphoanhydrates, such as adenosine triphosphate (ATP) are called Protein Tyrosine kinases (PTKs). PTKs are a multiprotein family and essential mediators of signal transmission for cellular processes such as growth, metabolism or apoptosis[164,165]. They have been identified to contribute to diseases including cancer. Within the human genome 90 genes have been identified, exclusively encoding PTKs which can be divided into two classes, the transmembrane receptors known as receptor tyrosine kinases (RTK) with 20 subfamilies, and the intracellular kinases, PTKs with 10 subfamilies. Of the 90 tyrosine kinase genes, 58 encode for RTKs, and 32 encode for PTKs[166].

1.6 RTKs

RTKs are type I single-pass transmembrane receptors. Their function relies on the kinase domain, located in the intracellular domain. With the exception of the insulin-receptor (IR), the RTKs are single transmembrane proteins, which are able to form non-covalent dimers. The IR family-members, insulin-like growth factor I-receptor (IGF-IR) and insulin receptor-related receptor (IRR), are expressed as single unit, however, they undergo processing into α and β polypeptides. These can assemble into a heterotetramer, consisting of 2 α and 2 β units, or into a homodimer, linked by disulfide bonds[167].

1.6.1 RTK modular organization

Generally the RTKs consist of 3 domains, the N-terminal extracellular domain (ECD), the transmembrane region and the C-terminal intracellular domain (ICD). The ECD is variable in length and composed of different structural domains, thus leading to 20 distinct subclasses. Domains that are present within the 20 subclasses are, leucine-rich domains, cysteine-rich domains, immunoglobulin-like domain, EGF-regions, type-L domain, Ephrin binding-domain, furin-like domain or fibronectin type III domains (Table 3). Within the ECD there are multiple disulfide bonds and N-linked glycosylation sites. The variability of the ECD enables high specificity for ligands such as growth factors. ECD and the C-terminal ICD are linked by a transmembrane

hydrophobic region. The ICD contains the conserved kinase domain, which is flanked by tyrosine residues, and a C-terminal tail. Both the tyrosine kinase domain and the tail, differ in size and tyrosine residues within the RTK family. Especially the total number of tyrosines is variable, for instance the EGFR family shows the highest number of tyrosine residues, with 20, of which 12 can be phosphorylated[167]. The ATP-binding site of the kinase domain is surrounded by N-lobe and C-lobe, and becomes accessible upon RTK activation.

Table 3 Overview of the 20 RTK family members

Receptor tyrosine kinase-family name	Family members	ECD-characteristics
EGFR (epidermal growth factor receptor)	EGFR, ERBB2, ERBB3, ERBB4	2 cysteine-rich domains
IR (insulin receptor)	INSR, IGF-1R, IRR	2 chains α and β, one cysteine rich and 2 FNII domains
PDGFR (platelet-derived growth factor receptor)	PDGFR-a, PDGFR-b, CSF-1R, KIT/SCFR, FLK2/FLT3	5 Ig-like domains
VEGFR (vascular endothelial growth factor receptor)	VEGFR1, VEGFR2, VEGFR3	7 Ig-like domains
FGFR (fibroblast growth factor receptor)	FGFR-1, FGFR-2, FGFR-3, FGFR-3, FGFR-4	3 Ig-like domains, 1 acidic box
KLG/CCK (colon carcinoma kinase)	CCK4	7 Ig-like domains
NGFR (nerve growth factor receptor)	TRKA, TRKB, TRKC	2 Ig-like domaisn, leucin-rich domains
HGFR (hepatocyte growth factor receptor)	MET, RON	1 transmembrane α-chain, linked with one ICD β-chain
EPHR (ephrin receptor)	EPHA1, EPHA2, EPHA3, EPHA4, EPHA5, EPHA6, EPHA7, EPHA8, EPHB1, EPHB2, EPHB3, EPHB4 EPHB5, EPHB6	1 Ig-like, 1 cysteine-rich, and 2 FNIII-like domains
AXL (a Tyro3 PTK)	AXL, MER, TYRO3	2 Ig-like, 2 FNIII-like domains
TIE (tyrosine kinase receptor in endothelial cells)	TIE, TEK	2 Ig-like, 1 1 EGF, and 3 FNIII-like domains
RYK (receptor related to tyrosine kinases)	RYK	1 transmembrane β-chain, linked with one ECD α-chain
DDR (discoidine domain receptor)	DDR1, DDR2	1 discoidin-like domain
RET (rearranged during transfection)	RET	1 cadherin-like domain
ROS (PPTK expressed in some epithelial cell types)	ROS	6 FNIII-like domains
LTK (leukocyte tyrosine kinase)	LTK	1 cysteine-rich domain
ROR (receptor orphan)	ROR1, ROR2	1 Ig-domain, 1 cystein-rich domain, 1 kringle-like domain
MUSK (muscle-specific kinase)	MUSK	4 Ig-like and 1 cysteine-rich domain
LMR (Lemur)	AATYK, AATYK2, AATYK3, ALK	a short ECD
NN (not named)	RTK106	A short receptor chain with a short ECD

1.6.2 RTK activation

RTKs become activated upon ligand binding to the extracellular binding domain. The ligand is able to concurrently interact with two receptor monomers, which leads to dimer formation[168]. The dimerization of the RTKs leads to the juxtaposition of the intracellular tyrosine kinase domains, subsequently inducing trans-autophosphorylation of tyrosines, revealing the nucleotide and substrate binding-sites. Within the RTK family there are four distinct activation mechanism. For instance EGFR-family RTKs are activated upon growth factor binding which reveals a dimerization arm, exposed after domain rearrangement, leading to receptor dimerization[169]. PDGFR-family RTKs, such as KIT, dimerize upon ligand binding to the D1-D3 Ig-like ECD-domains. D4-D5 Ig-like domains of the KIT-ECD undergo a sterical change upon dimerization, leading to kinase activation[170]. FGFR-family RTKs, dimerize by contact of two FGFR monomers via their ECD Ig-like D2 domain, which is accompanied by accessory proteins, such as heparin, and additionally the FGFR-ligand FGF bound to D2 and D3 Ig-like domains[171]. NGFR-family RTKs dimerize upon ligand binding. The ECD of both monomers does not contact one another, the monomers are linked via Ig-like C2 domains binding to the ligand[172]. To summarize, RTK dimerization is either exclusively ligand mediated, without prior receptor contact, or the ligand leads to direct binding of the receptor monomers. However, in some cases, receptor dimerization can involve a combination of both[173]. The essential function of RTK dimerization and trans-autophosphorylation is the generation of cytoplasmic ligand binding sites for downstream signalling- or adaptor-proteins containing Src homology-2 (SH2) domains, phosphotyrosine binding sites (PTB) or phosphotyrosine recognition domains, and the activation of the receptor enzymatic function, as tyrosine kinase[174,175].

1.6.3 The HGFR family

The hepatocyte growth factor receptor (HGFR) family comprises two family members, the macrophage stimulating protein receptor, recepteur d'origine Nantais (RON), and the hepatocyte growth factor receptor (cMET) (Table 3). RON and cMET showing 25% sequence homology of the ECD and 63% sequence homology within the ICD[176]. The ligands of cMET and RON also show 45% sequence homology. The RON ligand is the hepatocyte growth factor receptor-like (HGF-like) protein secreted by hepatocytes, whereas the cMET ligand is HGF and secreted by mesenchymal cells. cMET was identified in 1995 by Humphreys *et al.*, expressed in androgen independent prostate cancer cell lines, DU145 and PC3, with lower expression in

LNCaPs. However, upon androgen deprivation, cMET expression was upregulated in LNCaPs. They identified cMET in 45% of patients' prostate carcinoma, and it was significantly overexpressed in patients with metastatic growth[177].

1.6.3.1 cMET

The cMET receptor, predominantly expressed on epithelial tissue, was identified by Giordano *et al.* in 1988. They described it as 190 kDa tyrosyl phosphoprotein, a product of the *c-met* proto-oncogene located on chromosome 7q21-31[178,179]. cMET is synthesised as 190 kDa precursor, in the post-Golgi compartment, and is cleaved into an extracellular 50kDa α-subunit and a transmembrane 145kDa β-subunit. Both subunits become glycosylated, which is essential for formation of the mature αβ-heterodimer linked by disulfide bonds.

The ECD is composed of a semaphorin (Sema) domain, a plexin-sema-integrin (PSI) domain and four Ig-like domains also found in plexins, semaphorins and transcriptional factors (IPT) domains. α-chain and β-chain are linked via the Sema domain. The ICD contains a juxtamembrane region with a serine at position 975 and a tyrosine at amino acid position 1003. Both residues keep the cMET kinase in an inactive state. Downstream of the juxtamembrane domain, the catalytic domain is situated, containing the tyrosine residues 1234 and 1235, which are able to modulate the kinase activity. Towards the C-terminal end, the multi-adaptor protein docking site is located containing the terminal tyrosines at position 1349 and 1356[180] (Figure 1.8).

1.6.3.1.1 The cMET ligand HGF

HGF was identified by Nakamura *et al.* in 1989 as unknown hepatotrophic factor[181], and by Weidner *et al.* in 1991, as Scatter factor (SF)[182]. They were able to isolate HGF via heparin-affinity chromatography from rat platelets as HGF shows high affinity for heparin. By SDS-PAGE they were able to identify a 84 kDa band. However, under reducing conditions a 69 kDa, the α-chain, and 34 kDa band, the β-chain, were detectable, indicating a dimeric molecule linked by disulfide bonds[183]. The hepatocyte growth factor (HGF) belongs to the plasminogen family and is secreted by mesenchymal cells as inactive matrix-associated precursor, pro-HGF. It is involved in embryogenesis, cell scattering, cell motility, morphology, cellular invasion, angiogenesis and mitogenesis[177].

It is proteolytically processed into a two chain protein by the HGF-activating serine protease (HGFA) to the mature HGF (Figure 1.8). The serine protease, matriptase, involved in the proteolytic cleavage of pro-HGF was identified by Shimomura *et al.* in 1997[184]. HGF consists of a N-terminal hairpin loop domain, followed by four kringle

domains, K1-K4, the α-chain, and the C-terminal β-chain domain consisting of a serine protease homology (SPH) domain. HGF α and β-chain are formed by cleavage of the linker between the K4-domain and the SPH-domain. The single chain pro-HGF is able to bind to cMET, however, this does not activate the receptor[180,185]. There is an ongoing discussion in literature, whether the α or β-chain lead to receptor activation[186,187].

1.6.3.1.2 cMET activation

The Sema domain of the cMET receptor is responsible for HGF binding, which leads to receptor dimerization and trans-phosphorylation of the tyrosine residues 1234 and 1235 in the active site. Additionally, the multiple binding site (MBS) tyrosines, 1349 and 1356 become phosphorylated. The docking site enables protein binding of SH2 domain containing adaptor proteins such as growth factor receptor-bound protein 2 (Grb2), Grb2-associated adaptor protein (Gab1), phospholipaseC-γ, son of sevenless (SOS), the adaptor protein Shc, Src homology protein tyrosine phosphatase 2 (Shp2), phosphatidylinositol-3-kinase (PI3K), SH2 domain containing inositol phosphatase-1 (Ship1), and signal transducer and activator of transcription 3 (STAT3) [188–190]. Proteins associating to the cMET docking motifs activate downstream signalling pathways, inducing cell proliferation, invasion, migration, such as the Erk/MAPK and STAT3 pathway or they induce survival upon PI3K/Akt activation.

Although HGF is the only known ligand for cMET, activation of cMET can occur in different ways. Conrotto *et al.*, showed that cMET is able to interact with plexins via its Semaphorin domain, in a ligand independent manner[191]. Plexin B1 associates with cMET via the extracellular semaphorin domain. Upon binding to plexin B1, cMET becomes transphosphorylated, leading to cell invasion and proliferation. Trusolino *et al.* identified that upon HGF activation of cMET, $\alpha_6\beta_4$ becomes phosphorylated and associates with PI3K and Shc, multiplying the cMET signaling, enhancing cell invasion[192]. Orian-Rousseau *et al.* identified that the CD44 splice variant v6 enables HGF activated cMET to be linked to the actin cytoskeleton via Grb2 and SOS, leading to Ras-ERK signalling[193].

cMET activation via RTK crosstalk has been extensively investigated in the literature. It is especially important in tumour resistance to treatment interventions. In the absence of HGF, cMET is able to interact with EGFR after ligand stimulation of EGFR with TGF-α and EGF[194]. cMET is also known to interact with RON[195], PDGFR-α and Axl[196], leading to transphosphorylation and activation of cMET in the absence of HGF.

To control cMET downstream signalling within the cell, protein tyrosine phosphatases (PTP) dephosphorylate tyrosines at the catalytic site or at the docking site, leading to kinase inactivation[197].

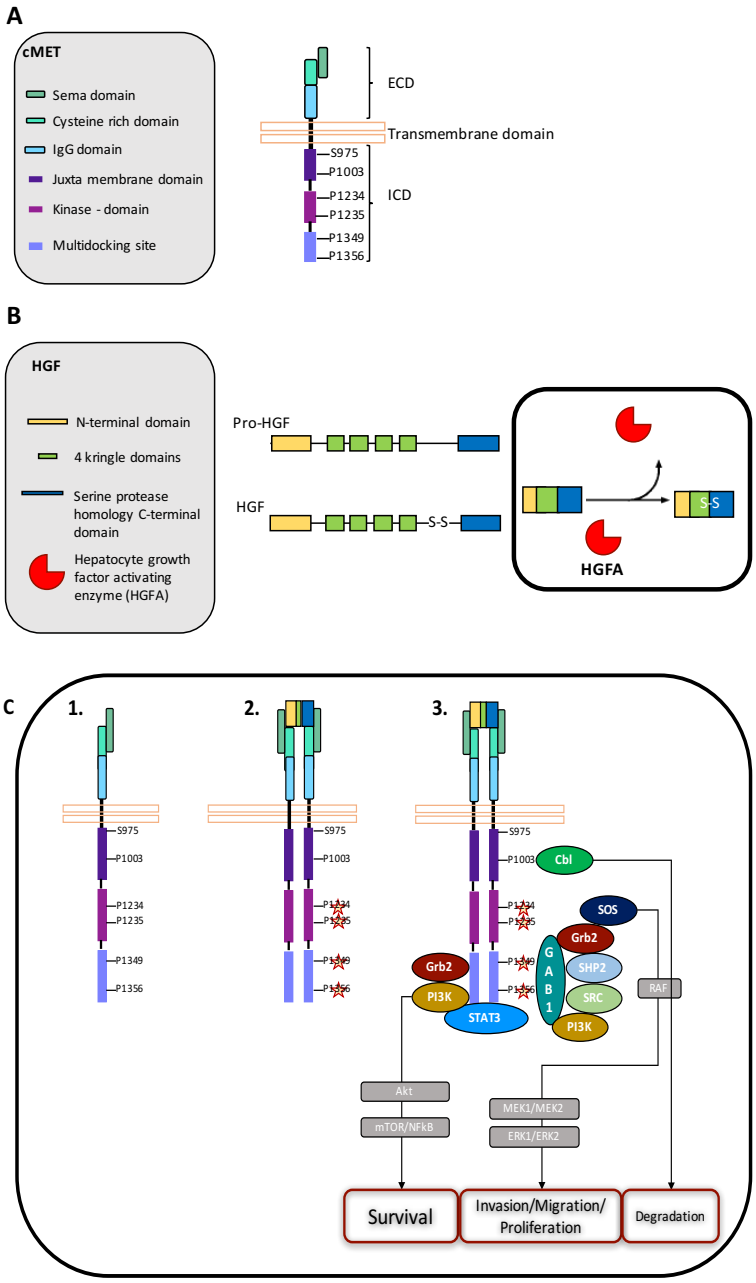

Figure 1.10 The cMET/HGF signalling cascade

(A) Schematic structure of cMET, top, and HGF, bottom. cMET consists of 3 ECDs and two ICDs, connected via a transmembrane region. (B) HGF, is synthesized as inactive precursor pro-HGF. Via the serine protease HGFA, it becomes activated. (C) cMET is present in the cell as monomer (1). HGF activation by HGFA, enables HGF binding to the sema-domain of cMET (2), inducing the dimerization of cMET and downstream transphosphorylation of the cMET kinase domain. The cMET transphosphorylation enables the association of downstream signalling mediators to the multidocking site (3), such as Gab1, Grb2, PI3K or STAT3. Gab1 further allows binding of multiple proteins, when bound to cMET. Association of proteins to the mutidocking site leads to induction of survival, invasion, migration or proliferation. Association of Cbl to P1003, upstream of the kinase domain, leads to lysosomal degradation of cMET.

1.6.3.1.3 The cMET adaptor proteins Grb2 and Gab1

Growth factor receptor bound protein 2 (Grb2) and Grb2 associated binding protein 1 (Gab1) are important regulators of cMET signalling, however they do not have enzymatic activity themselves[198]. The C-terminal MBS of cMET from position 1344 to 1361 includes the Grb2 and Gab1 binding phosphotyrosines Y1356 and Y1349, allowing them to associate and initiate key signalling pathways involved in cell invasion, proliferation, migration or cell cycle progression[199] (Figure 1.8).

Grb2 is a 25kDa protein, containing one SH2 domain, flanked by two SH3 domains at the C- and N-terminus. Via its SH2 domain, Grb2 can associate directly with RTKs, such as cMET, and via its SH3 domain, it can bind proline rich regions[200]. Grb2 can associate directly with cMET at Y1349, or indirectly via Gab1[201]. When bound to cMET, Grb2 can induce invasion of tumour cells via the interaction with son of sevenless (SOS), which links this complex to membrane bound RAS. SOS activates RAS by GDP/GTP exchange enabling the RAS mediated activation of RAF (MAPKKK), which leads to downstream activation of MEK (MAPKK) and Erk (MAPK) phosphorylation[202–204] (Figure 1.10). This leads to Erk translocation to the nucleus enabling the control of gene transcription, cell proliferation and cell motility[197]. Inhibition of the Grb2 SH2-domain leads to decrease in cell motility, due to decreased Grb2 localization to the membrane in A-341 epidermoid carcinoma cells[205].

Gab1 belongs to a group of proteins that are substrates for RTKs such as cMET. Gab1 has an N-terminal PH-domain targeting it to the plasma membrane, and a central phosphotyrosine binding (PTB) domain enabling the association with RTKs. Lock *et al.*, identified a unique 13 amino acid sequence, enabling the direct binding to cMET, MET binding site (MBS)[206]. Binding to cMET initiates Gab1 phosphorylation and the recruitment of Gab1 adaptor proteins, such as Shp2, PI3K, or PLC-γ via their SH2 domains. Adaptor protein recruitment to cMET leads to activation of the MAPK/Erk pathway. Schaeper *et al.*, identified the importance of the Gab1-Shp2 coupling to activate the MAPK/Erk pathway, as only Shp2 binding to Gab1 in MDCK cells induced branching morphology[207]. Grb2 can associate with cMET via the SH2 domain and binds Gab1 via SH3 stabilizing the Gab1-cMET association[207]. Disruption of Grb2 association to Y1349 in mice was found to reduce presence of limb muscle[208].

1.6.3.1.4 cMET endocytosis and degradation

cMET signalling is terminated by endocytosis, which involves invagination of the plasma membrane resulting in vesicl formation. It involves rapid internalization upon activation and transport to the lysosome leading to degradation. Endosomal signalling

of cMET is an important regulator of cell function, and further enables the direct transport of the cMET complex to its intracellular targets[209].

Binding of HGF leads to cMET dimerization and recognition by clathrin, present at the cell membrane. The recognition via clathrin follows the rapid internalization of cMET into clathrin coated vesicles, called peripheral endosomes[189]. cMET trafficking from the peripheral endosomal compartment to the perinuclear compartment to the Golgi, is guided by the microtubule network, and is mediated by protein kinase Cα (PKCα) [210]. The internalization and degradation of cMET can be inhibited by the proteosomal inhibitor lactacystin[211]. Within the endosomal compartment, cMET remains active. The active state of cMET is required for full activation of the ERK1/2 and Rac-1 pathways. Activated ERK1/2 relocates to the plasma membrane and associates with the focal adhesion complexes. The regulator for ERK1/2 and Rac-1 relocation is PKCε. This leads to the formation of lamellipodia, resulting in the HGF/cMET induced cell migration, mediated by PKCε. Alongside the microtubule network, cMET traffics, guided by PKCα, from the early endosomal compartment, to the perinuclear compartment leading to the accumulation and translocation of STAT3[212].

A different way of cMET signal termination is the binding of casitas B-lineage lymphoma (c-Cbl) to tyrosine 1003 located at the juxamembrane domain of cMET, leading to ubiquitination and endocytosis. Endocytosis leads to accumulation of cMET in multivesicular bodies, which subsequently fuse with the lysosome leading to degradation of cMET. The point-mutations D1246N and M1268T within the tyrosine kinase domain of cMET lead to cMET being constitutively recycled and relocalized to the plasma membrane. Jeffers *et al.* justified this finding, with a change in receptor conformation altering the association of SH2-binding proteins, such as c-Cbl[213].

Degradation of cMET can also be induced via proteolytically active transmembrane proteins, such as ADAMs. ADAM10 and 17 cleavage of cMET results in an extracellular domain fragment, known as 'decoy' fragment, able to interfere with dimerized cMET leading to impaired signalling[214]. Proteolytic cleavage can be enhanced by phorbol esters, such as PMA[214]. Further processing of cMET is performed intracellularly by γ-secretase. The generated fragment is internalized and degraded within proteasomes[215].

1.6.4 The cMET/HGF axis

1.6.4.1 Physiological activity

cMET is essential for normal development, as it is a key promotor of morphogenic differentiation and tissue remodelling. Using knock out of cMET in a cell model,

Schmidt *et al.* and Ebens *et al.,* showed that cMET is important for cell migration, liver and placental development[216,217]. Knock out mice embryos showed reduced liver and size, and reduced placental size, which led to death of embryos *in utero*. Liver or kidney damages also require cMET activation and signalling, which was shown in a liver cirrhosis and renal fibrosis patient study conducted by Tsubouchi *et al.* and Nakamura *et al.*[218,219]. Patients showed increased cMET signalling due to increased HGF expression, which leads to the conclusion that the cMET/HGF axis is involved in tissue regeneration in those patients.

Expression of cMET in haematopoeitic cells is needed to regulate immune functions. Galimi *et al.* showed that HGF is able to induce cell migration and secretion of cytokines in monocytes, and further, it can activate monocytes to secrete HGF, in an autocrine manner[220]. Van der Voort *et al.* identified cMET/HGF axis as regulator of B-cell adhesion, since upon HGF stimulation, integrin-mediated adhesion to fibronectin and VCAM-1 was enhanced. They concluded, that HGF was able to induce migration and morphogenic response of B-cells[221].

In a recent study, Baek *et al.* showed that the HGF/cMET axis is able to induce dendritic cell migration in the skin[222]. They showed that cMET signalling was required to initiate dendritic cell release from the soft tissue, to reach the draining lymph node, maintaining immune function of the skin, where it regulates MMP2 and 9 activity, which in turn enables dendritic cells to migrate through the ECM[222].

1.6.4.2 cMET in cancer as a therapeutic target

cMET mutations, translocations, amplifications and transcriptional upregulation, or ligand independent signalling are the key principles of cMET contributions to tumourgenesis[223]. There is a need to develop tumour therapies that allow blockage of the cMET downstream signalling pathways in cancer.

Cooper *et al*. identified cMET as oncogene in an osteosarcoma cell line[224]. cMET was fused to the translocating promoter region (TPR) leading to cMET overexpression. When expressed in an animal model, TPR-cMET leads to multiple mammary tumour formation[225]. Additionally, TRP-cMET translocation was found in 22 gastric carcinoma patients[226].

Gene amplification of cMET is found in many metastatic tumours such as in liver, prostate, and oesophageal carcinomas, however, not in primary tumours, indicating that cMET amplification might be a gain-of function during cancer progression.

Amplification of cMET in lung cancers shows treatment resistance to EGFR inhibitor, which might be an indication for a combined drug treatment in those patients[180].

Although genetic alterations, such as translocations, play a role in dysregulation of the HGF/cMET axis in cancer, cMET transcriptional upregulation without gene amplification is the most common. Hypoxia is one cause of cMET transcriptional upregulation, as the transcription factor hypoxia inducible factor 1α (HIF1α) activates the cMET promoter, leading to increased transcription[227]. cMET transcriptional upregulation can be particularly induced by the HGF ligand itself[228].

In cancer, ligand dependent activation of cMET is based on an autocrine HGF-loop. Tumour cells are able to overexpress cMET and HGF simultaneously, leading to constitutive autocrine cMET activation. Cancers that have been identified with autocrine cMET activation are breast, lung, osteosarcomas, and prostate cancers, which has been linked to a poor patient prognosis[180,229–231].

Based on the evidence provided previously, cMET and HGF present valid clinical targets in various solid cancers, where increased signalling via this axis has been identified to contribute to rapid tumour growth and metastasis.

Monoclonal antibodies, targeting HGF have been tested in clinical settings; one of those is Rilotumumab (AMD-102), a monoclonal IgG2 antibody (Figure 1.11). It neutralizes HGF upon binding and further prevents downstream signalling. Rilotumumab is supposed to have antineoplastic potential, leading to tumour cell apoptosis. Phase I/Ib (NCT01791374) studies showed a 70% increase in relapse free survival for 8 to 40 weeks in patients with advanced-carcinomas and lymphomas [232,233]. However, in glioblastoma patients, Rilotumumab treatment in 60 patients was ineffective[234].

Onartuzumab (MetMAb), is a monoclonal antibody, which binds to the sema-domain of cMET, inhibiting HGF binding to cMET, receptor dimerization and downstream activation. In a phase II study, 137 NSCLC patients did not show a significant difference on Onartuzumab monotherapy. However, combined treatment with the EGFR inhibitor erlotinib significantly increased the survival to 2.9 months[235] (Figure 1.11).

An obvious target site to block cMET is the tyrosine kinase domain. However, the challenge here is the high degree of homology of the ATP binding site across different families and thus existing tyrosine kinase inhibitors (TKIs) are either non-selective

and broad spectrum, or MET-selective and both TKI sets may have advantages or disadvantages in cancer therapy, which will be discussed below.

The non-selective TKI cabozantinib, inhibits a broad spectrum of TKs such as, VEGFR, AXL, TIE2, RET and cMET. Cabozantinib (Cabometyx, Exelixis, Inc.) was approved by FDA and EMA in 2016 for treatment of medullary thyroid cancer and advanced renal cell carcinoma[236]. The administered form of cabozantinib is the s-malate salt, which is orally bioavailable, and was used in patients with metastatic thyroid cancer, where an application of a daily dose 140 mg showed a 28% response rate and increased relapse free survival in 47% of patients for more than 14 months[237]. Currently cabozantinib is in clinical trials for triple negative breast (NCT01738438) and metastatic prostate cancer (NCT01834651).

A selective MET TKI is tivantinib (Figure 1.11), the most developed and extensively studied TKI until now. It is orally bioavailable and has an anti-neoplastic effect. It binds to unphosphorylated, inactive cMET, and inhibits cMET autophosphorylation. This in turn leads to disruption of the signalling pathway, leading to apoptosis, decreased invasion and reduction of angiogenesis[238]. In a Phase I clinical trial, tivantinib was able to reduce cMET phosphorylation, and reduced circulating tumour cells in 30% of patients[239]. A study in NSCLC showed that patients with *KRAS* mutations responded better to combined tivantinib and erlotinib (EGFR-inhibitor) treatment, as patient relapse free survival was increased to 3.8 months, compared to the 2.3 month survival of the control group[240].

Broad spectrum inhibitors are more effective in clinical trials than selective MET inhibitors. Therefore, the broad spectrum inhibitors are approved by EMA and FDA for thyroid and renal cancer.

As discussed, primary PCa is androgen-dependent and usually treated with androgen ablation therapy or surgery[241]. However, metastatic PCa is androgen-independent and other treatments have to be applied. RTKs play a role in disease initiation, progression, metastasis and tumour growth, which is why TKIs gained compliance as effective treatment option[35,242,243].

The most successful applied chemotherapeutic drugs for metastatic PCa are Docetaxel[244], the second generation taxene Cabazitaxel[245], or Estramustine[246] to mention only a few. Taxenes such as Docetaxel or Cabazitaxel, or the alkylating agent Estramustine are antimitotic drugs and act on microtubule formation by promoting the assembly and inhibiting the disassembly of microtubules. Inhibition of

microtubule disassembly leads to the stabilization of microtubules, an inhibition of mitosis and induces the apoptotic cell death.

RTKs however play a role in disease initiation, progression, metastasis and tumour growth, which is why TKIs gained compliance as effective treatment option (Table 4). Clinical studies for PCa with TKIs such as AMG208, Cabozantinib showed lack of efficacy when applied in patients. However, results of a re-designed study for Cabozantinib treatment of PCa patients are highly anticipated as a daily dose showed efficacy to slow down disease progression or and prevent disease relapse in a small patient population (NTCT01834651).

Table 4 FDA approved studies for cMET inhibitors for treatment of PCa

Agent	Target site	Conditions	Interventions	Study Code	Finished	
AMG102 (Rilotumumab)	HGF	PCa	15mg/kg every 3 weeks IV (12 cycles)	NCT00770848	2014	No results posted
AMG 208	RTKi	PCa	400mg/day orally in 6 weeks cycle	NCT02420587	2015	withdrawn prior to enrolment
Cabozantinib	RTKi	PCa	60mg orally daily until disease progression	NCT01834651	on going	
	RTKi	PCa	60mg orally	NCT01428219	2016	terminated due to negative results
Tivantinib	RTKi	PCa	nn	NCT01519414	on going	

The major site of metastasis in prostate cancer is the bone. In a study by Tu *et al.,* the cMET inhibitors PHA-665752 and PF-2341066 were used to assess tumour formation and progression in *in-vitro* and *in-vivo* models. cMET inhibition with PF-2341066 showed reduction of androgen-dependent tumours in mice and further reduced the tumour progression in castrated mice[247]. The overexpression of cMET can be correlated with a reduced survival of PCa patients[248]. This makes cMET a promising target for PCa therapy. Although TKIs seem to be a promising target, their

effect in PCa related studies can only be seen in a subset of patients, which makes it even more important to understand the underlying mechanisms[249–251].

cMET is a valid clinical target for multiple cancers. However, combined treatments are favourable for patients as cMET can be activated by RTK cross-talk via EGFR for example. The major challenge that research is facing now, is to identify cMET dependent tumours which have become resistant to TKI therapy. New selective biomarkers for individual patients need to be identified, to inhibit the HGF/cMET on the long run, which in turn would extened relapse free survival[188,252,253].

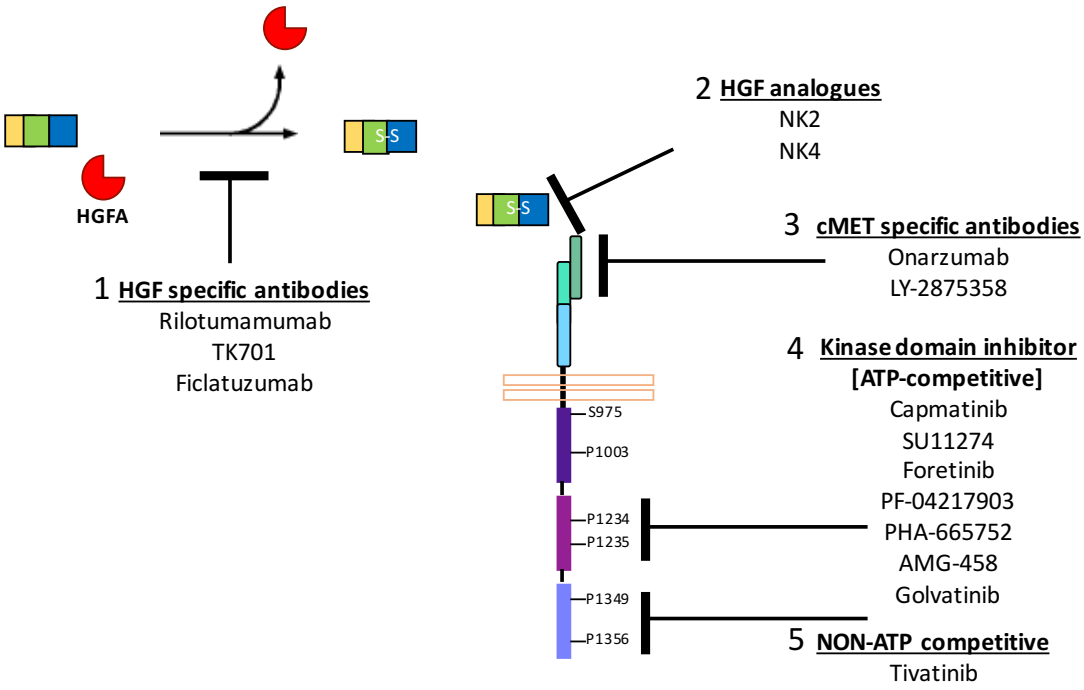

Figure 1.11 Target sites of the cMET/HGF axis

Five different targets have been validated to inhibit the HGF/cMET axis. (1) HGF specific antibodies, and (2) HGF analogues inhibit HGF activation or HGF binding to cMET. (3) Two cMET specific antibodies have been developed, both targeting the sema-domain of cMET, inhibiting HGF binding and dimerization of cMET. The next target of the cMET receptor is the ICD, containing the kinase domain and the multiple docking site. The kinase domain is target site for ATP-competitive inhibitors (4), whereas the multiple docking site inhibitor is Non-ATP-competitive (5).

1.7 Intracellular PTKs

PTKs are subdivided into 10 families, due to their homology of domain structures such as Sarcoma family kinase (Src) Homology-1 (SH1), SH2, SH3, integrin binding domains, or DNA binding domains[254,255] (Table 5). PTK members are i.e. the Src

members, located within the cytoplasm, or Abelson murine leukemia (Abl) family members, which are found predominantly in the nucleus. However, on a genetic level during cancer development these pathways are often altered and due to this PTK functions are impaired leading to an enhancement of processes which are usually under strict control. As a result, TKs are termed oncoproteins[256].

Table 5 The family of intracellular protein tyrosine kinases (PTKs)

Cytoplasmic protein tyrosine kinases-family name	Family members	Key-domains
Src	FGR, FYN, SRC, YES1, BLK, HCK, LCK, LYN	SH2, SH3
ABL	ABL1, ARG	SH2, SH3, DNA-binding, Actin-binding
JAK	JAK1, JAK2, JAK3, TYK2	Integrin-binding, pseudokinase-domain
ACK	ACK1, ACK2	SH3, Cdc42-binding
CSK	CSK, MATK/CTK	SH2, SH3
FAK	FAK, PYK2	Integrin-binding
FES	FER, FES	CIP4-homology domain, SH2
FRK	PTK6, FRK, SRMS	SH2, SH3
TEC	BMX, BTK, ITK, TEC, TXK	Pleckstrin homology domain, SH2, SH3, Btk motif
SYK	SYK, ZAP70	Two SH2 domains

1.7.1 SRC

The largest subgroup of the PTKs is the Src family, which includes 9 family members Fyn, Lck, Hck, Lyn, Blk, Fgr, Yes, Yrk and Src (Table 5). They are ubiquitously expressed in human cells and are signal transducers and regulators of the cellular response towards cytokines, growth factors, or cell adhesion. The SH1, SH2 and SH3 domains are conserved within the Src family. They further contain an N-terminal membrane-targeting SH4 domain, a myristoylation sequence. Src is located within the cytoplasma the perinuclear or the endosomal membrane. Src was identified as an oncogene by Simmons *et al.* in 1989 and localized to chromosome, 20q11.23[257]. Src is highly overexpressed in various human cancers, and the upregulation of Src correlated with its activity, leading to cancer progression, growth and invasion[258].

1.7.1.1 Src domain structure

Src has a molecular weight of 60kDa, consisting of 535 amino acid. Starting from the N-terminus Src contains a myristoylation sequences. The myristoylation of Src is a post-translational modification, in which the N-terminal methionine is replaced and the now exposed glycine becomes myristoylated. The myristoylation of Src targets it to the plasma membrane. The SH3 domain, downstream of the N-terminus comprises 60 amino acid and is able to associate with proline-rich regions in a variety of proteins. The SH2 domain of Src is composed of 100 amino acid and allows Src association to phosphorylated tyrosines (Figure 1.12). The SH1 domain of Src is subdivided into two units by the catalytic site, which exhibits the ATP and substrate binding site, facilitating phosphate transfer. The catalytic site forms the activation loop, in which the activating tyrosine (Y419) is located. At the C-terminus Src contains an autoinhibitory phosphorylation site, located at position 530. Two kinases have been identified in regulating Src inactivation, which are Csk[259] and Chk[260]. The C-terminal phosphorylation of Src causes the association with SH2 leading to the autoinhibitory conformation of Src, and masking Y419 activation (Figure 1.12).

1.7.2 Scr-like tyrosine kinases, the FRK family

The FRK-family of tyrosine kinases comprises SRMS, PTK6 and FRK. They are related to the Src-family kinases, however they show an exon-intron structure deviant from Src-family members[261]. FRK family members consist of a tyrosine kinase domain, an SH2 and SH3 domain and an autoinhibitory domain at the C-terminus. Different from Src-family members, FRK-members lack a myristoylation sequence. As a result, they can shuttle within different cellular compartments. FRK itself contains a nuclear localization sequence within its SH2 domain, which can target FRK to the nucleus[262].

1.7.3 PTK6

Protein tyrosine kinase 6 (PTK6) or BRK (Breast tumour kinase) belongs to the Src-related kinases lacking the C-terminal regulatory tyrosine and N-terminal myristoylation sites (SRMS) of RTKs[263]. Herein, the term PTK6 will be used. PTK6 was first identified by Lee *et al.* (1993) in human melanocytes and later in breast tumour cells by Mitchell *et al.*(1994)[263]. Via FISH analysis the human chromosomal region 20q13.3 was identified to contain PTK6.

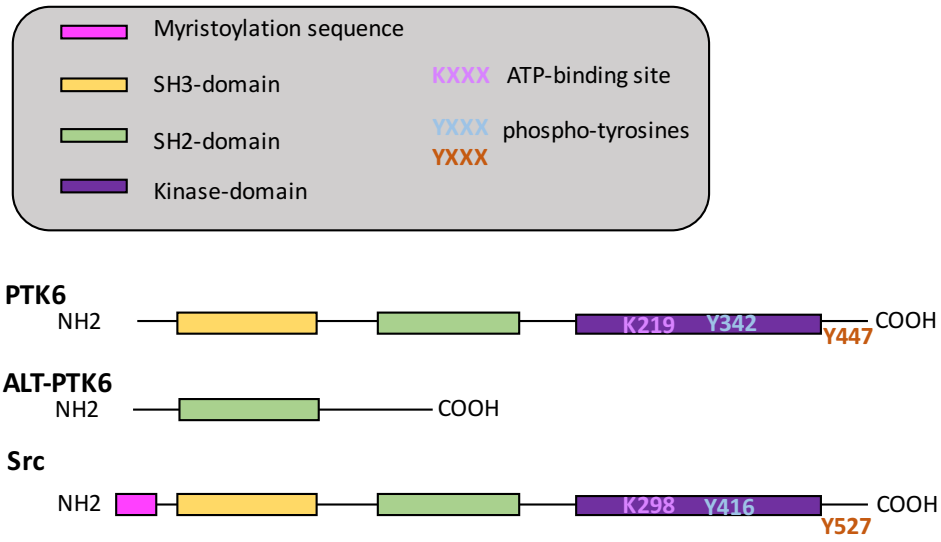

Figure 1.12 Schematic overview of Src and PTK6 protein structure.

The protein structure of PTK6 consists of three domains, the C-terminal kinase domain, the SH2 domain, and the N-terminal SH3-domain, containing the ATP-binding site at position 219 and the Y342, which becomes autophosphorylated upon PTK6 activation. The Y447 downstream is necessary for PTK6 autoinhibition. The splice variant of PTK6, ALT-PTK6 lacks the SH3- and kinase-domain. Although PTK6 and Src show a sequence homology of 44%, Src contains an N-terminal myristoylation sequence, targeting it to the membrane.

1.7.3.1 Characteristics of PTK6

PTK6 consists of 451 amino acids and has an estimated molecular weight of 52kDa. The structure of PTK6 varies, as the SH3 domain consists mainly of β-sheets, whereas the SH2 domains consist of α-helices and β-sheets. Tyrosines (Y) in PTK6 are essential for its activation and inhibition. Upon autophosphorylation of Y342, PTK6 activity is increased. However, phosphorylation of Y447 results in decreased activity as it binds to the SH2 domain (Figure 1.12). When Y447 was mutated to phenylalanine (F), PTK6 became up to 2.5fold more active as the auto-inhibition via P-Y447-SH2 interaction cannot occur [264,265,266]. By mutating K219 the kinase domain became inactive due to the change of the ATP-binding site, required for kinase activity (Figure 1.12).

The sequence homology of PTK6 with Src family members is approximately 44% which includes the exon boundaries between exon 1/2 and 7/8. These boundaries are of high significance as they code for the Src-Homology-3 (SH3) and SH2 domains and the C-terminal region of the kinase domain. Compared to Src-family members, PTK6 lacks the SH4 domain which targets Src-family members to the plasma membrane which results in increased flexibility in the intracellular localization of PTK6

in epithelial cells. One splice variant for PTK6 has been identified so far. Alternative splicing results in the exclusion of exon 2 leading to a frameshift and a premature stop-codon at position 172 lacking the SH2 and the kinase domain, and this is known as ALT-PTK6[264] (Figure 1.12). ALT-PTK6 is thought to negatively regulate growth and promote the PTK6 related inhibition of its substrate β-catenin. Upon co-expression of PTK6 and ALT-PTK6, ALT-PTK6 induced PTK6 nuclear translocation and inhibited PTK6-inhibition of β-catenin transcription. Expression of ALT-PTK6 lead to reduction of β-catenin targets cyclin D1 and c-Myc in PC3, resulting in reduced proliferation and growth[267]. Transcription factors that have been identified to regulate PTK6 expression are NF-κB and Sp1 [268].

1.7.3.2 PTK6 expression and physiological role

PTK6 is expressed in the epithelial tissue, with the purpose to regulate cell differentiation and negatively regulate cell proliferation. Vasioukhin *et al.* identified PTK6 expression to be exclusively restricted to the proliferative zone of the epithelium[269]. PTK6 gene disruption in mice leads to increased growth and reduced differentiation of the small intestinal epithelium. Moreover, AKT activation was increased, suggesting a physiological role of PTK6 in AKT inhibition[270]. *Ptk6*$^{-/-}$ mice showed increased nuclear localization of β-catenin within the small intestinal crypts, proposing an inhibitory role for PTK6 in regulating β-catenin nuclear translocation[270].

The highest expression level of PTK6 is found in the gastrointestinal tract (GI), in the non-dividing villus epithelium of the small intestine, as well as in the crypt cells[271]. Within the GI, PTK6 is essential for growth and differentiation of the small intestine, as *Ptk6*$^{-/-}$ mice showed impaired differentiation and growth of the GI tract[272]. In the prostate, PTK6 is found in the nucleus of prostate epithelium where it regulates gland tissue differentiation[273]. Nuclear expression of PTK6 was also confirmed for oral epithelium[274]. Within the skin, PTK6 is found predominantly within the suprabasal keratinocytes where it positively regulates the differentiation in a calcium dependent manner[269]. Recently, Peng *et al.* confirmed the expression of inactive PTK6 in normal mammary gland tissue. Active PTK6, phospho-PTK6 (pPTK6), was detectable in tumour tissue predominantly at the plasma membrane[275].

1.7.3.3 PTK6 signalling partners

The physiological role of PTK6 is characterized as differentiation regulator, whereas in cancer, it facilitates proliferation and cell survival.

PTK6 is known to associate with other membrane proteins, such as the ErbB receptor family, ADAM15 and IGF-1R. Within the cytoplasm, PTK6 interaction partners are

AKT, paxillin, STAT3, STAT5, IRS-4 and β-catenin, while it interacts with Sam68, SLM-1 and SLM-2 in the nucleus. All four ErbB family members are known to interact with PTK6, leading to downstream substrate activation. Co-expression of ErbB3 leads to increased EGF signalling by AKT and PI-3K. The insulin receptor substrate-4 (IRS-4) was identified by Qui *et al.* as a PTK6 interaction partner, as IRS-4 presence induces PTK6 phosphorylation. IGF signalling is linked to poor prognosis for breast cancer patients, and may contribute to trastuzumab treatment resistance[276]. Zheng *et al.* identified that AKT is a direct substrate of PTK6. PTK6 phosphorylates AKT on Y315 and Y326, leading to AKT activation[277]. AKT signalling facilitates cell growth, proliferation and survival, as Haegebarth *et al.* showed that overexpression of PTK6 in Rat1a cells did not activate AKT[272]. The ADAM15/PTK6 interaction was identified by Zhong *et al.*, and only ADAM15 splice variants A and B were shown to interact with PTK6. ADAM15-A and B expression in breast cancer was linked to decreased relapse-free survival, whereas expression of ADAM15-C was linked to better patient prognosis[81]. PTK6 is able to activate STAT3 and STAT5b, known regulators of differentiation, proliferation, and apoptosis. STAT3 was identified by Liu *et al.*, as tyrosine phosphorylated substrate for PTK6[278]. PTK6 was able to phosphorylate STAT5b at Y699, leading to enhanced transcriptional activity. Knock down of either PTK6 or STAT5b in BT-20 breast cancer cells resulted in decreased DNA synthesis[279]. Derry *et al.* identified the co-localization of Sam68 and PTK6 within small nuclear bodies (SNBs). The RNA-binding function of Sam68 is negatively regulated by PTK6 expression, as phosphorylated Sam68 is inactive. The Sam68-like mammalian proteins 1 and 4 (SLM-1, SLM-4) are also inactivated upon phosphorylation by PTK6. Phosphorylation of SLM-1 and SLM-4 leads to reduced RNA-binding and cell cycle disruption, which impact posttranslational epithelial development and differentiation[280] (Table 6).

Table 6 PTK6 interaction partners

Localization	Factor	
Membrane	ADAM15	Zhong *et al.* (2008)
	ErbB1	Kamalati *et al.* (1995)
	ErbB2	Aubele *et al.* (2008)
	ErbB3	Kamalati *et al.* (2000)
	ErbB4	Aubele *et al.* (2008)
Cytoplasm	AKT	Zhang *et al.* (2005)
	MAPK	Aubele *et al.* (2008)
	Paxillin	Qui *et al.* (2005)
	STAT3	Liu *et al.* (2006)
	STAT5b	Weaver *et al.* (2007)
	β-catenin	Palka-Hamblin *et al.* (2010)
Nucleus	Sam68	Derry *et al.* (2000)
	SLM-1	Haegebarth *et al.* (2004)
	SLM-2	Haegebarth *et al.* (2004)

1.7.4 PTK6 role in prostate cancer

As mentioned in the previous paragraph, PTK6 lacks the myristolation sequence, which would target it to the cell membrane. In normal epithelial cells, PTK6 is thought to inhibit proliferation but enhances differentiation, which was calcium dependent. Increased calcium levels lead to increased PTK6 expression in those cells[269]. PTK6 further plays a key role in the regulation of apoptosis pathways in non-transformed cells[272].In prostate epithelia, PTK6 localization is predominantly nuclear. However, during prostate cancer development PTK6 is found to be cytoplasmic. In the LNCaP, androgen dependent prostate cancer cell line, PTK6 is predominantly found in the nucleus. However, the androgen independent prostate cancer cell line PC3 shows predominantly cytoplasmic PTK6 expression[273]. Re-localization of PTK6 in prostate cancer has been used as an indicator for disease progression, as it induces epithelial mesenchymal transition[281].

1.8 Work leading to this project

ADAM15 ICD is subject to alternative splicing. These variants show differences in abundance of their proline rich regions, allowing them to associate with SH3-domain containing cytoplasmic proteins. Our group has identified that ADAM15 splice variants A and B interact with PTK6, however splice variant C does not[81]. Preliminary data further showed that this interaction is independent of the PTK6 kinase activity. In breast cancer cells, data from our group further indicated a HGF-dependency of ADAM15 and PTK6 complex formation, as upon HGF treatment the interaction was enhanced. The HGF/cMET axis is a major regulator for cell invasion and migration. Individually, ADAM15[105] and PTK6[282] have been linked to promote cell invasion and migration.

Unpublished data from our lab showed differences in the splice profile of ADAM15 in the androgen dependent prostate cancer cell line LNCaP and the androgen independent prostate cancer cell line PC3. LNCaP express predominantly splice variants A and D, whereas PC3 predominantly express A. In breast cancer, our group linked expression of splice variant A and B to a poor prognosis for patients, whereas splice variant C was considered to be favourable for patients prognosis[81].

Our data indicate an important role for the ADAM15 and PTK6 interaction in prostate cancer progression. This interaction could further represent a promising target for prostate cancer therapy.

1.9 Aims of the project

To elucidate the importance of ADAM15 ICD splicing as well as the ADAM15 complex formation with PTK6 and cMET in prostate cancer progression the aims of this project are:

Aim 1

- To analyse a splice profile of ADAM15 with samples from prostate cancer patients and correlate this profile with
    - disease relapse
    - Gleason score
    - nodal Status
    - and tumour grade

Aim 2

- To investigate the role of ADAM15 splice variant overexpression on
    - cell size
    - cell cycle
    - actin cytoskeleton rearrangement
    - migration
    - and invasion of the prostate cancer cell lines PC3 and LNCaP.

Aim 3

- To assess the effect of ADAM15 overexpression on PTK6 localization in PC3 and LNCaP cells.
- To identify the splice variant dependent interaction of ADAM15 and PTK6 in PC3s and LNCaPs.
- To identify if PTK6 activity is needed for the interaction and if it can be enhanced via the HGF/cMET signalling axis.

Aim 4

- To elucidate the role of the cMET signalling axis in the complex formation between ADAM15 and PTK6.
- To elucidate the role of cMET inhibition of prostate cancer cell invasion.
- and moreover, to elucidate the role of ADAM15 catalytic function in prostate cancer cell invasion.

2 Materials and Methods

2.1 Cell Culture

The human androgen dependent prostate cancer cell line LNCaP, the androgen independent aggressive human prostate cancer cell line PC3, the human embryonic kidney cell line HEK293FT and the breast cancer cell line MDA-MB-231 were previously purchased from ATCC and kindly provided by Dr. Z. Poghosyan.

2.1.1 Subculturing of cell lines

Cell lines were cultivated at 37 °C in humidified air, supplemented with 5 % CO_2. Upon confluency, cells were passaged. They were washed with PBS (without Mg^{2+} and Ca^{2+}), and incubated for either 5 min for HEK293FT or 60 min for PC3 and LNCaP with 1 mL trypsin/EDTA (0.5 g/L porcine trypsin and 0.2 g/L EDTA *4Na) per 75 mm^2 flask. To stop trypsinisation, 5 mL cell culture medium (Table 7) was added, and cells were resuspended by pipetting up and down. Cells were diluted to the following ratios; 1:5 for PC3, and 1:3 for LNCaP and HEK293. PC3 cells were passaged once a week, whereas LNCaPs and HEK293FT were passaged twice a week.

Table 7 Cultivation medium for PC3, LNCaP and HEK293FT

Cell line	Origin	Medium	Supplements	Concentration
PC3	Human prostate adenocarcinoma	F12K +L-glutamine	FBS	10 %
			Penicillin/Streptomycin	100 µg/mL
LNCaP	Human prostate adenocarcinoma	RPMI	FBS	10 %
			Penicillin/Streptomycin	100 µg/mL
			L-Glutamine	2 mM
HEK293FT	Human embryonic kidney	DMEM	FBS	10 %
			Penicillin/Streptomycin	100 µg/mL
			L-Glutamine	2 mM
			NEAA	1 mM
			NA-Pyruvate	1 mM
MDA-MB-231	Human breast tumour cells	DMEM	FBS	10 %
			Penicillin/Streptomycin	100 µg/mL
			L-Glutamine	2 mM
			Hygromycin	450µg/mL

2.1.2 Freezing and thawing of cell lines

Cell lines were kept in liquid nitrogen for long term storage. Cells were removed from liquid nitrogen storage and thawed at 37 °C in a water bath. Cells were transferred into a new centrifugation tube containing 5 mL cell culture medium and centrifuged at 200 xg for 10 min. The supernatant was aspirated and the cells were resuspended in new culture medium and transferred to a new T75 flask.

Freezing of cell lines was performed as follows. Cells were trypsinized, resuspendend in culture medium, centrifuged at 200 xg for 10 min and resuspended in freezing medium (10 % DMSO, 40 % FBS and 50 % culture medium). Cells were transferred to the Mr. Frosty™ Freezing Container and slowly frozen overnight (O/N) in a - 80 °C freezer, then transferred to liquid nitrogen for long term storage.

2.1.3 Stable transfection of PC3 and LNCaPs using lentiviral transduction

Replication incompetent lentiviral particles of the ADAM15 expression vectors in pcDNA4-V5/His-A were produced and kindly provided by Dr Z. Poghosyan (Supplementary Data Figure 8.1). Within this system three packaging plasmids (PLP1, PLp2 and pLP/ VSVG) were provided which supply helper functions, structural and replication proteins (Supplementary Data Figure 8.2).

LNCaP and PC3 were seeded in 24 -well tissue culture dishes at a cell density of 1.2 x10^5/ well in growth medium without antibiotics. Cells were incubated for 24 h and infected with lentiviral particles. Polybrene (8 µg/ µL) was used as an infection enhancer. Cells were maintained in DMEM containing 10 % FBS. Afterwards, cells were trypsinized and transferred to T75 flasks containing selection medium (Table 8). Cells were kept in selection medium for 3 weeks. Afterwards, they were cultured in medium containing penicillin/streptomycin (Table 7 and Table 8).

Table 8 Selection medium for LNCaP and PC3 stable expressing the ADAM15 splice variants

Cell line	Medium	Supplements	Concentration	Selection	Concentration
PC3 ADAM15-A-E and Vector	F12K	FBS	10 %	G418	500 µg/mL
LNCaP ADAM15-A-E and Vector	RPMI	FBS L-Glutamine	10 % 2 mM	G418	500 µg/mL

2.1.4 ADAM15 proteolytic activity E349A mutant

PC3 cells stably expressing the ADAM15 splice variant proteolytically inactive E349A mutants, were made and validated and kindly provided by Dr. Z. Poghosyan. Expression plasmids of ADAM15 EA mutants were designed and validated by Dr. Z. Poghosyan.

2.1.5 MDA-MB-231 breast cancer cells

MDA-MB-231 vector control and ADAM15-A stably expressing cells were made, validated and kindly provided by Dr. Z. Poghosyan.

2.1.6 Stable transfection of PC3 with shRNA encoding plasmids

PC3 cells expressing shRNA targeting PTK6 were validated and kindly provided by Dr. Z. Poghosyan (Table 9). Cells were cultivated in F12K medium, containing 10 % FBS, 100 µg/mL penicillin/streptomycin and 1 µg/mL puromycin as the selection marker.

Table 9 shPTK6 and sh non-target sequences

Target	Catalogue number	Hairpin sequence	Vector	Clone ID	Region
Human PTK6	TRCN0000196912	5'-CCGG-GTGCAGGAAAGGTTCACAAAT-CTCGAG-ATTTGTGAACCTTTCCTGCAC-TTTTTTG-3'	pLKO.1	NM_005975.2-1506s1c1	3'UTR

Target sequence	Oligo design for arrayed cloning FWD	Oligo design for arrayed cloning REV
GTGCAGGAAAGG TTCACAAAT	5'-CCGGGTGCAGGAAAGGTTCACAAATCTCGAGATTTGTGAACCTTTCCTGCACTTTTTG-3'	5'-AATTCAAAAAGTGCAGGAAAGGTTCACAAATCTCGAGATTTGTGAACCTTTCCTGCAC-3'

2.1.7 Transient transfection of HEK293FT with overexpression plasmids

Plasmids for full-length ADAM15-A was provided by Dr. Z. Poghosyan, and PTK6-wild type and PTK6 K219M-mutant, were kindly provided by Dr. Amanda Harvey (Brunel University, London).

HEK293FTs were transiently transfected using Lipofectamine 2000, in a 3:1 Lipofectamine to plasmid ratio. Cells were seeded in culture medium without antibiotics at a density of 5 x10^5 cell / well of a 6-well-dish, and incubated for 24 h. Lipofectamine was diluted in serum-reduced Opti-MEM and incubated for 5 min.

Plasmids were diluted to a final concentration of 2.5 µg plasmid/transfection in Opti-MEM and added to the Lipofectamine, followed by 15min incubation at room temperature (RT) (Table 10). The complexes were added onto the cells and incubated for 24 h. Following the 24 h incubation period, the medium was changed to culture medium and cells were cultured for 24 h post-transfection before they were further analysed. For co-transfection of plasmids, plasmids were mixed at ratio of 1:1.

Table 10 Plasmid overview used for transient HEK293FT transfection

	Plasmid backbone	Tag
ADAM15-A	pcDNA-4- A	V5, His
PTK6 wild type	pcMV3	FLAG
PTK6 K219M-mutant	pcMV3	FLAG

2.2 Molecular biology methods

2.2.1 RNA extraction

For RNA extraction cells were grown in 60 mm tissue culture dishes until they were 80 % confluent. Cells were harvested, resuspended in PBS, followed by centrifugation at 200 xg for 5 min. The supernatant was aspirated. RNA extraction was performed as detailed in the RNeasy Qiagen Kit.

2.2.2 DNA and RNA quantification

DNA and RNA quantification was performed using the NanoDrop Spectrophotometer. 1 µL of sample was quantified by measuring the absorbance at 260 nm or 280 nm. Concentration was calculated using the Lambert-Beer law. Measurements were repeated three times, the mean calculated to determine the nucleic acid concentration in ng/ µL.

2.2.3 cDNA synthesis

The Superscript II kit (Invitrogen) was used, using 1 µg RNA per reaction. All steps were performed according to the manufacturer's protocol in a total volume of 20 µL (Table 11). RNA, dNTPs, Random Hexamers and H_2O were added and incubated for 5 min at 72 °C. 5 x single strand buffer and DTT were added and samples were incubated for 2 min at 25 °C in the Thermocycler. Superscript II was added and samples were incubated for 10 min at 42 °C, 50 min at 72 °C and 15 min at 70 °C. cDNA-Samples were stored at – 80 °C until further processed.

Table 11 Composition of RT reaction

Compounds	Concentration	Volume
RNA	1 μg	
dNTPs	0.5 mM	1 μL
Random Hexamers	0.4 μM	1 μL
5 x single strand buffer	1 x	4 μL
DTT	0.01 M	2 μL
Superscript II		1 μL
H_2O		to 20 μL

2.2.4 Primer design for PCR

Primer design for PCR and qPCR was done via the Primer BLAST tool from NCBi (https://www.ncbi.nlm.nih.gov/tools/primer-blast/). The NCBI Reference Sequences of the genes of interest were acquired using the Pubmed gene database (Table 12). The following parameters were applied for each primer design: Primer must span an exon-exon junction, 3' end of primer contain C or G residues, the GC content of the primer should be less than 60%, primer-dimer formation should be avoided. Primers were purchased from Eurofins

Table 12 NCBI Reference Sequence overview

Gene of interest	NICB Reference Sequence
ADAM15-A	NM_003815.4
ADAM15-B	NM_207194.2
ADAM15-C	NM_207196.2
ADAM15-D	NM_207191.2
ADAM15-E	NM_207195.2
ADAM15-MP	NM_003815.4
PTK6	NM_001256358.1
GAPDH	NM_001256799.2

2.2.5 PCR and Agarose gel electrophoresis

For PCR, the KAPA HiFi PCR kit was used. A PCR mix for a final reaction volume of 25 µL was prepared, containing PCR-grade water, forward and reverse primers (Table 13) at a final concentration of 0.3 µM, in 2.5 mM $MgCl_2$, 0.3 mM dNTP, 0.5 U

of KAPA Hifi HotStart DNA Polymerase and 100 ng of template DNA. Cycler conditions are shown in Table 14. Samples were analysed using 1 % agarose gels containing 1:10,000 gelRED®.

Table 13 PCR primer overview

Primer	Sequence 5'-3'	T_m
ADAM15-FWD	CTT GGT GCC AGC TAC TGG TAC CGT GCC CG	60
ADAM15-REV	CAG AGG TAG AGC GAG GAC ACT GTC GGA GG	
GAPDH-FWD	CGTCAAGGCTGAGAACGGGAAGCTTGTCATCAATG	66
GAPDH-REV	CATGCCAGTGAGCTTCCCGTTCAGCTCAGGGATG	

Table 14 PCR cycler conditions

	Temperature	Duration	Cycles
Initial denaturation	95 °C	3 min	1
Denaturation	95 °C	30 sec	
Annealing	Primer T_m dependent	30 sec	25
Extension	72 °C	1 min	
Final extension	72 °C	10 min	1

2.2.6 qPCR using KAPA SYBR® Fast

To detect the relative gene expression level of ADAM15 A-E splice variants and PTK6 using cDNA samples generated from prostate cancer patients' RNA, quantitative PCR (qPCR) was used.

A standard qPCR protocol was set up according to the MIQE-Guidelines by Bustin *et al.* (2009). cDNA was used as template for qPCR, using the KAPA SYBR® Fast mix. 30 ng cDNA was mixed with 400 nM of forward and reverse primers per reaction. Primer sets and cDNA was diluted in ultra pure DNAse/RNase-Free deionized H_2O. 5 µL of diluted cDNA was added to 96-well plate. 5µl master-Mix containing the primers(Table 15) and the KAPA SYBR® Fast mix was prepared and added per reaction. The final reaction volume per qPCR sample was 10µL. For each primer-set, a No-Template-Control (NTC) was used. The thermal cycler BioRad CFX was used with the following protocol (Table 16). Data analysis was performed according to the instrument-specific instructions, using the ADAM15 splice variant or PTK6 C_t, divided by the C_t value of the endogenous control, GAPDH.

Table 15 qPCR primer sets for prostate cancer patients ADAM15 splice profile and PTK6 expression level analysis

Primer Sets		Sequence (5'->3')	T_m
ADAM15-A	FWD	GTGACAGCAACAGGCACTGCTACTG	66
	REV	GCCCCTGAGACTTAGTGCCTC	
ADAM15-B	FWD	CGAGGCACTAAGCAGGCTAGTGCTC	64
	REV	GCCCCTGAGACTGGAGTCTC	
ADAM15-C	FWD	CGAGGCACTAAGGCTAGTGCTCTC	66
	REV	GCCCCTGAGACTTCGGGCTTC	
ADAM15-D	FWD	GTGACAGCAACAGGCACTGCTACTG	64
	REV	GCCCCTGAGACTGTACTGGC	
ADAM15-E	FWD	CGAGGCACTAAGGCTGAGCTGG	66
	REV	GCCCCTGAGACTTCGGGCTTC	
ADAM15-MP	FWD	GCTGATCACTCGGAGGCCCAGAAATACCGGGACTTC	66
	REV	CCTGGTAGGAAGTCTGTGGAGGCCTCC	
GAPDH	FWD	GGCACCGTCAAGGCTGAGAACGGGAAGC	64 and 66
	REV	CCCTGCAAATGAGCCCCAGCCTTCTCC	
PTK6	FWD	GATCAGGGTCAGCGAGAAGC	64
	REV	GGCCCTGTGGTAGTTCACAA	

Table 16 qPCR condition cycle overview

	Temperature	Duration	Cycles
Enzyme activation	95°C	3min	1
Denaturation	95°C	10sec	39
Annealing/extension	Primer T_m dependent	30sec	
Dissociation/ Melt curve	Primer T_m dependent - 95°C	increment 0.5°C for 5sec	1

2.3 SDS-PAGE & Western blot

2.3.1 Preparation of whole-cell lysate

All steps were performed on ice. Cells were washed twice with ice cold PBS. RIPA lysis buffer (20mM Tris-HCl pH7.5, 150mM NaCl, 1mM Na_2EDTA, 1mM EGTA, 1% NP-40, 1% SDS, 2.5mM Sodium Pyrophosphate, 1mM β-glycerophosphate, 1mM Na_3VO_4, 1ug/ml leupeptin) containing phosphatase (25x PhosphoStop, Roche), protease inhibitors (20x Proteinase inhibitor, Sigma), and phenanthroline 10 mM (pan-metalloproteinase inhibitor) was added. Cells were incubated for 5 min and detached using a cell scraper. The lysate was transferred into a pre-cooled test tube, incubated for 10 min on ice and sonicated 3 times (Bioruptor-Sonicator, Diagenoide) for 30 sec at 50% amplitude. Lysates were centrifuged at 14800 rpm for 10 min at 4 °C, and the supernatant was transferred into a new test tube. Lysates were stored at – 80 °C.

2.3.2 Protein quantification

The protein concentration was assessed in whole cell lysates, using the bicinchoninic acid (BCA) Pierce assay kit. This assay kit is based on a copper redox reaction leading to the formation of coloured complexes with BCA. The assay was performed in 96 -well plates according to the supplier's protocol. Samples were assayed in triplicate. Plates were incubated for a 2 h period at 37 °C after the addition of 200 µL BCA working reagent. Absorbance was measured at 562 nm on a plate reader. Sample protein concentration in µg /mL was calculated from a standard curve using a 3rd order polynomial trend line function in Microsoft Excel.

2.3.3 Sample preparation

Following cell lysis and protein quantification, samples were diluted to a total protein amount of 20- 40 µg/ 20 µL in RIPA-buffer. 6 x loading dye (Table 17) was added and samples were incubated for 5 min at 95 °C. Samples were centrifuged for 2 min at 14800 rpm before loading on gels.

Table 17 6x protein loading dye

	Final concentration in Buffer	Volume
0.5 M Tris pH 6.8	300 mM	6 mL
Bromophenol blue (1 %)	0.05 %	0.5 mL
Glycerol	20 %	2 mL
SDS (10 %)	1.5 %	1.5 mL
β-mercaptoethanol		0.625 mL

2.3.4 SDS-Polyacrylamide gel casting

Resolving and stacking gel solution were prepared, as shown in Table 16 and Table 17, and stored at 4 °C wrapped in wet tissue and cellophane for 24 h.

Table 18 SDS-Polyacrylamide resolving gel schematic overview

	6 %	8 %	12 %
H_2O	6 mL	5.5 mL	4.5 mL
1.5 M Tris pH 8.8	2.5 mL	2.5 mL	2.5 mL
40 % Acryl:Bis 29:1	1.5 mL	2 mL	3 mL
10 % SDS	100 µL	100 µL	100 µL
10 % APS	100 µL	100 µL	100 µL
TEMED	10 µL	10 µL	10 µL

Table 19 SDS-Polyacrylamide stacking gel schematic overview

	4 %
H_2O	6.5 mL
0.5M Tris pH 6.8	2.5 mL
40% Acryl:Bis 29:1	1.0 mL
10% SDS	100 µL
10% APS	100 µL
TEMED	10 µL

2.3.5 Electrophoresis

Gels were assembled in the electrophoresis cell. Inner and outer chamber were filled with 1 x SDS-PAGE running buffer, diluted 1:10 from 10 x SDS-PAGE Running buffer

stock (Table 20). The electrophoresis cell was connected to the power supply for 90 min at 100 V. Afterwards the electrical leads were disconnected and the gel cassette was opened. The gel was removed by floating it off the plate into 1 x transfer buffer (Table 21).

Table 20 SDS-Page running buffer

	Compound concentration	For 1L
10 x SDS-PAGE Running buffer/ L	250 mM Tris-Base	30.28 g
	1.92 M Glycine	144.13 g
	1 % SDS (from 20 %)	50 mL

2.3.6 Western blot

The 1x transfer buffer (prepared from 10x (Table 21) and supplemented with 0.02% SDS, 20% Methanol) was prepared 24 h in advance and stored at 4 °C. PVDF membranes were incubated for 10 min in 100 % methanol and transferred to 1 x transfer buffer (Table 21). Filter paper and fiber pads were soaked in 1 x transfer buffer. The blot was transferred for 2 h at 400 mA. Upon run completion the cassette was disassembled and PVDF membranes were incubated at RT for 1 h in 5 % non-fat milk dissolved in 1 x TBST, i.e. 1x TBS containing Tween-20 (1:1000), with gentle shaking (Table 21).

Table 21 Western blot transfer and wash buffer

	Compound concentration	For 1 L
10 x TBS pH 7.6 stock	200 mM Tris-Base	24.2 g
wash buffer	150 mM NaCl	88 g
10 x Transfer buffer stock	0.1 M $NaHCO_3$	8.4 g
	0.03 M Na_2CO_3	3.1 g
1x Transfer buffer	1:10 10 x transfer buffer	100 mL
	0.02 % SDS	2 mL
	20 % Methanol	200 mL

2.3.7 Detection

The primary antibody was diluted in 5% BSA dissolved in 1x TBST (Table 22). Following PVDF membrane blocking, the primary antibody was added and incubated over night at 4°C with gentle shaking. The primary antibody was removed and membranes were washed 3 x in TBST for 15 min. The blot was incubated with secondary antibody (Cell Signaling Anti-mouse (7076) or Anti-rabbit (7074) IgG,HRP-linked Antibody) diluted in 5% non-fat milk in 1x TBST, for 1h at RT. The secondary antibody was removed and membranes were washed 3 x with TBST for 15min. The Pierce™ ECL plus (Thermo Fisher) was added per membrane and incubated for 3 min at RT. Membranes were exposed to ECL films. Films were developed using an automated ECL film developer (Xograph).

Table 22 Western Blotting primary and secondary antibody dilution

Antibody	Supplier	Catalogue number	Species	Detected bands	Primary antibody	Secondary antibody
4G10 (pan phosphor tyrosine)	Merck Millipore	05-1050	mouse	45kDa	1:1000	1:3000
Actin	Sigma	A2066	rabbit	42kDa	1:5000	1:6000
ADAM15 (ICD)	Abcam	Ab39159	rabbit	95-115kDa (splice variant dependent)	1:1000	1:3000
ADAM10	Abcam	Ab39177	rabbit	100kDa	1:1000	1:2000
Gab1	Cell signalling	3232	rabbit	110kDa	1:1000	1:3000
Grb2	Cell signaling	3972	rabbit	25kDa	1:2000	1:4000
Grb2	Santa Cruz	sc-255	goat	25kDa	1:2000	1:4000
Met-ECD	Millipore Merck	05-1049	mouse	170kDa	1:1000	1:3000
pMet	Millipore Merck	07-810	rabbit	150kDa	1:1000	1:3000
pPTK6-Y342	Millipore Merck	09-144	rabbit	45kDa	1:1000	1:3000
pPTK6-Y447	Invitrogen	PA5-38413	rabbit	45kDa	1:1000	1:3000
PTK6	Invitrogen	PA5-14787	rabbit	45kDa	1:1000	1:1000
PTK6	Invitrogen	MA5-15328	mouse	45kDa	1:1000	1:3000
V5	Sigma	46-0705	mouse	95-115kDa (detecting exogenous ADAM15)	1:5000	1:8000

2.3.8 Densitometry

Protein band intensities were quantified using ImageJ. Scanned membranes (600dpi) were loaded into ImageJ and the relative density per lane was identified using the *plot lane* option. The resulting peaks, displayed in a separate window were enclosed using the *straight line* tool, by drawing a line across the peak base. The *wand* tool was used

to quantify the peak height, and obtained values were copied to Excel. Protein band intensities were compared to the actin loading control and the ratio was calculated. For statistical analysis, blots from three independent experiments were analysed.

2.3.9 Immunoprecipitation (IP) using Dynabeads®

A total volume of 15 µL (5 µg protein binding capacity) Protein G Dynabeads® were used per IP reaction. First, the antibody-Dynabead® (Table 23) incubations were performed at 4 °C for 1 h with gentle rotation, followed by sample incubation at 4 °C O/N. Samples were washed 3 times with 200 µL RIPA buffer. As elution buffer the 6 x loading buffer was used. Samples were analysed via SDS-PAGE and Immunoblotting as described before.

Table 23 Overview of antibodies used for IP

Antibody	Catalogue number	Supplier	Species	Concentration	µg protein/ volume
cMET	sc-161	Santa Cruz	rabbit	5 µg/IP	400µg/200µL
PTK6	PA5-14787	Invitrogen	rabbit	2.5 µg/IP	350µg/200µL
Grb2	3972	Cell signaling	rabbit	10 µg/IP	200µg/200µL

2.3.10 IP using V5-coated agarose beads

A total volume of 5 µL agarose coated V5 beads were used per IP reaction. They were incubated in a total volume of 300 µL containing 250 µg total lysate, diluted in RIPA buffer, O/N at 4 °C. Samples were centrifuged for 1 min at 14,800 rpm. The supernatant was aspirated and 200 µL of RIPA buffer were added. This step was repeated three times. As elution buffer the 6 x loading buffer was used. Samples were analysed via SDS-PAGE and Immunoblotting as described before.

2.4 Immunocytochemistry and Confocal Microscopy

2.4.1 Sample preparation

Coverslips were transferred into 35 mm tissue culture dishes and coated using cell line specific medium for 24 h at 37 °C/5 % CO_2 in the incubator. 4 x10^5 cells were grown on coverslips afterwards for 3 days. Cells were washed 3 x with PBS and fixed using 4 % paraformaldehyde for 15 min at RT. Cells were permeabilized using 0.1 % of Saponin in PBS for 5 min at RT. Blocking was performed with 1 % BSA in PBS for 30 min at RT. The primary antibody was added and samples were incubated at 4 °C O/N (Table 24). The following day, coverslips were washed three times with PBS, the

fluorochrome labelled secondary antibody was added, and incubated for 1 h at RT in the dark (Table 24). The mounting medium containing the counter stain DAPI was added onto a microscope slide, following three times washing with PBS, the coverslip was placed on top of the mounting medium with the cells facing the microscope slide. Microscope slides were incubated at RT in the dark O/N. For long term storage they were kept at 4 °C in the dark. They were analysed using the Leica TCS SP5 Confocal Microscope.

Table 24 Antibodies used for Immunocytochemistry

Antibody	Supplier	Catalogue number	Species	Primary antibody dilution	Secondary antibody dilution
PTK6	Invitrogen	PA5-14787	Rabbit	1:600	Anti-rabbit AlexaFluor®488 1:1000
V5	Sigma	46-0705	Mouse	1:1000	Anti-mouse AlexaFluor®568 1:1000

2.4.2 Immunocytochemistry- image acquisition

The Leica TCS SP5 Confocal Microscope equipped with argon (488 line) and HeNe (543 and 633 lines) lasers was used for IF-image acquisition. Cells were analysed using the HCX PL APO CS 63.0x1.4 Oil UV objective. The LAS AF lite software was used to acquire the images. A positive control was used to adjust the settings for confocal analysis. Gain was adjusted until saturated pixels appeared and reversed until pixels completely disappeared in the lookup-table. The offset was set to 0. Zoom was set between 1.5 and 2 or 4 for detailed structural analysis.

2.5 Cell volume (cell size) determination using Flow cytometry

The cell volume of each cell line was determined using flow cytometry. Cells were seeded in 35 mm dishes and incubated for 48 h. Cells were counted and harvested at a concentration of 0.5 $x10^6$/ mL. They were centrifuged for 5 min at 200 xg and resuspended in 200 µL PBS. Cells were centrifuged, resuspended in 1.5 mL ice cold ethanol and incubated for 1 h at - 20 °C, centrifuged and washed with 1 mL PBS three times. Cell suspensions were measured using the BD Accuri C6 flow cytometer. The side scatter -areas (SSC-A) was plotted versus the forward scatter-area (FSC-A). Cell

aggregates and debris were removed from the analysis by gating the cells (Figure 2.1). Doubles were excluded by plotting FSC-A versus the FSC-height (FSC-H). Living cells (live cells) were than shown as histogram using the FL-2 channel. To obtain the initial cell size, by determine the median, living cells were plotted as histogram and the median was determined automatically by Flow Jo V10, and used as a read-out of cell size.

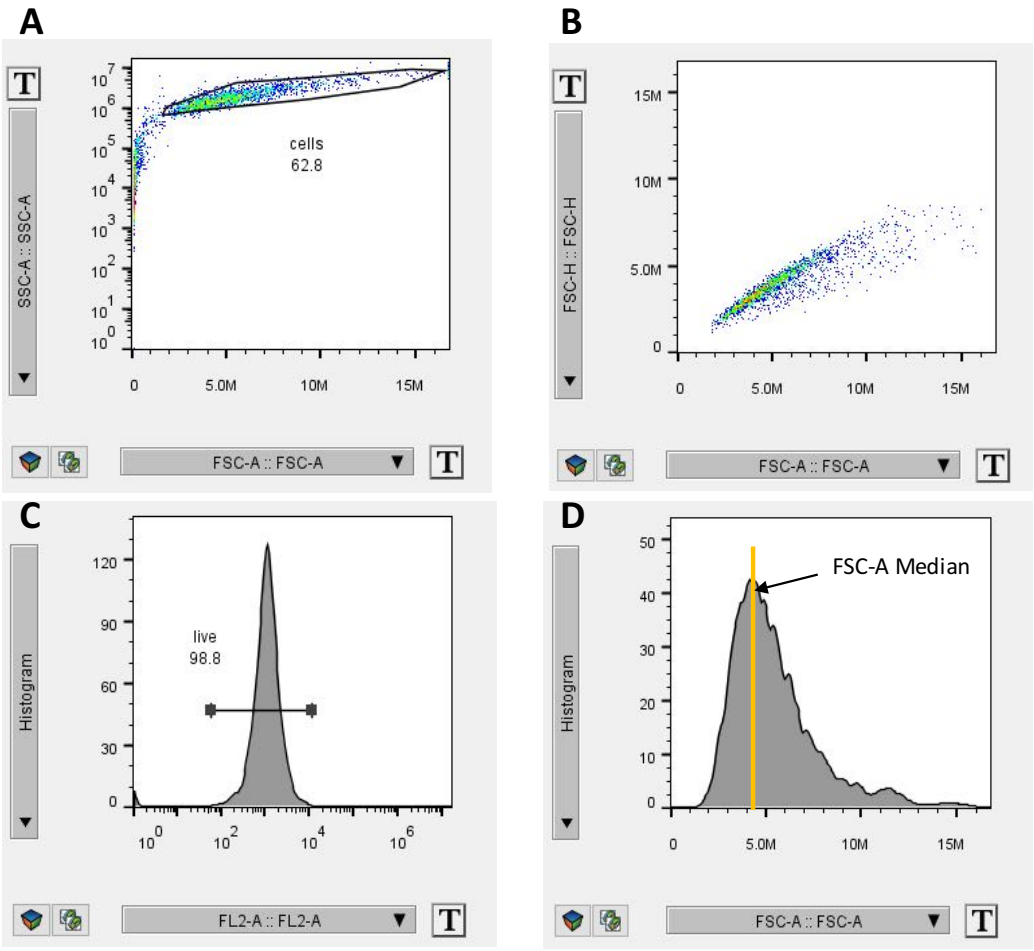

Figure 2.1 Overview of cell size analysis using flow cytometry

(A)FSC-A was plotted versus the SSC-A to exclude cell debris and gate the cells. (B) Gated cells are shown via FSC-H versus FSC-A, excluding doublets. (C) Histogram plot of living cells using the FL1-A channel. (D) By choosing the FSC-A channel in the histogram option, Flow Jo V10 determined the FSC-A Median, which is given as dimensionless number and used as read out for the cell volume (cell size).

2.6 Cell cycle analysis

The NucleoCounter NC-3000 was used and the two-step cell cycle analysis protocol was followed. 1 x10^6 cells were used per analysis and the assay was performed in triplicate. Cells were grown in 35 mm dishes for two days, trypsinized, counted and

harvested in PBS after centrifugation (1 x10 ^{6}cells per analysis). The DAPI containing solution was added and cells were incubated for 5 min at 37 °C. Cells were analysed by quantifying cellular fluorescence and DNA content, and were shown as histogram on the screen of the NC-3000 software®. Percentile values for each cell cycle stage (i.e. G_1/G_0, S, G_2/M) were exported and analysed using GraphPad Prism.

2.7 PTK6 kinase assay

PC3 vector and ADAM15-A expressing cells were seeded and grown until 80 % confluent. They were serum starved for 30h, followed by 30 min of HGF treatment (20ng /mL). Cells were lysed and 500 μg/200 μL of total protein was used per IP with anti-PTK6. IPs were incubated O/N at 4 °C rotating. Samples were washed 3 times with RIPA-buffer and resuspended in 40 μL kinase buffer (Table 23) supplemented with 5 μM ATP. Samples were incubated shaking for 1 h at 37 °C. The reaction was terminated using 6 x loading dye. Samples were analysed using western blotting, and probing with a pan-phospho tyrosine antibody 4G10.

Table 25 Kinase assay buffer components

Kinase assay buffer	
Compounds	**Concentration**
MOPS	25 mM pH 7.2
β-glycerol-phosphate	12.5 mM
$MgCl_2$	20 mM
$MnCl_2$	12.5 mM
EGTA	5 mM
EDTA	2 mM
DTT	0.25 mM

2.8 cMET and PTK6 treatments

For the PC3 and LNCaP cell panels inhibitor treatments (Table 26) were used targeting either cMET or PTK6. $1x10^5$- $1x10^6$ cells were grown in tissue culture plates (35 mm-100 mm) until 80 % confluent and serum starved (serum free culture medium containing antibiotics) for 30 h.

Table 26 Overview of inhibitor concentrations

Inhibitor	Company	Target	Stock concentration	Final concentration
Capmatinib	Selleckchem	cMET	2 µM	200 nM
SU11274	Selleckchem	cMET	100 nM	10 nM
Tifrinib	Axon Medchem	PTK6	10 µM	1 µM

Following serum starvation, the medium was removed and cells were treated with either a single or combined treatment of the inhibitors (Table 27). Control cells were supplemented with HGF 20 ng/mL as stimulation control, or 0.001 % DMSO as solvent control. After the treatment, cells were lysed, the total protein amount was quantified, followed by IP and analysis via western blotting.

Table 27 LNCaP and PC3 treatment overview

	Capmatinib	SU11274	Tilfrinib
single	30 min	30 min	30 min
combined	30 min + 30 min HGF 20 ng/mL	30 min + 30 min HGF 20 ng/mL	30 min + 30 min HGF 20 ng/mL

2.9 Metabolic Cell proliferation Assay

The colorimetric MTS ([3-(4,5-dimethylthiazol-2-yl)-5-(3-carboxymethoxyphenyl)-2-(4-sulfophenyl)-2H-tetrazolium) metabolic cell proliferation assay was used for the PC3 ADAM15 A-E panel. The MTS is reduced by the dehydrogenase enzyme of viable cells into the coloured formazan, which is detectable at an absorbance of 490 nm.

Cells were seeded in triplicate at 3 x10^3 /100 µL in a 96-well plate. The plates were incubated for 24 h in the 37 °C/5 % CO_2 incubator. After 24 h, 20 µL of the CellTiter 96® AQueous One Solution Reagent was added per well. After 1 h incubation, the absorbance was measured at 490 nm using a plate reader.

2.10 Invasion assay

Corning Matrigel Matrix, was thawed at 4 °C O/N. All materials i.e. pipet tips, 24-well plate, invasion chambers (transparent PET membrane with 8 µm pores) were chilled prior to the start of the experiment. All coating steps were performed on ice. The coating solution, containing the Matrigel Matrix at a final concentration of 0.3 mg /mL, was prepared using the sterile coating buffer (0.01 M Tris (pH 8.0), 0.7 %NaCl). The

solution was mixed gently and kept on ice. 50 µL of the coating solution were added to the invasion chambers and distributed equally. Plates with invasion chambers were incubated for 2 h at 37 °C in the incubator. The remaining liquid was removed carefully. 2 x10^4 cells, in 0.5 mL serum free medium, were seeded into each coated invasion chamber. Cells were incubated O/N with serum free medium in top chamber at 37 °C in the incubator. The next day, 0.75 mL of the chemo-attractant, cell culture medium containing 10 % FBS or 20 ng /mL HGF, were added to the bottom of each well, followed by 24h incubation at 37 °C in the incubator.

The Opti-MEM medium was removed by pipetting and a moistened cotton swab was inserted on top of the invasion chamber to gently remove the non-invaded cells. The invaded cells on the lower surface were stained using a 1 % crystal violet aqueous solution for 10 min followed by a 2 min methanol (100 %) fixation step. The invasion chambers were then rinsed with H_2O to remove excess staining solution. The invasion chambers were air dried O/N with the bottom facing up. Invaded cells were analysed under the microscope at 4 x magnification. Invaded cells in 4 different fields of view were counted manually in triplicate. The number of invading cells was calculated by dividing the mean number of invaded cells, divided by the number of seeded cells. Manual cell count was performed using ImageJ, by clicking on each cell individually. Data analysis was performed using GraphPad Prism and One-way-ANOVA.

2.11 cMET dependent cell invasion

PC3 ADAM15 splice variant expressing cells were used in invasion assay, as described previously (Section 2.10). Cells were incubated for O/N in serum free medium at 37°C in the incubator. On the next day, the inhibitor was added 1h prior to HGF to the top chamber. HGF was added to the bottom chamber and cells were incubated for 24h at 37°C in the incubator. Cells were analysed as described earlier (Section 2.10).

Table 28 Invasion assay treatment overview

	untreated	HGF	SU11274	SU11274/HGF
top chamber	serum free medium	serum free medium	10nM	10nM
bottom chamber	serum free medium	20ng/mL	serum free medium	20ng/mL

2.12 Cell migration using permeable supports

Cells were seeded at 2 x10^4 /0.5 mL in permeable supports (8 µm pore size) to analyse cell migration. For each time point, one permeable support per cell lines was used. The following time points were used, 1 h, 8 h, 24 h and 48 h after seeding. Cells were fixed using 100 % methanol for 2 min followed by 10 min staining with 1 % crystal violet. Migrated cells were analysed under the microscope at 4 x magnification. Migrated cells in 4 different fields throughout the membrane were counted in triplicate. The number of migrated cells was calculated by dividing the number of seeded cells. Cells were counted manually using ImageJ. Data analysis was performed with GraphPad Prism using One-Way-ANOVA.

2.13 Detecting ADAM15 dimers by crosslinking

To assess ADAM15 dimerization, chemical crosslinking of ADAM15-A and D stably expressing cells or transiently transfected HEK293 cells was applied.

HEK293 cells, transiently transfected with pcDNA4-ADAM15-A or D, or PC3 ADAM15-A and D stably expressing cells were grown until confluent on 10 cm dishes and harvested, resuspended in homogenization buffer and sonicated to lyse the cells (Table 29). Homogenates were centrifuged at 14,800 rpm for 10 min at 4 °C, and 18 µL aliquots were subsequently crosslinked with 2 µL of the crosslinker glutaraldehyde (0.0025 % v/v). Samples were incubated for 2, 5, 10, 15, 20, 30 and 60 min with the cross-linker solution and stopped with 2 µL of 20 % hydrazine per sample. The control sample (zero time point) did not contain any cross-linker, but was treated also with 2 µL of hydrazine. 6 x loading dye was added to each sample and samples were analysed via SDS-PAGE and western blotting.

Table 29 Homogenisation buffer composition for chemical cross linking

Buffer	Compound concentration
Homogenisation buffer pH7.4	5mM Hepes 0.3M Sucrose

2.14 Zymogram

To assess proteolytic activity of ADAM15-A-WT and mutant ADMA15-A-EA in PC3 cells, a gelatin zymogram was used.

PC3 cells expressing either ADAM15-A-WT or ADAM15-A-EA and vector control were grown and serum starved for 30 h using serum free culture medium. Cells supernatants were collected and 40 μL were run on a zymogram containing 100μg/mL gelatine in a 6% SDS-PAGE gel. Sample loading dye was prepared without β–mercaptoethanol or other reducing agents. The gel was run followed by a 1h incubation in wash buffer (Table 30), and O/N incubation in developing buffer (Table 30), and 2h staining in Coomassie brilliant blue. Three independent repeats of collected cell supernatants were run on the same zymogram.

Table 30 Zymogram buffer overview

Buffer	Compounds and concentration
Wash buffer	0.05mM Tris HCl 5mM $CaCl_2$ 2.5% Triton-X-100
Developing buffer	0.05mM Tris HCl 5mM $CaCl_2$

2.15 Statistical analysis

Within this Thesis if not stated otherwise statistical analysis was performed using GraphPad Prism 6.01 for Mac. One Way Anova was performed with the following setting: Experimental design: no matching or pairing; Assume Gaussion distribution: Yes; Multi Comparison: Compare the mean of each column with the mean of every other column; Options: Correct for multi comparison, Test Tukey; Confidence interval: 0.05. The error bars are shown

as standard error of the mean (SEM), to show the precision of the sample mean.

2.16 Prostate cancer patient samples

83 prostate cancer patient RNA samples were kindly provided by the Welsh Cancer Bank (WCB). RNA was extracted from frozen tissue blocks using the QIAgen RNAeasy Minikit. All steps were performed according to the WCB SOP EN01. Ethics approval to the Welsh Cancer Bank was given by the Wales Research Ethics Committee (WEC) 3, as "a research tissue biobank to collect and issue biomaterials for cancer related research".

3 ADAM15 splice profile in prostate cancer patients

3.1 Introduction

Biomarkers are defined as molecules found in blood or other body fluids indicating a change from normal to disease processes within the body. They can be further divided into prognostic biomarkers evaluating the disease outcome of the patient regardless of the treatment, or into predictive biomarkers, that evaluate the effect of treatment and the treatment response [283–285]. Biomarkers can be proteins, epigenetic DNA changes, DNA or RNA, or metabolites. In the clinic, biomarkers are used to address seven main clinical questions such as: What is the patients risk? Does earlier detection decrease mortality? Who is at risk? What is the clinical outcome? Which is the appropriate therapy? Which therapy is effective? What is the risk of adverse reaction?[286].

In prostate cancer, the main diagnostic biomarker, despite its limitations, is prostate specific antigen (PSA). Until today, PSA is used in the clinic to diagnose prostate cancer, however it cannot address the clinical needs to identify patients with low PSA levels (<10 ng/mL), and it fails to distinguish benign from aggressive, metastatic disease[286].

Members of the ADAMs family have a key role in cancer formation and progression due to their role in regulating a number of signalling pathways[79]. Aberrant expression of especially ADAM9, ADAM10, ADAM15 and ADAM17 has been linked to cancer progression and it can contribute to decreased survival in breast cancer[81], prostate cancer[132] and NCSL[157]. Consequently, they have been considered as predictive markers for cancer patients.

The predictive potential of ADAM9 and ADAM10 was assessed in a study with 259 samples from estrogen receptor positive breast cancer patients, showing disease relapse upon Tamoxifen treatment. High expression levels of ADAM9, but not ADAM10, showed a significant higher efficacy in tamoxifen therapy. Sieuwerts *et al.* concluded that high ADAM9 expression levels predict good outcome in response to tamoxifen therapy[287]. Contrary to the beneficial effect of ADAM9 expression in breast cancer, Fritzsche *et al.* used ADAM9 expression as a PSA-independent marker in prostate cancer (PCa). High ADAM9 expression levels were linked to decreased relapse-free survival in PCa patients[104]. They suggested ADAM9 as a prognostic marker for disease aggressiveness and tumour behaviour.

ADAM17 is known to promote proteolytic cleavage of growth factors, including TGF-α, amphiregulin, and TNF-α among others. It is considered to promote cancer onset and progression and was used by McGowan *et al.* as a prognostic readout for breast cancer patients. The expression levels were independent from tumour size, lymph node stage, estrogen status or age. Patients with high ADAM17 expression levels showed reduced survival. Furthermore, McGowan *et al.* suggested ADAM17 as predictive for patients that are resistant to EGFR and HER-2 targeting therapies, as ADAM17 is known to cleave the EGFR ligand TGF-α.

ADAM15 is associated with aggressive prostate cancer[105] and breast cancer[100]. DNA levels were examined in cDNA microarrays, and ADAM15 expression was found to be dominant in prostate and breast carcinomas, and was linked to disease progression by Kuefer *et al.*[288]. Prior to this, Ortiz *et al.* identified the alternative exon use of ADAM15, which affects the intracellular domain composition, in breast cancer cells and they suggested an extensive investigation to characterize clinical tumours[134]. These findings and suggestions were taken further by Kleino *et al..* In 2007, Kleino *et al.* identified in total 13 splice variants and analysed the abundance of those transcripts in normal human tissues. ADAM15 splice variant A was predominantly expressed (up to 88%) in all analysed tissues such as, ovary, placenta, kidney, liver and colon. ADAM15 splice variant D was also expressed but with an abundance of 10 to 40%[289]. Zhong *et al.* assessed the function of the ADAM15 ICD splice variants, A-D, in breast cancer patients. In their study cohort, ADAM15-B and C were found to be significantly higher when compared to healthy tissue. ADAM15-D was hardly detectable and excluded from further patient analysis. In a next step, 229 breast cancer patient samples with a follow-up period of up to 15 years were analysed for their ADAM15-A, B and C expression. ADAM15 expression levels were correlated against age, menopausal status, tumour size or grade, nodal status, Nottingham Prognostic Index, or steroid hormone receptor status. Relapse-free survival was assessed by Cox regression analysis. ADAM15-A and B were linked with poor prognosis in patients although they were lymph node metastasis free. Strikingly, patients with lymph node metastasis and high expression levels of ADAM15-C were found to have a better prognosis. These findings led to the conclusion that alternative ADAM15 splicing has functional relevance and ADAM15-A and B may drive disease progression. They might affect the site of the primary tumour, i.e. initiating the spread of cancer cells. ADAM15 splice variant C was suggested to have a positive influence and might have an impact on metastatic spread. However, the splice variant specific effect in breast cancer is complex and might affect both the tumour origin and the

metastatic site[81]. Based on Zhong *et al's.* findings, Maretzky *et al.* found a splice variant specific interaction of ADAM15-B with the tyrosine kinase Src. The interaction led to enhanced proteolytic activity of ADAM15- B, when compared to ADAM15-A, and cleavage of FGFR2iiib. Src has been linked to aggressive breast cancer, however, FGFR2iiib is considered as tumour suppressor. The interaction of Src with ADAM15-B and the enhanced cleavage of the FGFR2iiib could be used to treat breast cancer patients, as the authors suggested that enhanced cleavage of the tumour suppressor FGFR2iiib by ADAM15-B leads to disease progression.[156]

A recent study by Burdelski *et al.* (2017), analysed total ADAM15 expression in 9826 prostate tumour tissue microarrays. High staining levels for ADAM15 were linked to high Gleason grade and advanced tumour stage. Additionally, PCa aggressiveness was linked to high ADAM15 expression levels in a small patient population[132].

Prognostic markers are important as they help to classify cancer as either benign or malignant. Prognostic markers are needed to prevent over or under treatment of patients. Herein, we want to validate and establish a qualitative qPCR method to analyse the splice profile of ADAM15 in PCa patients. Another prostate cancer marker, which is abundantly expressed, is PTK6. PTK6 relocates during prostate cancer progression from the nucleus to the cytoplasm leading to signalling pathway disruption and phenotypic changes in tumour cells[273]. PTK6 interacts with ADAM15 in a splice variant specific manner and will be analysed in parallel[81].

3.1.1 Aim of the chapter

The aim of this chapter was to develop and validate a quantitative PCR diagnostic method and to analyse the ADAM15 splice profile in PCa patients, in order to test whether the ADAM15 splice profile may predict disease outcome.

Accordingly, a qPCR method was established and assessed for specificity, accuracy, sensitivity and reproducibility.

qPCR with the ADAM15 splice variant specific primers was optimized, and validated. As endogenous control GAPDH was chosen. PTK6 primers were designed and validated accordingly. Cell lines expressing ADAM15 splice variants were initially used to validate the qPCR method. Subsequently, RNA samples with RIN values > 6 of PCa patients, obtained from the Wales Cancer Bank, were analysed for their ADAM15 splice profile and PTK6 expression levels. The ADAM15 splice profile was correlated with clinical data. In addition to PCa patient tissue, RNA from 8 healthy

prostate tissue samples, kindly provided by Dr. Lin Ye (Cardiff University, School of Medicine), were analysed for ADAM15 splice variant and PTK6 expression.

3.2 Results

3.2.1 ADAM15 splice variant specific primers

To analyse a quantitative ADAM15 splice profile in PCa patients, splice variant specific primers, designed against the ICD of ADAM15 A-E, were kindly provided by Dr Christian Roghi (University of East Anglia, UK) (Figure 3.1).

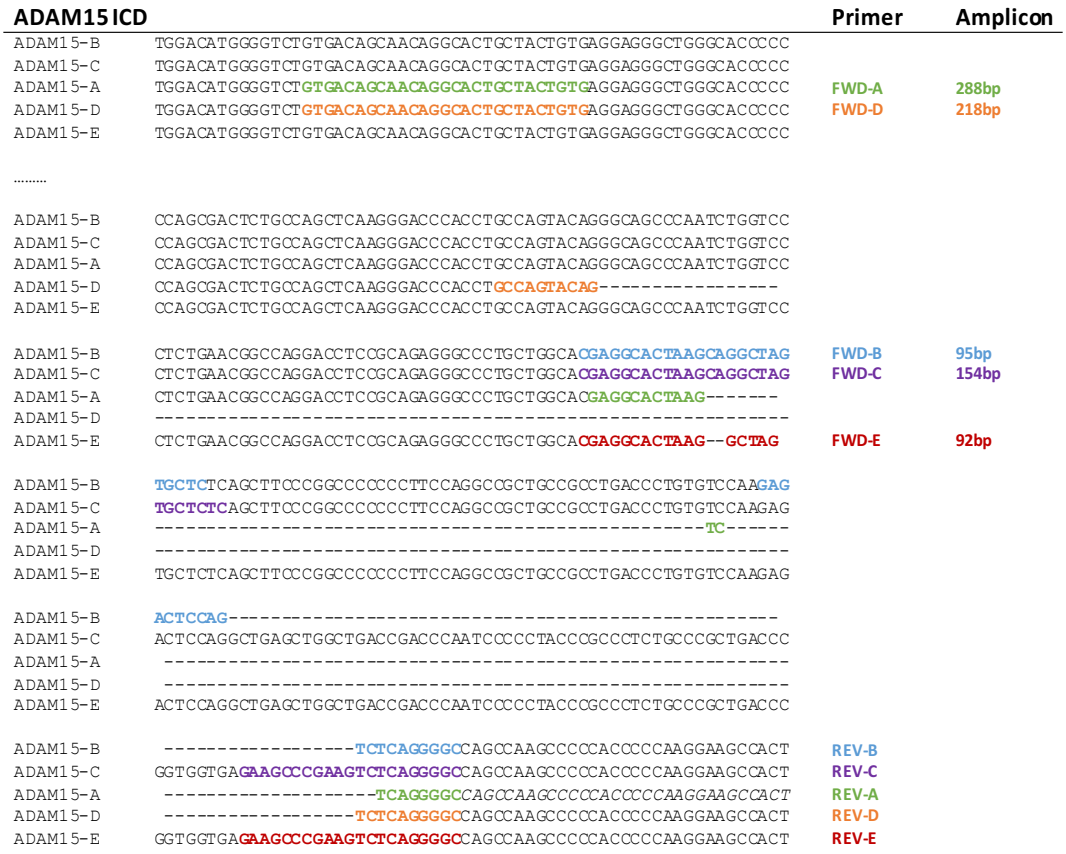

Figure 3.1 Schematic overview of the ADAM15 ICD splice variant specific primer design.

The primer design for the ADAM15 splice variants is shown, using the cDNA sequences of the ADAM15 ICDs for each variant. Primer pairs for each splice variant are shown in different colours, the calculated amplicon size is shown next to each FWD primer. Primer pairs were designed across exon-intron boundaries to ensure specificity.

In addition, primers for the endogenous control, GAPDH, and PTK6 were designed. To analyse the total expression of ADAM15 in the patient samples, primers against the extracellular metalloproteinase domain of ADAM15 were designed and included in the subsequent analysis (Table 31).

Table 31 Sequence overview for qPCR primer sets.

Primer Sets	NCBI-ID		Sequence (5'->3')	Start-Stop	Amplicon size bp
ADAM15-A	NM_001261464.1	FWD	GTGACAGCAACAGGCACTGCTACTG	2101-2125bp	288
		REV	GCCCCTGAGACTTAGTGCCTC	2388-2368bp	
ADAM15-B	NM_207194.2	FWD	CGAGGCACTAAGCAGGCTAGTGCTC	2367-2391bp	218
		REV	GCCCCTGAGACTGGAGTCTC	2463-2444bp	
ADAM15-C	NM_207196.2	FWD	CGAGGCACTAAGGCTAGTGCTCTC	2367-2390bp	95
		REV	GCCCCTGAGACTTCGGGCTTC	2532-2512bp	
ADAM15-D	NM_207191.2	FWD	GTGACAGCAACAGGCACTGCTACTG	2101-2125bp	154
		REV	GCCCCTGAGACTGTACTGGC	2318-2299bp	
ADAM15-E	NM_207195.2	FWD	CGAGGCACTAAGGCTGAGCTGG	2367-2388bp	92
		REV	GCCCCTGAGACTTCGGGCTTC	2460-2440bp	
ADAM15-MP	NM_00126146.1	FWD	GCTGATCACTCGGAGGCCCAGAAATACCGGGACTTC	1040-1074bp	237
		REV	CCTGGTAGGAAGTCTGTGGAGGCCTCC	1305-1279bp	
GAPDH	NM_001289746.1	FWD	GGCACCGTCAAGGCTGAGAACGGGAAGC	274-301bp	170
		REV	CCCTGCAAATGAGCCCCAGCCTTCTCC	443-417bp	
PTK6	NM_005975.3	FWD	GATCAGGGTCAGCGAGAAGC	365-384bp	163
		REV	GGCCCTGTGGTAGTTCACAA	527-508bp	

3.2.2 Analysis of ADAM15 splice variants, PTK6 and GAPDH primers

To ensure that obtained primers were optimally designed to perform high quality qPCR, all primer sequences were first checked using the OligoEvaluator software (Sigma-Aldrich) for secondary structures, self-dimers and cross-dimer formation. The ΔG values, Gibbs Free Energy G, to break secondary structures were required to be up to – 5 kcal/mol for self dimer and – 6 kcal/mol for cross-dimers for each primer pair, but none of the ADAM15 ICD primers showed self or cross-primer dimer formation (Table 32). Secondary structures were found for all ICD primers, with the exception of ADAM-15-E FWD. The ADAM15-C and E REV primers showed secondary structures, which were found to be very strong, however, they were below the calculated annealing temperature and therefore irrelevant.

Table 32 Overview of secondary primer structures for the qPCR primer sets.

Primer		Secondary Structure	T_m of secondary structure < annealing T_m	ΔG <-5kcal/mol (Self-dimer)	ΔG <-6kcal/mol (cross dimer)	Expected self and cross dimers
A	FWD	moderate	Yes	Yes	Yes	no
	REV	weak	Yes	Yes	Yes	no
B	FWD	strong	Yes	Yes	Yes	no
	REV	moderate	Yes	Yes	Yes	no
C	FWD	strong	Yes	Yes	Yes	no
	REV	very strong	Yes	Yes	Yes	no
D	FWD	moderate	Yes	Yes	Yes	no
	REV	moderate	Yes	Yes	Yes	no
E	FWD	none	Yes	Yes	Yes	no
	REV	very strong	Yes	Yes	Yes	no
ADAM15-MP	FWD	Moderate	Yes	Yes	Yes	no
	REV	weak	Yes	Yes	Yes	no
GAPDH	FWD	Strong	Yes	Yes	Yes	no
	REV	moderate	Yes	Yes	Yes	no
PTK6	FWD	moderate	Yes	Yes	Yes	no
	REV	Weak	Yes	Yes	Yes	no

3.2.3 Temperature and primer concentration optimization

The melting temperature (T_m) of ADAM15 ICD specific primers, PTK6, ADAM15-MP and GAPDH primers was also calculated using the OligoEvaluator (Sigma-Aldrich). Based on this evaluation, temperature gradients for each primer sets were chosen and tested (Table 33). Splice variant specific expression plasmids were kindly provided by Dr. Z. Poghosyan. 10ng of either pcDNA4-ADAM15 A to E plasmids for the ADAM15 splice variant specific primers, or 100 ng of PC3 PCa cell line cDNA, for GAPDH, PTK6 and ADAM15-MP primers were used to run temperature gradients. All samples were analysed in triplicate in the iQ 96-Well real time semi skirted PCR plates which were sealed with an adhesive seal. Primer titrations from 100 nM-400 nM per reaction were used per temperature step. Annealing temperature for ADAM15-A, C, E and MP primers was optimized to 66 °C, whereas ADAM15-B, D and PTK6 primers were optimized to 64 °C. The GAPDH primer set was optimized for both temperatures, as they were needed as endogenous controls (Table 33). Primer concentrations for all primer sets were optimized to 400 nM (Table 33).

Table 33 Overview of primer concentration and T_m optimization.

Primer		Calculated T_m °C	Gradient °C	Optimized T_m°C	Primer concentration gradient nM	Optimized primer concentrations nM
A	FWD	66.3	59 - 71	66	100- 400	400
	REV	63.7				
B	FWD	67.9	59 - 72	64		
	REV	63.5				
C	FWD	66.1	61 - 71	66		
	REV	65.7				
D	FWD	66.3	59 - 71	64		
	REV	63.5				
E	FWD	65.8	60 - 70	66		
	REV	65.7				
ADAM15-MP	FWD	73	60-73	66		
	REV	71				
GAPDH	FWD	70	60-73	64+66		
	REV	72				
PTK6	FWD	66.4	59-69	64		
	REV	64.9				

qPCR was performed using the CFX Connect Real–Time PCR Detection System from Bio-Rad, using the protocol shown below (Table 34).

Table 34 qPCR cycle condition overview.

	Temperature	Duration	Cycles
Enzyme activation	95°C	3min	1
Denaturation	95°C	10sec	39
Annealing/extension	Primer T_m dependent	30sec	
Dissociation/ Melt curve	Primer T_m dependent - 95°C	increment 0.5°C for 5sec	1

3.2.4 Product specificity

To ensure product specificity of the ADAM15 A-E splice variant specific primer sets, following annealing temperature and primer concentration optimization, the melting curves were analysed using ADAM15 A-E splice variant specific expression vectors as the template.

ADAM15 A-E splice variant specific products showed a single melt peak with no shoulder, representing a single amplicon for all splice variants. As a representative

example, ADAM15- D was chosen. The negative first derivative (- d (RFU)/dt) of the change in fluorescence (RFU), is plotted versus the temperature, showing a single peak for ADAM15- D and no detectable peak for the non-template controls (NTCs) (Figure 3.2 A). Agarose gel electrophoresis for PC3 cDNA samples, analysed for all primer sets, showed PCR amplicons of the correct size (Figure 3.2 C). However, ADAM15- MP domain primers showed two products on the gel, which were not detectable by qPCR (Figure 3.2 D). As expected from the melt curve analysis, a single band for all primer set amplicons, with exception of the ADAM15- MP primers, was detectable. No product amplification was detectable for NTCs (Figure 3.2 B).

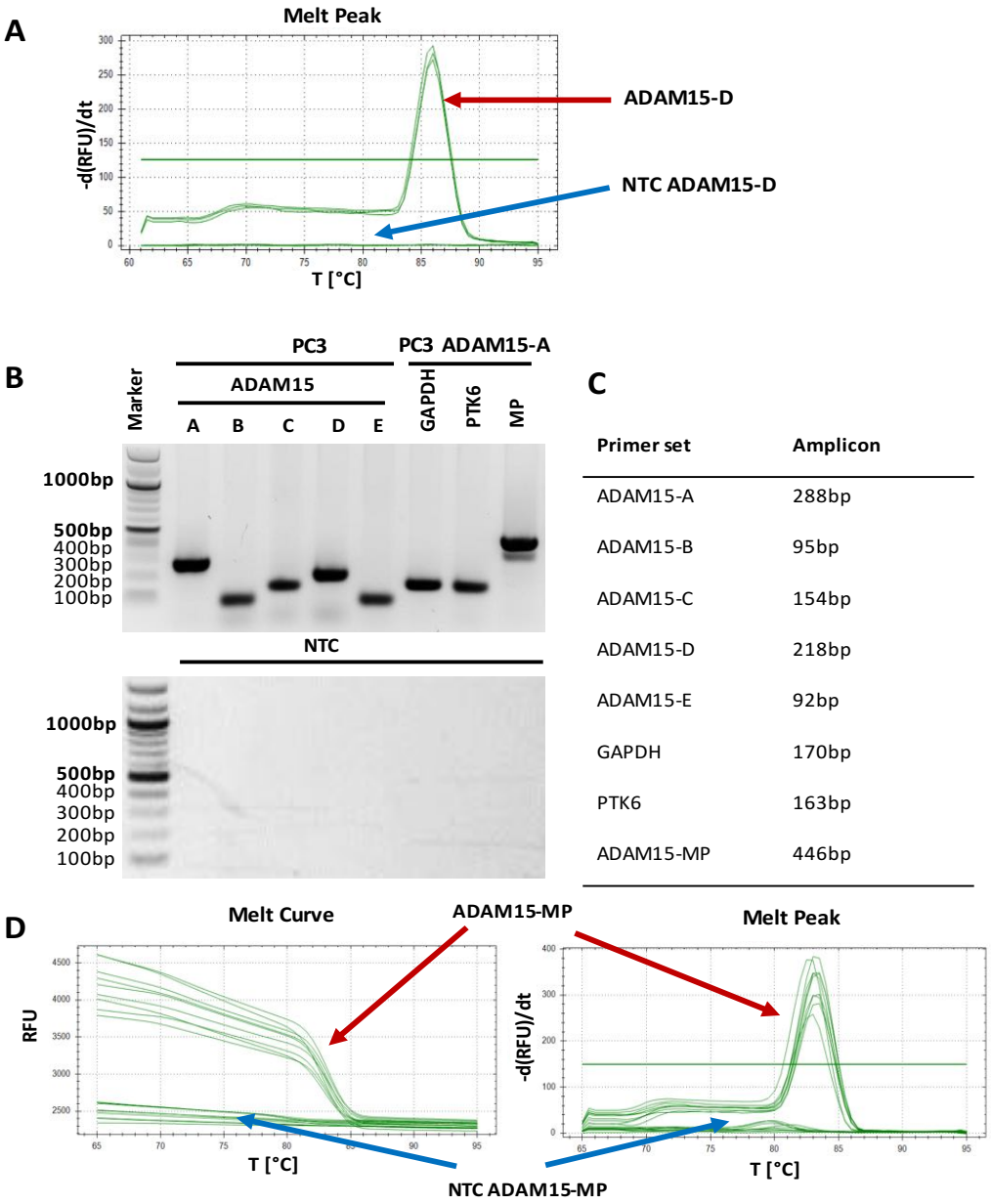

Figure 3.2 qPCR method specificity verification using melt curves and agarose gel electrophoresis.

(A) Melt curve analysis of generated products for all primer sets were generated. An example is shown for ADAM15-D. The expression plasmid, pcDNA-4-ADAM15-D, was used as template. The plot for the negative first derivative of the fluorescence versus temperature (-d(RFU)/dt vs T) shows 1 single peak for each the ADAM15-D triplicates, using a T_m of 64°C, and no peak for the NTC control is detectable. (B) An 1% agarose gel was used to analyse the qPCR products from PC3 cells isolated cDNA. All primer sets showed presence of amplification product of the expected calculated amplicon size, with exception of the MP-domain which showed a second slightly smaller amplicon(C). qPCR results for Melt curve and melt peak for ADAM15-MP primers, showing no second peak. NTC are free from amplification products (D).

3.2.5 Taq-Polymerase optimization for GC – rich templates

To validate the Taq-polymerase efficiency used for the amplification of ADAM15 splice variants, two different Taq polymerases were tested using the cDNA from the PC3 prostate cancer cells. The iQ SYBR Green supermix and the KAPA SYBR Fast were compared. GC content for all ADAM15 splice variant specific templates was calculated using the EndMEMO DNA GC content calculator.

ADAM15 A-E templates are GC-rich, as their calculated GC-content is > 75 % (Figure 3.3 A). qPCR using both SYBR green mixes, revealed equal splice variant amplification for splice variants A, B, D and E. In contrast, the iQ SYBR green supermix failed to amplify splice variant C (Figure 3.3 B). However, using the KAPA SYBR Fast mix for GC rich templates, amplification of splice variant C was possible (Figure 3.3 B).

A

	GC content
ADAM15-A	76%
ADAM15-B	77%
ADAM15-C	78%
ADAM15-D	75%
ADAM15-E	78%
GAPDH	56%

B

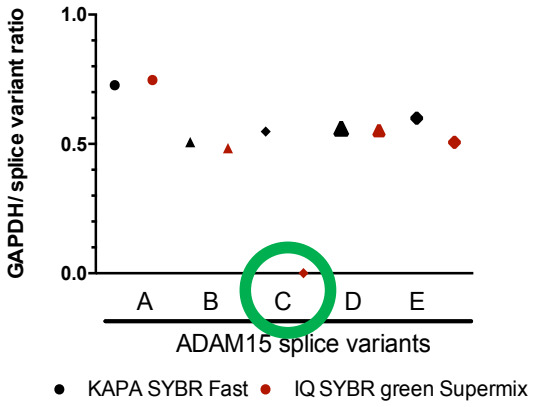

Figure 3.3 Validation of SYBR green polymerase for GC-rich templates.

The GC-content of the ADAM15 A-E splice variant primer amplified templates was calculated using the EndMEMO DNA GC content calculator. The GC content is shown in (A), GAPDH GC content is shown as control. All ADAM15 splice variant amplified templates showed a GC content ≥75%. To validate the KAPA SYBR FAST qPCR mix for the amplification of GC-rich templates, the BioRad SYBR Green Master Mix was used in comparison. All splice variants were amplified using the KAPA SYBR green, whereas the BioRad SYBR green was not able to amplify the ADAM15-C splice variant (B), indicated by the green circle. C_t values for GAPDH were divided by each splice variant and were plotted as GAPDH/splice variant ratio.

3.2.6 Standard curves and qPCR efficiency optimization

To guarantee equal amplification for all ADAM15 splice variants, ADAM15-MP and PTK6, standard curves were used in a range of 10^{-1} to 10^{-4} ng of the splice variant specific expression plasmids. For PTK6, the pcMV3-PTK6 expression vector was used. ADAM15-MP standard curves were generated using the ADAM15-A specific expression vector.

qPCR efficiency (ε) was calculated following annealing temperature and primer concentration optimization, and calculated using the following equation, $\varepsilon = 100*(10^{-1/slope}-1)$ (Figure 3.4 A). The efficiency of the splice profile analysis was in the recommended range of 90-105%, and all splice variants, ADAM15-MP and PTK6 showed a similar amplification efficiency of 90-94 %. R^2 for all standard curves was calculated with > 0.98 (Figure 3.4 B). C_t values for replicates were in a similar range.

A

	Slope	Amplification efficency (ε) $\varepsilon=100*(10^{-1/slope}-1)$	Linearity (R^2) ≥ 0.98
ADAM15-A	-3.592	90%	0.99
ADAM15-B	-3.556	91%	0.99
ADAM15-C	-3.519	93%	0.99
ADAM15-D	-3.605	90%	0.99
ADAM15-E	-3.521	92%	0.99
ADAM15-MP	-3.465	94%	0.99
PTK6	-3.474	94%	0.99

B

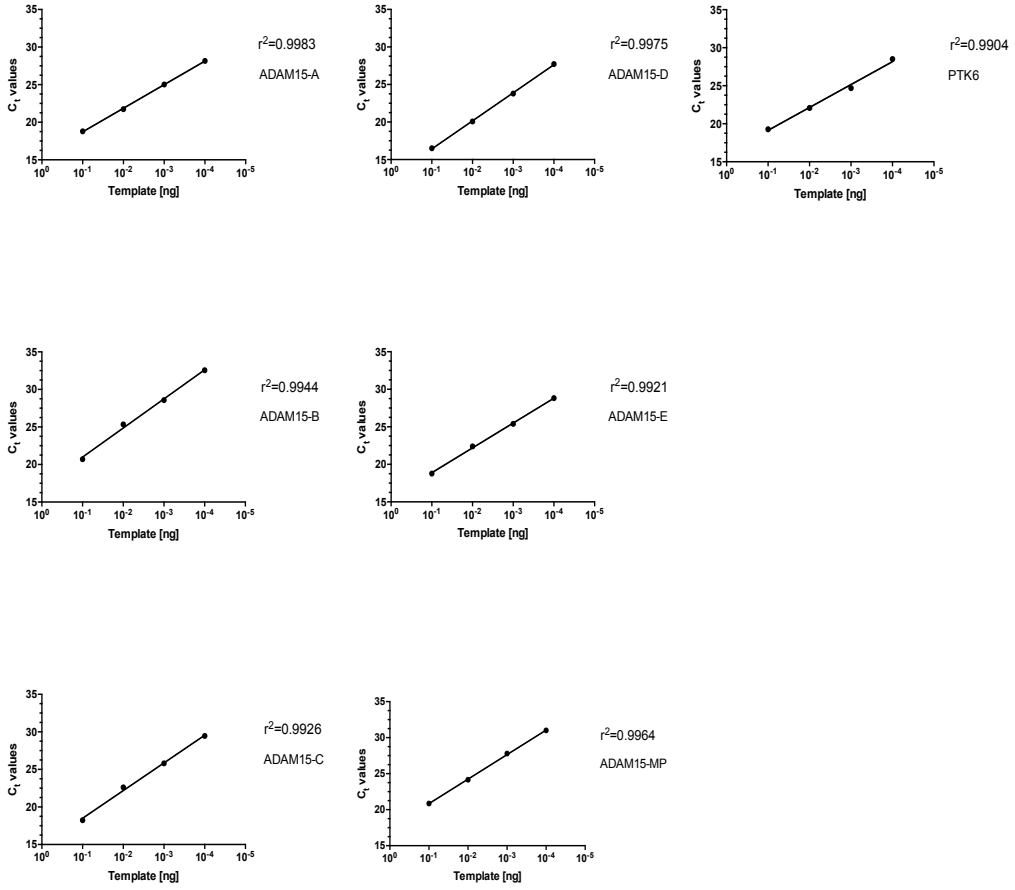

Figure 3.4 Determination of qPCR reaction efficiency using standard curves.

(A) Standard curves were used to assess the qPCR amplification efficiency (90-105%) and the linear dynamic range (R^2 >0.980). Amplification efficiency (ε) is shown for each primer set. Harmonized amplification efficiency was obtained for all primer sets after temperature and primer amount optimization. (B)Standard curves using the ADAM15 splice variant specific mammalian expression vectors in pcDNA4-A and the mammalian expression vector pcMV3-PTK6 for PTK6. Standard curves were titrated from a range of 0.1ng to 100fg.

3.2.7 Analysis of the ADAM15 splice profile in prostate cancer cell lines

Initially, the splice profile of ADAM15 expression in the prostate cancer cell lines PC3 and LNCaP was analysed. ADAM15 splice variant A, C, E, ADAM15-MP and GAPDH were run on one plate, as annealing temperature was optimized to 66 °C. ADAM15-B and D, PTK6 and GAPDH were run on a separate plate, as the annealing temperature was optimized to 64 °C for those primer sets. Standard curves for all splice variants were run on the corresponding plates. The GAPDH C_t values were divided by C_t values for each ADAM15 splice variant and plotted as GAPDH ratio.

qPCR analysis of the ADAM15 splice profile in PC3 and LNCaP showed differences in expression levels for each splice variant. PC3 cells showed presence of predominantly splice variant A, weak presence of splice variant B, and similar levels of splice variant C, D and E (Figure 3.5 A). In LNCaPs, expression of splice variant A and D was found predominantly (Figure 3.5 B). ADAM15-MP primers, which were initially designed to show the overall ADAM15 expression, as they detect total ADAM15, however, for both cell lines the overall amount of ADAM15 present in the cell lines could not be determined. This might be linked to the fact that two amplified bands were present on the gel (Figure 3.2 B), and thus excluded this primer set from further analysis. PTK6 expression levels were enhanced in PC3 cells, when compared to LNCaPs (Figure 3.5 C).

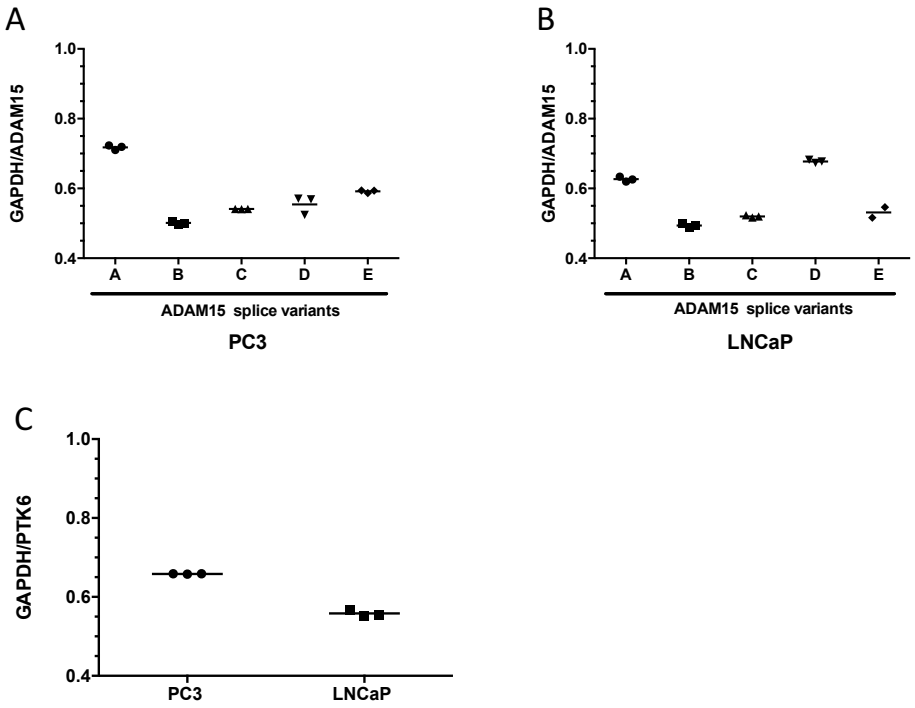

Figure 3.5 ADAM15 splice profile and PTK6 expression in prostate cancer cell lines.

ADAM15 A-E splice variants, and PTK6 expression was analysed by qPCR in the prostate cancer cell lines PC3 (A) and LNCaP (B). GAPDH was used as endogenous control. GAPDH-C_t values were divided by C_t values for the targets and are expressed as GADPH ratio. PTK6 expression between the two cell lines was compared and plotted as GAPDH/PTK6 ratio (C).

3.2.8 Validation and reproducibility of the ADAM15 splice profile in patients

To start the analysis of the ADAM15 splice profile and PTK6 levels in PCa patient samples, 5 patient RNA samples were randomly chosen and analysed twice by qPCR. As an additionally quality control, PCa patient samples with an RNA integrity number of (RIN) >6 were included in the analysis, samples with a RIN value below 6 were excluded, due to high RNA degradation.

An ADAM15 splice profile was obtained for all patient samples. PTK6 expression was also detectable for all patient samples. Splice variant specific differences for each patient were obtained, when the GAPDH value was divided by that of the splice variants and plotted as GAPDH ratio. Reproducibility of the splice profile and PTK6 expression was achieved for all patient samples (Figure 3.6).

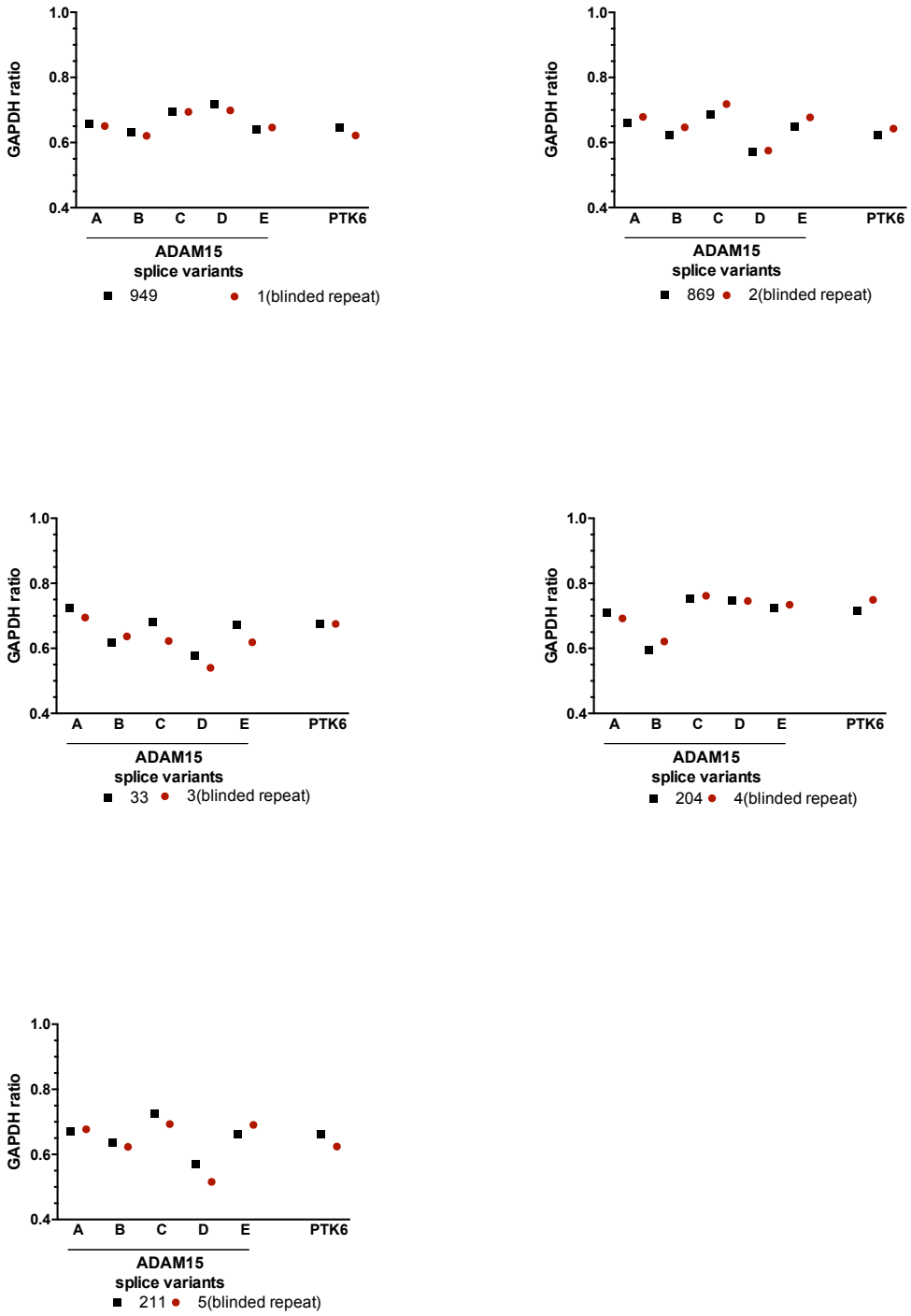

Figure 3.6 qPCR method validation using patient samples.

Five patient samples were analysed via qPCR for the expression of the ADAM15 splice variants and PTK6. Samples were re-analysed blinded, shown in red. Each graph represents the qPCR analysis for one patient and the blinded repeat. GAPDH-C_t values were divided by C_t values for the ADAM15 splice variants and PTK6 and are expressed as GADPH ratio.

3.2.9 ADAM15 splice variant and PTK6 expression is significantly lower in healthy prostate tissue compared to PCa patient samples

To assess differences of ADAM15 splice variant and PTK6 expression, prostate cancer patient samples and healthy tissue samples were analysed using qPCR. 83 prostate cancer patient samples obtained from the Wales Cancer Bank, and 8 healthy prostate samples, obtained from Dr. Lin Ye (Cardiff University, School of Medicine), were analysed.

Significant upregulation of all ADAM15 splice variants and PTK6 was found when splice profiles from patient samples and heathy tissue were compared (Figure 3.7 A). In healthy tissue samples, splice variant B was expressed highest, in contrast to the patient samples, where splice variant C was the most abundant (Figure 3.7 A). Assessing statistically significant changes (Figure 3.7 C) within the splice variants, One-way-Anova, comparing each splice variant for healthy tissue and prostate cancer samples, revealed, that ADAM15-C is significantly higher expressed, compared to splice variants B, D, E and compared to PTK6. Significant changes for splice variants and PTK6 are summarized in Figure 3.7 C.

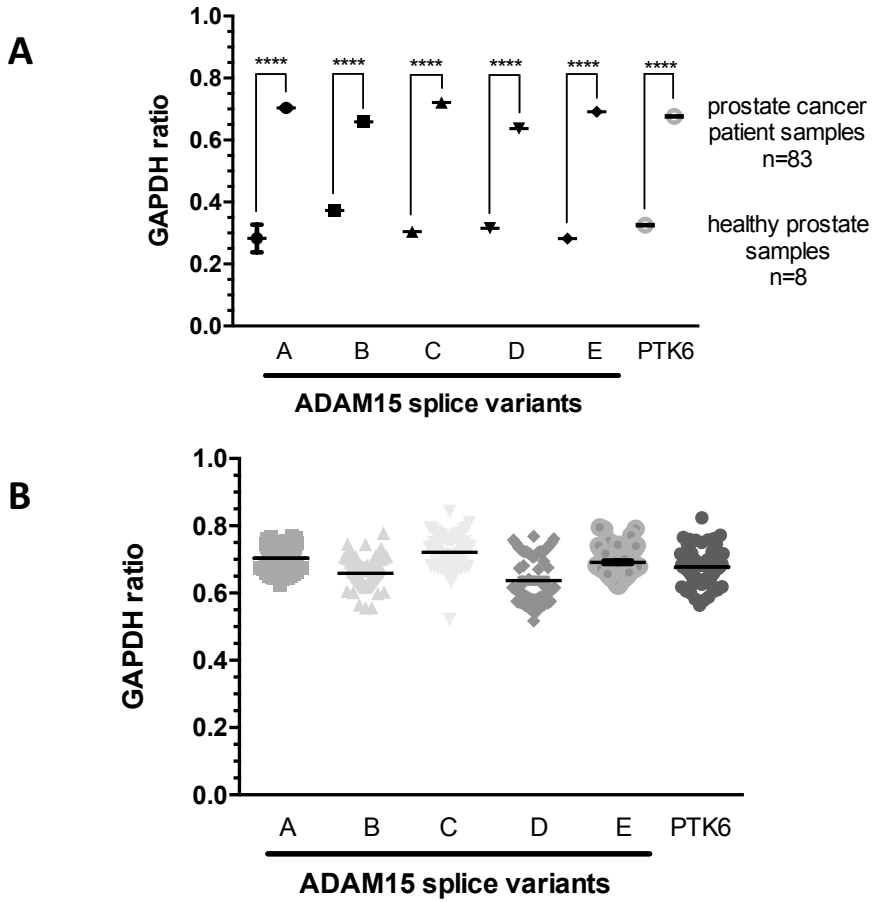

C

	ADAM15-A	ADAM15-B	ADAM15-C	ADAM15-D	ADAM15-E	PTK6
ADAM15-A		**		****		**
ADAM15-B	**		****	*	***	
ADAM15-C		****		****	***	**
ADAM15-D	****	*	****		***	*
ADAM15-E		***	***	***		
PTK6	**		**	*		

Figure 3.7 ADAM15 and PTK6 expression profile in healthy prostate tissue and prostate cancer patients.

Using qPCR with ADAM15 splice variant specific primers and primers for PTK6 and GAPDH as control an expression profile was generated. (A) Expression profile of mean values for healthy prostate tissue (n=8) and prostate cancer samples (n=83). Significant overexpression of ADAM15 splice variants and PTK6 was found when compared to healthy tissue. (B) Splice profile in prostate cancer patients, showing all analysed patients individually. Ct values were normalized against GAPDH. (C) Statistical analysis of the splice profile generated in patients. Using One-Way-Anova, ADAM15 splice variants and PTK6 were compared with each other. Significant changes of the splice variants with each other and PTK6 are summarized in the table. $p>0.05$ *, $p<0.01$ **, $p<0.001$ ***, $p<0.0001$ ****.

3.2.10 ADAM15 splice profile in healthy tissue and PCa patients

To assess a difference in splice variant expression between healthy tissue and PCa patients, a Forest plot analysis was conducted by calculating the mean difference between healthy and PCa patients plotted for each splice variant and PTK6. Resulting calculated values, represents the change in expression from healthy to cancerous tissue for each splice variant.

In Figure 3.8 A, the mean difference in expression of ADAM15 splice variants and PTK6 revealed that ADAM15 splice variant A shows the highest change in expression, followed by splice variants C and E, when comparing healthy tissue and PCa patient samples. Splice variant B and D showed the lowest change in expression, even lower than the change in PTK6 expression levels.

A

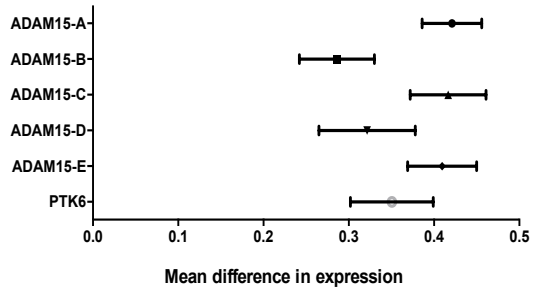

B

	Healthy Tissue		PCa patients					
	Mean GAPDH ratio	SD	Mean GAPDH ratio	SD	Mean difference in expression	Standard Error	Lower Confidence Interval (LCI 95%)	Upper Confidence Interval (UCI 95%)
A	0.2827	0.1260	0.7037	0.0329	0.4210	0.0175	0.3861	0.4559
B	0.3731	0.1258	0.6590	0.0402	0.2859	0.0220	0.2422	0.3296
C	0.3049	0.1412	0.7216	0.0447	0.4167	0.0223	0.3723	0.4611
D	0.3155	0.1259	0.6369	0.0716	0.3214	0.0286	0.2646	0.3782
E	0.2819	0.1369	0.6914	0.0404	0.4095	0.0202	0.3693	0.4497
PTK6	0.3252	0.1623	0.6759	0.0499	0.3507	0.0245	0.3021	0.3993

Figure 3.8 Forest plot of mean difference between ADAM15 splice variants and PTK6 in healthy tissue and PCa patients.

A Forest plot was conducted to plot the mean difference of the GAPDH ratios for each splice variant and PTK6 in healthy tissue and PCa patients (A). The mean values and standard deviation for each splice variant and PTK6 were calculated. The mean difference was calculated by subtracting PCa patient means from healthy tissue means. Upper and lower confidence intervals (95%) were calculated for each data point, and plotted for each data point as error bars. The calculated means in difference between healthy tissue and PCa patients for each splice variant and PTK6 are shown in the Forest plot above. The Forest plot was generated using GraphPad Prism. (B) Summary of data and performed calculations, used for the Forest plot analysis.

3.2.11 Correlation of clinical patient data with the ADAM15 splice profile

Clinical data such as Gleason score, tumour grade, disease relapse, deceased patients were obtained for the patient cohort we analysed here, and were arranged in a table and presented as overall percentage. Since for 17 patients clinical data for Gleason score, and for 20 patients clinical data for tumour grade were missing, those patients are presented as unknown.

Patient classification by Gleason score is shown in Table 35. 42 patients showed a score of 7, 23 patients a score of 6 (Table 35). Patients with a Gleason score of 8, 9 and 10 were excluded, as for each of the scores, only one patient was available for analysis (Supplementary data Figure 8.3). The most abundant tumour grades was 2,

with 25 patients, and then tumour grade 3a, with 21 patients. Overall, 13 patients suffered from disease relapse, and 5 patients were eventually deceased (Table 35).

Table 35 Overview of clinical patient data

		Number of patients
Gleason score	6	23
	7	42
	unknown	17
Tumour grade	2	25
	3	6
	3a	21
	3b	8
	unknown	20
Relapse		13
Deceased		5

In order to analyse potential correlation of ADAM15 splicing with clinical parameters such as Gleason score, tumour grade, disease relapse or patient's death, Forest plot analysis was performed after unblinding the patient samples (Figure 3.9).

Upon calculating the mean difference between each setting with the overall patient splice profile and PTK6 expression, the analysis revealed that the changes in ADAM15 splice variant expression and PTK6 within the different patient groups were very low, and further showed a very high variation, which can be explained due to the limited amount of patient samples (Figure 3.9A-D). Correlation of patient data with a high Gleason score of 9 (n=1) or 10 (n=2) could not be performed as this patient cohort was too small. ADAM15-D showed overall the highest variability (Figure 3.9), which might be linked to the distribution of patient expression levels around the overall mean. This might suggest, that there might be two cohorts having low and high values (Figure 3.7 B).

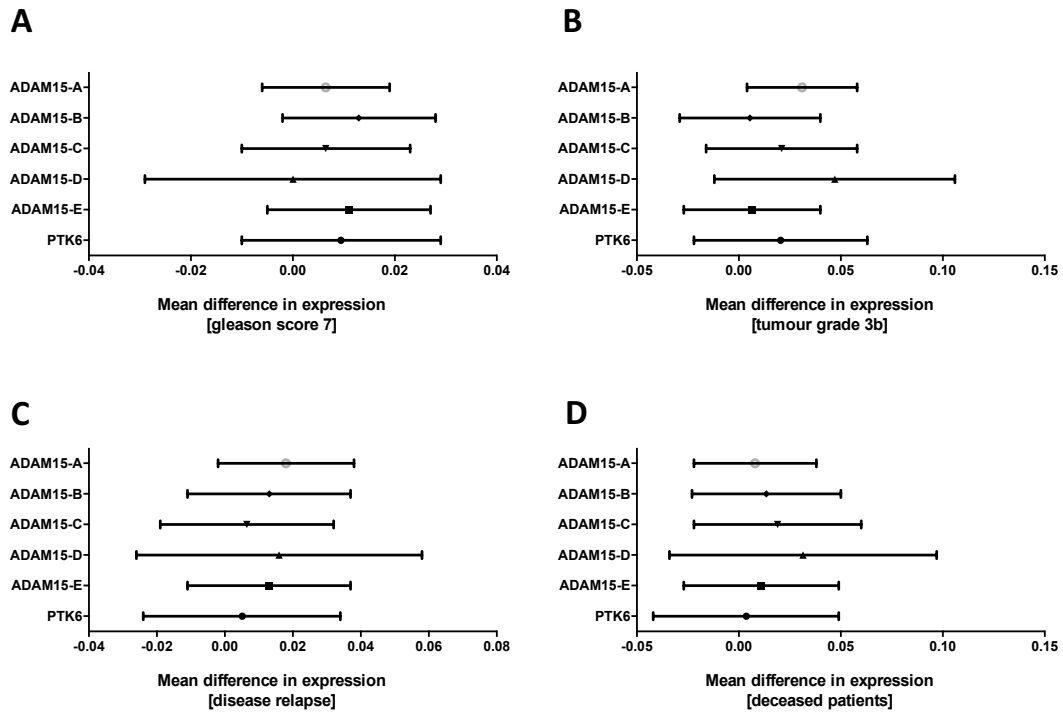

Figure 3.9 Forest plot analysis for the correlation of clinical patient data with the ADAM15 splice profile and PTK6.

Forest plot were used to assess a change in expression within the clinical patient data and expression of ADAM15 splice variants and PTK6. The mean difference is plotted for each of the ADAM15 splice variants and PTK6.

3.3 Discussion

In this chapter, we analysed and validated for the first time the ADAM15 splice profile in prostate cancer patients, and compared this to healthy tissue and available clinical data.

According to the MIQE guidelines (**M**inimum **I**nformation for Publication of **Q**uantitative Real-Time PCR **E**xperiments)[290], we established successfully a method to analyse the ADAM15 splice profile in PCa patients, using splice variant specific primers. We were able to generate a robust method, as standard curves showed a qPCR efficiency between 90-94 %, data were reproducible, and all splice variants were amplified to a similar extent when using the KAPA SYBR fast Master mix. Using cell lines, we validated our method, by analysing the ADAM15 splice profile and PTK6 expression.

In prostate cancer patients (n=83) we found significant overexpression of ADAM15 splice variants and PTK6 when compared to healthy tissue (n=8). Using a Forest plot,

we showed that ADAM15-A shows the highest change in expression when healthy tissue and PCa patient samples were correlated. In a recent study 12,427 PCa patient samples were analysed by immunohistochemistry for total ADAM15 expression using tissue microarray[132]. ADAM15 staining was found to be present in PCa tissue from patients, however not in normal prostate tissue[132]. Burdelski *et al.* grouped ADAM15 staining from these samples into negative (87.7 %), weak (3.3 %), moderate (5.6 %) and strong (3 %). Patients showing strong ADAM15 staining were linked to high Gleason score, high tumour grade, and positive nodal stage[132]. Our overall splice profile of the 83 patients revealed that the ADAM15 splice variants A and C were the most abundant in prostate cancer, in contrast to ADAM15-B which is high in breast cancer[81]. However, when correlating the splice variant expression and clinical data using Forest plots, our analysis failed to identify a change in expression for the splice variants, as the study cohort in our case was too small and lacked high tumour grade samples. In prostate cancer until today, no ADAM15 splice profile is available, as the study by Burdelski *et al.*, only assessed the presence of total ADAM15 and does not assess splice variants individually. Zhong *et al.* could identify, that in breast cancer patients suffering from disease relapse, ADAM15-C expression is most favourable, although patients were lymph node positive. In our study, unblinding of samples revealed, either a nodal score of NX (i.e. cannot be evaluated) or of N0 (i.e. cancer has not spread). Similar to this, only samples with a metastatic score of 0 were present in our study. At this stage, no correlation of nodal score and beneficial ADAM15 splice variant expression can be made.

Zhong *et al.* conducted Cox regression analysis, to assess the correlation between relapse free survival and splice variant expression. In a subpopulation, they were able to correlate relapse-free survival to high expression of splice variant C[81]. Our data however, lack extensive follow up of patients and also a defined time point for disease onset. At this point, with regard to available patient sample data, neither Cox regression nor Kaplan Maier analysis can be conducted. Using the Forest plot, we were able to identify that ADAM15-A shows the highest change in expression, however, additional PCa patient samples, which are categorized as benign hyperplasia as this would help to define a non-effect point and also those with higher Gleason score and tumour grades, are required to complete this study.

Although we see a trend in our data that a high tumour grade might be linked to high ADAM15 expression, which was also found by Burdelski *et al.* using 12,427 samples[132], we cannot draw any further conclusions, as clinical data are missing and

the study cohort is too small. However, the data indicate that ADAM15-A may involved in prostate cancer progression and thus lead us to analyse this splice variant in more detail, using an overexpression model in the PCa cell lines LNCaP and PC3 (Chapter 4,5 and 6).

In summary, within this chapter we showed the establishment of a robust qPCR method to assess the ADAM15 splice profile in prostate cancer patients. Further, we showed that ADAM15 splice variants were differently expressed in the prostate cancer cell lines PC3 and LNCaP. We further demonstrated, that ADAM15 splice variants A showed the highest change in expression when compared to the healthy tissue. Although our data indicate differences in splice profiles of androgen dependent and androgen independent cell lines we would further aim to elucidate the role of splice variant expression differences by including more prostate cancer cell lines in our analysis. To enhance the statistical power of our data we would need to include a larger patient cohort and further we would access the samples unblinded. Unblinded samples would help to ensure to include enough patients for each group such as benign, advanced and metastatic prostate cancer.

4 ADAM15 splice variant specific impact on prostate cancer cell characteristics

4.1 Introduction

Expression of ADAM15 correlates with disease aggressiveness, in as much as it controls cell adhesion, migration, proteolysis of growth factors, growth factor receptors, and modulate cytokine signalling.

ADAM15 has been suggested to enhance prostate cancer metastasis by modulating the tumour endothelial cell-cell interaction[105]. Using shRNA to downregulate ADAM15 in PC3 cells, Najy *et al.* showed that migration of shADAM15 PC3 cells was significantly reduced in a wound closure assay, when compared to vector control cells. Furthermore, cellular adhesion to fibronectin, laminin and vitronectin, was significantly reduced. Najy *et al.* showed that ADAM15 was additionally involved in proteolysis of N-cadherin. A different study by Dong *et al.* in NSCLC cells, confirmed the ADAM15 dependent reduction of cell invasion, when MMP9 was downregulated[157]. ADAM15 expression levels were associated with decreased survival and ADAM15 mechanistically upregulated MMP9 expression and also activated pro-MMP9 promoting invasion. The findings correlate with Martin *et al.*, confirming that the proteolytic activity of ADAM15 is necessary to promote migration. Upon metalloproteinase inhibitor treatment, migration of mesangial cells was significantly reduced[153].

Splice variant specific differences in cell characteristics were found upon overexpression of splice variant A and B in the breast cancer cell line MDA-MB435. ADAM15-A expressing cells showed increased adhesion and migration compared to vector control and ADAM15-B cells. Furthermore, the ADAM15 levels affected the actin cytoskeleton organisation. ADAM15-B expressing cells had shorter actin fibres and a strong cortical actin staining, whereas ADAM15-A expressing cells showed actin resembling similar to the vector control[81].

ADAM15 was shown to interact with various intracellular kinases involved in cancer progression, including the tyrosine kinase PTK6, which interacts with ADAM15 A and B but not with C[81]. These data indicated that ADAM15 may play a role in regulating PTK6 localization. Knock out of PTK6 in PC3 cells significantly reduced invasion, proliferation and colony formation, and increased survival and reduced metastatic disease spread in a mouse model[263].

During prostate cancer progression, tumour cells gain metastatic potential and shift from androgen dependent to androgen independent status[32]. PTK6, unlike other Src-family kinases, lacks a myristoylation sequence. Derry *et al.* showed, that the altered localization of PTK6 in PCa patient biopsies is dependent on tumour grade. In androgen dependent LNCaP PCa cell line, PTK6 was predominantly nuclear, whereas in the androgen independent PC3 PCa cell line, expression was cytoplasmic, which might be an indicator of prostate cancer progression[273].

4.1.1 Aims of the chapter

In this chapter, the impact of the ADAM15 splice variant overexpression on cell characteristics of LNCaP and PC3 PCa cells will be investigated. Additionally, the impact of ADAM15 splice variants on PTK6 localization and expression in both cell panels, will be evaluated.

PC3 and LNCaP were stably transfected with the ADAM15 splice variants A-E and analysed for changes in cell morphology, cell size, cell cycle, and actin cytoskeleton. The ADAM15 splice variant specific impact on cell migration and invasion was assessed. The ADAM15 splice variants on PTK6 localization were assessed using immunofluorescence staining.

4.2 Results

4.2.1 Overexpression of ADAM15 splice variants in PC3 and LNCaP

As shown in Chapter 1 (Figure 3.5), PC3 and LNCaP PCa cell lines express certain ADAM15 splice variants. PC3 cells express predominantly ADAM15-A, whereas ADAM15-A and D are expressed in LNCaPs. To study the splice variant specific effect of ADAM15 overexpression in prostate cancer, two cell panels, stably overexpressing the splice variants individually, were generated in the PC3 and LNCaP cell line by Lentiviral transfection with plasmids containing the coding sequence of human ADAM15-A, B, C, D, and E, and an additional C-terminal V5-tag (Figure 4.1 A). Cell lines expressing the empty pcDH vector, were used as a vector transfection control cell line. ADAM15 splice variant expression was confirmed using western blotting by staining with an anti-V5 antibody, for both cell panels (Figure 4.1 B). Stable overexpression was confirmed in both cell panels using qPCR with the splice variant specific primers (Figure 4.1 C).

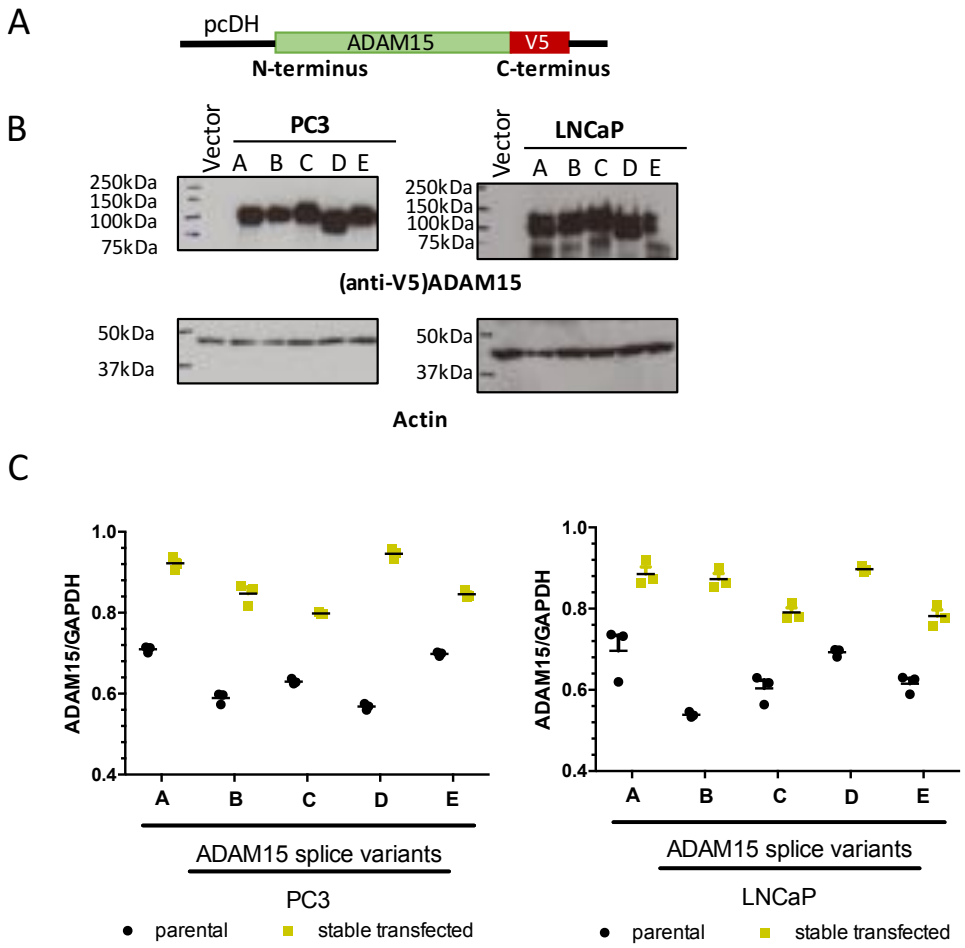

Figure 4.1 PC3 and LNCaP cell lines, stably overexpressing ADAM15 splice variants A-E

(A) Lentiviral transfection was applied to generate PC3 and LNCaP stable cell lines expressing the ADAM15 splice variants A-E using the human expression vector pcDH or the empty pcDH-Vector as a transfection control. (B) Western blot analysis of the cell lysates from ADAM15 splice variants A-E expressing cells as indicated. (C) Quantitative overexpression after stable transfection was assessed using qPCR with the splice variant specific primers.

4.2.2 Analysis of cell morphology, cell-size and cell cycle in ADAM15 A-E overexpressing PCa cell lines

To evaluate whether ADAM15 A-E variants affect cell morphology, phase contrast images were acquired from PC3 and LNCaP stably overexpressing ADAM15 A-E at 72h post trypsinization and cultivation in 35mm dishes. The heterogeneous morphology of the PC3 cell panel was maintained when compared to the vector control (Figure 4.2). LNCaP cell morphology also remained unaffected (Figure 4.3).

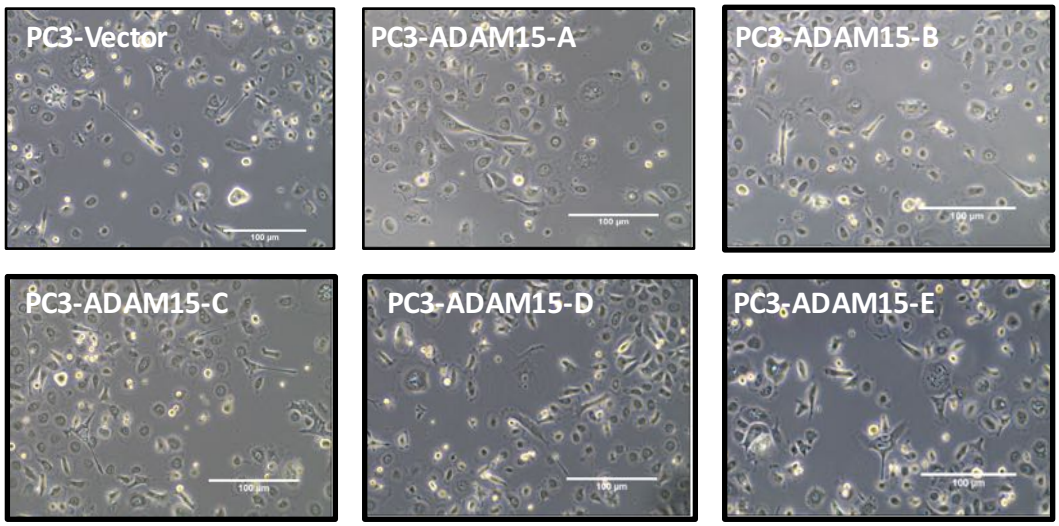

Figure 4.2 Analysis of cell morphology changes in PC3 cells overexpressing ADAM15 A-E.

Phase contrast images of the PC3 cell panel were taken randomly 72h post trypsinization.

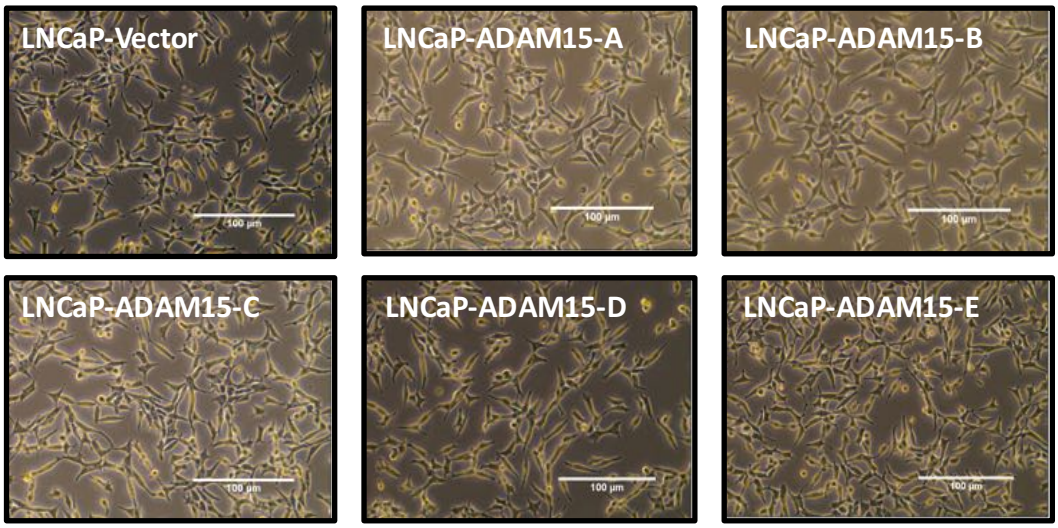

Figure 4.3 Analysis of cell morphology changes in LNCaP cells overexpressing ADAM15 A-E.

Phase contrast images of the LNCaP cell panel were taken randomly 72h post trypsinization.

Cell-size was determined by flow cytometry, by determining the cell volume shown as median forward scatter, which remained identical for both cell panels (Figure 4.5 A and B).

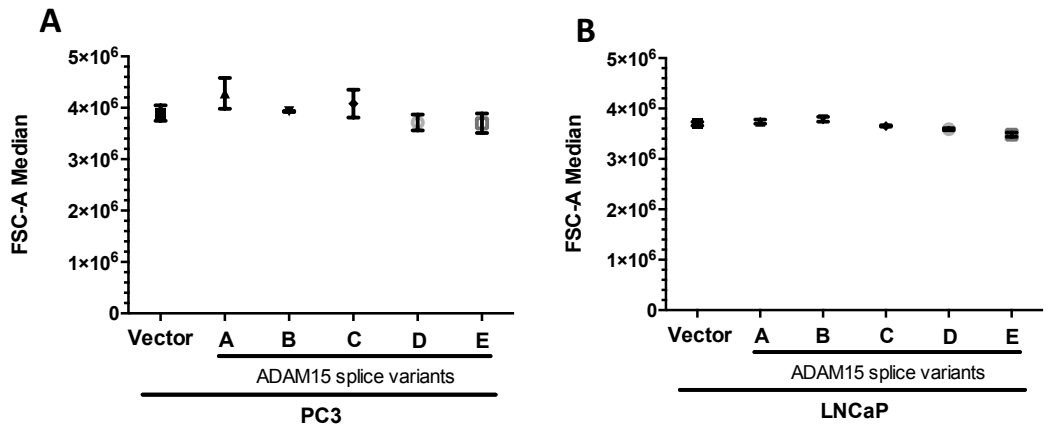

Figure 4.4 Cell size analysis for the PC3 and LNCaP cell panel

(A-B) The cell size after stably overexpressing the ADAM15 splice variants was assessed using flow cytometry. The cell volume was determined using a single parameter histogram and the median forward scatter (FSC-A). The FSC is proportional to the cell surface area and is plotted as dimensionless unit, the median of FSC-A (FSC-A Median) versus the splice variants.

Cell cycle analysis for both cell panels was performed, by analysing changes in G1/G0, S-phase and G2/M phase. ADAM15 splice variant expressing PC3 and LNCaP cells were distributed equally among the phases, when compared to vector control (Figure 4.5 A,B). Additionally, a calorimetric metabolic cell proliferation (MTS) assay was performed using the PC3 cell panel. No changes in cell proliferation within the cell panel were observed (Figure 4.5 C).

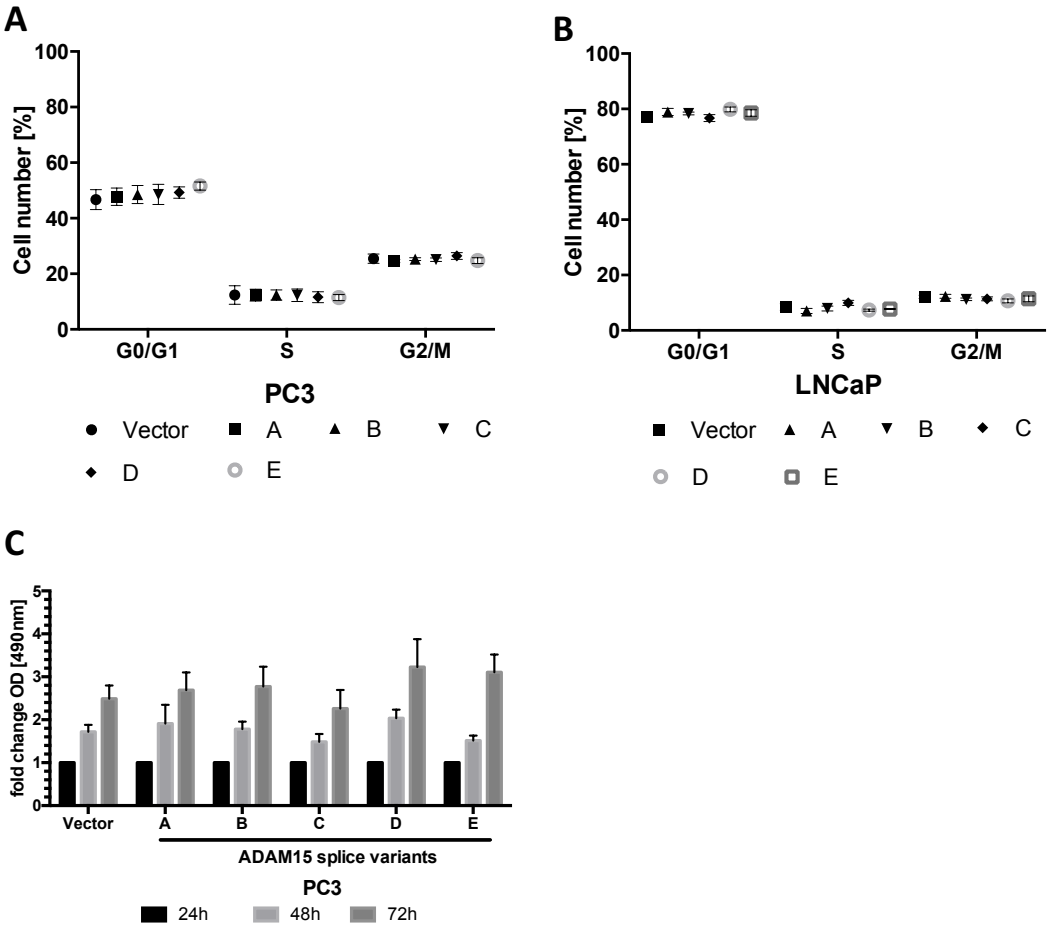

Figure 4.5 Cell cycle analysis and proliferation analysis for the overexpressing ADAM15 A-E cell panels

(A,B) DAPI stained cells were analysed using the NuceloCounter®NC-3000 by quantifying the DNA content, results are displayed as percentile amount of cells in the different cell cycle stages, and shown to be identical to vector controls in both cell panels. All experiments were performed three times for each cell line. (C) MTS cell proliferation assay in the PC3 cell panel. The fold change in OD (490nm) normalized against the 24h time point is shown for each splice variant and the vector control over a time frame of 72h. Statistical analysis was performed by One-Way-Anova, using Graph Pad Prism. n=3. Error bars are shown as Mean ± SEM.

4.2.3 Actin organisation in ADAM15 A-E expressing cells.

In order to substantiate the phase contrast image analysis shown in Figure 4.2 and Figure 4.3., the ADAM15 expression in the cell lines was analysed using the V5-epitope antibody. The actin cytoskeleton was visualized using phalloidin prior to confocal analysis. ADAM15 A-E expression in PC3 and LNCaP is shown in red in Figure 4.6 A and B. In LNCaP (Figure 4.6 A) and PC3 (Figure 4.6 B), ADAM15 staining was localized around the nucleus, in vesicle like intracellular structures, and at the plasma membrane, suggesting the ADAM15 A-E are expressed by all cell lines

analysed, and they all traffic to the cell surface. In the PC3 ADAM15 A-E cell panel, ADAM15 was localized to membrane protrusions, as the representative example for ADAM15-D shows (Figure 4.6 C). An example is shown for PC3 ADAM15-B, localized to focal adhesion like assemblies. However, as this investigation was not pursued further, no conclusion about splice variant specific differences can be drawn. In the LNCaP ADAM15 A-E cell panel, ADAM15 was found in cell-cell junctions and vesicle like structures (Figure 4.6 D). The distribution of ADAM15 across the cell panels was identical among all splice variants. Actin cytoskeleton staining using phalloidin, shown in green, revealed no differences when compared to the vector control, for both cell panels as judged by cortical actin staining, cell appearance, and cell spreading (Figure 4.6 A,B). For LNCaP, cortical actin staining was hardly detectable, compared to cortical actin staining present in PC3 (Figure 4.6 B). Cells were equally spread and did not reveal any changes in cell appearance for both cell panels. The PC3 cell panel showed a diverse morphology of cells, however, similar for all of the splice variants and vector control (Figure 4.6 B).

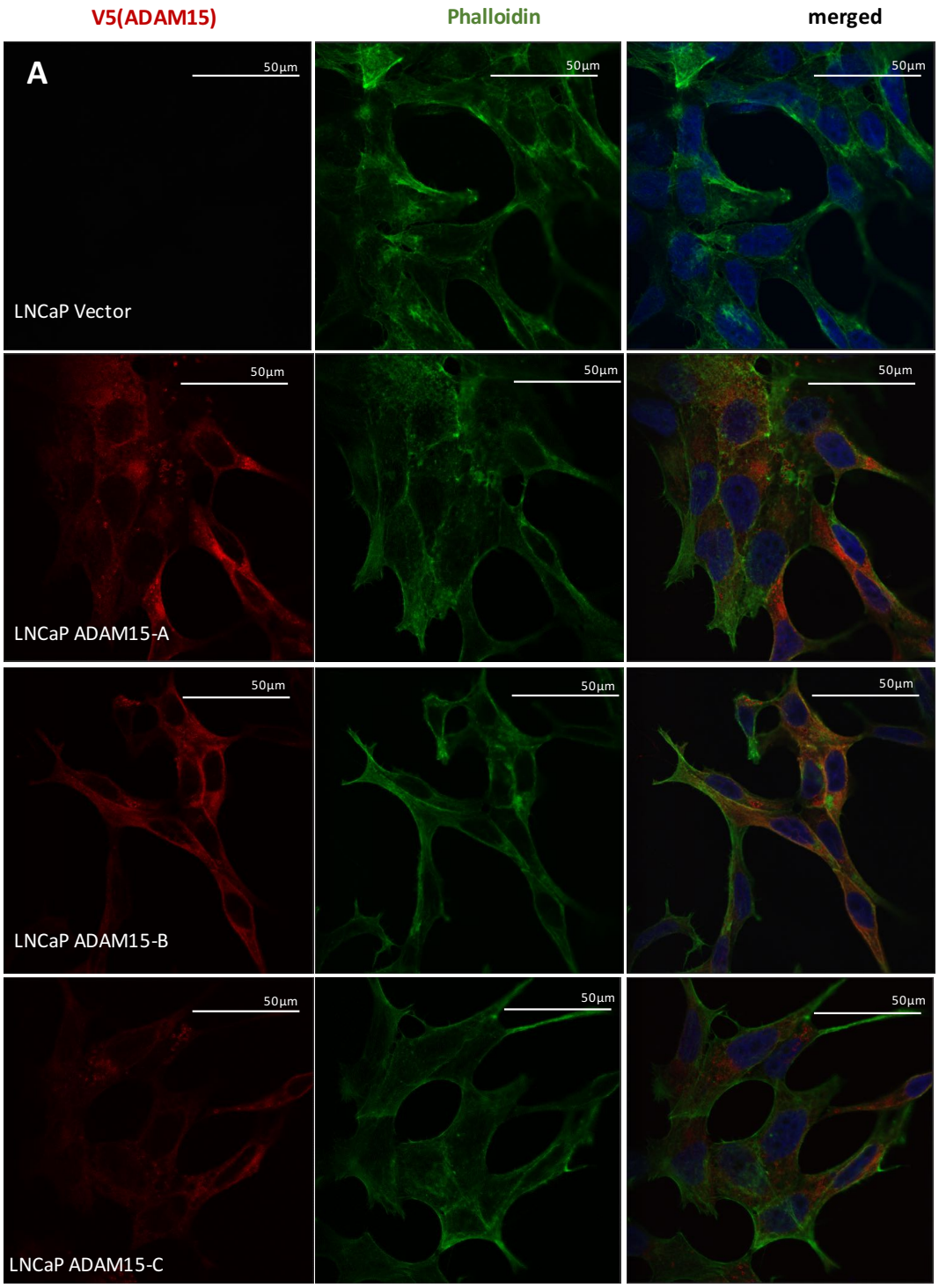
V5(ADAM15)
Phalloidin
merged
A
50µm
LNCaP Vector
LNCaP ADAM15-A
LNCaP ADAM15-B
LNCaP ADAM15-C

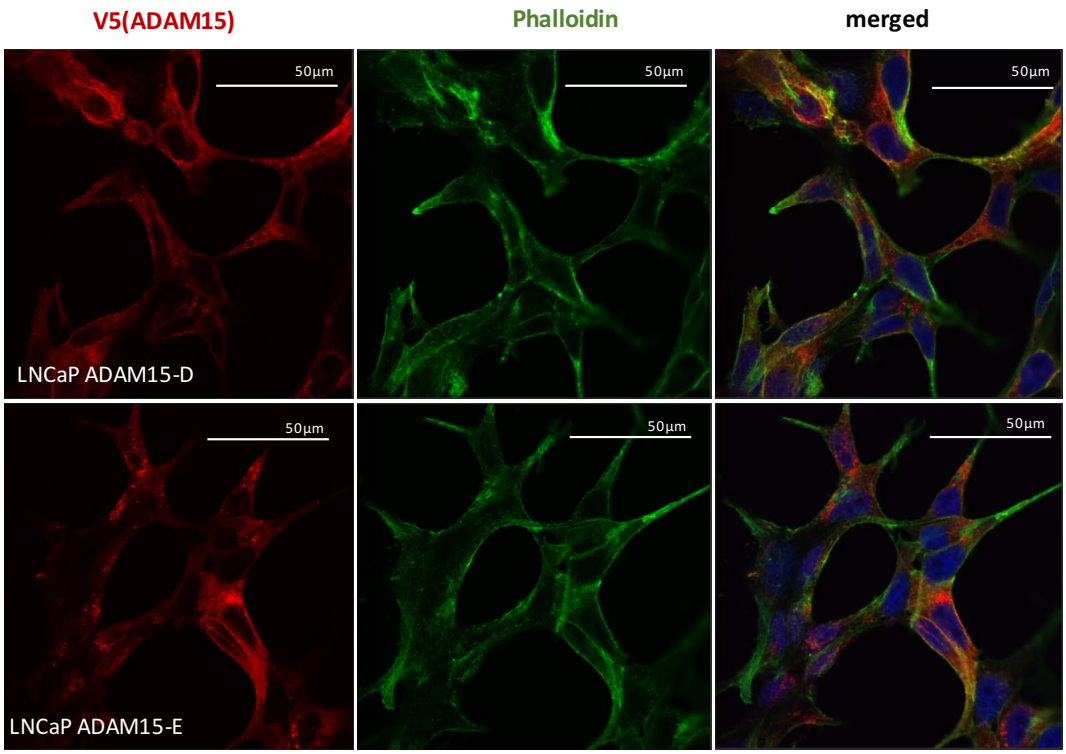
V5(ADAM15)
Phalloidin
merged
50µm
LNCaP ADAM15-D
LNCaP ADAM15-E

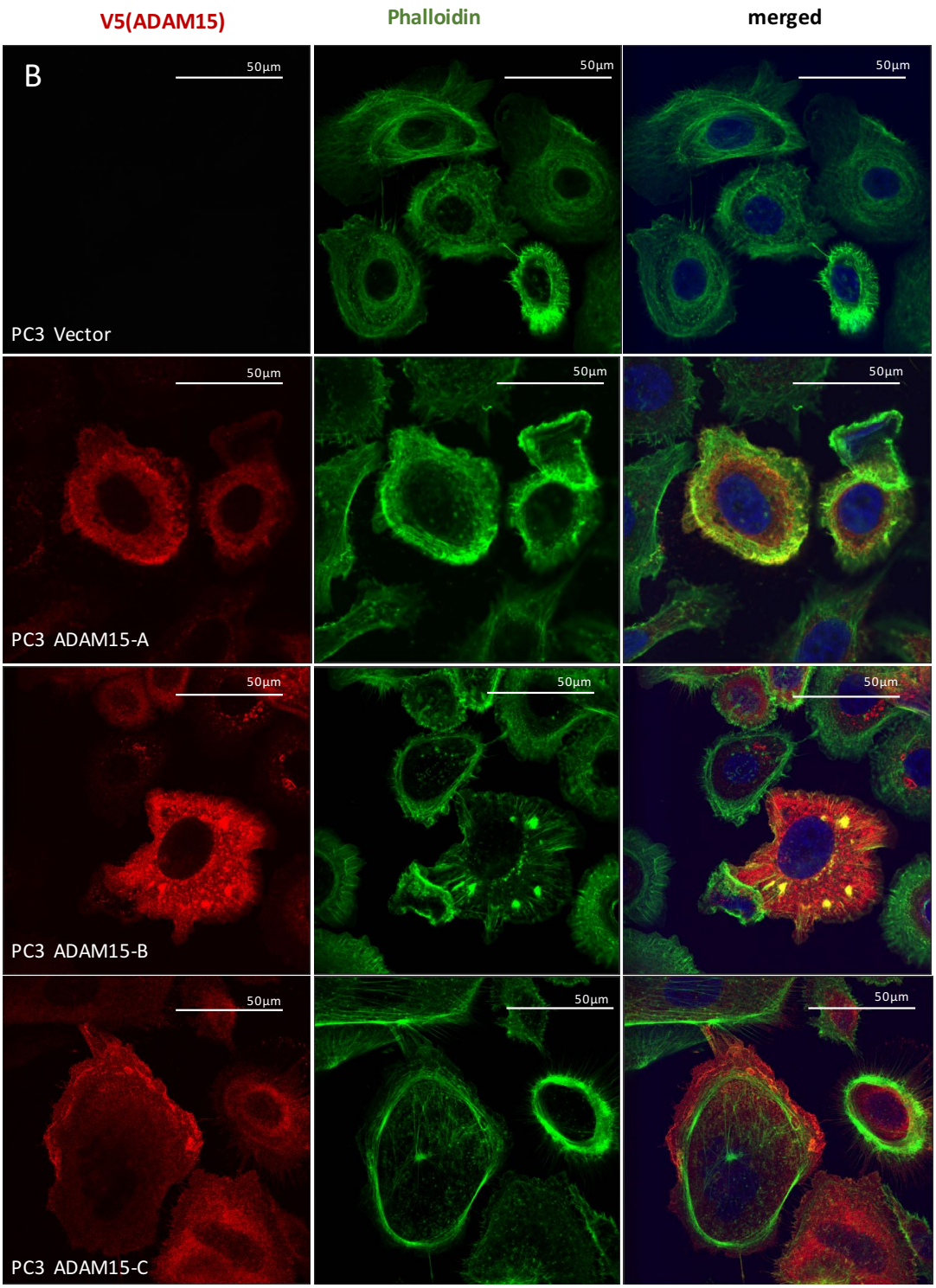
V5(ADAM15)
Phalloidin
merged
B
50μm
PC3 Vector
PC3 ADAM15-A
PC3 ADAM15-B
PC3 ADAM15-C

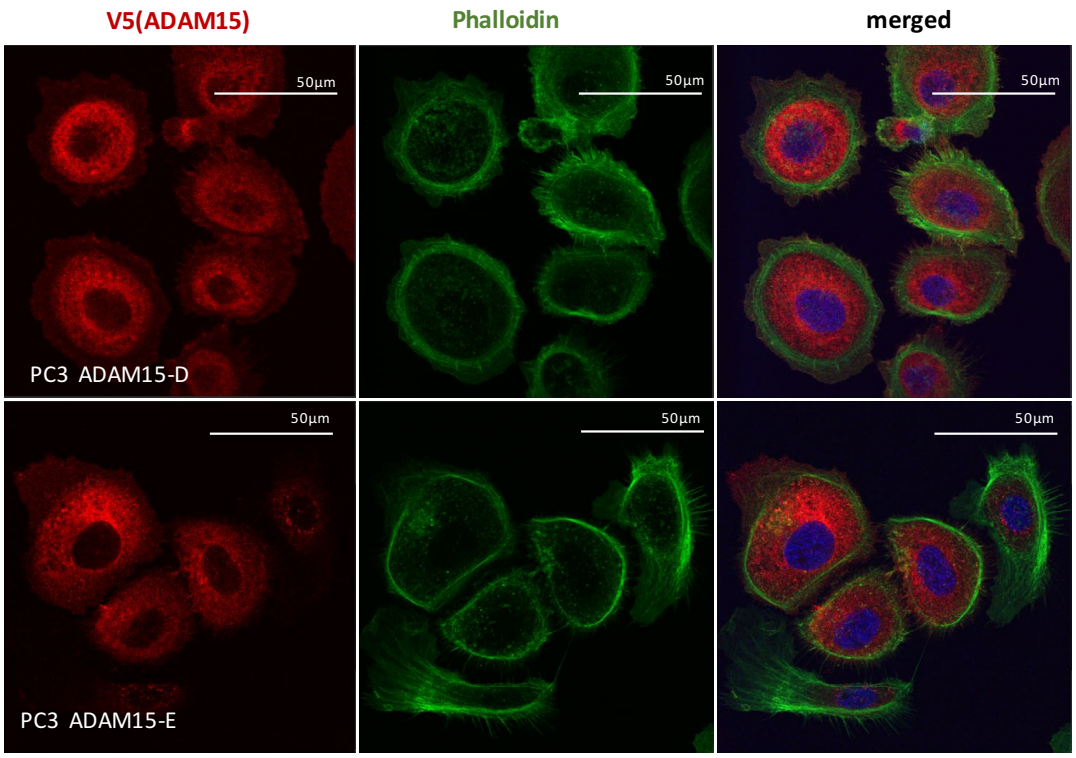
V5(ADAM15)
Phalloidin
merged
50µm
PC3 ADAM15-D
PC3 ADAM15-E

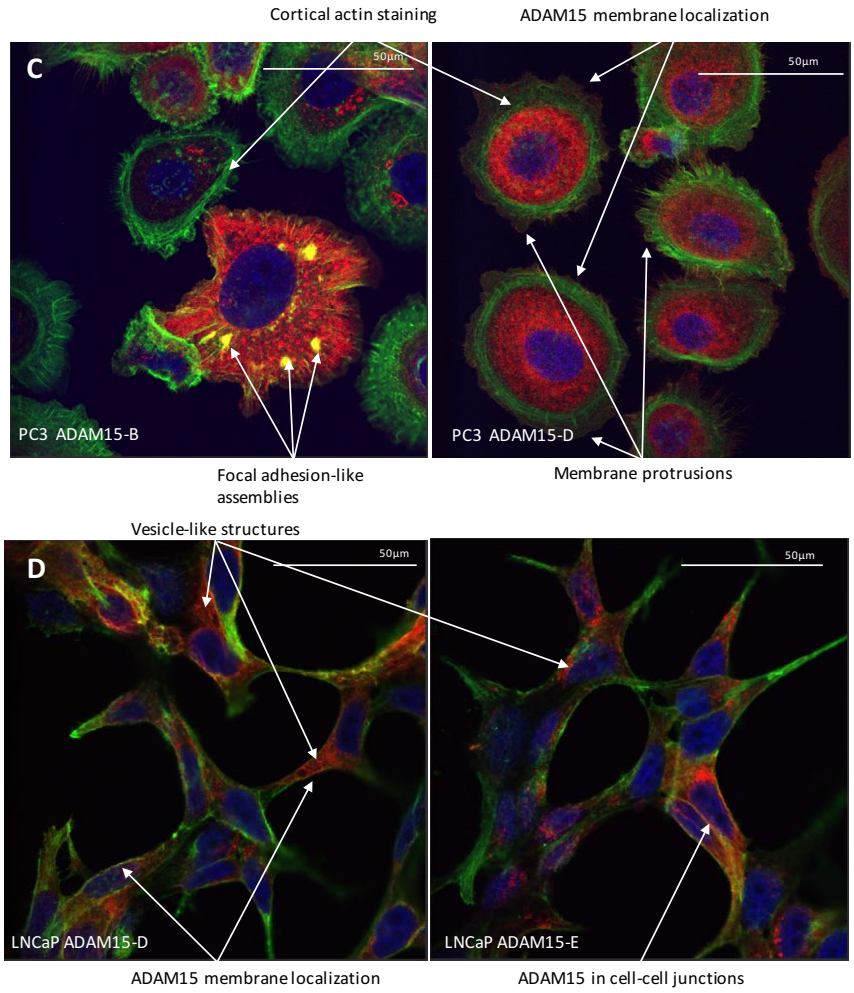

Figure 4.6 ADAM15 localization and actin cytoskeleton organization in PC3 and LNCaP ADAM15 cell panel.

Cells were fixed, permeabilized and stained using the primary mouse anti-V5, secondary mouse anti-AlexaFlour568, and phalloidin-AlexaFlour488. DAPI was used as nuclear counter stain. (A) in LNCaP ADAM15-V5 (red pseudo colour), was detectable in the plasma membrane and within cell-cell junctions. (B) In PC3, ADAM15 was detectable inside the cytoplasm and at the plasma membrane (C). Cytoskeleton architecture was visualized (green pseudo colour) in the PC3 and LNCaP cell panel. In PC3, cortical actin staining was predominantly detectable. ADAM15 was detectable in membrane protrusions and also localised with actin to focal adhesion like structures, as shown as an example for splice variant B in PC3. (D) In LNCaP, ADAM15 was localized to the membrane and was detectable in cell-cell junctions and in vesicle-like structures.

4.2.4 PTK6 localisation is not altered by ADAM15 splice variants overexpression

In order to test the hypothesis that PTK6 localization is altered in LNCaP and PC3, as stated by Derry et al., and ADAM15 might contribute to this re-localization, both cell panels were assessed for PTK6 localization using confocal microscopy. A stable PTK6 knock down cell line in PC3 cells was used as negative control. A significant

PTK6 knock down was confirmed by western blotting and densitometry (Figure 4.7). Confocal microscopy of the PC3 shPTK6 cell line showed reduced staining for PTK6 (green) in the cytoplasm and the absence of detectable membrane staining, when compared to the PC3 shRNA non-target control cell line (Figure 4.7).

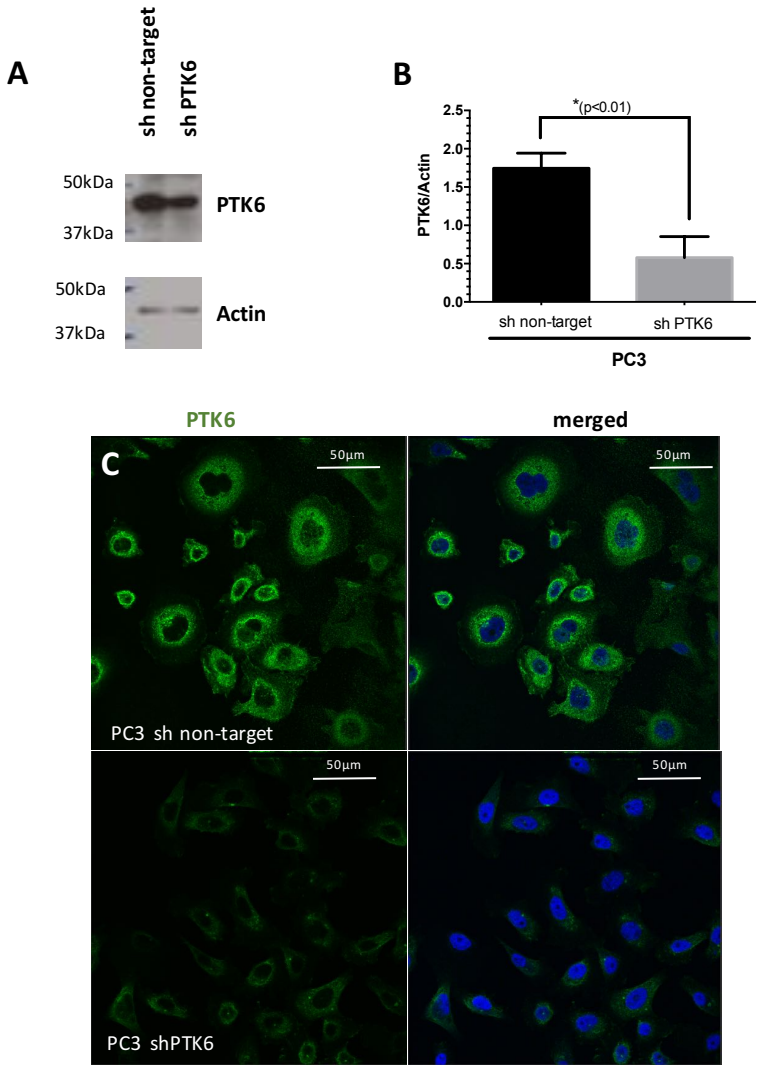

Figure 4.7 PTK6 knockdown

(A,B) Western blot results and densitometry, confirmed PTK6 knock-down in PC3, *p<0.05. The experiments were performed with n=4. (C). The PC3 non-target and shPTK6 cells were stained using the primary anti-PTK6-mouse, secondary anti-mouse-AlexaFlour488 (green pseudo colour). The mounting media contained DAPI (blue pseudo colour), which was used as nuclear counter stain.

In the PC3 cell panel, PTK6 localization was found to be cytoplasmic and at the plasma membrane (Figure 4.8 A). In LNCaP cells, localization of PTK6 was found predominantly, in the cytoplasm and within cell-cell junctions, but nuclear localization could not be detected (Figure 4.8 B). For both cell panels, no splice variant related difference in PTK6 localization was found.

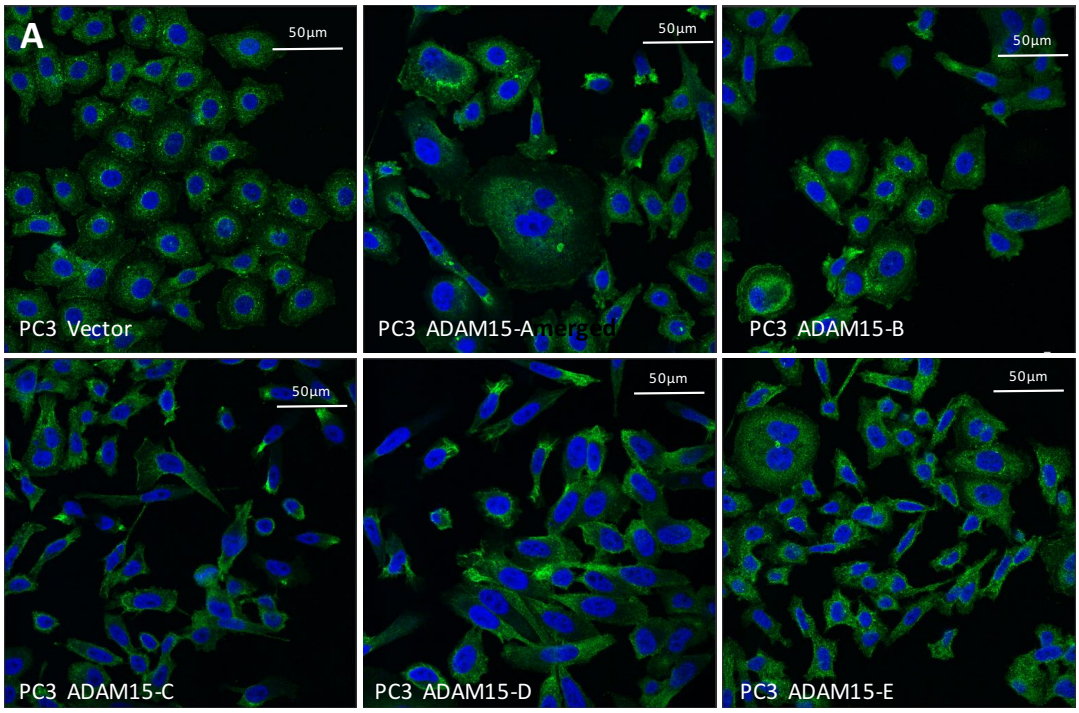

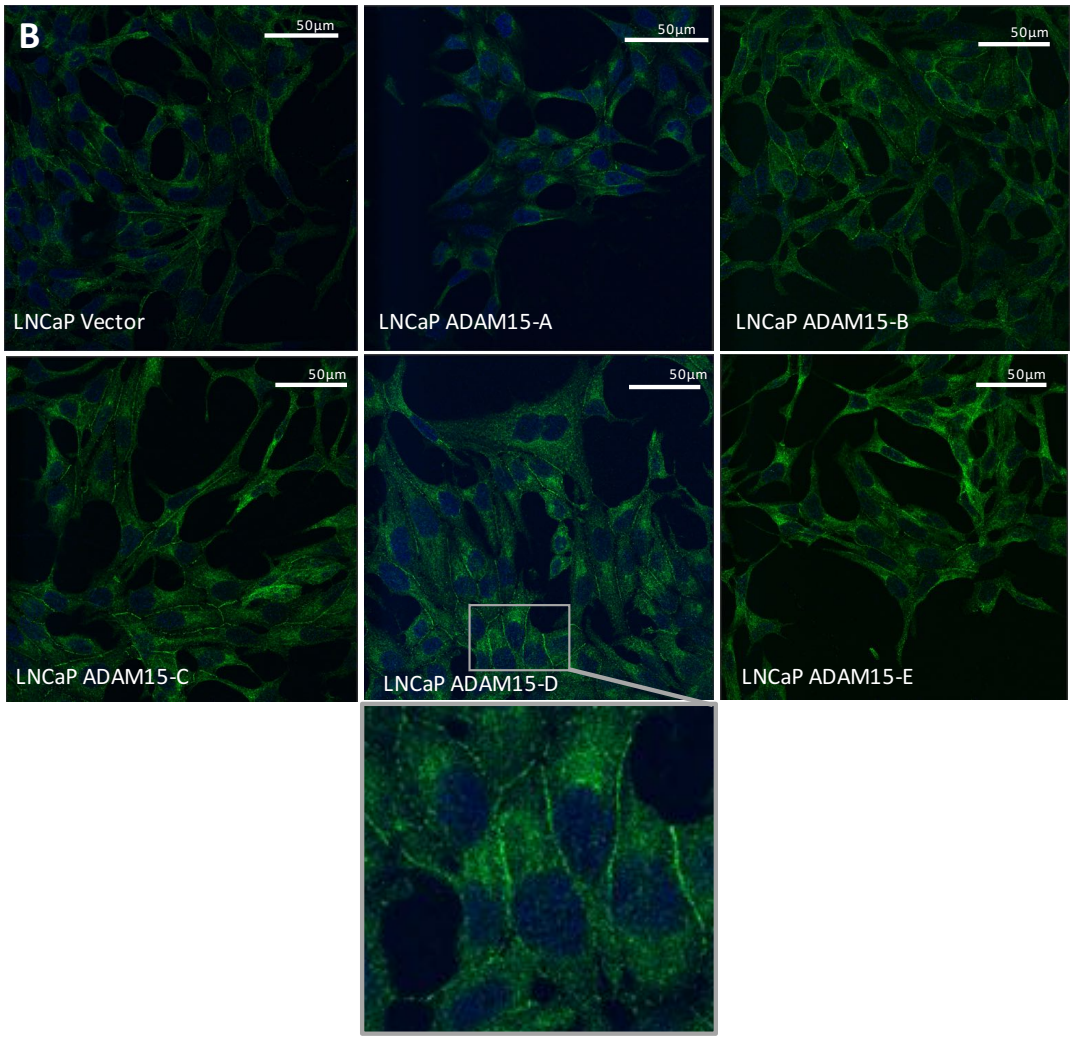

Figure 4.8 PTK6 localization in PC3 and LNCaP cell panels.

The PC3 and LNCaP ADAM15 cell panels were stained using the primary anti-PTK6-rabbit, secondary anti -AlexaFlour488-mouse (green pseudo colour). The mounting media contained DAPI (blue pseudo colour), which was used as nuclear counter stain. Representative pictures for the PC3 and LNCaP cell panel are shown. (A) In PC3-Vector and PC3-ADAM15-A cells, PTK6 (green) was detectable within the cytoplasm and the plasma membrane. (B) For LNCaP-Vector and ADAM15-A expressing cells, PTK6 (green pseudo colour) was detectable in the cytoplasm and in membrane junctions. LNCaP ADAM15-D expressing cells show a representative example for the presence of PTK6 in membrane junctions in the LNCaP ADAM15 cell panel.

4.2.5 The expression of ADAM15 does not change the rate of cell migration

The effect of ADAM15 A-E splice variant overexpression in regulation of LNCaP or PC3 migration was assessed using a transwell migration assay, and 10% serum as chemoattractant in the bottom chamber.

When compared to the vector control cells, both cell panels, showed identical numbers of migrating cells, over a timeframe of 8 and 24h (Figure 4.9 A, B). LNCaP cells did not show any splice variant specific differences in migrating cells, when compared to the vector control (Figure 4.9 A). After 48h, the LNCaP cell panel showed, approximately 1.5 fold reduction of migrating cells, when compared to the PC3 cell panel. PC3 cells overexpressing ADAM15-B migrated towards the chemotactic gradient more efficiently than A, C, D or E (Figure 4.9 B). To exclude that the enhanced migration seen for ADAM15-B is proliferation dependent, data obtained from the calorimetric metabolic cell proliferation (MTS) assay were checked, showing no enhanced proliferation of ADAM15-B in PC3 (Figure 4.5 C). Additionally, cell proliferation of the ADAM15 splice variant panel was identical to the proliferation rate seen for the vector control cell line.

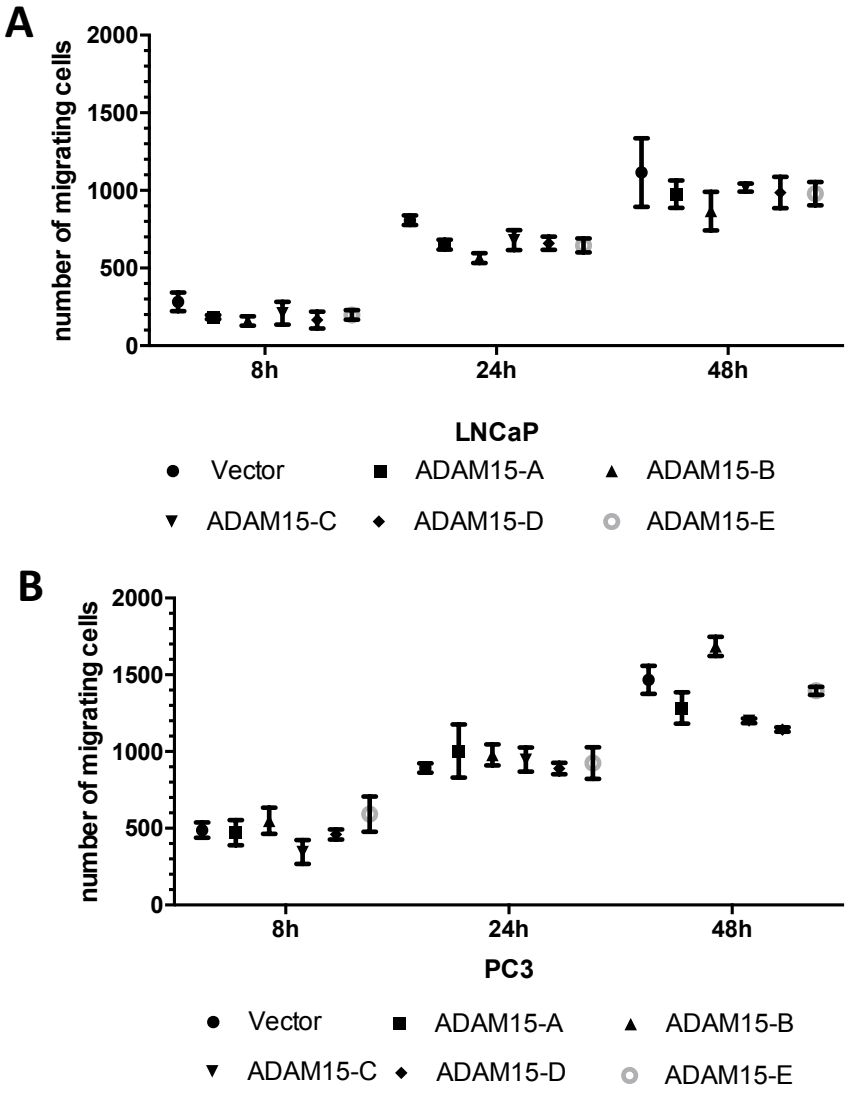

Figure 4.9 ADAM15 splice variants do not alter PC3 or LNCaP cell migration

(A-B) 20,000 cells were seeded in transwell inserts and incubated with FBS containing medium in the bottom chamber, for 8, 24 and 48h. They were fixed, stained and analysed using ImageJ. The number of migrating cells is plotted versus the indicated time points.

4.2.6 ADAM15-A expression enhances the invasion of PC3 cells via its proteolytic activity

In order to determine whether ADAM15 A-E overexpression influenced the invasion of LNCaP and PC3 cells, matrigel invasion assays were performed and invaded cell numbers determined at the 24h time point using serum free conditions or in response to 10% serum in the bottom chamber.

As shown in Figure 4.10 A, LNCaPs overexpressing ADAM15 A-E showed identical invasive behaviour compared to vector control cells, indication that ADAM15 variants do not affect LNCaP invasion. When overexpressing the splice variants in PC3 cells, ADAM15-A expression led to a 2-fold increase in the number of invading cells, when compared to vector control cells in either condition tested (Figure 4.10 B). In contrast, ADAM15 B-E cellular invasion levels were identical to vector control cells (Figure 4.10 B). To test whether the enhanced invasion of ADAM15-A cells, is mediated by its proteolytic domain, a proteolytically inactive ADAM15-A mutant was generated and a corresponding PC3 cell line established. The ADAM15 mutant carries an amino acid change in the active site, from E to A at position 349 of the metalloproteinase domain. ADAM15-A-E349A mutant expressing cells showed similar levels of invasion, when compared to the vector control cells (Figure 4.10 C).

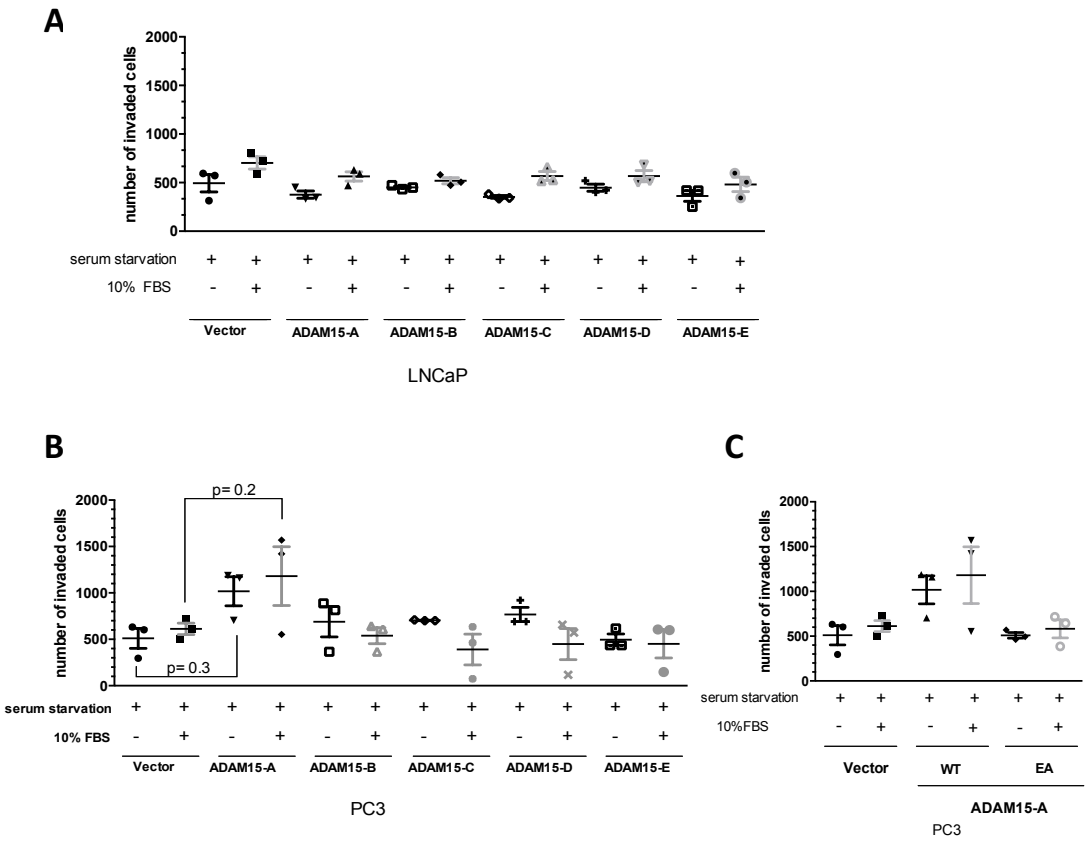

Figure 4.10 The enhanced invasion of ADAM15-A in PC3 is dependent on ADAM15 proteolytic activity.

The PC3 and LNCaP expressing ADAM15 cell panels were seeded into matrigel coated invasion chambers and treated for 24h with or without 10% FBS in the bottom chamber. (A) LNCaP invasion is independent of ADAM15 A-E expression. (B) In PC3, an increase in cell invasion was found in ADAM15-A overexpressing cells. (C) Upon an amino acid change from glutamic acid (E) to alanine (A) at position 349 in the ADAM15 proteolytic domain, the ADAM15-A cell invasion was reduced, below Vector invasion. The number of invaded cells was analysed using ImageJ, and plotted against the treatment. Statistical analysis was performed by One-WAY-Anova, using Graph Pad Prism. The experiment was performed with n=3. Error bars are shown as Mean ± SEM.

4.3 Discussion

The aim of this chapter was to assess the effect of ADAM15 splice variants on PCa cell characteristics in response to stable overexpression.

ADAM15 expression for the PC3 cell panel was found at the plasma membrane in membrane protrusions, however predominantly in the cytoplasmic region, within ER-like structures, which suggested the trafficking of ADAM15 A-E splice variants to the plasma membrane. Although ADAM15 is a transmembrane protein confocal images show predominantly cytoplasmic localization of ADAM15, which might be caused due to saturation due to the overexpression or a high protein turn-over rate. For ADAM15 detection, a V5-antibody was used, as ADAM15 contained a C-terminal V5-tag. In LNCaP ADAM15 A-E expressing cells, vesicle-like structures were more prominent compared to PC3 cells. However, ADAM15 was also localized at the plasma membrane and cell-cell junctions.

The overexpression of ADAM15 A-E splice variant did not result in obvious changes in cell morphology, cell size or cell cycle, when compared to the vector control in either PCa cell panel. In PC3 and LNCaP cells, ADAM15 A-E overexpression did not alter actin cytoskeleton arrangement. Cells were equally spread and showed similar actin staining, however weaker detectable in LNCaP. This is in contrast with the data in MDA-MB-435 breast cancer cells, where ADAM15-B expressing cells appeared smaller compared to ADAM15-A and vector expressing cells[81]. Changes in actin cytoskeleton were assessed, as in MDA-MB-435 breast cancer cells, Zhong *et al*. found differences in cytoskeleton arrangement, when overexpressing ADAM15-B. Vector control cells were well spread, with distinct actin stress fibers. ADAM15-B expressing cells were less spread, and showed shorter actin fibers. ADAM15-A expressing cells, however, showed similar spreading, and distinct actin stress fibers spreading, like the vector control[81].

PTK6 is expressed in normal prostate epithelia regulating growth and differentiation. In LNCaP and PC3 parental cells, differences in PTK6 expression levels were found (Chapter 3). PTK6 was expressed higher in PC3s when compared to LNCaPs. Upon analysing the ADAM15 A-E splice variant cell panel, PTK6 expression was equal throughout (Supplementary data Figure 8.7). Change in androgen response, as well as PTK6 upregulation, correlates with disease progression[9,291]. Zheng *et al.* showed in patient data from the NCBI human genome microarray that PTK6 mRNA expression levels during prostate cancer progression were significantly increased

compared to normal tissue[292]. Derry *et al.* reported the altered localization of PTK6 in the prostate cancer cell lines PC3 and LNCaP. In the androgen dependent LNCaPs, PTK6 was found in the nucleus, whereas in the androgen independent cell line PC3, PTK6 was found in the cytoplasm[273]. In the present study, when analysing the cell panels for PTK6 localisation after overexpression of the ADAM15 splice variants no changes were found. Further, when comparing nuclear or cytoplasmic localization of PTK6 in both cell panels, only cytoplasmic and membrane localization of PTK6 was detectable, in contrast to Derry's findings. However, our findings are in agreement with the results by Zheng *et al.* as they showed predominantly cytoplasmic localization of PTK6 in LNCaP and PC3 cells[263]. The generated stable PC3 shPTK6 cell panel, showed weak PTK6 staining within the cytoplasm. The expression of ADAM15 splice variants did not alter PTK6 localization in either cell panel.

Cell migration is one essential characteristic for cancer cell tumourigenicity and was assessed for both PCa cell panels. Knock down of ADAM15, via lentiviral shRNA in PC3, showed reduced migration compared to the control, in a wound healing assay[105]. qPCR analysis of the parental PC3 and LNCaP cDNA, revealed, that ADAM15 splice variants are differently expressed in these two cell lines. For instance, PC3s show predominantly endogenous expression of ADAM15-A, whereas LNCaPs show, expression of splice variant D and A (Chapter 3). For LNCaPs, stably overexpressing the ADAM15 A-E splice variants, no splice variant specific difference was found in a transwell assay over 48h, with 10% serum as chemoattractant. In the PC3 cell panel, ADAM15-B overexpressing cells showed a higher number of migrating cells after 48h, however it did not reach statistical significance when compared to the vector. Zhong *et al.* showed that overexpression of ADAM15-A but not B in MDA-MB-435 breast cancer cells led to enhanced migration[81]. To exclude a proliferation dependent effect for the ADAM15-B enhanced migration, a proliferation assay was performed, showing no changes in proliferation throughout the panel. Additionally for PC3 ADAM15-A, B, D and vector cells, a scratch wound assay was performed however, cells overgrew and wound closure after 48h was only 50%, and therefore PC3 ADAM15 splice variant specific migration was not further assessed using this methodology (Supplementary Data Figure 8.4). As our data indicate that ADAM15-B expressing cells might show an enhanced migration trend, however not significant to vector control cells , a new assay set up with different pore sizes of the transwell inserts might be reasonable to assess migration.

ADAM15 has been shown to increase cell invasion of the human bladder cancer cell lines UM-UC-9 and UM-UC-6. Knock down of ADAM15 in those cell lines significantly reduced cell invasion[162]. In lung cancer, Dong *et al.,* confirmed the ADAM15 dependent invasion[157]. In MDA-MB-435 breast cancer cells splice variant A was found to significantly enhance invasion, compared to splice variant B and the vector control[81]. For LNCaP prostate cancer cell, Najy *et al.* found only weak invasion ability, when compared to PC3 cell lines[105]. In this study, with both PCa cell panels, Matrigel invasion assays were performed, and 10% serum was used as chemoattractant. The LNCaP ADAM15 A-E cell panel showed no change in invasion, when splice variants were compared, with each other or the vector controls, which confirms the findings by Najy *et al.*[105]. Within the PC3 ADAM15 cell panel, only the overexpression of ADAM15-A led to a 2-fold increase in the number of invading cells compared to vector control. As ADAM15s metalloproteinase domain is known to result in degradation of the ECM, the proteolytically inactive ADAM15EA mutant was generated, having an amino acid change from E to A at position 349, in the active metalloproteinase site. Maretzky *et al.* showed., that ADAM15 E to A mutants, showed a reduction in proteolytic activity, as shedding of the FGFR2iiib was decreased compared to ADAM15 wild type[156]. When comparing ADAM15-A wild type (WT) and E349 A (EA) mutant using the matrigel invasion assay, the enhanced number of invaded cells seen for ADAM15-A WT was reduced to vector invasion levels in the inactive ADAM15-A-EA mutant.

In summary, the data of this chapter showed that ADAM15 splice variant overexpression did not lead to a change in cell size, cell cycle, actin cytoskeleton rearrangement or migration in either of the two cell lines. Moreover, PTK6 expression in both cell panels was not altered after overexpression of the splice variants. In PC3 cells overexpression of splice variant A lead to a trend of increased cell invasion which we could further link to the catalytic function of ADAM15. LNCaP cells overexpression the ADAM15 splice variants did not lead to enhanced invasion. As we could confirm ADAM15 splice variant expression in both cell lines we would further need an ADAM15 knock-out cell lines as additional control to the vector cells. To tackle this approach we would used the genome editing technology of Clustered Regularly Interspaced Short Palindromic Repeats (CRISP) cas-9. We would further focus on splice variant specific structures for both cell panels in confocal microscopy such as focal adhesion assemblies when assessing changes in the actin cytoskeleton in more detail. With the knock-out cell line we would further assess changes in PTK6

localization, as the endogenous ADAM15 might have caused the cytoplasmic localization in both cell panels.

5 ADAM15 interaction with the prostate cancer promotor PTK6

5.1 Introduction

The intracellular domain of ADAM15 is subject to alternative splicing leading to 13 splice variants, differing in the number of their proline rich regions. Proline rich regions enable the association with SH3-domain containing proteins inside the cytoplasm. ADAM15 splice variants, A to E, which the subject of this study, contain 3 to 5 proline rich regions. ADAM15-C contains 5 proline rich regions, whereas B and E contain 4, and ADAM15-A, only 3. A frame shift mutation upstream of exon 19, results in a premature stop codon in splice variant D, and the absence of any proline rich regions[81]. Proteins that were identified to interact via their SH3-domains with the proline rich ADAM15 ICD, are Src family kinases such as Lck, Abl and Src, or sorting nexins such as SNX9 and SNX33, adapter proteins such as Grb2 and Nck, and the tyrosine kinases such as Btk and PTK6[144,145,150]. The interaction of the ADAM15-ICD with these proteins suggests a potential role of ADAM15 in regulation of cell signalling pathways and cell function.

Kleino *et al.* showed that alternative exon use influences not only the ability, but also the strength and specificity to associate with SH3-domain containing proteins. For example splice variants B, C and E show a strong association with nephrocystin, whereas splice variant A shows a weak association[144]. Prior to this, Zhong *et al.* identified the ADAM15 splice variant specific impact on patient survival in breast cancer[81]. Although ADAM15-A was identified to interact with the tyrosine kinases Src and the adaptor protein Nck, compared to ADAM15-B and C the interaction was much weaker, which was likely dependent on proline rich regions, present in ADAM15-B and C. Martetzky *et al.* linked the splice variant specific interaction with Src to enhanced proteolytic activity of ADAM15-B. Upon comparison of splice variants ADAM15-A and B, B showed enhanced proteolytic cleavage of the FGFR2iiib, which was linked to breast cancer progression[293]. Inhibition of Src via inhibitor treatment or via knock down, confirmed the Src dependent enhancement of ADAM15-B activity[156]. ADAM15-B was suggested as a possible target in breast cancer.

PTK6 is related to the Src family kinases, and is linked to prostate cancer progression and disease aggressiveness[294]. PTK6 was identified to associate with ADAM15 A and B but not to C in breast cancer[81]. Breast cancer patients expressing high levels of ADAM15-C had enhanced relapse-free survival, compared to ADAM15-A and B expressing patients. PTK6 contains an N-terminal SH3 domain followed by an SH2-

domain, the linker region and a C-terminal kinase domain. PTK6 localization is flexible due to a lack of a myristoylation sequence. This allows shuttling of PTK6 between cell compartments and the interaction with proteins in the nucleus, the cytoplasm or the plasma membrane. The SH2-domain of PTK6 enable the interaction with phospho-tyrosines of other interaction partners, such as Sam68 in the nucleus, or AKT within the cytoplasm. In normal prostate epithelium, PTK6 is found in the nucleus, where it co-localizes with Sam68[295]. Zheng *et al*. showed that PTK6 directly associates with AKT via its SH3 domain. The interaction is enhanced upon SH2 domain interactions, leading to AKT tyrosine phosphorylation at position 315 and 326[277]. AKT can be phosphorylated by growth factor signalling, such as EGFR, promoting cell proliferation. Knock down of PTK6 in BHP-1 PCa cells showed reduced phosphorylation of AKT in response to EGF stimulation, suggesting a direct influence of PTK6 on AKT signalling and cell proliferation[277].

5.1.1 Aims of the chapter

The aims of this chapter were to assess splice variant dependent interactions of ADAM15 and PTK6 in PCa cell lines, and to identify whether the activity of PTK6 itself is necessary for the interaction with ADAM15.

Therefore, PC3 and LNCaP ADAM15 A-E cell panels were used in immunoprecipitation assays to determine the splice variant specific interaction with PTK6 in both cell panels. Immunofluorescence and confocal microscopy were used to determine the spatial overlap of ADAM15 and PTK6. A kinase assay was used to detect changes in ADAM15 phosphorylation by PTK6. To further elucidate the role of active or inactive PTK6 on the ADAM15 interaction, HEK293FT cells were transiently co-transfected using PTK6-wildtype or the inactive kinase mutant, PTK6-K219M, with ADAM15-A.

5.2 Results

5.2.1 All ADAM15 splice variants form a complex with PTK6

In order to identify an ADAM15 splice variant specific interaction with PTK6, total cell lysates of PC3 ADAM15 A-E overexpressing cells were used for immunoprecipitation (IP) of either the endogenous PTK6 or the overexpressed ADAM15. IPs were performed both ways, i.e. immunoprecipitating ADAM15 and testing for the presence of PTK6 by western blotting, and in the reverse order, i.e. immunoprecipitating PTK6 and testing for the presence of ADAM15 by western blotting.

PC3 cells expressing ADAM15 A-E tagged with the V5 epitope, were grown and lysed in RIPA buffer. 350μg/200μL total lysate for the IP using rabbit-anti-PTK6 coated Dynabeads, and 250μg/200μL for the reverse IP using anti-V5-coated agarose resins were used. Eluted proteins were separated by SDS-PAGE, and western blotting was performed with anti-V5 and anti-PTK6 antibodies, respectively. Total lysate was probed additionally for actin as a loading control (Figure 5.1 A). PC3 vector cells were used as negative controls for V5-IPs. PTK6-IP was validated using the PC3-shPTK6 cell panel (Supplementary data Figure 8.8).

Western blotting for V5 in the PTK6-IPs revealed that all ADAM15 splice variants were found in PTK6-IPs (Figure 5.1 A), indicating that PTK6 interaction is not ADAM15 splice variant dependent. Due to the lack of proline rich-regions in ADAM15-D, it was surprising to detect it in the PTK6 IPs. To exclude sample contamination, supernatants of washing steps after O/N incubation were run on SDS-PAGE gels and probed for V5 and PTK6. Supernatants were found to be negative for V5 and PTK6 (Supplementary data Figure 8.8). The reverse IP, using anti-V5-coated agarose resins was performed simultaneously. PTK6 was found in all ADAM15 splice variant IPs, whereas no PTK6 was detectable in the vector control IP serving as negative control (Figure 5.1 A). To quantify potential differences in splice variant association, densitometry was applied for the PTK6-IPs and normalized against total lysate actin levels. ADAM15/PTK6 ratios are plotted for each splice variant (Figure 5.1 B). No significant difference for the ADAM15 splice variant specific interaction with PTK6 was detectable. However, as shown in Chapter 3, PC3 cells endogenously express ADAM15, which might have an impact on the exogenous splice variant association with PTK6, and this will be discussed later in this chapter.

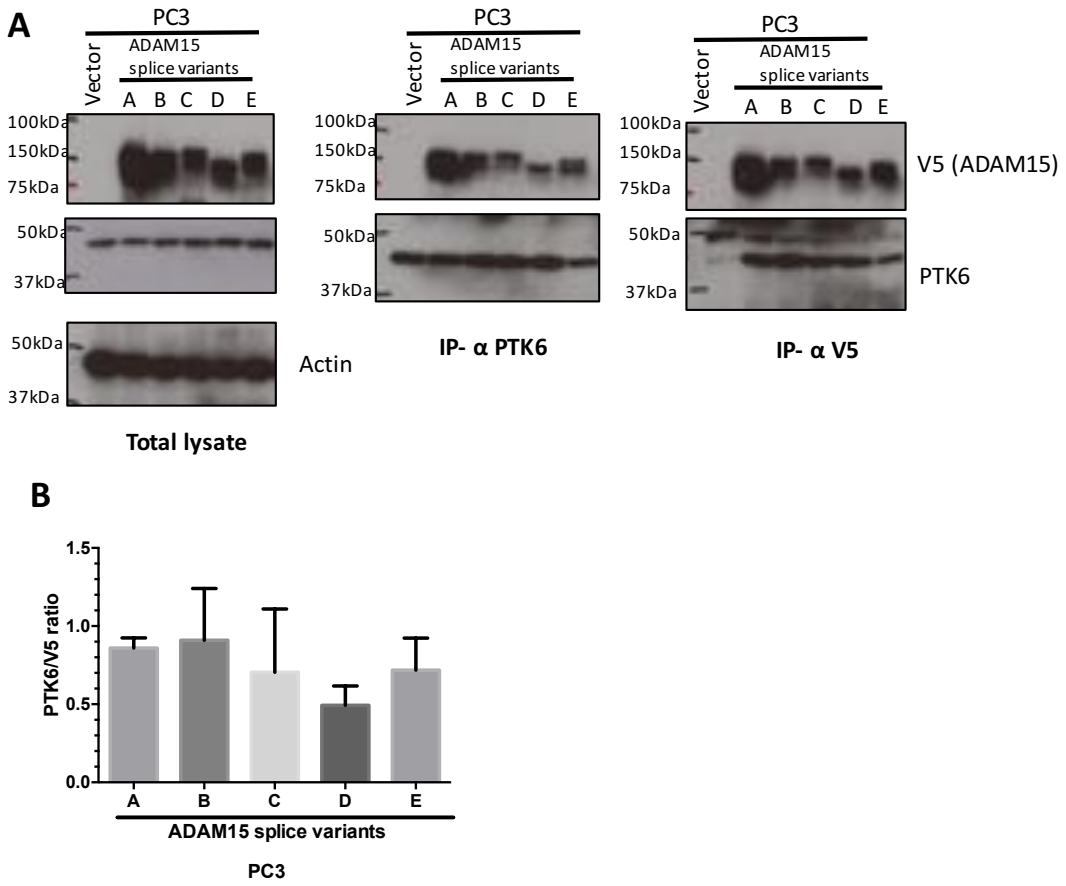

Figure 5.1 ADAM15 splice variant A-E and PTK6 interaction in PC3 cells.

Total lysates of PC3 ADAM15 A-E expressing cells were used for Immunoprecipitation.(A) Endogenous PTK6 or overexpressed ADAM15 tagged with V5, were immunoprecipitated, using rabbit anti-PTK6 coated Dynabeads or mouse anti-V5 coated agarose beads, respectively. Western blotting was used with mouse anti-PTK6 and mouse anti-V5 antibodies, and actin as loading control. Membranes were cut prior to probing with V5-ADAM15 (100kDA), PTK6 (45 kDA), and actin (40kDA). (B) ADAM15 A-E and PTK6 association was analysed using densitometry for PTK6-Ips. Each splice variant is plotted against the PTK6/ADAM15(V5) ratio. Statistical analysis was performed using Graph Pad Prism, One-Way-Anova (n=6), error bars are shown as Mean±SEM.

5.2.2 The interaction is cell line independent

To assess, whether the ADAM15/PTK6 interaction is cell line dependent, the LNCaP ADAM15 A-E expressing cell panel was subject to immunoprecipitation as described in the previously paragraph. Additionally, MDA-MB-231 ADAM15-A and vector control breast cancer cells, were analysed.

The LNCaP cell panel showed that all ADAM15 splice variants in PTK6-IPs. Moreover, in the reverse IPs using the V5-resin, PTK6 was present for all splice variants but it was not detectable for the vector negative control (Figure 5.2 A). MDA-MB-231 cells also showed the presence of ADAM15 in the PTK6-IPs, and the

presence of PTK6 in the V5-IPs, suggesting a cell line independent ADAM15/PTK6 interaction (Figure 5.2 B).

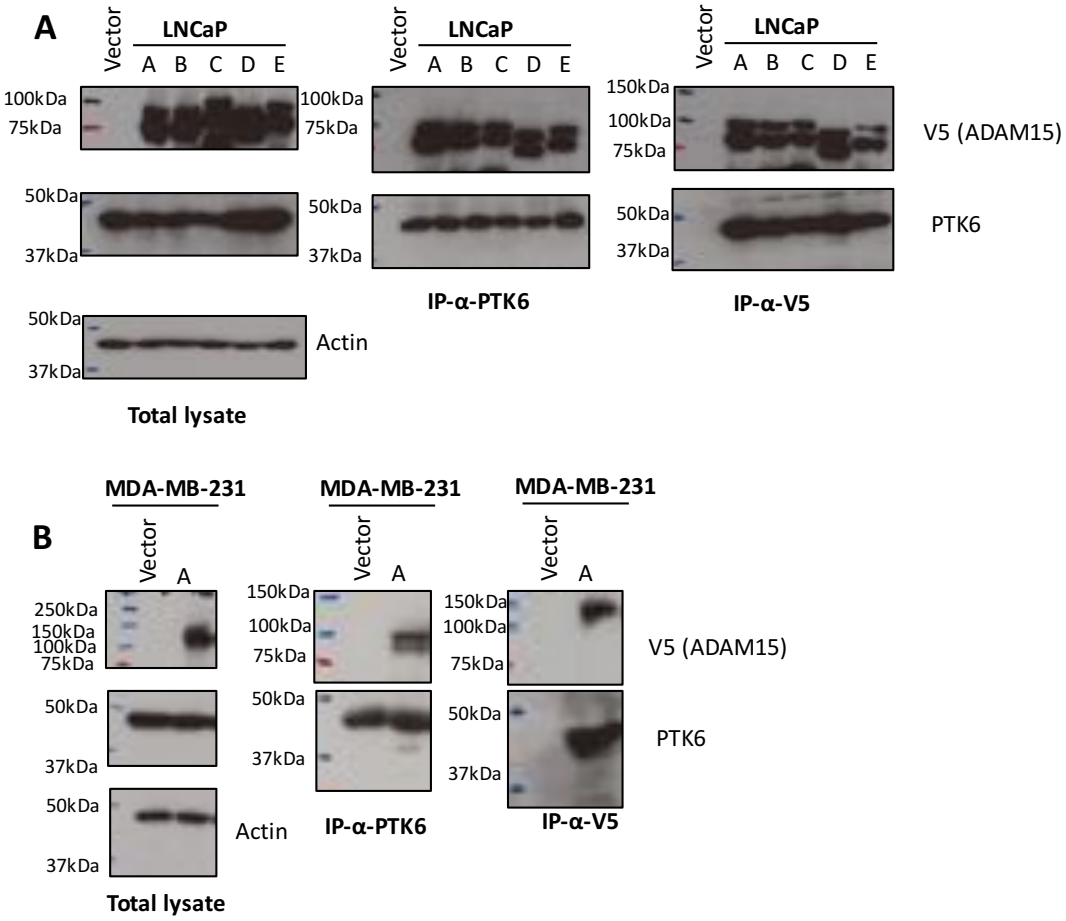

Figure 5.2 ADAM15 splice variant A-E and PTK6 interaction in LNCaP and MDA-MB-231 cells.

Total lysates of LNCaP ADAM15 A-E expressing cells were used for IP. (A) Endogenous PTK6 or overexpressed ADAM15 tagged with V5, were immunoprecipitated, using rabbit anti-PTK6 coated Dynabeads or mouse anti-V5 coated agarose beads, respectively. Western blotting was used with mouse anti-PTK6 and mouse anti-V5 antibodies. Actin was used as IP loading control. Membranes were cut prior to primary antibody probing. For PTK6-Ips, 350µg, and for V5-IPs 250 µg of total protein were used. n=3 (B) MDA-MB-231 breast cancer cells expressing ADAM15-A, and vector control, were used for IP with V5 and PTK6, n=1.

5.2.3 Endogenous ADAM15 is present in ADAM15-D-V5 IPs

In 5.2.1 we showed that all ADAM15 splice variants form a complex with PTK6. However due to lack of proline-rich regions ADAM15-D was unlikely to interact with PTK6. To investigate the ADAM15-D/PTK6 complex formation, anti-V5-IPs were probed for endogenous ADAM15, with an ADAM15-ICD specific antibody. This approach would show whether ADAM15-D was forming complexes with the

endogenous ADAM15 present in PC3 cells (Chapter 3). The antibody was raised against the most C-terminal part of ADAM15-A, B, C and E, which is absent in ADAM15-D, and thus cannot detect ADAM15-D.

Anti-V5-IPs were performed from PC3 vector and ADAM15-A cells as the controls, and ADAM15-D total cell lysates (Figure 5.3 A). The IPs were split and run on two separate gels. Western blotting was performed with antibodies to V5, ADAM15-ICD and PTK6. Anti-V5 immunoblotting confirmed the presence of overexpressed ADAM15 in total lysates and V5-IPs. PTK6 was present in the anti-V5-IPs for both splice variants (Figure 5.3 A). Probing for ADAM15 using the ADAM15-ICD antibody, showed presence of endogenous ADAM15 in the vector control, and the ADAM15-A and D cells in the total lysate (Figure 5.3 B). In anti-V5-IPs, exogenous ADAM15 was not detectable in the vector control cells. Interestingly, exogenous ADAM15-A and ADAM15-D-IPs showed presence of endogenous ADAM15 (Figure 5.3 B), suggesting an interaction between the endogenous ADAM15 present in PC3 and the overexpressed ADAM15-D.

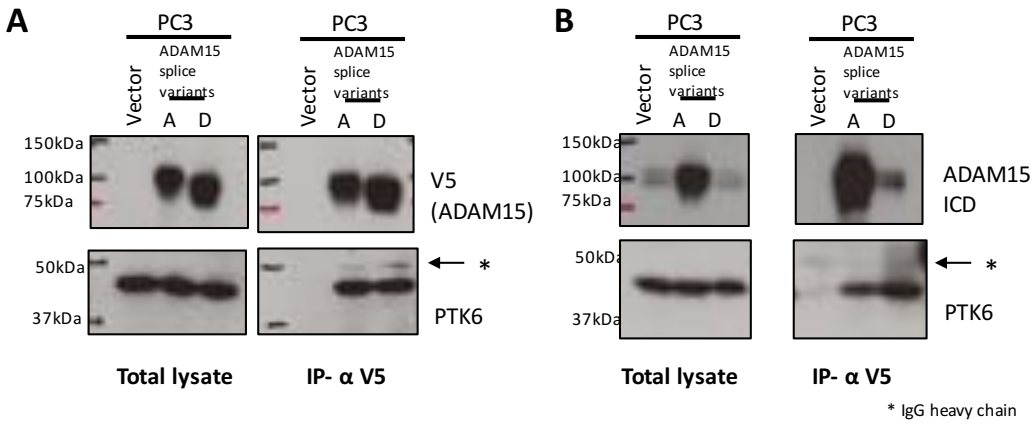

Figure 5.3 Endogenous ADAM15 is present in anti-V5-ADAM15-D IPs.

PC3 ADAM15 A and D and vector cells were used for anti-V5-IPs. IPs were split in half and run on two gels, membranes were probed for V5 and ADAM15 using an antibody to the most C-terminal part of the ADAM15-ICD, which is absent in ADAM15-D. (A) V5-IPs and total lysate for PC3 ADAM15 A, D and Vector cells, showing V5-ADAM15 present in ADAM15-A and D, and PTK6. The vector control shows no detectable PTK6. (B) V5-IPs and total lysate for PC3 cells expressing ADAM15 A and D and vector as control. This time membranes were probed using the ADAM15-ICD specific antibody. Endogenous ADAM15 was detectable in all lysates. In the IPs, endogenous ADAM15 was detectable in ADAM15 D V5-IPs. (n=3)

5.2.4 ADAM15 can dimerize, allowing ADAM15-D complex formation with PTK6

To confirm if the protein-protein interaction of endogenous ADAM15 and overexpressed ADAM15-D is caused by the ADAM15 ability to dimerize, a stable chemical linkage of the transient protein-protein interaction was achieved by chemical crosslinking. The homobifunctional crosslinker, glutaraldehyde was used, carrying two reactive carbonyl groups on both ends, enabling reaction with primary amines, present at the N-terminus of each polypeptide and the side chain of lysines present in ADAM15 (Figure 5.4 A). PC3-ADAM15-A and D expressing cells, and additionally HEK293FT cells transiently transfected with ADAM15-A and D were used, as HEK293 cells express only small amounts of ADAM15. Cells were harvested in homogenisation buffer and sonicated. Glutaraldehyde (0.0025%v/v) was added to the lysate for 2, 5, 10, 15, 20, 30 and 60min. The reaction was terminated using 20% hydrazine. Samples were analysed by SDS-PAGE and western blotting, probing for V5.

In HEK293FT and PC3 cells, the ADAM15-A and D monomer was equally detectable for each time-point at 80-100kDa (active ADAM15 80kDa, inactive ADAM15 100kDa) by V5-antibody. Importantly, ADAM15-A and D dimers running at 190-200kDa, were detectable after 5min and increased over time (Figure 5.4 B). A representative example of ADAM15-D dimerization is shown. Dimer formation in PC3 cells, stably overexpressing the ADAM15 splice variants A and D, was analysed, and the monomer to dimer ratio is plotted for each splice variant for the 0 and 60min time points. The dimer/monomer ratio was significantly increased after 60min for both splice variants (Figure 5.4 C).

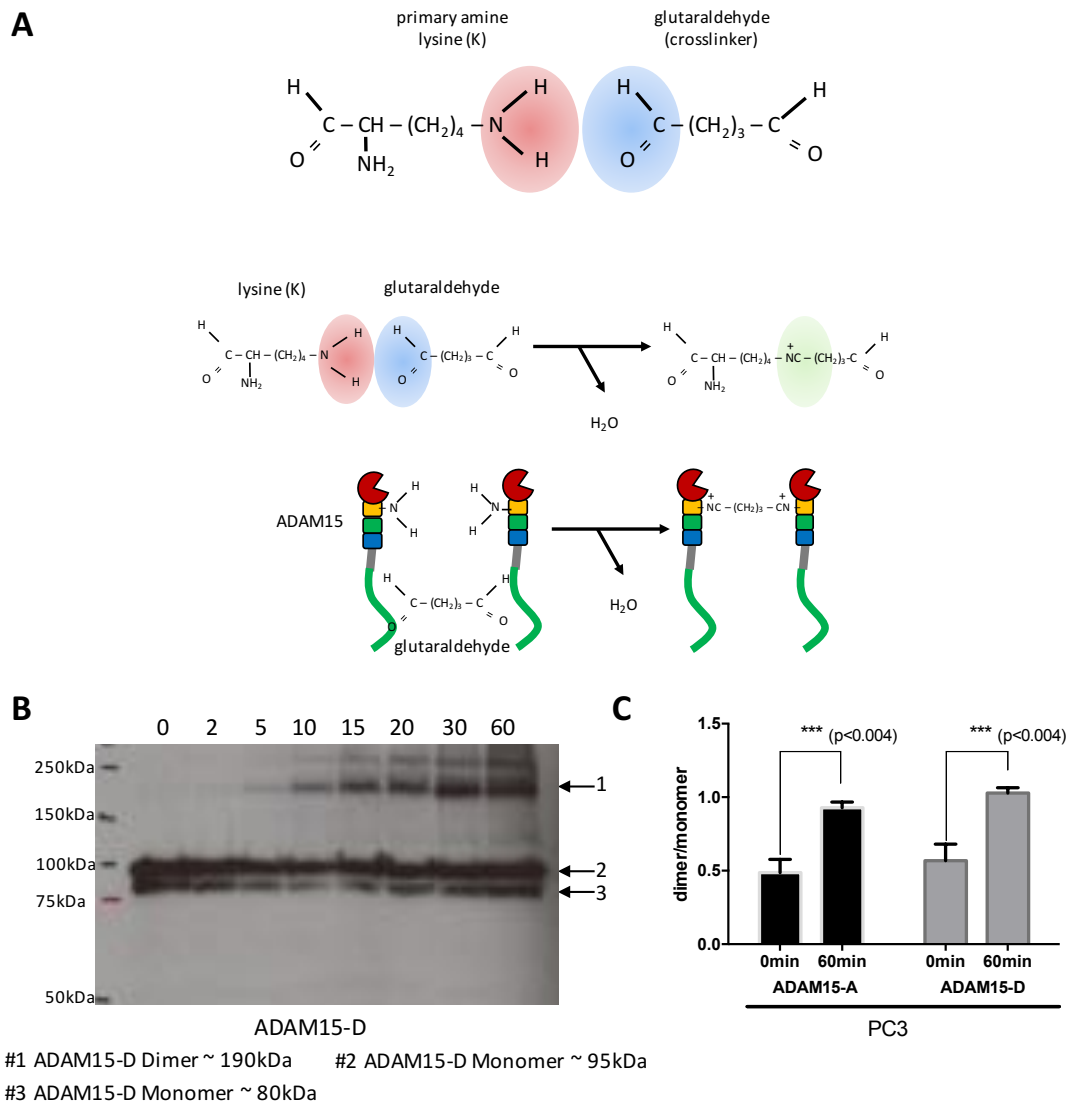

#1 ADAM15-D Dimer ~ 190kDa #2 ADAM15-D Monomer ~ 95kDa
#3 ADAM15-D Monomer ~ 80kDa

Figure 5.4 ADAM15 dimerization using cross-linking.

A time response for ADAM15-A and D dimerization was performed using the homobifunctional crosslinker glutaraldehyde. (A) Schematic overview of chemical crosslinking. Lysine amino acid side chains, can from a stable amino bond with the crosslinker's glutharaldehyde, carbonyl reactive groups. Lysines are present in the ADAM15 ECD and ICD allowing the stable dimer formation after crosslinking, detectable using the V5-antibody. (B) Crosslinking time response of ADAM15-D in HEK239FT cells. Cells were homogenized and run on 6% SDS-gels after crosslinking. Membranes were probed using the V5-antibody. The ADAM15-D active monomer without the pro-domain (80kDA) and the inactive ADAM15-D monomer (95kDa) are present throughout. The ADAM15-D dimer (190kDa), is detectable after 5min, and increases over time. (C) Densitometry results of dimer to monomer ratio in PC3 ADAM15-A and D expressing cells. A significant increase in ADAM15 dimer to monomer ration was detectable, when comparing the 0 and 60 min time points. Statistical analysis was performed using Graph Pad Prism and One-Way-Anova. n=3.

5.2.5 ADAM15 splice variants and PTK6 co-localize in PC3 and LNCaP cells

In as much as it was possible to show ADAM15 splice variant A-E and PTK6 interactions using IP, confocal microscopy was further used to visualize the complex formation within the PC3 and LNCaP cell panels. Cells were fixed and permeabilized, using 4% paraformaldehyde and 0.01% saponin, followed by co-staining with the primary mouse anti-V5 and rabbit anti-PTK6. Anti-mouse-AlexaFlour-568nm (red) and rabbit-anti-AlexaFlour-488nm (green) were used as secondary antibodies, and cells were mounted in DAPI containing media (blue). PC3-shPTK6 and vector cell lines were used as PTK6 and V5-control.

In the PC3 cell panel, PTK6 and ADAM15 were detectable within the cytoplasm and at the plasma membrane (Figure 5.5 A). In ADAM15-A and ADAM15-B expressing PC3 cells, a co-localization for ADAM15 and PTK6 at the plasma membrane was detectable. For ADAM15-C, D and E co-localization was found predominantly in the cytoplasm (Figure 5.5 A). In LNCaP ADAM15 A-E expressing cells PTK6 and ADAM15 were detectable in the cytoplasm and cell-cell junctions (Figure 5.5 B), ADAM15 was detectable in vesicle-like structures, and the cytoplasm, however not as predominantly in the membrane or in cell-cell junctions as seen before for PC3 cells. A co-localization for PTK6 and ADAM15 was found in the cytoplasm for all splice variants. Co-localization was also visible for all splice variants within cell-cell junctions, however less distinct than for PC3 cells. A difference in abundance of co-localization within the cell panels and splice variants was not found. The co-localization seen for PC3 ADAM15 A and B, could not be quantified due to the variations in ADAM15 expression for the individual cells and also due to expression of endogenous ADAM15 which could have influenced PTK6 localisation. Since ADAM15 dimerizes, a PC3 ADAM15 knock out cell line would be necessary to reduce background endogenous ADAM15/PTK6 association levels. Moreover, as both cell lines showed variation of ADAM15-V5 expression for individual cells, a clonal selection might be further required to reduce the experimental variation within the cell panels.

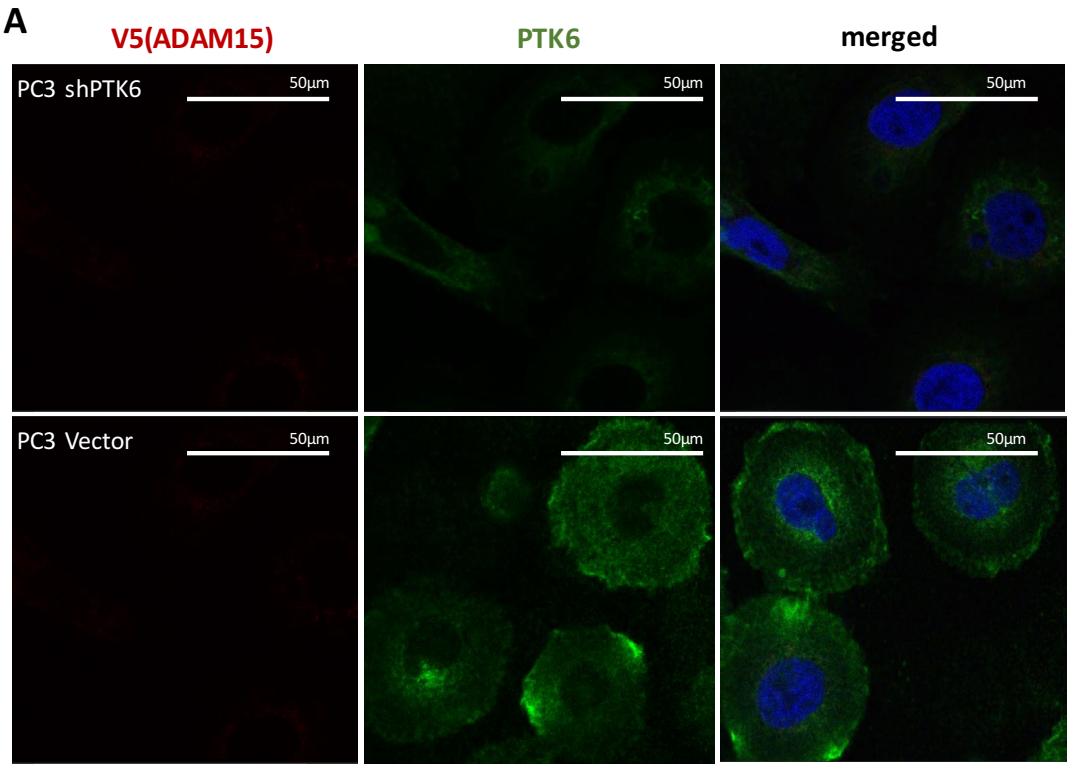
A
V5(ADAM15)
PTK6
merged
PC3 shPTK6
PC3 Vector
50μm

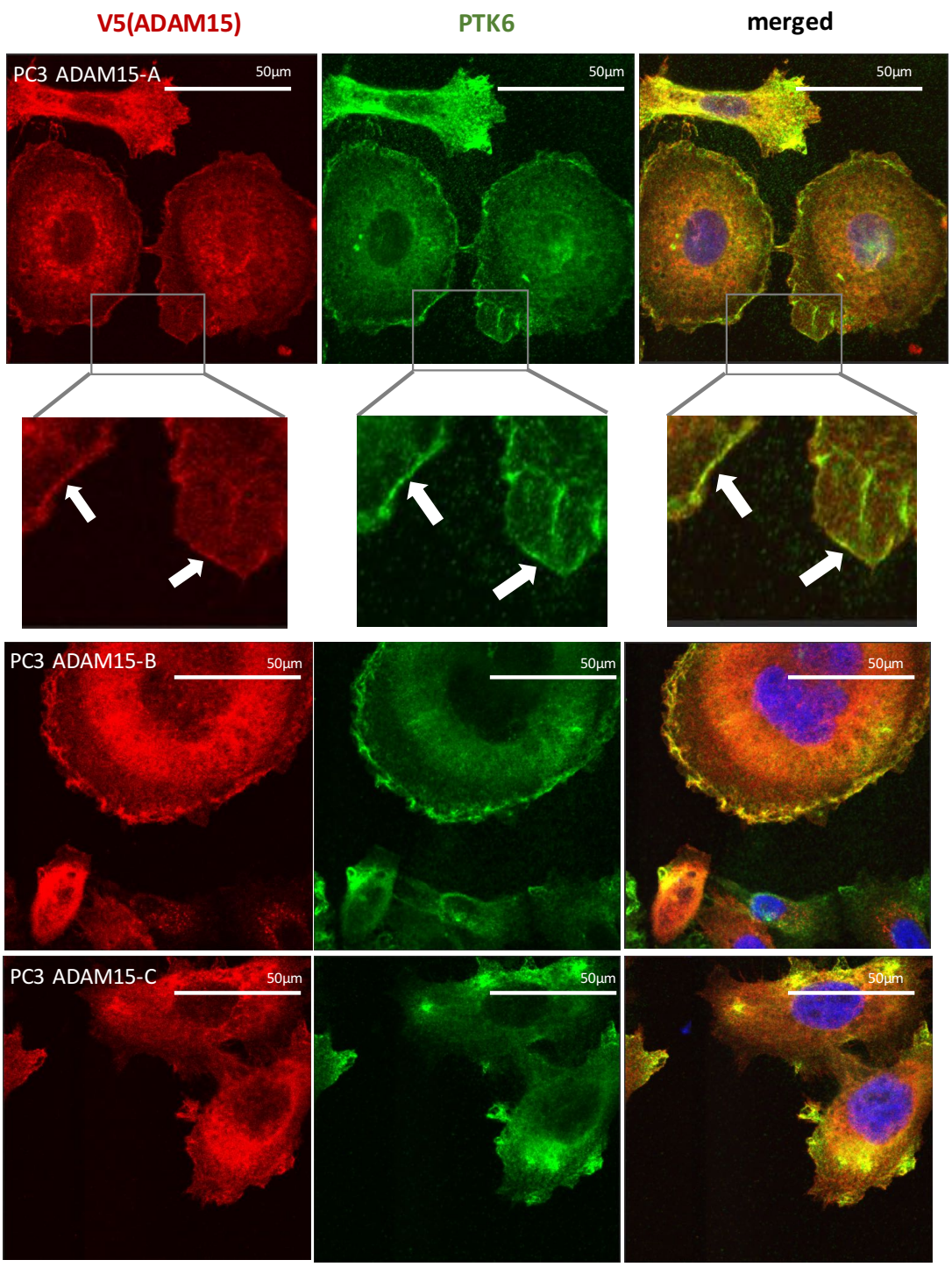
V5(ADAM15)
PTK6
merged
PC3 ADAM15-A
PC3 ADAM15-B
PC3 ADAM15-C
50μm

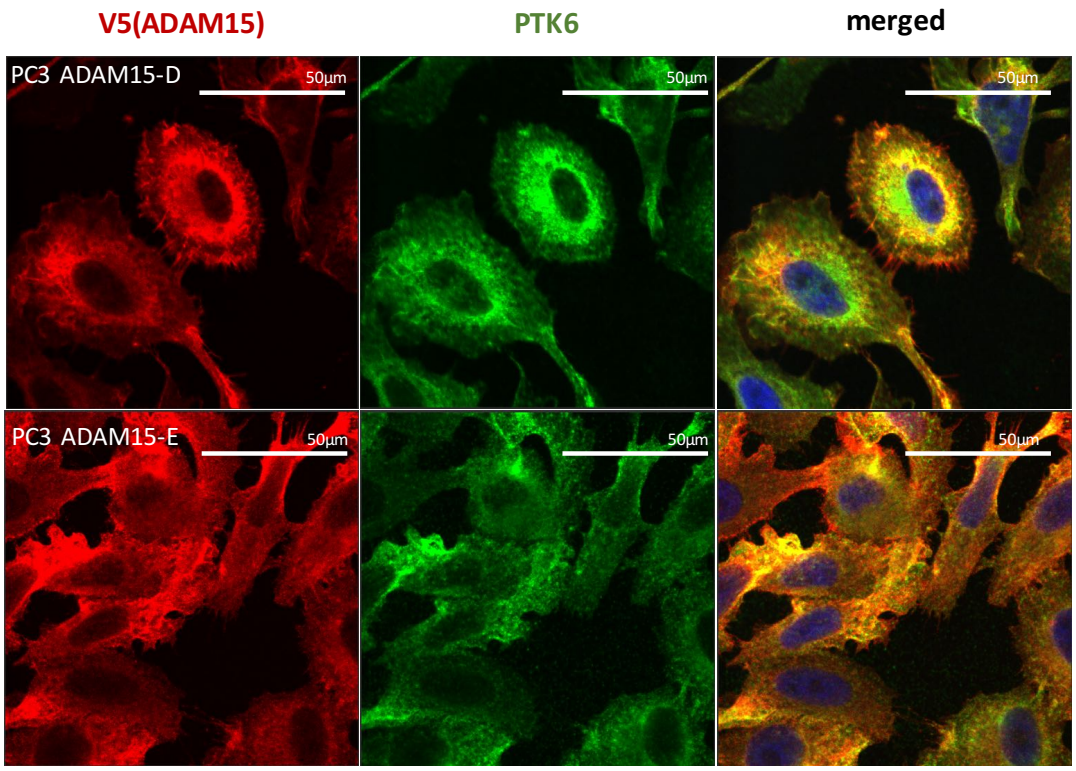
V5(ADAM15)
PTK6
merged
PC3 ADAM15-D
PC3 ADAM15-E
50μm

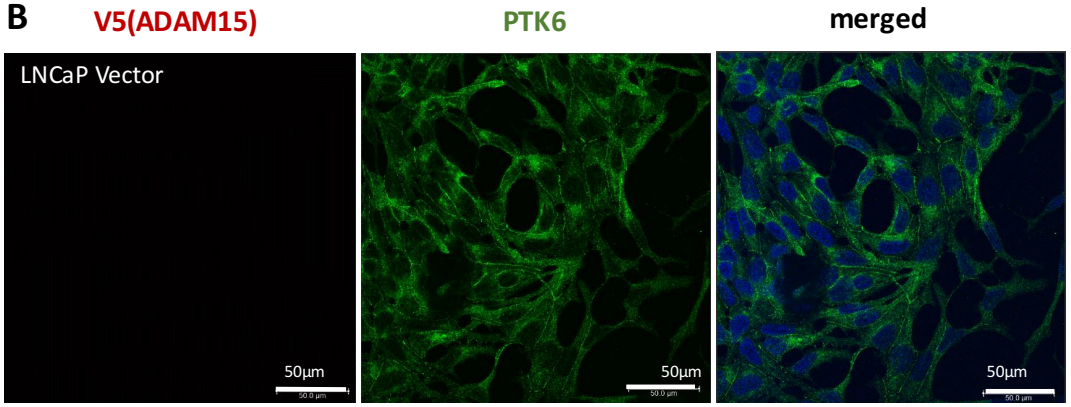
B
V5(ADAM15)
PTK6
merged
LNCaP Vector
50μm

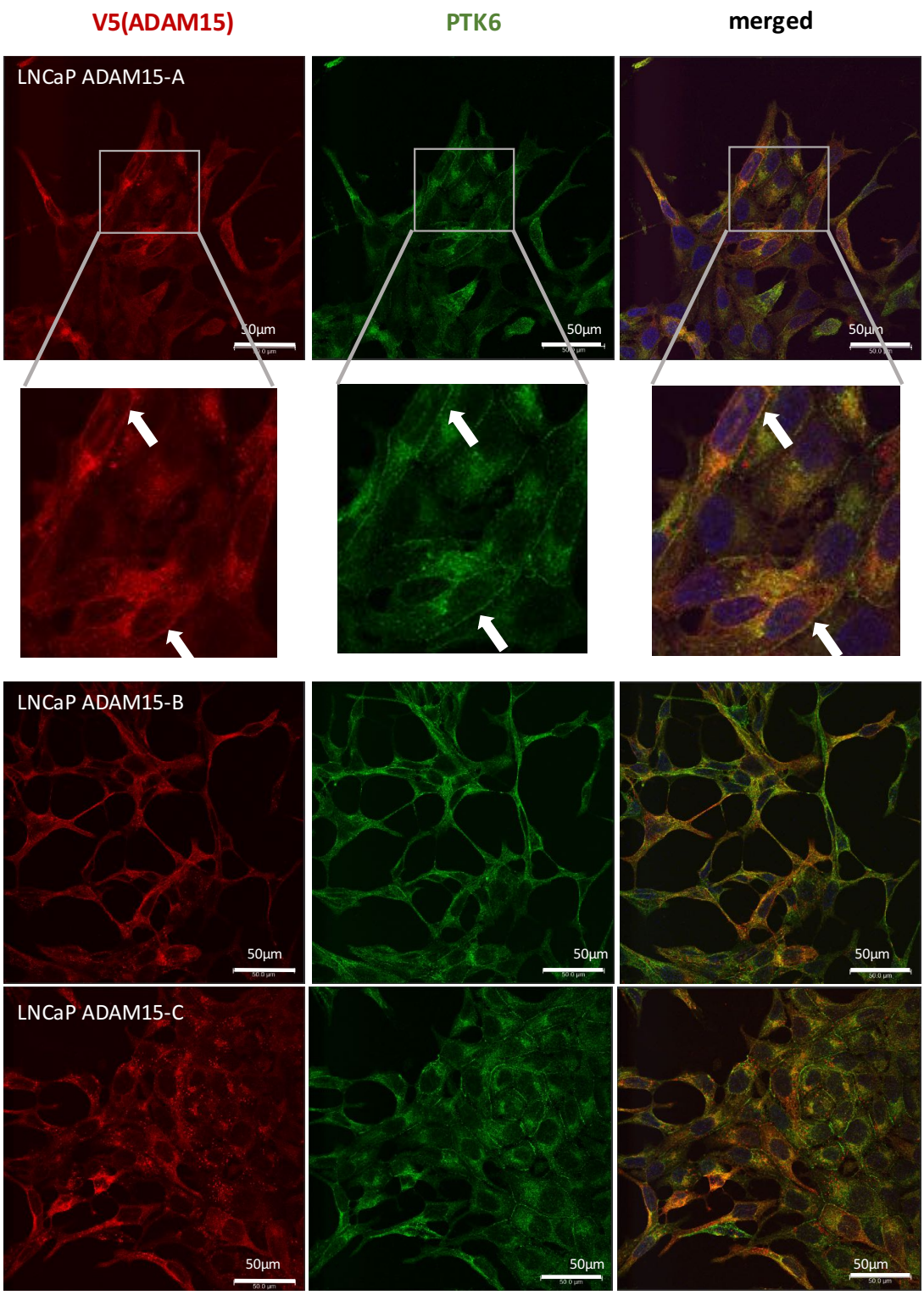
V5(ADAM15)
PTK6
merged
LNCaP ADAM15-A
LNCaP ADAM15-B
LNCaP ADAM15-C
50µm

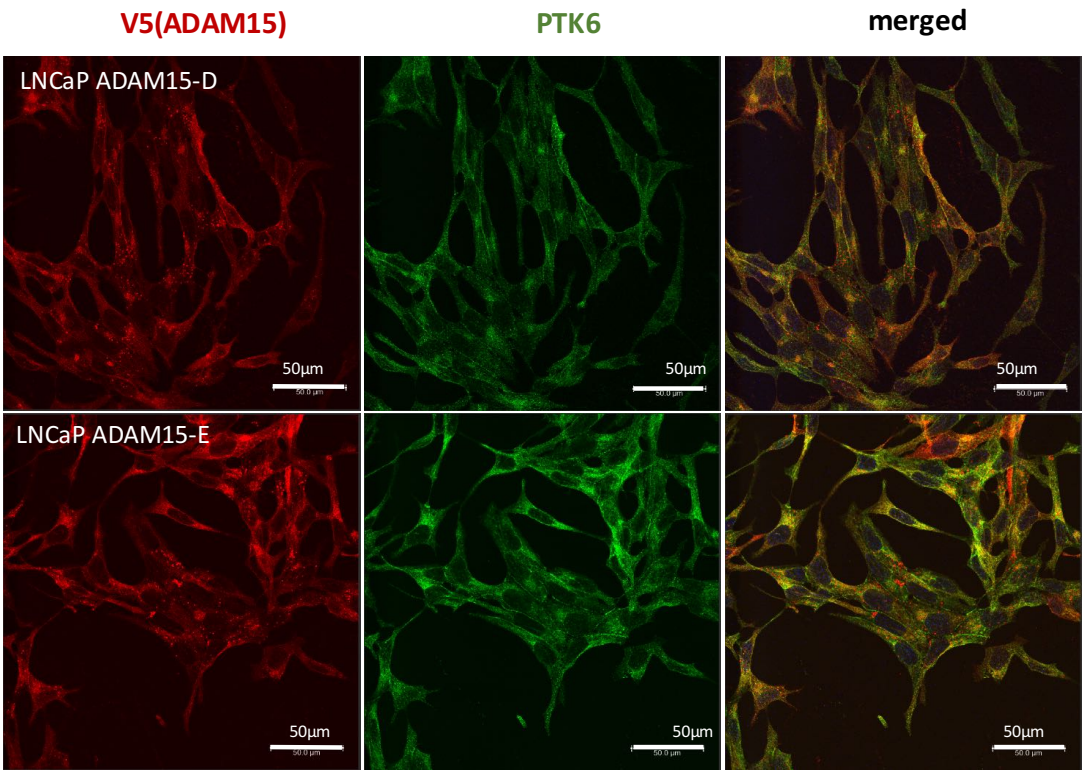

Figure 5.5 Co-localization of ADAM15 A-E splice variants and PTK6 in PC3 and LNCaP.

The PC3 and LNCaP ADAM15 A-E and PC3 shPTK6 cell panels were co-stained using the primary rabbit anti-PTK6, labelled with the secondary anti-rabbit-AlexaFlour-488 (green), and the primary mouse-anti-V5, labelled with the secondary anti-mouse-AlexaFlour-568 (red). The mounting media contained DAPI, as nuclear counter stain. Cell panels were analysed using confocal microscopy (A) The PC3 ADAM15 A-E panel showed a co- localization of PTK6 and ADAM15 in the plasma membrane for splice variant A and B (white arrows). A representative picture for the co-localization of ADAM15 and PTK6 at the plasma membrane is shown for splice variant A. Cytoplasmic localization was detectable for all splice variants. (B) In LNCaP co-localization of ADAM15 and PTK6 was detectable in the cytoplasm for all splice variants. PTK6 and ADAM15 in LNCaP were found for all splice variants in the cytoplasm and in cell-cell junctions. An example for PTK6/ADAM15 co-localization in cell-cell junction is given for splice variant A, indicated by white arrows. The experiment was performed for both cell panels with n=3.

5.2.6 Presence of active and inactive PTK6 in anti-V5-IPs of ADAM15-A and D expressing PC3 cells.

To identify whether active or the inactive kinase PTK6 was present in the anti-V5-IPs, membranes were probed with specific antibodies, detecting either the active kinase phosphorylated at tyrosine 342 (p-342), or the inactive kinase phosphorylated at tyrosine 442 (p-442).

In the PC3 vector and ADAM15- A and D expressing cells, PTK6 and V5 were detectable in total lysate and IPs. Probing for active PTK6, using the pY342 antibody,

showed weak staining in the total lysate at 48kDa, as well as high background and unspecific staining (Figure 5.6). Probing of the IP membrane showed small amounts of pY342 PTK6 at 48kDa and also background staining. Using the pY442-antibody, background staining levels were even higher, although blocking and washing conditions were optimized. In total lysate, a band at 48kDa was detectable, which was also present in IPs using ADAM15-A and D. However, for both antibodies, high background staining was present, which did not allow assessment of changes in association between active or inactive PTK6 and ADAM15-A and D, as PTK6 bands were close to the detection limit (Figure 5.6).

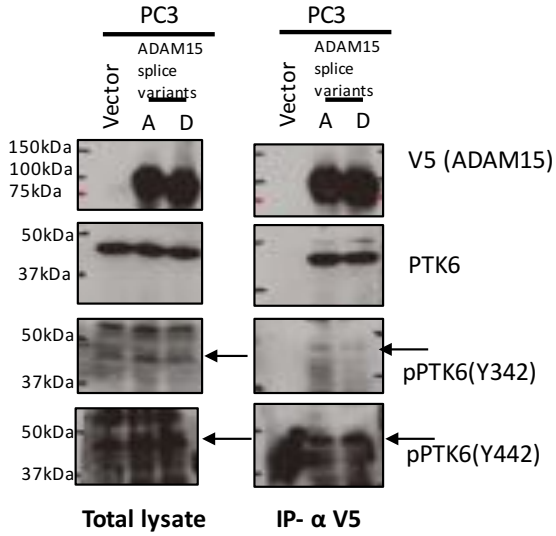

Figure 5.6 Difference in active and inactive PTK6 in anti-V5-IPs

To assess if the ADAM15/PTK6 interaction is dependent on PTK6 activity, anti-V5-IPs with ADAM15-A and D expressing PC3 cells and vector control cells were performed. Differences in the presence of active PTK6, pPTK6 Y342, or inactive PTK6, pPTK6 Y442, was assessed. Phospho-PTK6 antibodies were used. 250µg of total protein was used per IP. Western blotting results for total lysate and anti-V5-IPs, probing for V5, PTK6, pPTK6 (Y342) and pPTK6 (Y442). No difference was detectable, for the active and inactive form of PTK6 in both IPs, (n=2).

5.2.7 PTK6 activity is not required for the complex formation with ADAM15

To assess whether the interaction between ADAM15 and PTK6 is dependent on PTK6 kinase activity, HEK293FT cells were co-transfected with PTK6 expression vector for the active and inactive kinase and ADAM15-A. PTK6 inactive kinase expression plasmids containing an amino acid change from lysine (K) to methionine (M) at position 219 in the active site of the kinase, was kindly provided by Dr. Amanda Harvey (Brunel University, London) (Figure 5.7 A). Co-transfected cells were

incubated 48h post-transfection, harvested and lysed. PTK6 and anti-V5-IPs were performed with cell lysates to assess differences in complex formation.

HEK293FT cells, co-transfected with PTK6-wild type (WT) or PTK6-KM and ADAM15-A, showed similar expression levels for both PTK6 and ADAM15-A in total cell lysates. IPs, using either PTK6 or V5, did not reveal a difference in association between ADAM15-A and active or inactive PTK6, suggesting that the interaction is independent of PTK6 activity (Figure 5.7 B).

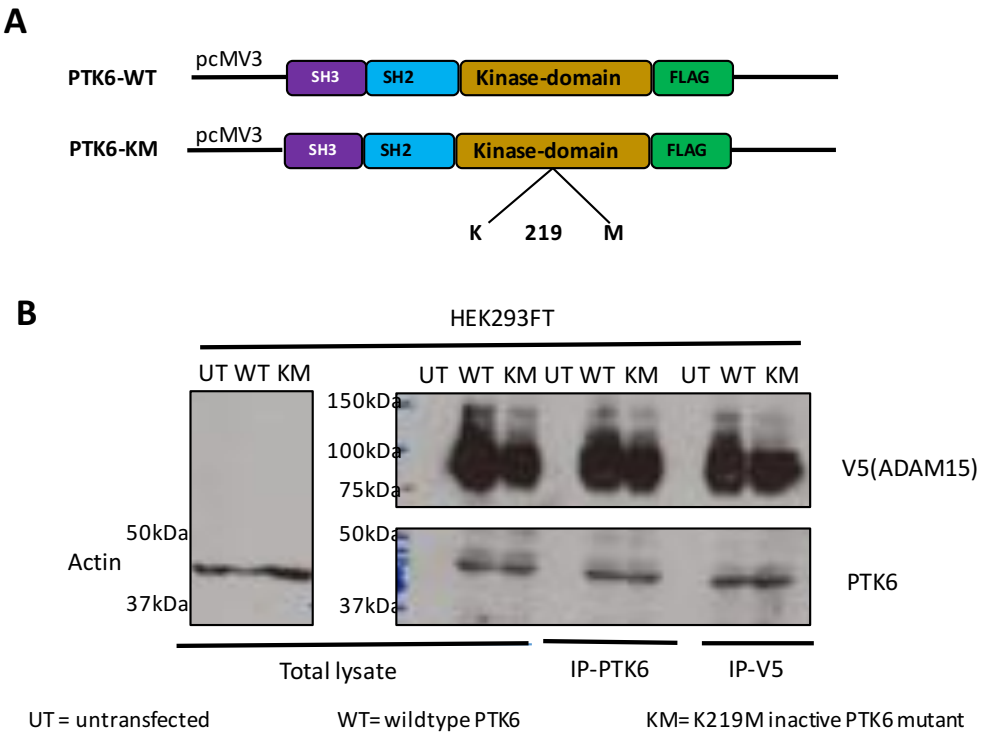

Figure 5.7 ADAM15/PTK6 interaction is independent of PTK6 activity.

(A) pcMV3 expression plasmids containing human PTK6 wild type (WT) or the KM-mutant, FLAG-tagged. (B) HEK293FT cells were transiently co-transfected with ADAM15-A and PTK6-wildtype or inactive K219M mutant, in a 1:1 ratio. IPs with anti-PTK6 and anti-V5 were performed and analysed using western blot probing for V5 and PTK6,respectively; actin was used as loading control n=4.

5.2.8 No changes in ADAM15/PTK6 association upon PTK6 kinase activation

To assess whether the kinase activity of PTK6 has an impact on ADAM15 phosphorylation, a kinase assay was performed. Endogenous PTK6 from PC3-ADAM15-A expressing cells, serum starved for 30h and treated for 30min with HGF (20ng/mL) or serum free medium, was immunoprecipitated. IP samples were resuspended in kinase buffer, containing 20nM $MgCl_2$ and 5µM ATP, and were incubated for 1h at 37°C followed by western blotting probing for phospho-tyrosines

using the pan-phospho-tyrosine antibody 4G10. HGF was used to enhance the association between ADAM15 and PTK6, as unpublished data from our lab showed an increase in association upon HGF treatment in MDA-MB-435 cells.

Western blotting results for PC3-ADAM15-A total lysate, treated as indicated, did not show any differences in phosphorylation when membranes were probed with the 4G10 antibody (Figure 5.8). Kinase activation of PTK6 by ATP after immunoprecipitation, did not show any detectable bands present at the estimated molecular weight of PTK6 (48kDa). Additionally, no difference in association of ADAM15/PTK6, upon HGF treatment, was detectable when probing for V5. 4G10 western blotting results did not show detectable bands for the molecular weights of ADAM15 (100kDA) or PTK6 (48kDa) in the PTK6-IPs (Figure 5.8).

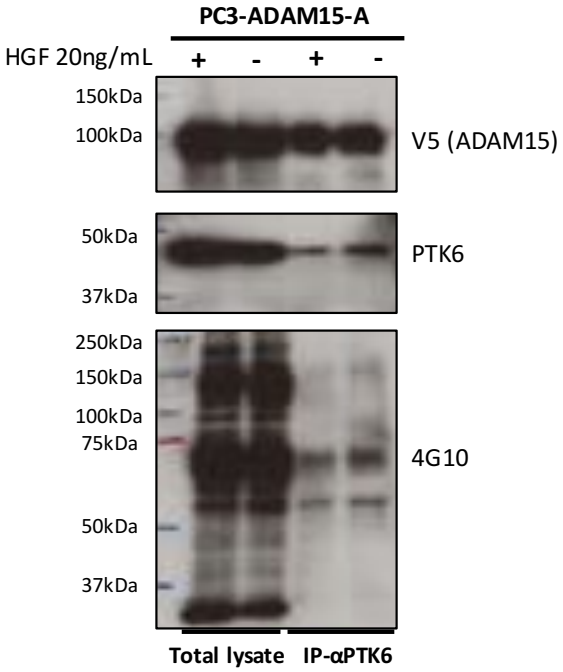

Figure 5.8 No changes in ADAM15/PTK6 association upon HGF treatment.

A kinase assay was used to identify an increase in ADAM15 or PTK6 phosphorylation upon PTK6-kinase activation. Cells were treated with or without HGF (20ng/mL) and incubated for 30min. 500µg total protein was used per anti-PTK6-IP. A pan phospho-tyrosine antibody, 4G10, was used to detect changes in phosphorylation of either ADAM15 (100kDa) or PTK6 (48kDa), (n=2).

5.3 Discussion

The aim of this chapter was to identify an ADAM15 splice variant dependent interaction with the prostate cancer promotor PTK6, and to identify whether the interaction was dependent on the kinase activity of PTK6 itself.

The cytoplasmic domain of ADAM15 varies in its number of proline rich binding motifs, allowing binding of cytoplasmic proteins containing SH3 domains. Poghosyan *et al.* showed, that the ICD of ADAM15 can interact with SH3 domains of Src family kinases such as Lck, Fyn, Abl and Src in a pull-down assays from Jurkat, THP-1, U937 and K562 haematopoieitic cell extracts[145]. Using GST-ADAM15-A, B and C ICD fusion proteins, Zhong *et al.* confirmed a splice variant specific interaction of PTK6 and ADAM15-A and B, but not C.

Using the PC3 ADAM15 A-E expressing cell panel immunoprecipitations were performed using either PTK6 coated Dynabeads or anti-V5-conjugated agarose resins. All ADAM15 splice variants were found in the PTK6 IP samples. By performing the reverse IP using anti-V5, PTK6 was found in all ADAM15 splice variant IPs. IPs using the LNCaP ADAM15 cell panel, also showed interactions of all splice variants with PTK6. Compared to the prostate tissue, where PTK6 is expressed in both healthy and cancerous tissue, PTK6 is not detectable in healthy breast tissue, but only in breast cancer[296]. MDA-MB-231 cells are known to express high levels of endogenous PTK6. The ADAM15/PTK6 interaction was also shown for MDA-MB-231 ADAM15-A expressing breast cancer cells, suggesting a cell line and cell type independent interaction. ADAM15 ICD splice variants show differences in the number of their proline rich binding motifs, however, no difference in complex formation with PTK6 was found in our experiments. However, Maretsky *et al.* showed a difference in Src association for ADAM15-A and ADAM15-B, due to the additional proline rich region, present in B [156]. Confocal microscopy revealed co-localization of PTK6 and ADAM15 A-E splice variants, in PC3 cells at the plasma membrane and in the cytoplasm. However, when trying to quantify the ADAM15/PTK6 membrane staining for ADAM15 splice variants A and B in PC3s, no difference between the splice variants was detectable, as individual cells showed high variation in ADAM15 expression. As no clonal selection was used after Lentiviral infection with the ADAM15 viral particles, the cell panel appeared diverse in ADAM15 expression, which influences the confocal microscopy results. To quantify the ADAM15/PTK6 membrane staining seen in PC3, equal expression of ADAM15 among cells would be necessary. For LNCaP, spatial overlap of ADAM15 and PTK6 was detectable in the cytoplasm. Although PTK6 cell-cell junction staining was very prominent for the LNCaP panel, ADAM15 staining was detectable in cell-cell junctions, however not as distinct as PTK6. A difference between cytoplasmic and nuclear localization, as found by Derry *et al.*[273], for the PC3 and LNCaP panel could not be detected. ADAM15 A-E splice variant overexpression did not result in detectable differences in PTK6/ADAM15 spatial overlap. For confocal

microscopy, PC3 and LNCaP cells with knock down of ADAM15 would be necessary, as endogenous ADAM15 present in both cell panels, might contribute to background spatial overlap.

Due to the lack of proline-rich interaction motifs, ADAM15-D was not expected to form a complex with PTK6. As PC3 cells express endogenous ADAM15 (Chapter 3), dimer formation between endogenous ADAM15 and overexpressed ADAM15-D was assessed. In PC3 ADAM15-D V5-IPs, endogenous ADAM15 was detectable using an ADAM15-ICD antibody, indicating dimer formation between ADAM15-D and the endogenous ADAM15. This suggested that the PTK6 interaction observed for ADAM15-D could be indirect, mediated via the endogenous ADAM15 ICD, i.e the ADAM15-D dimerization partner. Crosslinking experiments between ADAM15-A or D using transiently transfected HEK293FT cells, chosen due to their low expression level of endogenous ADAM15, showed a significant ADAM15 dimer formation as assessed by crosslinking. ADAM dimerization has been reported previously, although not for ADAM15 specifically. Xu *et al.* identified that ADAM17 is found in an inactive state, as a homodimer at the plasma membrane during basal conditions. Upon activation of the p38 MAPK pathway, ADAM17 monomer to dimer ratio changed, which resulted in an increase in ADAM17 monomer and enhanced proteolytic activity of ADAM17, such as shedding of TGF-α[297]. They further identified the homo dimerization of ADAM10, and suggested that dimer formation might be an inherent characteristic of ADAMs, regulating their functions as proteases or cytoplasmic signal transductors[297,298].

In an *in-vitro* kinase assay using ^{32}P-labeled phosphoproteins, Derry *et al.* showed higher activity of PTK6 in LNCaPs compared to PC3s[273]. This led to the conclusion that PTK6 localizing to the nucleus shows higher activity compared to PTK6 localized to the cytoplasm. Here, we used the PC3 ADAM15-A, D and vector cells in anti-V5-IPs to identify, whether active or inactive PTK6 is present in the ADAM15/PTK6 complex. SDS-PAGE and western blotting followed by probing with phospho-antibodies able to detect active or inactive PTK6, showed no difference in the PTK6 association pattern, as both antibodies showed high background levels. Furthermore, we identified that PTK6 activity is not necessary for the complex formation with ADAM15, as both WT-PTK6 as well as mutant, catalytically inactive KM-PTK6 immunoprecipitate equally with ADAM15.

Association of Src with the ADAM15-A and B ICD led to differences in ADAM15 proteolytic activity, i.e. shedding of the FGFR2iib, shown by Maretzky *et al.*. They

identified that the third tyrosine (Y), Y735, of the ADAM15-A-ICD is important for Src activation of ADAM15-B. Additionally for PTK6, Castro *et al.* showed, that the motogenic factor HGF, can increase PTK6 phosphorylation and activity in MDA-MB-231 breast cancer cells. Using a kinase assay, we assessed changes in ADAM15 phosphorylation upon PTK6 association after HGF stimulation using the PC3-ADAM15-A expressing cells. No changes in phosphorylation of ADAM15 and PTK6 were detectable using the pan-phospho-tyrosine 4G10 antibody in total lysate. Moreover, performing the kinase assay after immunoprecipitation of PTK6 in treated or untreated cells, western blotting did not reveal any phospho-tyrosine bands for the corresponding molecular weights of ADAM15 (100kDa) or PTK6 (48kDa), suggesting that PTK6 might not influence ADAM15 phosphorylation or activity, as shown for Src. Using a different approach, with radioactive labelled ^{32}P-ATP the assay sensitivity might increase and changes in phosphorylation might be detectable[299]. As PC3 cells express high levels of the HGF receptor cMET, self activation due to endogenous presence of HGF or spontaneous dimerization of cMET without HGF activation cannot be excluded. PC3 cells with HGF or cMET knock down would be required to exclude background HGF stimulation. The HGF treatment to activate the cMET/HGF axis in PC3 cells is questionable according to kinase assay data, since no difference in phosphoprotein content could be detected with or without HGF treatments, suggesting that the cMET pathway may be constitutively active. In this case, cMET inhibition using cMET kinase inhibitors might be required to assess differences in ADAM15/PTK6 complex formation.

In summary, our data showed that all ADAM15 splice variants interact with PTK6 in a cell line independent manner. We could further confirm that PTK6 activity itself is not needed for this interaction. Surprisingly we found that ADAM15 splice variant D was found in a complex with PTK6. Consequently, this lead to the observation that ADAM15 dimerizes, leading to a dimer formation between the endogenous and the overexpressed ADAM15. To further elucidate the role of ADAM15 dimerization we aim to identify the ADAM15 splice variant leading to the dimer formation. For this we would overexpress different combination of the ADAM15 splice variants in a PC3 ADAM15 knock-out cell line. Using total cell lysates, we would assess differences in ADAM15 monomer to dimer ratio. Using confocal microscopy we would further aim to quantify the co-localization of ADAM15 and PTK6. For this we would choose cells with equal ADAM15 overexpression. Using the Pearson's correlation coefficient we would assess the amount of co-localization for each splice variant.

6 ADAM15/PTK6/cMET complex formation

6.1 Introduction

Some aspects of tumourgenicity of cells is regulated by transmembrane tyrosine kinase receptors, such as the HGF receptor cMET. Dysfunction in the cMET/HGF axis is linked to initiation of cancer and correlates with disease progression, as cMET is a key driver of cell invasion, migration and proliferation, and EMT[247,300,301].

Han *et al*. used the androgen dependent, cMET negative, LNCaP PCa cell line, to assess the HGF/cMET dependent changes in EMT upon cMET overexpression. They showed that cMET overexpression caused EMT, indicated by loss of E-cadherin and gain of the mesenchymal marker vimentin. The cMET dependent increase in invasion and migration was also confirmed using LNCaP cMET overexpressing cells[300]. In the pancreatic cell lines MIA-Paca2 and PK-45H, inhibition of cMET upon treatment with the cMET inhibitor SU11274, showed reduction of invasion and proliferation[302].

Prostate cancer progression, due to the loss of androgen dependence after androgen ablation therapy, often correlated with cMET upregulation. Tu *et al.* showed that colony formation and proliferation was reduced in PC3 and DU-145 PCa cell lines, upon cMET kinase inhibitor PHA-665762 and PF-2311066 treatment[251]. Dai *et al.* showed in PC3 cells that cMET is constitutively active. While treatment using anti-HGF-neutralizing antibodies did not reduce invasion or proliferation, cMET tyrosine kinase inhibition reduced proliferation and invasion in PC3s[231]. In ovarian cancer, cMET/HGF signalling is associated with poor overall survival and the cMET inhibitor capmatinib (INC280) reduced proliferation, migration, invasion and reduced cMET phosphorylation in SKOV3, CaOV3 and OVCAR3 ovarian cancer cells. Further, capmatinib reduced adhesion of SKOV3 and OVCAR3 cells to the peritoneum[303].

cMET signalling can be targeted either via HGF-antagonists, cMET tyrosine kinase inhibitors, such as capmatinib or SU11274, or anti-cMET antibodies. Additionally, soluble cMET can disrupt the HGF/cMET signalling axis. Coxon *et al.* showed that a soluble cMET fragment, consisting of the cMET-ECD fused to Fc blocks HGF-dependent cMET signalling, and inhibits tumour growth *in-vivo*[304]. Targeting the cMET receptor with the anti-cMET antibody DN30, which binds to the ECD of cMET, led to enhanced proteolytic cleavage of cMET-ECD, generating a soluble cMET (s-cMET) decoy fragment, which in turn inhibits HGF binding. Schelter *et al.* revealed that ADAM10 was involved in cMET cleavage, and the generation of s-cMET[305]. Prior to this

finding, they suggested that ADAM10 was a cMET sheddase, as knock down of ADAM10 in NIH3T3 mouse embryonic fibroblast cells increased cMET surface levels, and reduced soluble cMET in the cell supernatant [121]. ADAM10 itself can be also proteolytically processed. Tousseyn *et al.* identified ADAM15 as an ADAM10 sheddase, cleaving the ECD of ADAM10 from the cell membrane. The metalloproteinase fragment of ADAM10 is subject to γ-secretase cleavage, the resulting ADAM10 ICD translocates to the nucleus, where it is thought to be involved in gene regulation[161].

As cMET is a key player in cell migration and invasion, Castro *et al.* found, that PTK6, downstream of cMET, mediates enhanced migration of MDA-MB-231 breast cancer cells upon HGF stimulation. Subsequently, ADAM15 was identified by Poghosyan *et al.* to associate with the cMET adaptor protein Grb2. The association was mediated by proline-rich binding motifs, present in the ADAM15-ICD, and the SH3-domain of Grb2[145]. Grb2, when bound to cMET, activates the Erk/MAPK pathway, which can upregulate MMP levels, such as MMP9, known to be upregulated by ADAM15 via Erk/MEK, leading to enhanced invasion in NCSCL[157]. cMET dependent interaction of Grb2, induces cell proliferation, cell-cycle progression and migration[199]. Grb2 can either bind directly to cMET or associates with the cMET adaptor protein Gab1[306]. HGF binding to cMET mediates receptor dimerization and transphosphorylation of the C-terminal multi docking site, enabling the association and phosphorylation of Gab1, which is important for cMET signal transduction. Upon overnight SU11274 treatment followed by 10min of HGF treatment of A549 cells, Gab1 phosphorylation was significantly reduced when compared to control[307].

6.2 Aims of the chapter

The aim of this chapter was to evaluate whether ADAM15 overexpression affects invasion in response to HGF and if this invasion can be decreased upon cMET signalling inhibition. Furhter we aim to assess if the ADAM15 catalytic function is involved in HGF dependent invasion of PC3 cells. Using zymography we aim to assess the cell supernatant of PC3 expressing ADAM15-WT and catalytically inactive cells with regard to differences in presence of MMPs. Lastly we aim to elucidate the role of how HGF/cMET signalling regulates the ADAM15/PTK6 complex formation in PC3s and MDA-MB-231 breast cancer cells.

6.3 Results

6.3.1 LNCaP invasion independent of cMET signalling

To assess the effect of HGF induced cell invasion in the LNCaP ADAM15 A-E splice variant expressing cells, a matrigel invasion assay was performed, where 20,000 cells were seeded in the top chamber, containing serum free RPMI culture medium. Cells were incubated for 24h following HGF addition to the bottom chamber, fixed and stained, and the number of invading cells were counted and plotted as number of invaded cells for each splice variant. For each splice variant, an untreated control, was used and compared to the vector cell line.

As shown in Figure 6.1 A, cellular invasion was independent of HGF treatment or ADAM15 splice variant expressed, when compared to vector control cells. When LNCaP parental cells were treated with HGF in a time dependent manner, cMET was detectable, using western blotting however, cMET dependent phosphorylation was not detectable (Figure 6.1 B).

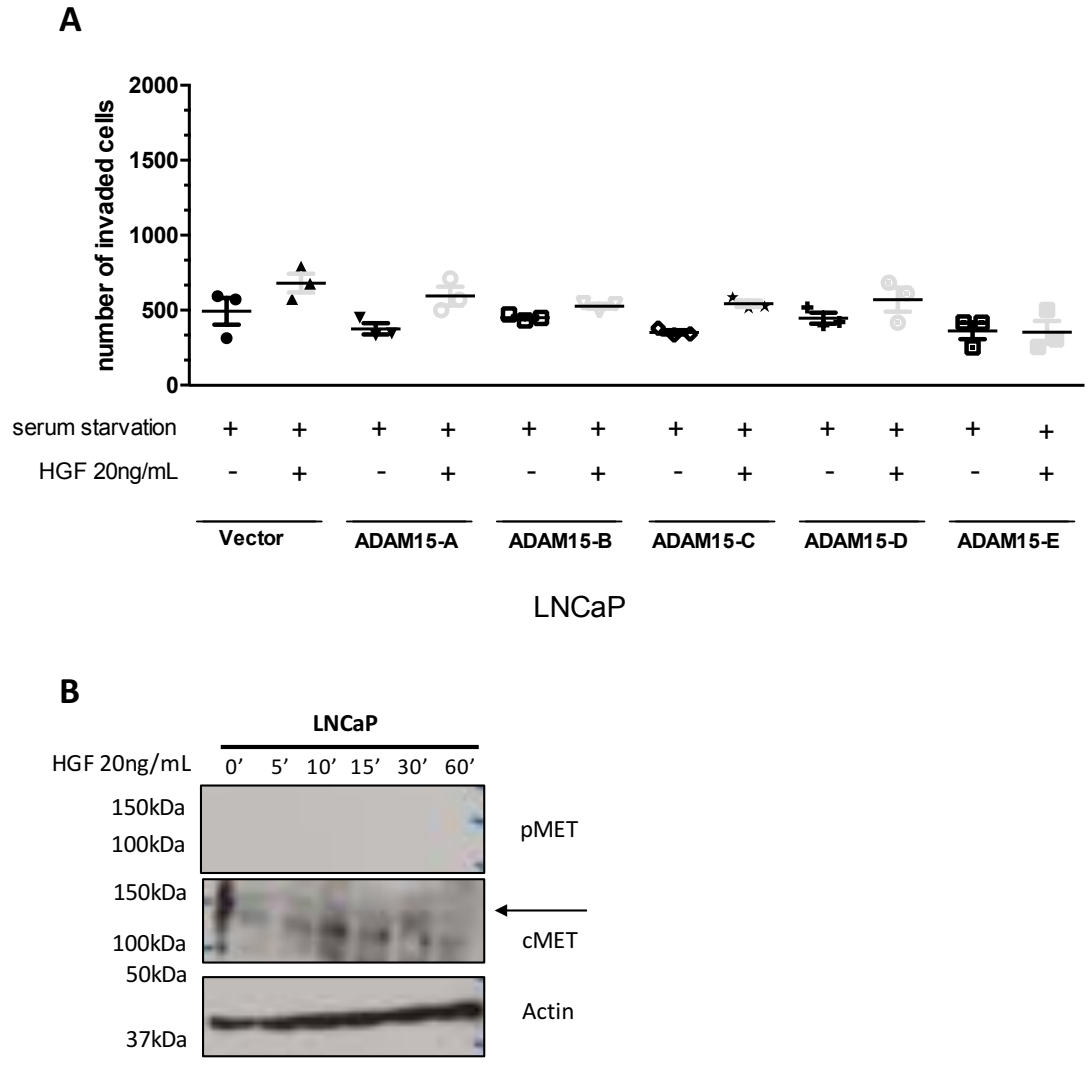

Figure 6.1 HGF treatment does not increase LNCaP ADAM15 A-E cell invasion.

(A)20,000 cells were seeded in invasion chambers, with serum free medium in the top and 20ng/mL HGF (added after O/N incubation) in the bottom chamber as chemoattractant. As invasion control, for each splice variant cells were seeded in an invasion chamber without HGF in the bottom chamber (serum starvation). Cell were incubated for 24h, fixed, stained and analyzed. No difference in cell invasion was found. Statistical analysis was performed by One-WAY-Anova, using Graph Pad Prism. The experiment was performed with n=3. Error bars are shown as Mean + SEM, * $p<0.05$; ** $p<0.01$; *** $p<0.001$, **** $p<0.0005$. (B) Western blotting results for HGF time course in LNCaP, using pMET and cMET specific antibodies. Actin was used as loading control. cMET time dependent phosphorylation was not detectable in LNCaP.

6.3.2 ADAM15-A overexpression promotes HGF dependent invasion in PC3

Previously we showed, that ADAM15-A overexpression led to a 2-fold increase in PC3 cell invasion in a proteolytically dependent manner (Chapter 3 Figure 4.10). In order to test, whether ADAM15 invasion may be regulated by cMET signalling, invasion assays

were performed in the presence and absence of HGF using the PC3 cell panel expressing ADAM15 A-E and compared to vector control cells.

PC3 vector cells showed a significant increase in invasion in response to HGF treatment. ADAM15-B to D expressing cells showed an increase in number of invading cells, however when compared to the control treatment this was not significant. ADAM15-A expressing cells showed significant increase in cell invasion in non-stimulated and HGF stimulated conditions, when compared to vector HGF control treated cells (Figure 6.2 A). Western blotting results for HGF time response using the PC3 vector expressing cells, revealed increased cMET phosphorylation over time (Figure 6.2 B).

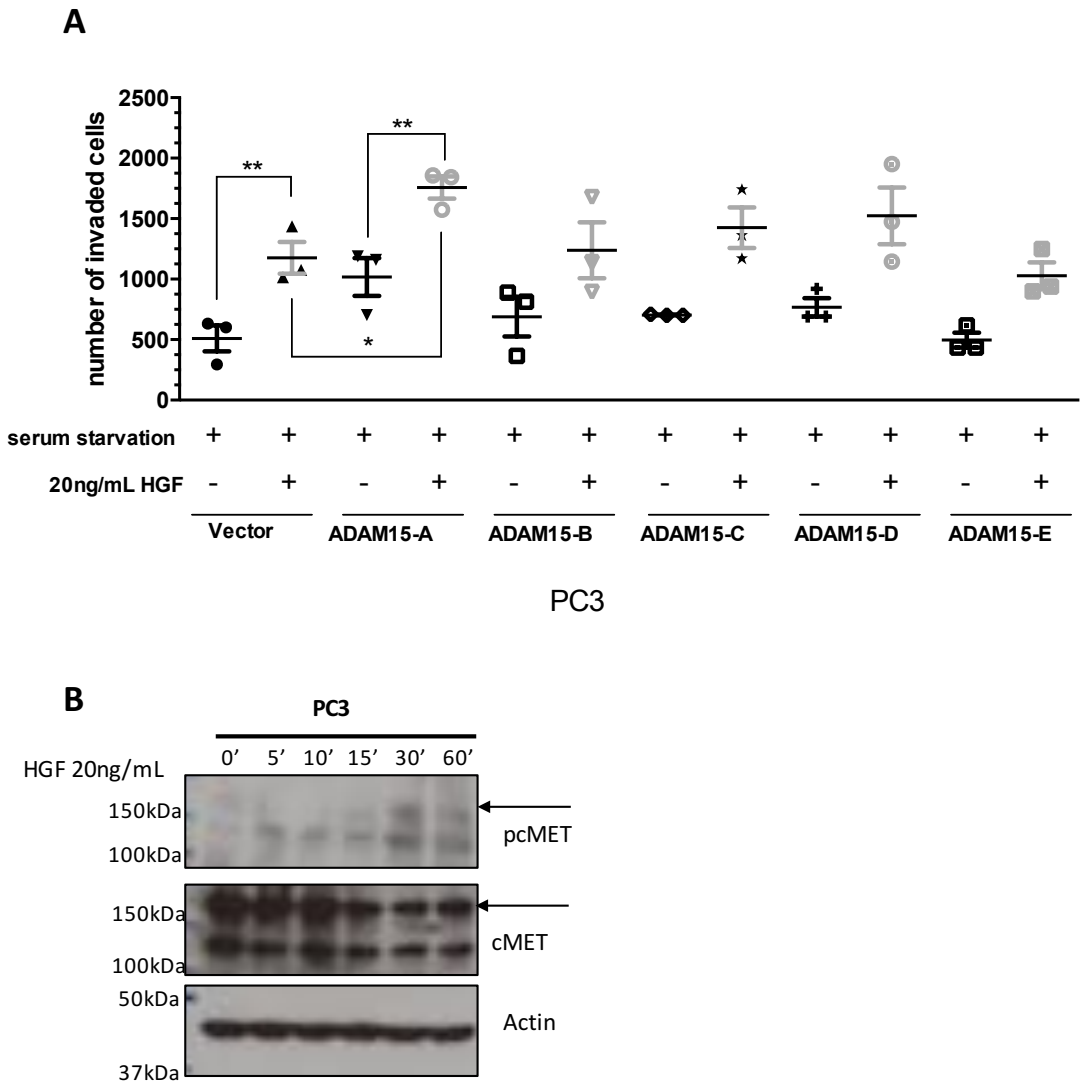

Figure 6.2 ADAM15-A cell invasion is significantly enhanced by HGF

(A) Invasion assays with PC3 ADAM15-A to E were performed as described before. ADAM15-A overexpressing PC3 cells showed a significant increase in cell invasion, in response to HGF treatment, when compared to vector control cells. Statistical analysis was performed by One-WAY-Anova, using Graph Pad Prism. The experiment was performed with n=3. Error bars are shown as Mean $\pm$ SEM, * $p<0.05$; **$p<0.01$; ***$p<0.001$, ****$p<0.0005$. (B) Western blotting results for the treatment HGF treatment time course in PC3, using pMET (black arrow) and cMET specific antibodies (black arrow). Actin was used as loading control. cMET time dependent phosphorylation increased after 30min of HGF treatment.

6.3.3 ADAM15-A HGF dependent invasion is dependent on ADAM15 proteolytic activity

To clarify the HGF dependent increased invasion seen for ADAM15-A overexpressing PC3 cells, we used the ADAM15-A-EA proteolyically inactive mutant overexpressing cells and subsequently analysed their invasion capability with the matrigel invasion

assay. To exclude a splice variant specific HGF dependent effect, EA-mutants were generated for all ADAM15 splice variants, as the HGF dependent invasion results showed trends of increased invasion for all splice variants, however these were only statistically significant for ADAM15-A, when compared to vector control cells.

Figure 6.3. shows that the ADAM15-A-EA mutant cells were significantly less invasive and importantly, HGF treatment failed to induce invasion (Figure 6.3). For ADAM15-B/C/D/E-EA or ADAM15-B/C/D/E-WT no significant results were obtained (Figure 6.3).

The data therefore show that the proteolytic activity of ADAM15A is required to promote PC3 cell invasion under basal and HGF stimulated conditions.

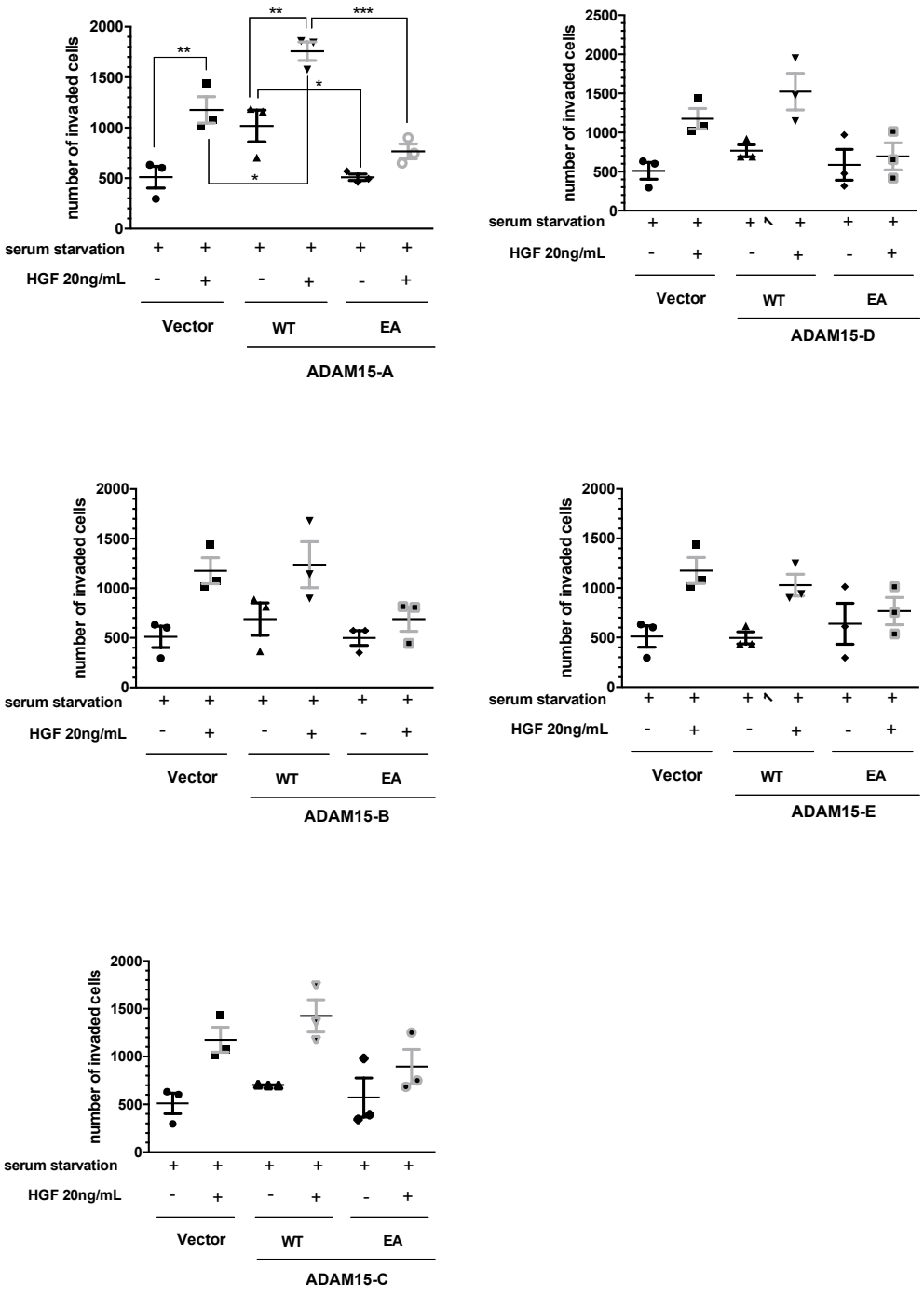

Figure 6.3 Comparison of invasion between active and inactive ADAM15 splice variant expressing PC3 cells.

The PC3 ADAM15 A-E WT and EA mutant panel were used for an invasion assay and incubated with 20ng/mL HGF for 24h in the bottom of the invasion chamber. ADAM15 splice variant A showed a significant enhanced invasion when compared to the vector control cells. Invasion was reduced to vector levels for the EA-mutant, when treated with HGF. All other splice variants, did not show a significant increase in invasion when compared to vector control cells. Statistical analysis was performed by One-WAY-Anova, using Graph Pad Prism. The experiment was performed with n=3. Error bars are shown as Mean ± SEM, * p<0.05; **p<0.01; ***p<0.001, ****p<0.0005.

6.3.4 Differences in the presence of MMPs in the supernatant of ADAM15-WT versus EA-mutant

To assess the differences in invasion seen for the proteolytically active ADAM15 expressing cells when compared to the inactive mutant, gelatinase levels of MMP2 and MMP9 in the supernatant were analysed using zymography.

Medium from the proteolytically active ADAM15-A-WT expressing cells showed increased presence of pro-MMP2 and MMP2 (Figure 6.4 A) at approximately 65kDA, when compared to vector and the EA-mutant, for all three repeats. A corresponding band for MMP9 activity at 100kDa could not be detected, however a band at 150kDa (1, shown with the arrow) was detectable, possibly showing an MMP9 complex or/and ADAM15. Enhanced gelatin degradation in ADAM15-A-WT compared to medium from vector and ADAM15-A-EA expressing cells was detectable also for those bands. ADAM15 is known as gelatinase, as Martin *et al.* described[153], however, as vector control and EA-mutant also showed gelatinase activity (Figure 6.4 A), which could be due to the endogenous ADAM15. ADAM15 knock down PC3 cells would be required to confirm our hypothesis, and moreover a control for MMP2 and also MMP9 would be required to confirm their identity. To accurately quantify the differences seen in the zymogram, the total protein amount per lysed dish cell lysates, were used for normalization against the zymogram bands (Figure 6.4 B). Total protein amount ratios were plotted for each cell line, confirming the increase in gelatinase activity of the ADAM15-A-WT cells compared to the vector control and inactive ADAM15-A-EA cells(Figure 6.4 B,C). For the pro-MMP2 band a significant increase for ADAM15-A-WT cells was determined, when compared to vector control and proteolytic inactive ADAM15-A-EA mutant cells (Figure 6.4 C).

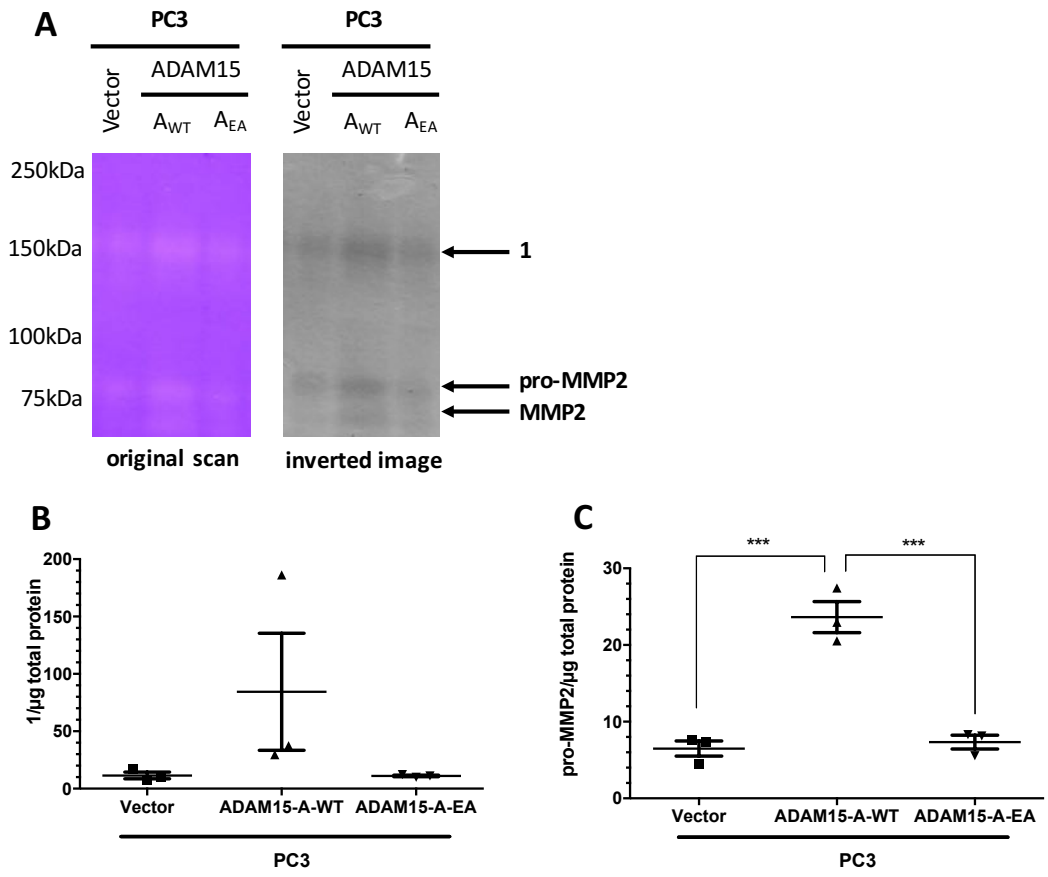

Figure 6.4 MMP levels in supernatants of proteolytically active and inactive ADAM15.

A zymogram was used to assess differences of MMP levels in conditioned medium. Supernatants of ADAM15-A-WT, inactive ADAM15-A-EA mutant and vector control PC3 cells were run on a 6% SDS-PAGE gel containing 100µg/mL gelatin. The gel was incubated in 0.05M Tris-HCl supplemented with 5mM $CaCl_2$ O/N at 4ºC, followed by 2h staining in Coomassie brilliant blue. (A) Enhanced gelatin degradation (white bands) was seen for ADAM15A-WT when compared to vector control and ADAM15A-EA, for the corresponding MW of pro-MMP2 and MMP2 at approximately 68kDa. Bands 1 at (150kDa), might correspond to a complex of ADAM15 and MMP9. (B,C) Quantification of zymogram bands was performed using the inverted image and Image J. Bands were normalized against the total protein amount per lysed dish. The ratios are plotted for each cell line for band 1(B) and the pro-MMP2 band (C). Error bars show Mean ±SEM, * p<0.05; **p<0.01; ***p<0.001, ****p<0.0005.

6.3.5 cMET inhibition reverses ADAM15-A dependent increase in invasion

In order to address the question whether the increase in cell invasion seen in PC3 ADAM15-A overexpressing cells requires functional cMET signalling, invasion assays were performed in the presence of the selective cMET tyrosine kinase inhibitor SU11274. Cells were seeded in the inserts on top of martigel, following over night incubation, the cMET inhibitor SU11274 was added for 1h, followed by the addition of HGF in the bottom chamber. The level of invasion was analysed 24h after addition of HGF.

cMET inhibition led to a significant reduction in PC3 ADAM15-A invasion, when compared to HGF alone (Figure 6.5). Further, upon comparison with the vector control, PC3-ADAM15-A dependent invasion was significantly increased for untreated control and HGF treated cells. The cMET inhibition showed similar levels of invading cells in vector control cells, and ADAM15-A cells.

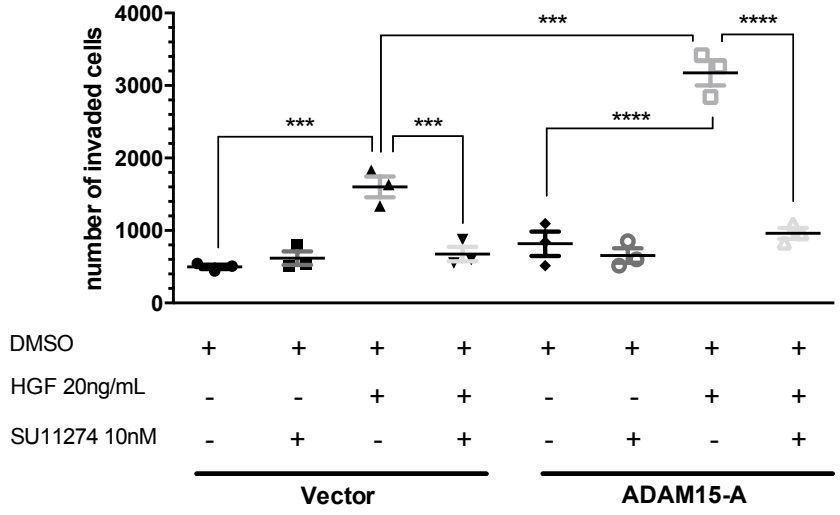

Figure 6.5 PC3 ADAM15-A invasion depends on HGF/cMET signalling.

PC3 ADAM15-A expressing cells and vector control cells were compared in an invasion assay for their HGF/cMET-dependent invasion. HGF was added as chemoattractant to the bottom chamber. 1h before HGF treatment, the selective cMET inhibitor SU11274 was added to the top chamber. Serum starved cells, containing the solvent control, HGF and SU11274 alone were used as control. The ADAM15-A HGF dependent invasion was reduced to background invasion levels with cMET inhibition by SU11274. Statistical analysis was performed by One-WAY-Anova, using Graph Pad Prism. The experiment was performed with n=3. Error bars are shown as Mean $\pm$ SEM, * $p<0.05$; ** $p<0.01$; *** $p<0.001$, **** $p<0.0005$.

6.3.6 Complex formation of ADAM15 and PTK6 is HGF dependent

Unpublished data from our lab suggested that the complex formation between ADAM15 and PTK6 in MDA-MB-231 breast cancer cells was enhanced upon HGF treatment. However, Kinase-assay data showed a high background phosphorylation present in PC3 and no detectable difference with or without HGF treatment (Figure 5.8). Using MDA-MB-231 ADAM15-A and PC3 ADAM15-A expressing cells we tested the hypothesis if the complex formation of ADAM15 and PTK6 can be enhanced using HGF.

In PC3 ADAM15-A expressing cells changes in phosphorylation after HGF treatment were not detectable, when probing total lysate with a 4G10 antibody (pan-phospho tyrosine antibody). Moreover, ADAM15/PTK6 complex formation remained unaffected

after IP with anti-PTK6 (Figure 6.6). However, in MDA-MB-231 ADAM15-A expressing cells, the complex formation between ADAM15 and PTK6 was affected by HGF treatment, as less complex was present in untreated cells, when compared to HGF treated cells, after anti-PTK6 IPs (Figure 6.6).

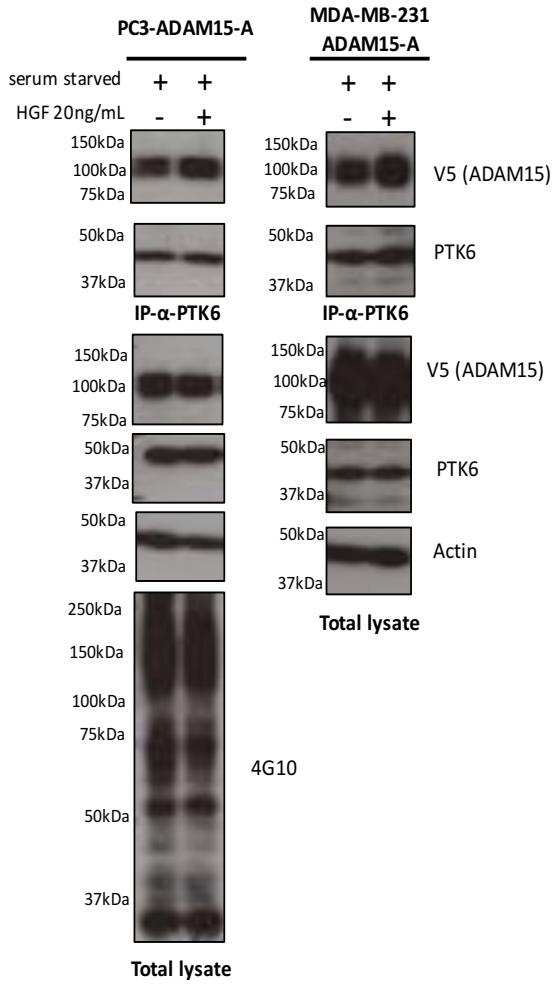

Figure 6.6 ADAM15/PTK6 complex formation in PC3 and MDA-MB-231 cells

PC3 ADAM15-A and MDA-MB-231 ADAM15-A expressing cells were serum starved for 30h followed by treatment with 20ng/mL HGF for 30min. Total cell lysates were used for IPs with anti-PTK6 followed by western blotting. MDA-MB-231 ADAM15-A expressing cells showed more complex formation of ADAM15 and PTK6 upon HGF addition. PC3 ADAM15- A expressing cells showed no enhanced complex formation in presence of HGF.

6.3.7 The interaction of ADAM15 and PTK6 is lost upon cMET inhibition

Although our data showed that HGF did not alter the ADAM15/PTK6 complex formation in PC3 cells, we assessed the hypothesis, whether the complex formation can be decreased when using specific cMET or PTK6 inhibitor. IP experiments were performed using cell lysates from cells treated either with SU11274 or a second selective cMET

inhibitor Capmatinib, which both target the cMET kinase domain. Additionally, the PTK6 inhibitor Tilfrinib was used to confirm that PTK6 activity is not required for the PTK6/ADAM15A complex formation.

Western blotting analysis of total cell lysates using a p-cMET specific antibody raised against the phosphorylated tyrosines at position 1234 and 1235 of the cMET kinase domain, showed that both cMET inhibitors reduced cMET phosphorylation levels compared to the control or the PTK6 inhibitor treatment (Figure 6.7). ADAM15-A, PTK6 and actin levels were consistent and independent of inhibitor treatment (Figure 6.7).

Analysis of PTK6-IPs revealed that cMET inhibition resulted in loss of ADAM15A/PTK6 association (Figure 6.7). The reverse IP performed with anti-V5 confirmed these findings, as ADAM15/PTK6 complexes dissociated when cMET signalling was interrupted due to cMET inhibition.

PTK6 inhibition did not alter ADAM15/PTK6 complex formation as evidenced by both PTK6-IP and V5-IP, confirming that PTK6 activity is not needed for ADAM15/PTK6 complex formation, which we also described previously in Chapter 5.

cMET activity was necessary for the complex formation between PTK6 and ADAM15 splice variants in PC3 cells. cMET inhibition with the selective cMET inhibitor SU11274 (n=2) led to ADAM15/PTK6 complex disruption for all ADAM15 splice variants (Supplementary data Figure 8.13).

To assess, whether the complex disruption of ADAM15 and PTK6 is cell line dependent, the LNCaP ADAM15-A and vector control cells were used, and IP experiments were performed as described before. Upon cMET inhibitor treatments, complex disruption of ADAM15/PTK6 was not seen in LNCaPs (Supplementary data Figure 8.10). Western blotting results which indicated low cMET levels in LNCaPs, and no detectable HGF dependent activation of cMET when probing with p-cMET (Figure 6.1 B), suggesting that the HGF/cMET pathway is not prominent in LNCaP cells.

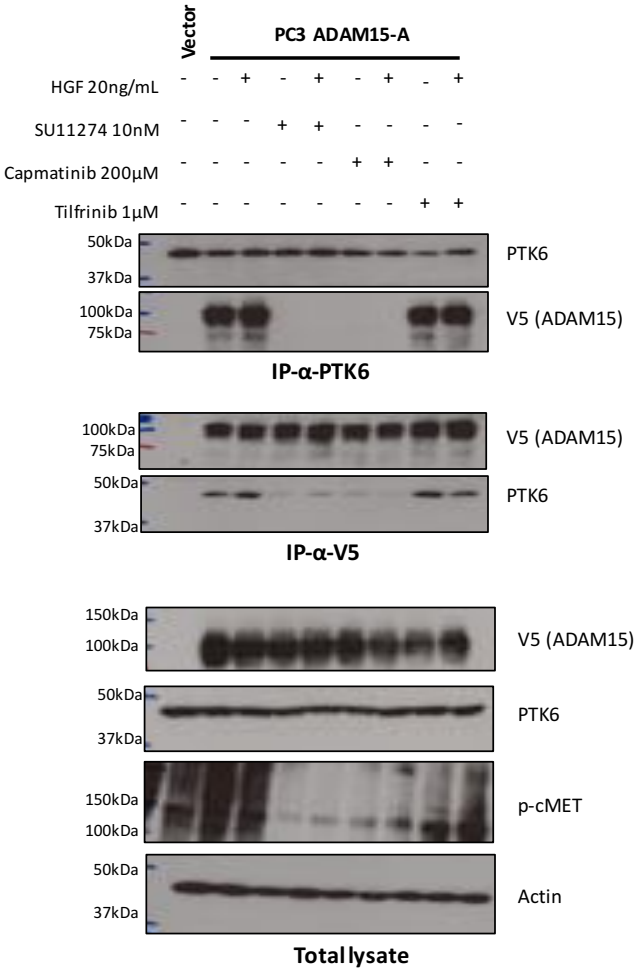

Figure 6.7 Loss of ADAM15/PTK6 interaction upon cMET inhibition.

PC3 ADAM15-A expressing cells were treated with the selective cMET inhibitor SU11274 or Capmatinib, additionally the PTK6 inhibitor Tilfrinib was used. As vehicle control, serum starved PC3 vector and PC3 ADAM15-A cells were used. Lysates were split in two and IPs were performed with either anti-PTK6-rabbit coated Dynabeads or anti-V5-mouse coated agarose resins. IPs and total lysate were analyzed by western blotting and probed for V5(ADAM15), PTK6, p-cMET and actin. Upon cMET treatment with both inhibitors, ADAM15/PTK6 complex formation was lost in PTK6 and V5-IPs when cMET inhibition treatment was applied. Treatment with the PTK6 inhibitor did not change the association between ADAM15 and PTK6. p-cMET detection revealed less phosphorylation present in cMET inhibitor treatments.

6.3.8 Loss of ADAM15/PTK6 complex upon cMET inhibition is dose dependent

To assess whether the loss of the ADAM15/PTK6 complex upon cMET inhibition is dose dependent a dose response with both inhibitors was performed. For this, cells were treated with decreasing doses of SU11274 inhibitor starting from 20nM to 1.25nM and for Capmatinib from 400µM to 25µM. Lysates were processed by performing IPs using anti-PTK6 and analysed by western blotting for ADAM15-A.

IP results revealed decreasing level of complex formation between PTK6 and ADAM15-A as the concentration of the inhibitors increased. The analysis of corresponding total cell lysates confirmed equal levels of ADAM15 and PTK6 throughout the experimental conditions (Figure 6.8 A and B).

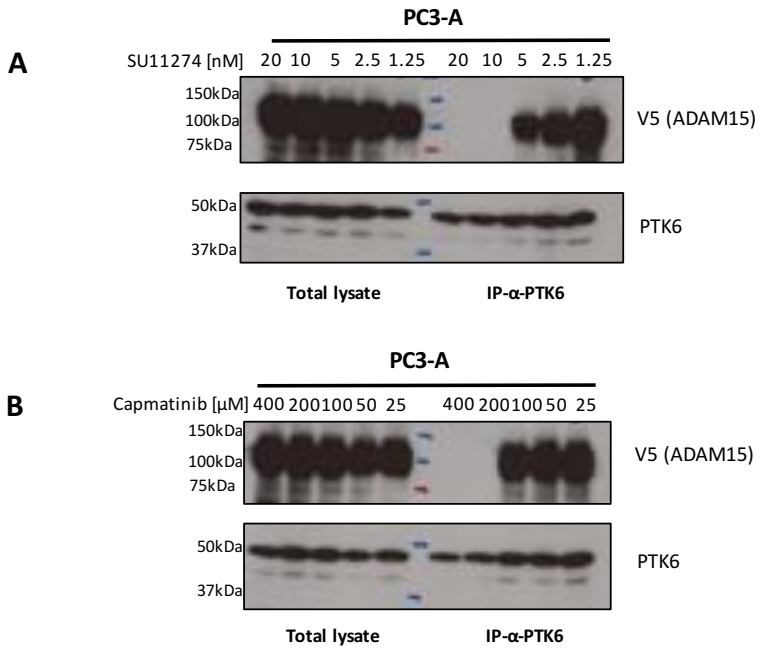

Figure 6.8 cMET inhibitor dose dependent ADAM15/PTK6 complex disruption in PC3 ADAM15-A expressing cells.

PC3 ADAM15-A expressing cells were treated with decreasing doses of SU11274 (A) or Capmatinib (B). Cell lysates were subjected to IP using anti-PTK6, and analysed by western blotting and probing for ADAM15 (V5) and PTK6.

6.3.9 Co-localization of ADAM15 and PTK6 in response to cMET inhibition

As IP analysis revealed loss of the ADAM15/PTK6 complex formation upon cMET inhibition, the co-localization of ADAM15/PTK6 interaction was assessed using confocal microscopy. PC3 ADAM15-A and vector cells, and additionally PC3 shPTK6, as a PTK6 negative control cell line, were seeded on coverslips, and grown for 3 days, prior to immune-histochemical analysis using permeabilizing conditions.

In Chapter 5, we demonstrated that PC3 ADAM15A-E expressing cells showed some co-localization with PTK6. Untreated PC3 ADAM15A cells, did not show a difference in co-localization of PTK6 and ADAM15, when compared to cells treated with HGF. However, cells treated with HGF showed more ADAM15 present at the plasma membrane compared to untreated cells. Upon treatment with the cMET inhibitors SU11274 and Capmatinib, ADAM15 staining was seen predominantly inside the cytoplasm and around the nucleus. For Capmatinib treatment, ADAM15 membrane

staining was detectable. PTK6 staining appeared distinctly weaker when compared to the untreated control. PTK6 staining was present in the plasma membrane and the cytoplasm, while cMET inhibitor treated PC3 cells showed PTK6 staining only in the cytoplasm. A clear co-localization as seen before for untreated and HGF treated PC3 cells was not detectable, which might be also because of the weak PTK6 staining. PTK6 inhibition by Tilfrinib on the other hand, showed a similar staining for the inhibitor alone or the combination with HGF, as seen for the untreated ADAM15-A and HGF treated cells. (Figure 6.9). Areas of co-localization for ADAM15A and PTK6 are indicated with white arrows.

PTK6 was localized within the cytoplasm and the plasma membrane in vector control and ADAM15A expressing cells. PC3 shPTK6 cells showed weak staining for PTK6 inside the cytoplasm but not at the plasma membrane. Overall, shPTK6 cells showed a much weaker staining, confirming antibody specificity. ADAM15, detected via V5, was seen for all cells with exception of the vector control and PC3 shPTK6, around the nucleus and at the plasma membrane (Figure 6.9).

To exclude that the weaker staining, seen for PC3 ADADM15A expressing cells, related to the cMET inhibitor treatment was due to degradation of PTK6 or cMET, protein and cDNA levels were assessed, without any detectable changes in either cDNA or protein expression level (Supplementary data Figure 8.11 Figure 8.12).

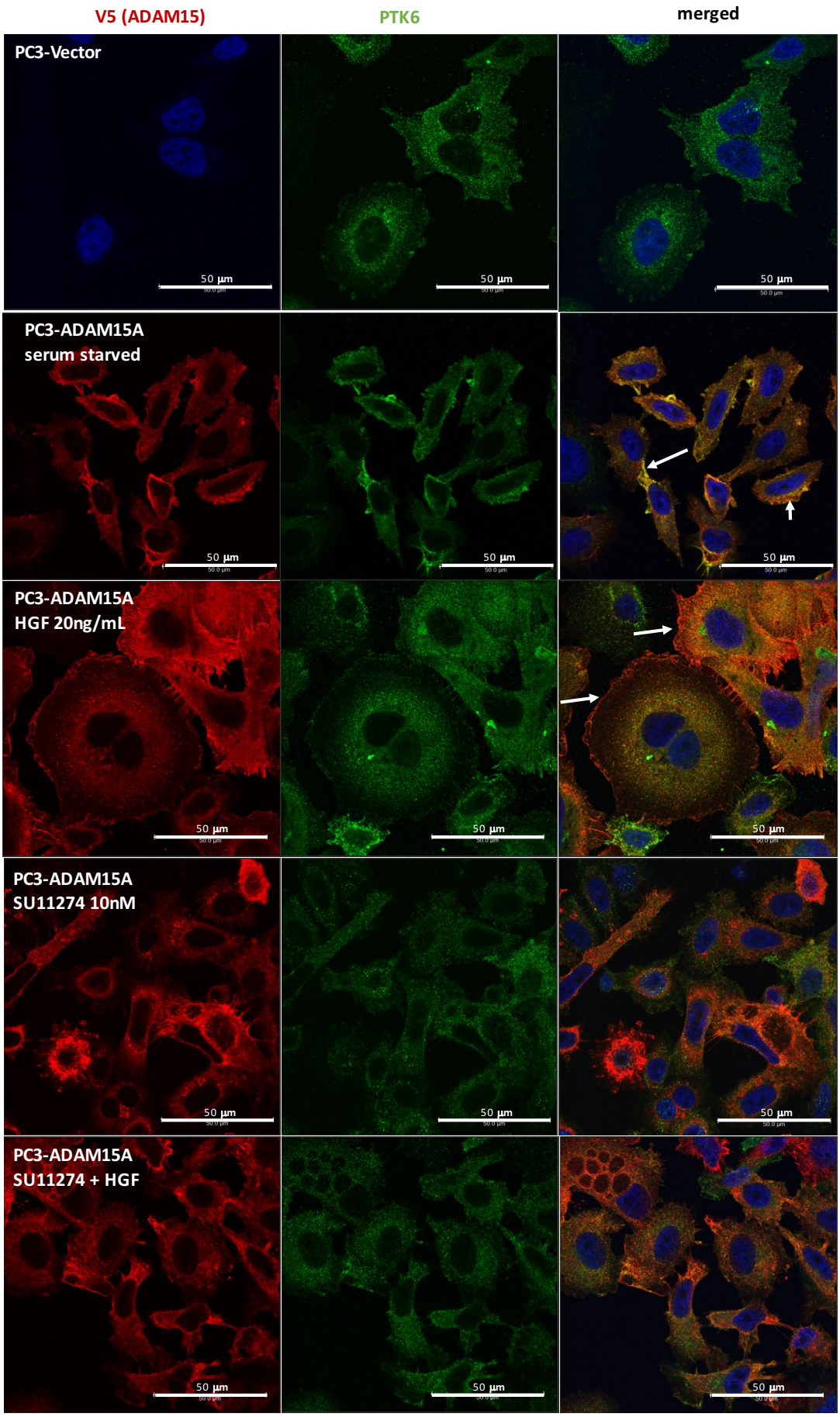
V5 (ADAM15)
PTK6
merged
PC3-Vector
PC3-ADAM15A
serum starved
PC3-ADAM15A
HGF 20ng/mL
PC3-ADAM15A
SU11274 10nM
PC3-ADAM15A
SU11274 + HGF
50 µm

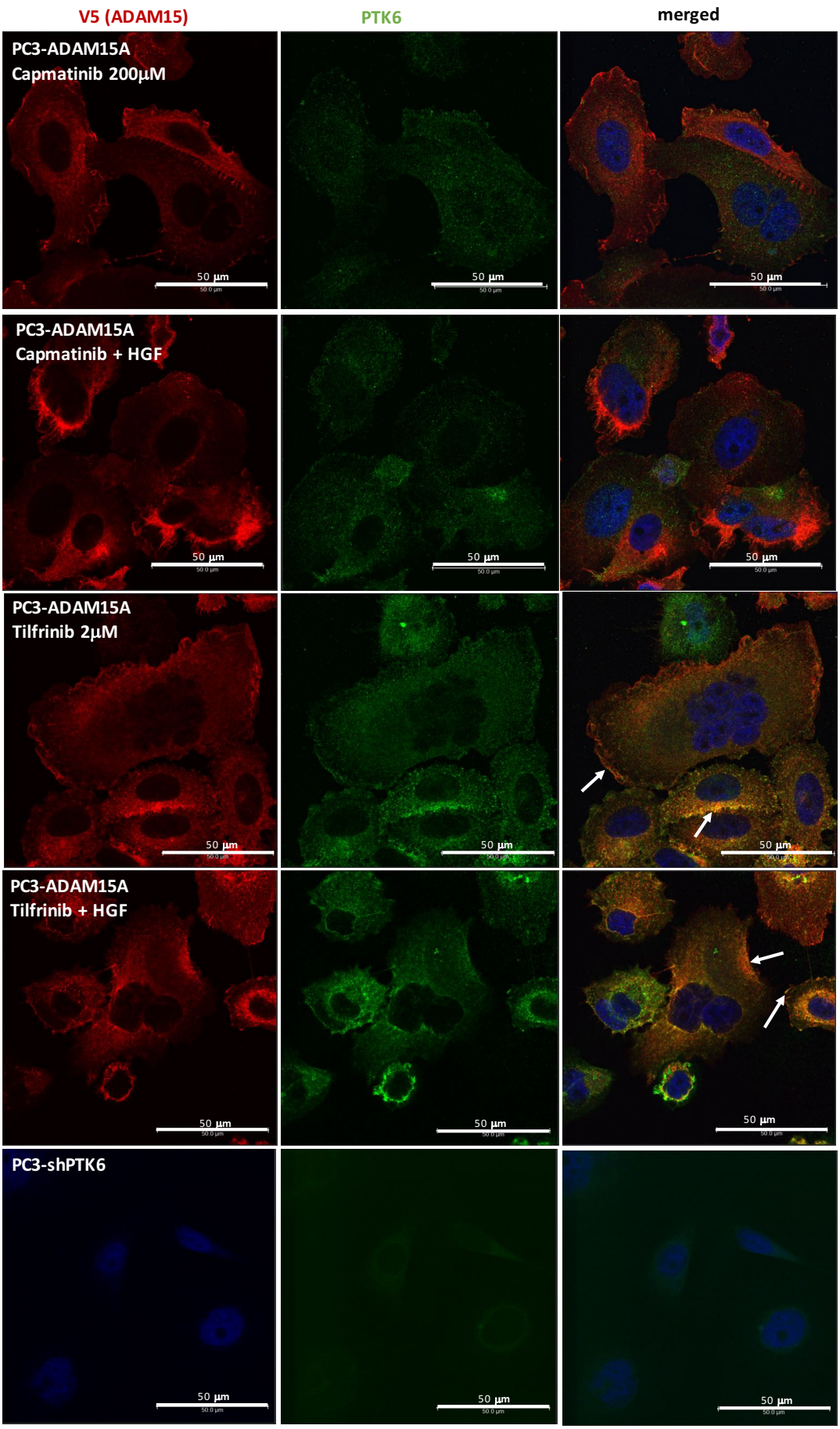
V5 (ADAM15)
PTK6
merged
PC3-ADAM15A
Capmatinib 200µM
PC3-ADAM15A
Capmatinib + HGF
PC3-ADAM15A
Tilfrinib 2µM
PC3-ADAM15A
Tilfrinib + HGF
PC3-shPTK6
50 µm

Figure 6.9 Co-localization of ADAM15/PTK6 after cMET inhibitor treatments in PC3.

PC3 ADAM15-A, vector control cells and shPTK6 antibody control cells were grown for 3 days on coverslips. Permeabilizing conditions were applied, and anti-PTK6 conjugated to AlexFlour-488nm and anti-V5 conjugated to AlexaFlour-568nm were used to analyze cells after treatment with cMET or PTK6 inhibitors using confocal microscopy. Co-localization for ADAM15 and PTK6 was detectable in serum starved control and HGF treated PC3 ADAM15A cells (white arrows). Tilfrinib treatment in presence or absence of HGF showed co-localization for ADMA15 and PTK6 (white arrows). In cMET inhibitor treatments, in presence or absence of HGF, PTK6 staining was indistinct and co-localization for ADAM15 and PTK6 could not be detected. Vector control cells were clear for ADAM15-V5 staining. shPTK6 cells showed reduced PTK6 staining suggesting antibody specificity.

6.3.10 Complex formation of ADAM15, and PTK6 and the adaptor protein Grb2

In order to determine whether the cMET signalling dependent interaction of ADAM15 and PTK6 required the ADAM15 and cMET adaptor protein Grb2, additional IP experiments were performed using a Grb2 antibody. This multi-protein complex formation would be possible via Grb2, which directly associates with ADAM15 via its SH3 domains, and via its SH2 domains either directly to p-cMET or to Gab1, which is bound to cMET.

In the first instance, IP analysis was performed with anti-Grb2 antibodies from PC3 ADAM15-A total cell lysates treated with HGF in the presence or absence of cMET inhibitors (Figure 6.10). As expected, ADAM15 was present in Grb2-IPs in all conditions, confirming its constitutive association with Grb2 (Figure 6.10). However, cMET and PTK6 were only present in Grb2 IPs in non-treated or HGF alone treated conditions. cMET inhibition resulted in a complete loss of cMET and PTK6 from Grb2 IPs. Treatment with the PTK6 inhibitor Tilfrinib showed presence of PTK6, ADAM15, and interestingly also cMET in the Grb2 IPs (Figure 6.10).

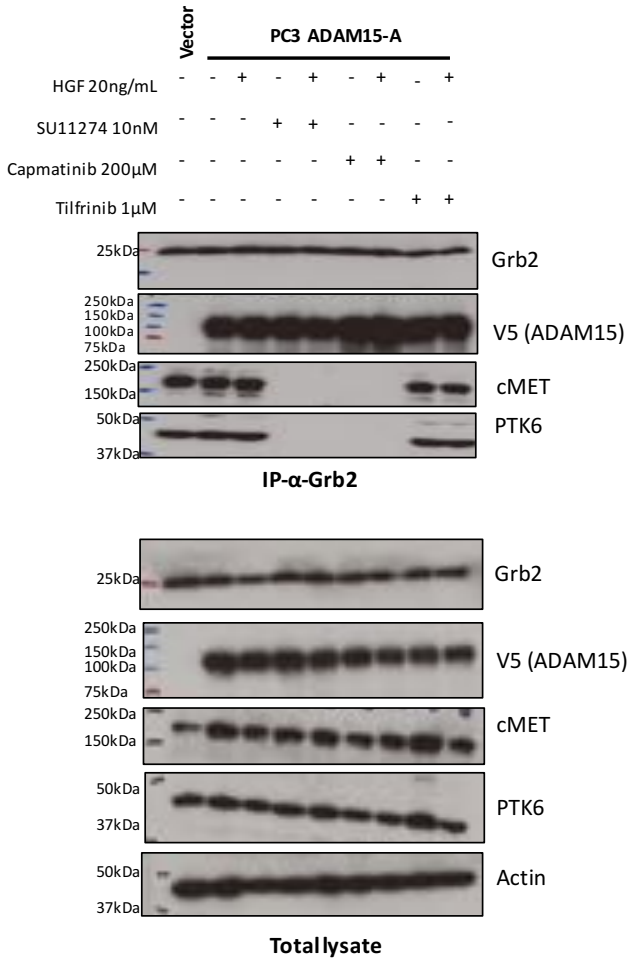

Figure 6.10 cMET activity is necessary for a multi-protein complex assembly containing ADAM15 and PTK6.

PC3 ADAM15A and vector control expressing cells were treated with cMET inhibitors SU11274 and Capmatinib, and the PTK6 inhibitor Tilfrinib. Grb2 was immunoprecipitated from PC3 cell lysates, followed by probing for ADAM15, Grb2, cMET and PTK6. Grb2-IPs showed the presence of ADAM15 regardless of any treatment, however cMET and PTK6 complexes were lost when cells were treated with both cMET inhibitors.

6.3.11 ADAM15 is in a complex with cMET

Additionally, to confirm the cMET-dependent complex formation, IP experiments were performed using a cMET antibody. Precipitates were then analysed for ADAM15, PTK6, Grb2 and the cMET adaptor protein Gab1.

Western blotting analysis of total lysates confirmed the presence of all proteins in the starting lysates (Figure 6.11). The cMET-IP contained Gab1 in untreated vector control cells. In ADAM15A expressing cells independent of HGF treatment, ADAM15, Gab1, Grb2, PTK6 and cMET were present. cMET inhibition led to the loss of Gab1, Grb2,

PTK6 and ADAM15 in the cMet-IP, suggesting that complex formation might require functional cMET signalling (Figure 6.11). Tilfrinib treatment did not influence the composition of the ADAM15-A multiprotein complex that we have shown here (Figure 6.11).

Probing cMET IPs with a p-cMET antibody specific for the phospho-tyrosine's 1234 and 1235 of the cMET kinase domain, did not give conclusive results (Supplementary data Figure 8.14).

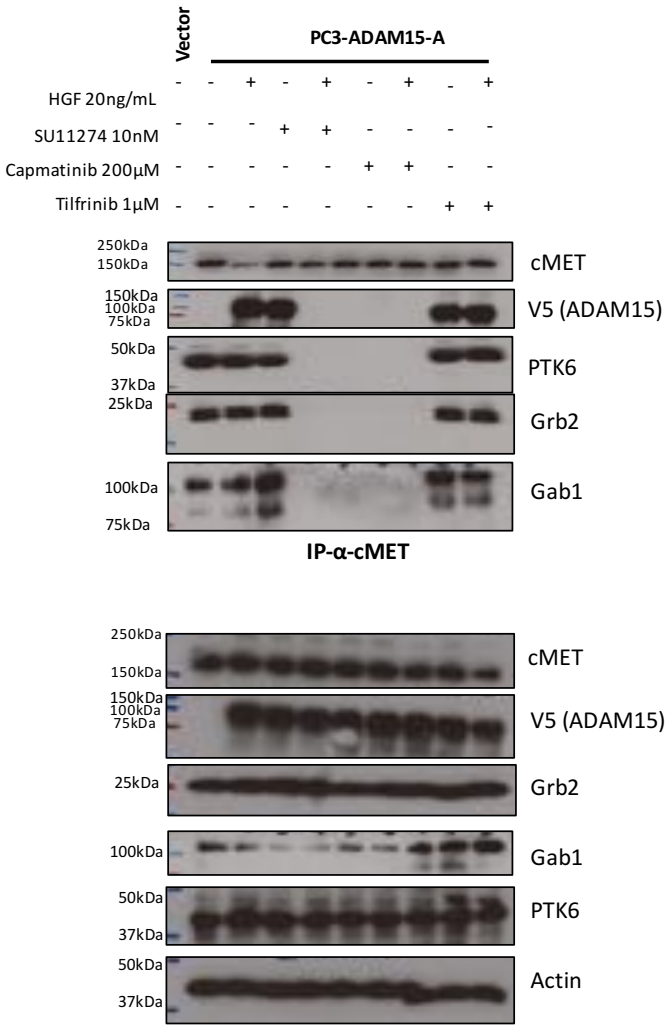

Figure 6.11 Loss of cMET interaction with ADAM15-A upon cMET inhibitor treatment.

Lysates of PC3 ADAM15A expressing cells and vector control cells were treated with the cMET kinase inhibitors SU11274 and Capmatinib and the PTK6 inhibitor Tilfrinib, and analysed by IP with a cMET specific antibody. cMET inhibitor treatment revealed the loss of interaction of ADAM15, PTK6, Grb2 and Gab1. Treatment with the PTK6 inhibitor did not influence the complex formation.

6.3.12 ADAM15/PTK6 complex disruption in MDA-MB-231 breast cancer cells

To assess whether the complex disruption of ADAM15/PTK6 is cell line and cell type independent, we evaluated the ADAM15/PTK6 complex formation and disruption via cMET inhibition in MDA-MB-231 breast cancer cells, stably overexpressing ADAM15-A.

In Chapter 5 we showed that ADAM15-A was found in a complex with PTK6 in MDA-MB-231 breast cancer cells, in 6.3.6 we showed that the complex formation in MDA-MB-231 cells is affected in the presence of HGF. Now, when applying the cMET inhibitors the complex formation between ADAM15 and PTK6 was lost in IPs with cMET, Grb2 and PTK6 (Figure 6.12). PTK6 inhibition did not lead to complex disruption in those performed IPs. As seen before in PC3 ADAM15-A cells, Grb2 remained in a complex with ADAM15. Increased complex formation of ADAM15 and PTK6 was observed for anti-PTK6-IPs in presence of HGF.

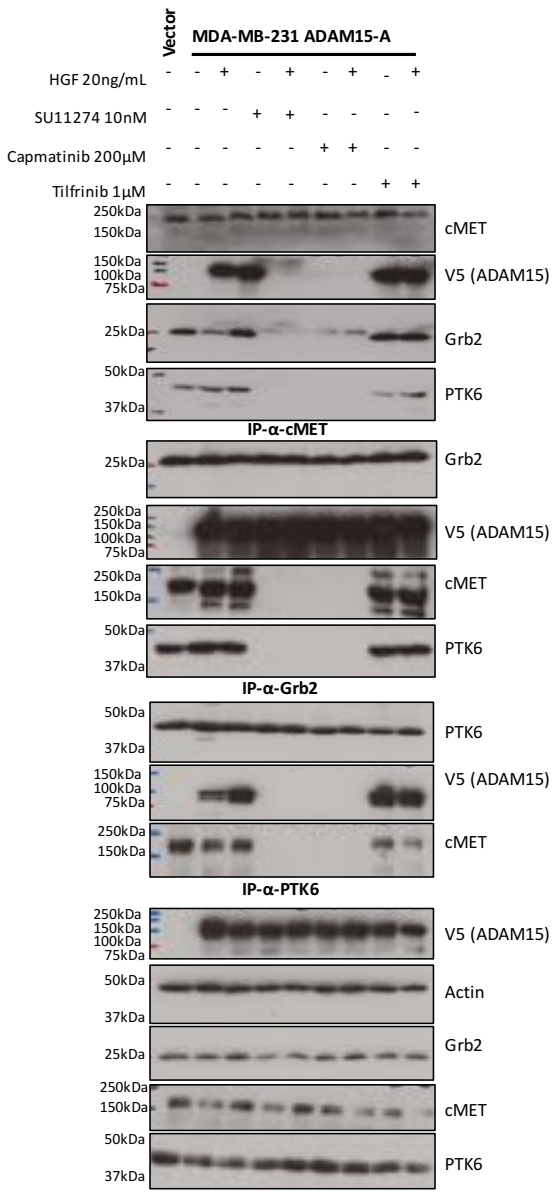

Figure 6.12 cMET/ADAM15 signal complex disruption in MDA-MB-231 ADAM15-A breast cancer cell line.

MDA-MB-231 ADAM15-A expressing cells were treated with the selective cMET inhibitor SU11274 or Capmatinib, additionally the PTK6 inhibitor Tilfrinib was used. As vehicle control, serum starved MDA-MB-231 vector and MDA-MB-231 ADAM15-A cells were used. Lysates were split in three and IPs were performed with either PTK6-rabbit, or cMET-mouse, or Grb2-goat coated Dynabeads. IPs and total lysate were analysed by western blotting and probed for V5(ADAM15), PTK6, cMET, Grb2 and actin. Upon cMET treatment with both inhibitors, a loss of cMET/ADAM15/Grb2/PTK6 interaction was found for performed IPs, as found in PC3s. Treatment with the PTK6 inhibitor did not change the association between ADAM15 and PTK6.

6.4 Discussion

In this chapter we describe for the first time, that ADAM15-A is found in a complex with cMET and the adaptor protein Grb2. We showed, that ADAM15-A invasion is significantly enhanced upon HGF treatment, and invasion can be set back to background levels when using the cMET inhibitor SU11274. Moreover, we identified that the proteolytic activity of ADAM15 led to enhanced presence of MMP2 in cell supernatants.

Upon HGF binding to cMET, dimerization and autotransphosphorylation of cMET is induced, leading to recruitment of proteins such as Grb2, Gab1, STAT3 or PI3K, initiating downstream signalling promoting invasion, migration, cell cycle progression, and upregulation of MMPs[199,202].

In the previous Chapter 4, we showed that PC3 ADAM15-A overexpressing cells displayed a 2-fold increase in number of invading cells, compared to the vector control cells, when incubated in 10% serum. Herein we show that PC3 ADAM15-A invasion was significantly induced by the cMET ligand HGF. Further HGF also induced invasion of vector control cells significantly, which might be due to the endogenous ADAM15 present in those cells. However, the PC3 ADAM15-A overexpressing cells still show significantly enhanced invasion in response to HGF treatment when compared to the vector control cells. In addition, all splice variants were tested, however invasion was not significantly different when compared to vector control. Han *et al.* identified a time and dose dependent reversal of EMT upon knock down of cMET by siRNA in PC3 cells. In a separate experiment, they showed, that reduction of E-cadherin, and increase of vimentin, decreased invasion of PC3 siRNA cells, compared to vector control[308]. Further, in those cells, phosphorylation of Erk was enhanced upon HGF stimulation when compared to cMET knock down PC3s, suggesting an important role in Erk signalling in PC3 EMT and invasion[308]. ADAM15 is endogenously expressed in PC3 cells and knock down of ADAM15 in those cells significantly reduced cell invasion[105] suggesting an ADAM15-A dependent effect on HGF induced invasion via Erk signalling.

Using inactive ADAM15-A-EA mutants in an invasion assay, using 10% serum as chemoattractant, in Chapter 4, we showed, that ADAM15 invasion was reset to serum starved invasion levels of PC3 cells. The proteolytically inactive EA-mutants showed reduced invasion for all splice variants upon HGF stimulation, and also compared to vector control. As Dong *et al*. identified an ADAM15 dependent effect on MMP9 activity, leading to enhanced invasion in A549 lung cancer cells[157], differences in MMP2 or MMP9 levels between ADAM15A-WT or ADAM15A-EA expressing cells were assessed by zymography. This revealed increased MMP2 levels in the WT compared to EA and

vector control PC3 cell medium. MMP2 is overexpressed in aggressive prostate cancer and was linked to disease relapse and Gleason score[309]. MMP levels may drive ADAM15-A invasion, however we need to include valid controls for MMP2 and MMP9 to confirm their identity. The LNCaP cell panel, lacked HGF induced invasion, which corresponds with literature findings by Han *et al.*, showing that overexpression of cMET in LNCaPs was required for HGF induced invasion[300].

In ovarian carcinoma cell lines, Koon *et al.* showed that upon treatment with the cMET inhibitor SU11274, cMET activation was abolished, indicating phosphorylation-dependent inhibition of cMET. Further, they showed that HGF dependent cell motility and invasion was significantly reduced upon SU11274 treatment after 24h[310]. Our results are consistent with the findings of Koon *et al.*. When treating the PC3 ADAM15-A expressing cells in an invasion assay with a combination of HGF and the selective cMET inhibitor SU11274, invasion was kept at untreated invasion levels, which shows that we block the cMET dependent invasion by using a specific cMET inhibitor. As future experiment, we could test the hypothesis that changes in the presence of cMET itself might influence the invasion in PC3 expressing ADAM15. For this, changes in total cMET and ADAM10 lysate levels between ADAM15-A-WT and inactive ADAM15-A-EA mutants could be assessed. ADAM10 was identified as a cMET sheddase by Schelter *et al.*[305], as knock down or ADAM10 inhibition led to enhanced presence of cMET at the plasma membrane. PC3 cells express endogenous ADAM10[311,312] and ADAM15, and since ADAM15 sheds ADAM10 ECD[161] and ADAM10 can cleave cMET, overexpression of ADAM15 might induce enhanced ADAM10 cleavage resulting in higher cMET levels thereby allowing enhanced signalling via the cMET/HGF axis. To test this hypothesis, we would assess soluble cMET decoy levels could be assessed in supernatants of ADAM15-A-WT or EA, which might provide evidence for a role of ADAM10 in PC3 ADAM15-A-EA reduced invasion.

The functional consequence of HGF stimulation and cMET inhibition was enhanced and decreased invasion, respectively, for the PC3 ADAM15-A overexpressing cells. To elucidate the mechanistic pathway, IPs were performed initially using anti-PTK6 and anti-V5 to assess the ADAM15/PTK6 association. In IPs, with PTK6 or V5 (ADAM15), of PC3-ADAM15-A cells treated with the cMET inhibitors SU11274 and Capmatinib. ADAM15/PTK6 interaction was lost upon cMET inhibitor treatments, but not upon PTK6 inhibition with Tilfrinib. Koon *et al.*[310], showed inhibition of cMET activity upon SU11274 treatment, which was confirmed in our study. Probing total lysate of treated cells with phospho cMET specific antibody, showed reduced phosphorylation when treated with cMET inhibitor, but not when treated with Tilfrinib as expected. Assessing the co-

localization of ADAM15/PTK6 interaction upon cMET inhibitor treatment by confocal microscopy gave unclear results, as PTK6 staining remained indistinct and weaker upon inhibitor treatment. As we showed in Chapter 5 that ADAM15 dimerizes, endogenous ADAM15 knock down PC3 cells are required, to get clearer results. This will reduce background association levels between endogenous ADAM15 and the exogenous ADAM15-V5. Endogenous ADAM15 may also lead to PTK6 membrane association, thus making it difficult to assess any changes due to ADAM15-V5 overexpression. Importantly though, we found no changes in PTK6 and cMET protein expression, irrespectively of PTK6 or cMET inhibitor treatment.

In Chapter 5, we showed the complex formation between ADAM15 splice variants and PTK6 in the prostate cancer cell lines PC3 and LNCaP, and additionally in the MDA-MB-231 breast cancer cells expressing ADAM15-A. We could further show in this chapter that HGF treatment did not enhance ADAM15/PTK6 complex formation, as high background phosphorylation levels are present in those cells (Figure 5.8), suggesting that cMET is already active as also reported by Dai *et al.*[231]. Here we uncovered, that cMET activity is necessary for complex formation between ADAM15 and PTK6 in aggressive PC3 cells, but not in hormone-dependent LNCaP cells. Additionally, we revealed the formation of a multiprotein complex containing cMET, ADAM15, PTK6 and the adaptor protein Grb2. We showed that in PC3 cells the complex between ADAM15, PTK6 and cMET exists without further cMET activation by HGF, which might be explained by high expression levels of cMET in PC3[231]. However, upon cMET inhibition, the complex dissociates. We were able to demonstrate that upon cMET inhibition, only the interaction between ADAM15 and Grb2 remained, while the remaining complex dissociated. To further elucidate whether cMET activation is needed for this complex formation, we repeated the analysis in MDA-MB-231 breast cancer cells overexpressing ADAM15- A. As seen before for PC3 cells, ADAM15/PTK6/cMET complex formation could be disrupted upon cMET inhibition, and Grb2 remained attached to ADAM15 independent of any treatment. More importantly, in these cells HGF mediated activation of cMET and enhanced complex formation of ADAM15 and PTK6.

Although we showed that Grb2 was also found in the ADAM15/PTK6 complex, the loss of the ADAM15/PTK6 complex required further elucidation, as we could show the loss of Gab1 in PC3-ADAM15-A cMET-IPs. Grb2 can bind to cMET either directly via the C-terminal docking site or indirectly via interaction with Gab1[199]. Gab1 associates with cMET via its multi protein binding site (MBS) identified by Weidner *et al.*[313], and once associated with cMET, offers binding sites for proteins such as Grb2, Shp, Src or PI3K,

some of which also interact with ADAM15[145,202]. Performing cMET IPs following cMET and PTK6 inhibitor treatment, revealed the loss of the interaction with Grb2 and the adaptor protein Gab1. In contrast, complexes remained intact in the presence of the PTK6 inhibitor. Loss of Gab1 might explain the decreased invasion seen for ADAM15-A expressing PC3 cells upon inhibitor treatment, as Seiden-Long *et al*. found that loss of Gab1/cMET in DLD-1 human colorectal cancer cell lines, reduced invasion, however, loss of Grb2 did not lead to reduced invasion[314]. Gab1$^{-/-}$ mice showed a delayed invasion and migration of myogenic precursor cells into the limbs[207]. In addition to that, Wang *et al.* showed that treatment of A549 cells with SU11274 leads to decrease in Gab1 phosphorylation, which not only affects Gab1 binding to cMET but further inhibits the signal transduction of cMET via Gab1[307]. As our findings suggest that ADAM15/PTK6/Grb2 complex formation with cMET might be also inhibited by reduced association of Gab1, and Gab1 is also lost upon cMET inhibitor treatment, anti-Gab1 IPs and Gab1 phosphorylation assessments are necessary, to further characterise the ADAM15/PTK6/cMET complex.

In summary, we could confirm that ADAM15-A is found in a complex with cMET and that this complex formation is dependent on cMET kinase activity. The cMET adaptor protein Gbr2 was constitutively bound to ADAM15, independent of cMET kinase activity. However, PTK6 and Gab1 were lost upon cMET kinase inhibition. Using invasion assays we could confirm that the cMET ligand HGF could induce a significant enhancement of cell invasion in PC3 ADAM15-A expressing cells which was dependent of ADAM15s catalytic function. Further this invasion was set to control levels using a specific cMET inhibitor. Assessment of cell supernatants showed presence of different MMP levels in ADAM15-WT or catalytic inactive mutant. With this results we would now aim to elucidate the complex formation of ADAM15 and cMET. For this we would generate Grb2 knock-out PC3 cells to identify the role of Grb2 in this complex. Further we would also assess the role of Gab1, in a first step we would perform IPs with Gab1 to identify a complex formation loss upon inhibitor treatment. In a second step we would generate a PC3 Gab1 knock-out cell line and assess the complex formation. As results for LNCaP cells showed that the complex formation was not disrupted, we would aim to overexpress cMET in those cells to identify if overexpression of cMET might lead to loss of complex formation upon inhibition of cMET. To elucidate the differences in MMP levels, we would include controls for MMP9 and MMP2. This would enable us to assess the differences seen for ADAM15-WT and the catalytic inactive ADAM15-EA mutant.

7 Discussion and Conclusions

7.1 Discussion, future perspectives

ADAM15 is reported to contribute to cancer progression and disease aggressiveness. Via its metalloproteinase function, ADAM15 is involved in disruption of cell-cell attachment[105], shedding of membrane-attached growth factors[158,159] or disruption of cell-ECM interactions[105] in various cancer types, such as breast[81], lung[157] or prostate cancer[105]. Functional consequences that could be related to a specific ADAM15 splice variant, A or B, were identified as enhanced invasion, migration, cell adhesion and attachment [81,100,105,157].

In this work, we established and validated a qPCR method to analyse the ADAM15 splice profile in PCa patients. With 83 patient samples (n=83), the analysis of the ADAM15 splice profile was successful, and when correlating it to healthy tissue (n=8) we found significantly enhanced ADAM15 expression. Overall, ADAM15-A and C variants were the most abundant and ADAM15-A showed the highest increase in expression. Burdelski *et al.* showed that a small subpopulation with aggressive prostate cancer, 3% of 9826 PCa samples, had high ADAM15 expression, and this was linked to high Gleason score and tumour grade[132]. We confirmed findings of Burdelski *et al.* that ADAM15 expression in healthy tissue is negative[132].

To validate the impact of ADAM15 splice variant expression in PCa, a larger sample cohort with defined clinical characteristics is required. To assess whether ADAM15-A expression correlates with high Gleason score and tumour grade, a large number of patients – not available for this study - with high Gleason score and tumour grade, and with a metastatic score of 1 and a nodal score of 1, as well as benign hyperplasia samples, should be investigated. By including patients who show metastasis and those with lymph node metastasis, we would be able to correlate patient data with disease outcome and relapse-free survival. To improve statistical power, we would need to include at least 1000 patients in this follow up study, and include clinical data, such as disease onset, relapse, and survival analysis. With this data, we could conduct Kaplan Maier plots and correlate the patient course of disease with ADAM15 splice variant expression. Currently our study focused on RNA samples isolated from PCa tumour samples, however as next step, we could also aim to include serum or plasma samples for those patients, to assess vesicle-ADAM15 levels in PCa patient serum and plasma, as ADAM15 is released into exosomes by macrophages[315]. Lee *et al.* showed that the presence of ADAM15-exosomes reduced tumour invasion and migration. We would aim to analyse the ADAM15 splice profile of those exosomes present in patient serum or

plasma, and correlate this to disease outcome and relapse-free survival. However, appropriate splice variant specific antibodies are currently lacking for this analysis.

As the *in-vitro* data show that disease aggressiveness is linked to the cMET pathway in prostate cancer[300], we could also assess cMET in our patient cohort by qPCR analysis. We could then correlate cMET and ADAM15 expression with the clinical data, and potentially establish a link between ADAM15-A/cMET expression, high Gleason score, tumour grade, disease relapse and metastasis score. For our analysis, we would further need an intense follow up of patients, as disease relapse might also correlate with cMET and ADAM15 expression. It would be desirable to further include samples of patients that were treated with cMET inhibitors, where we could assess ADAM15 expression and also downstream targets such as MMP2.

Zhong *et al.* as well as Poghosyan *et al.* showed that the ADAM15 A-C ICD splice variants can interact differently with a variety of SH3-domain containing proteins, due to differences in number of proline-rich motifs in the ADAM15 tail[81,145]. However, a functional consequence of these interactions was not identified. ADAM15 splice variant A was identified to associate with the cMET adaptor protein Grb2 and the prostate cancer promotor PTK6. Herein, we confirm these protein interactions in the cellular context of prostate (PC, LNCaP) and breast (MDA-MB-231) cancer cell lines. In addition, we describe for the first time, that ADAM15-A is in a complex with cMET. Treatment with selective cMET kinase inhibitors SU11274 and Capmatinib, which block cMET dimerization and downstream phosphorylation of the multiprotein docking site, resulted in dissociation of the cMET/Gab1/Grb2/ADAM15/PTK6 complex. Wang *et al.* showed that SU11274 treatment, reduced Gab1 phosphorylation[307] and Gab1 binding to cMET is an essential requirement for HGF/cMET signalling in cancer cells. We demonstrated that cMET inhibitor treatment led to Gab1 dissociation, and resulted in complex loss of Grb2/ADAM15/PTK6, which was not due to altered cellular protein levels of any of the complex's components.

Interestingly we found that while Grb2 remained in a complex with ADAM15, the PTK6 interaction was lost upon cMET inhibition. This suggests that although PTK6 can associate directly with ADAM15, as Poghosyan *et al.* showed when using purified recombinant ADAM15-ICD-GST constructs[145], in PC3 cells the ADAM15/PTK6 interaction is regulated by the cMET pathway and could involve Gab1. The loss of the ADAM15/PTK6 interaction was cMET treatment dependent for all splice variants. Considering our finding that ADAM15 dimerizes, a mixed ADAM15 splice variant dimer

formation, i.e. ADAM15-A+D, might enable different signalling partners to associate to the dimerized ICDs, which would usually not associate to a single ICD. As PC3 cells express ADAM15 endogenously, PC3 ADAM15 knock out cells are required to validate a splice variant dependent treatment effect.

Our data suggest that the interaction between ADAM15 and cMET could be mediated by Gab1 and/or Grb2 (Figure 7.1). Grb2 is able to bind to ADAM15 via its SH3 domain[145], and via its SH2 domain directly to cMET, or to Gab1 via its SH3-domain[198,207]. As cMET needs to be phosphorylated for Grb2 and Gab1 to attach[198], an interpretation of our data is that, upon cMET inhibitor treatment, Gab1 cannot bind to cMET, which further impairs the association of Grb2, leading to the loss of the Gab1/Grb2/cMET complex. As Grb2 binds to ADAM15 via its SH3 domain, the Grb2/ADAM15 complex stays intact. Although we showed loss of Gab1 in cMET-IP, we would further need to confirm the loss of Gab1 in the IPs of the other complex components, i.e. ADAM15, PTK6 and Grb2.

In an attempt to confirm the loss of the co-localization of the novel ADAM15/cMET/Gab1/Grb2/PTK6 complex upon cMET inhibitor treatment, confocal microscopy was used. Although a co-localization of the ADAM15/PTK6 was seen for untreated and HGF treated PC3 cells at the plasma membrane and within the cytoplasm, cMET inhibitor treated cells showed a weak and distinct staining for PTK6, which made assessment of co-localization difficult. In vector control PC3 cells, PTK6 staining was also detectable at the plasma membrane, which might be due to the endogenous ADAM15. To exclude this, PC3 ADAM15 knock out cells are required, which could be used to assess whether the membrane localization of PTK6 requires ADAM15 expression. Another approach to test the composition of the novel complex in the cellular environment is a proximity ligation assay. With this, we would use a pair of appropriate fluorescent probes for the V5-tag present on overexpressed ADAM15 and for detecting specifically PTK6, cMET, Grb2 or Gab1. Using this approach, we expect to obtain a specific fluorescence resonance energy transfer signal for the formed complexes. As the V5-tag is not present in vector control cells, a negative signal would be expected in control cells.

A functional consequence of ADAM15 overexpression was found using an invasion assay. We demonstrated that, among the five splice variants, only ADAM15-A showed significantly enhanced invasion in response to HGF stimulation. Further, we showed that this observation was cell type specific, as invasion assays performed in the LNCaP ADAM15-A-E panel did not lead to enhanced invasion upon HGF treatment, most likely

due to the very low levels of cMET expressed in these cells. When we took this observation further and used a combined treatment with HGF and the SU11274 cMET inhibitor, or the inhibitor alone, the invasion of ADAM15-A overexpressing PC3 cells was reduced significantly and was at control levels. Najy *et al.* showed that ADAM15 knock down in PC3 led to reduced invasion[105]. They further confirmed that ADAM15 knock down in MCF-7 cells led to reduced migration[100]. Our experiments using the PC3 and LNCaP ADAM15 A-E cell panels failed to show differences in migration, but we did see ADAM15 dependent invasion in PC3 cells linked to the cMET/HGF axis. As the cMET axis is a major target for cancer therapy[316–318], *in-vivo* models are now necessary to evaluate the role of ADAM15 overexpression on metastatic spread when cMET treatments are applied.

Moreover, we demonstrated that the proteolytic activity of ADAM15 is required for cell invasion, since proteolytically inactive ADAM15 mutants were less invasive, for splice variant A in PC3 cells. One possible mechanism for the enhanced invasion upon HGF treatment of ADAM15-A PC3 cells could involve the cMET sheddase ADAM10. ADAM10, which is a substrate for ADAM15-A, as shown by Tousseyn *et.al* using expression constructs for ADAM15-A[161], is also expressed in PC3 cells. ADAM10 is cleaved from the cell surface due to ADAM15 overexpression, resulting in higher cMET membrane levels. To address this question, expression differences of cMET surface levels in vector control or ADAM15-A overexpressing PC3 cells using confocal microscopy were assessed. For this cMET antibodies detecting either the cMET ECD or ICD were used, however, our data remain preliminary as they lack a valid cMET negative control (Supplementary data Figure 8.15).

The role of ADAM10 in the cMET/ADAM15 interaction needs to be clarified. ADAM10 is a cMET sheddase, it cleaves the cMET ECD, generating a N-terminal soluble cMET fragment (s-cMET)[198,214]. Assessing changes in cMET expression levels and proteolytic processing in ADAM15-A-WT or EA-mutant via western blotting, might be a possible approach. Another approach could make use of cMET ELISAs detecting the s-cMET that are commercially available. As a future experiment to monitor changes in cMET surface expression, we could generate a cMET knock down PC3 cell line, which we could use in confocal microscopy or FACS analysis. Using cMET ICD and ECD antibodies, to detect changes in membrane bound cMET, as well as ADAM10 antibodies to detect ADAM10 surface expression, our hypothesis could be further evaluated.

Our findings could also implicate the MMP2 as having a role in enhanced invasion observed for ADAM15-A expressing PC3 cells. Assessing supernatants, we found higher levels of pro-MMP2 and MMP2 in ADAM15-A-WT cells compared to ADAM15-A-EA and vector control cell medium. In a patient study, Xie *et al.* showed, that MMP2 expression levels in prostate cancer patients were linked to disease agressiveness[319]. In order to eliminate endogenous ADAM15 and ADAM10 activity in our experiments, when using PC3 cells, we could generate an ADAM15/ADAM10 double knock down cell line in PC3. Najy *et al.* showed that upon sh ADAM15 knock down, PC3 cell invasion was reduced[100]. Using the double knock down, we would therefore expect, significantly reduced cell invasion compared to the parental cell line, although HGF dependent invasion would not be inhibited, since in the absence of ADAM10 and ADAM15, cMET levels would be increased due to reduced shedding. ADAM15 and ADAM10 knock downs would help to elucidate the role of cMET and MMP2 in enhanced invasion of prostate cancer cells.

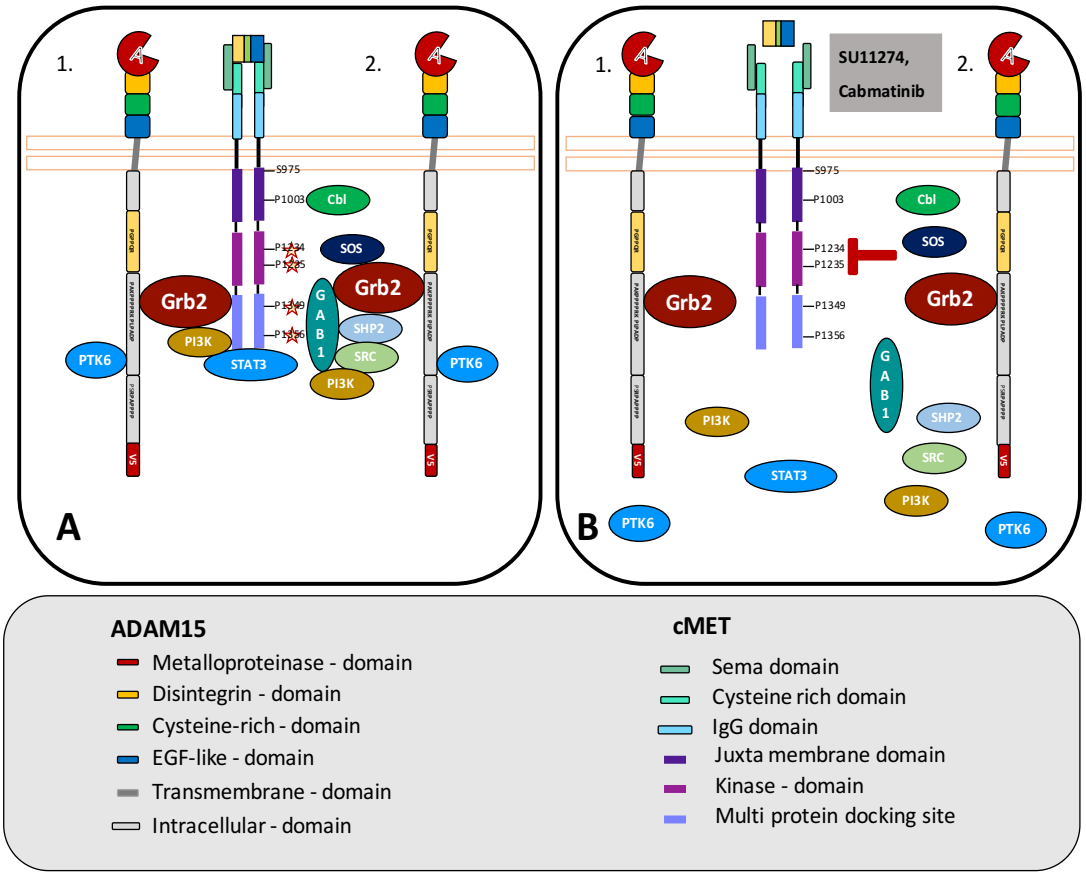

Figure 7.1 ADAM15/cMET complex formation

In in PC3, the hepatocyte growth factor receptor cMET can form a complex with ADAM15/Gbr2/Gab1/PTK6. Two possible ways of how this interaction is formed and further disrupted are shown in 1. and 2. (A) cMET dimerizes either upon HGF treatment (as indicated) or via overexpression and spontaneous dimerization (not shown, but more likely in PC3 cells), leading to downstream transphosphorylation, and allowing Gab1 to associate to the C-terminal multi protein docking site. Association of Gab1 to cMET allows binding of Grb2 and other adaptor proteins to one of its docking site. Grb2 contains one SH2 domain which is flanked on both sites by SH3 domains. Via one of its SH3 domain, Grb2 binds to the proline rich regions present in the ADAM15 intracellular domain. (B) Inhibiting cMET via selective kinase inhibitors, such as SU11274 and Capmatinib, results in inhibition of cMET phosphorylation. Adaptor proteins of cMET cannot bind to its C-terminal multi protein binding site leading to the complex loss of PTK6/Grb2/ADAM15 (B 1.) or to loss of PTK6/ADAM15/Grb2/Gab1 (B 2.). More factors might be involved in this multi protein complex, needing further elucidation.

An interesting observation was that MDA-MB-231 breast cancer cells, overexpressing ADAM15-A also required functional cMET signalling, for the cMET/ADAM15/Grb2/PTK6 interaction, since the complex was disrupted by the cMET inhibitor treatments, as seen for PC3 cells. However, unlike PC3 cells, in MDA-MB-231 cells the complex formation between ADAM15 and PTK6 was enhanced. MDA-MB-231 cells have high cMET levels[317], enabling to target this pathway via inhibitor treatment. Further, they are aggressive and hormone-independent, such as PC3 cells. This suggests, that cMET/ADAM15 complex formation might be an important target in aggressive cancer, however further *in-vitro* and *in-vivo* experiments are necessary to

elucidate its importance. Our preliminary data with the androgen dependent LNCaP PCa cell line expressing ADAM15-A, which are known to be cMET negative[300], showed that the ADAM15/PTK6 complex formation was not disrupted upon cMET inhibitor treatments (Supplementary data Figure 8.10).This suggests that the ADAM15/PTK6 interaction might be independent of cMET complex formation in LNCaP, unlike the aggressive PC3 and MDA-MB-231 cells. However, we cannot draw any firm conclusions before the finding in the LNCaP cells are repeated and quantified.

Future experiments in LNCaPs could elucidate the role of Gab1 in the PTK6/ADAM15 interaction. As Gab1 can be phosphorylated not only via cMET but also via VEGF[320] and other growth factor signalling pathways, we could determine the mechanism of Gab1 phosphorylation in LNCaP. Moreover, we could generate a LNCaP cell line co-expressing cMET and ADAM15 for the use with the cMET inhibitors, Capmatinib and SU11274, to test if we could recreate the cMET dependent complex seen in PC3 and MDA-MB-231 cells.

An important finding of this work is that PTK6 kinase activity is not required for the ADAM15 interaction. This is based on two lines of evidence. First, ADAM15-A was found to interact with both PTK6-WT and the catalytically inactive PTK6-KM mutant in HEK293FT cells. Second, although low levels of active PTK6 are present in PC3 cells[295], and using a kinase assay, to facilitate PTK6 activity, we could not detect ADAM15 phosphorylation. When we assessed differences in PTK6 expression in our PCa cell panel, no change in mRNA or in PTK6 localization upon ADAM15 overexpression were found. However, as discussed previously, endogenous ADAM15 is present in PC3 cells, which might influence PTK6 localization. Using PC3 ADAM15 knock out cells, it might be possible to identify a splice variant specific difference in PTK6 localization.

According to Zhong *et al.* the interaction between ADAM15 and PTK6 is formed via the proline rich regions of the ADAM15 ICD, and only ADAM15 splice variant A and B are able to associate with PTK6[81]. Strikingly, we found that all splice variants and moreover, the D-splice variant, lacking the proline rich binding motifs, is in a complex with PTK6 in both PC3 and LNCaP cell panels. When using confocal microscopy, co-localization of ADAM15 and PTK6 in PC3 and LNCaP cell panels for all splice variants was found. Although these results are suggestive of PTK6 interaction in a splice variant independent manner, there is an alternative explanation that involves ADAM15 dimerization with the endogenous protein. Indeed, qPCR data revealed that all

ADAM15 splice variants are endogenously expressed in PC3 and LNCaP cells, and western blotting confirmed the presence of endogenous ADAM15 in PC3 cells. Importantly, crosslinking experiments revealed dimer formation of ADAM15-A and D in a time dependent manner. Dimer formation is published for ADAMs, such as ADAM17 and ADAM10, and thought to regulate their protease function[321]. It is therefore possible that hetero dimerization of exogenous ADAM15 splice variants with the endogenous ADAM15-A takes place in cells, and exogenous ADAM15 is indirectly associated with PTK6 via the endogenous ADAM15-A. As Zhong *et al.* used isolated ADAM15-ICDs, tagged with GST they found specific binding of PTK6 to splice variants A and B individually, however, this approach did not take hetero dimerization of ADAM15 splice variants in cellular settings into account.

ADAM15 dimer formation could play a physiological role and it could be worth investigating further. ADAM17 dimer disruption was previously linked to the MAPK and Erk-pathway, with pathway activation leading to a shift from ADAM17 dimer to monomer and enhanced activity of ADAM17[297]. Xu *et al.* found, that the ADAM17 cytoplasmic tail is required for its dimerization. In this inactive-dimer state, ADAM17 associates with TIMP3 at the plasma membrane, leading to ADAM17 inactivation. Activation of MAPK or ERK pathway led to dissociation of TMP3 and the activation of ADAM17[297]. Using the PCs ADAM15 knock down cell line we could further investigate the dimer formation of ADAM15. Further, we could investigate, whether the ADAM15 dimer can be disrupted upon cMET pathway activation or upon inhibitor treatment, as well as whether dimer formation is necessary for ADAM15 to interact with its protein partners and enhance PCa cell invasion.

Assessing cell characteristic of our cell panels such as cell size, morphology, actin cytoskeleton, or cell cycle, no changes were found for LNCaP or PC3 stable expressing the ADAM15 splice variants, which was surprising, as Zhong *et al.* could show splice variant specific differences in cell characteristics upon overexpression in breast cancer cells[81].

7.2 Conclusions

In the present study, we showed that enhanced invasion of PC3 ADAM15 overexpressing cells is dependent on the HGF/cMET signalling axis and on the proteolytic activity of ADAM15.

Further, we demonstrated that ADAM15 is found in a complex with cMET/PTK6/Grb2, which could be disrupted in the aggressive cancer cell lines, PC3 and MDA-MB-231, by cMET inhibition.

In prostate cancer patients, expression of all ADAM15 splice variants was significantly higher than in healthy tissue.

In conclusion, our data suggest that ADAM15 overexpression might represent a promising clinical target for the prognosis of prostate cancer disease aggressiveness.

.

8 Supplementary Data

8.1 Chapter 2

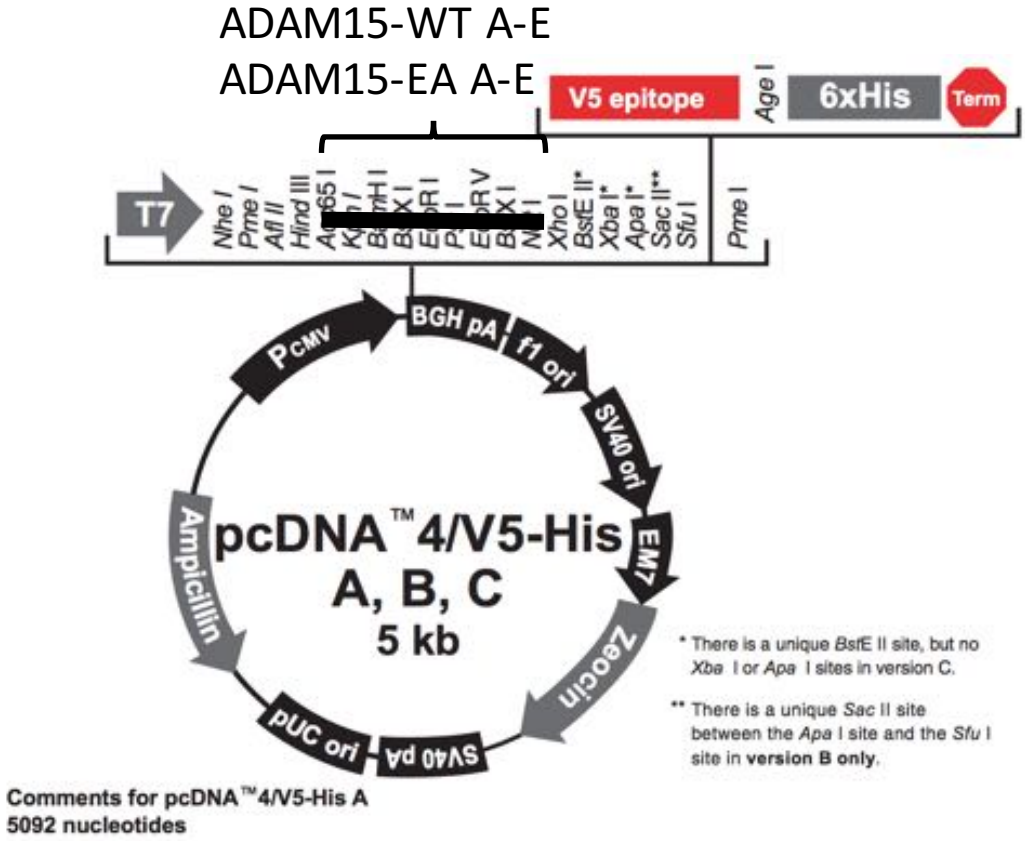

Figure 8.1 ADAM15 Vector Map

pcDNA5/V5-His –A was used to generate the ADAM15 A-E splice variant specific primer. The restriction sites of HindIII and XhoI were used to clone the ADAM15 DNA inside. Both enzymes were chosen as they were not present within the ADAM15 sequence itself, it is important to note that ADAM15 contains an endogenous EcoRI site which was remove out of the multiple cloning site using the sites for HindIII and XhoI. Adapted from Thermo Fisher (https://assets.thermofisher.com/TFS-Assets/LSG/manuals/pcdna4v5his_man.pdf)

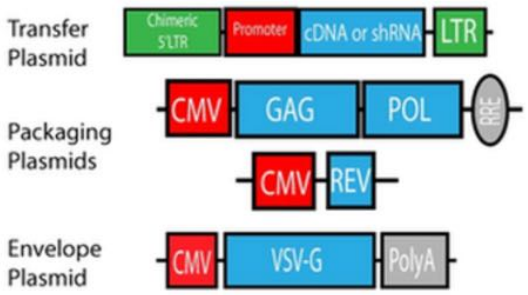

VSV-G	Vesicular stomatitis virus G glycoprotein
Gag	Particle containing Matrix, Capsid and Nucleocapsid components
Pol	Containing Reverse Transcriptase and Integrase
RRE	Rev Response Element
Rev	Binds to the Rev Response Element (RRE) within unspliced and partially spliced transcripts to facilitate nuclear export.
LTR	Long terminal repeats

Figure 8.2 Schematic overview of the Lentiviral packaging system

Overview of the Lentiviral components. The Transferplasmid containing the gene of interest and the LTR to integrate into the host genome, the Packaging plasmid containing the Reverse Transcriptase (Pol) and the Nucleocapsid. The Envelope plasmid contains the VSV-G envelope protein, allowing a broad tropism. Adapted from Addgene (https://www.addgene.org/viral-vectors/lentivirus/lenti-guide/).

8.2 Chapter 3

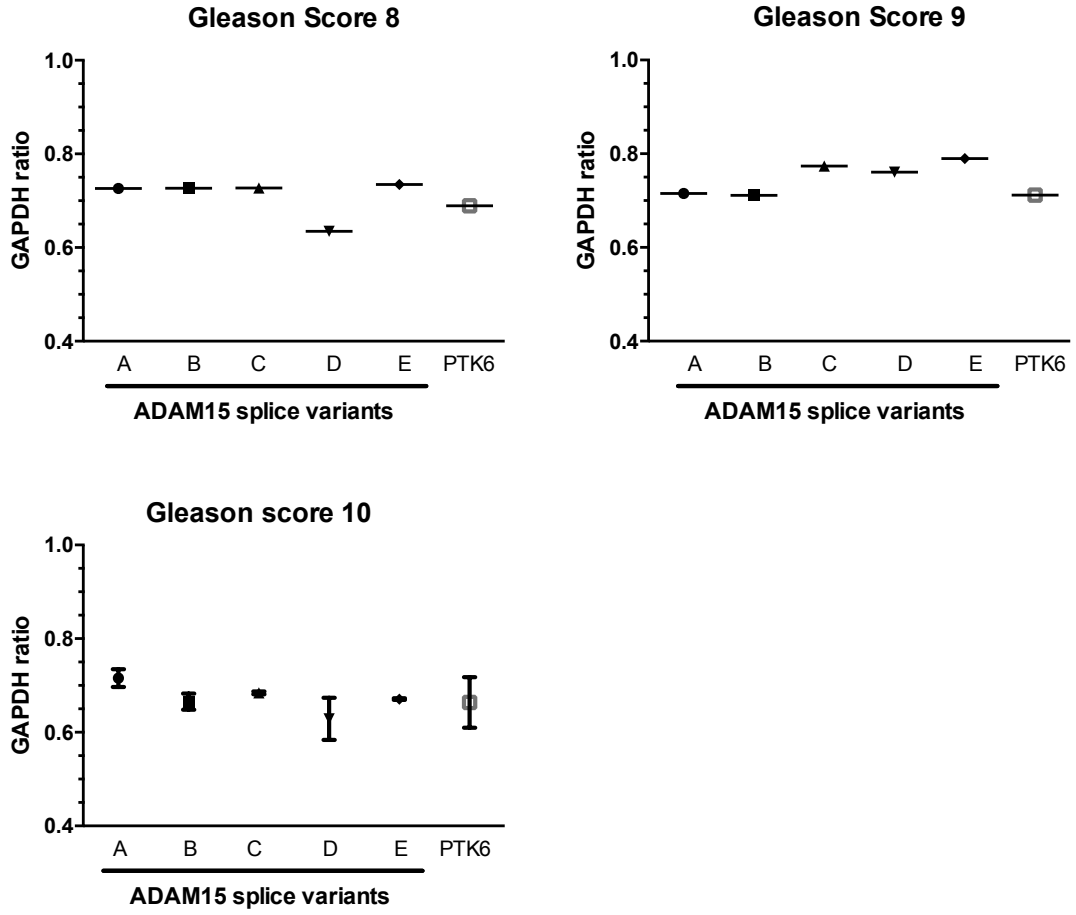

Figure 8.3 ADAM15 splice profile and PTK6 expression in PCa patients with Gleason score 8,9 and 10.

After unblinding of clinical data from the analyzed PCa patients, the number of patients with a Gleason scores of 8 and 9 was 1 and for a Gleason score of 10, two patients were included. The ADAM15 splice profile and PTK6 expression levels are shown for the patients with a Gleason score of 8, 9 and 10.

8.3 Chapter 4

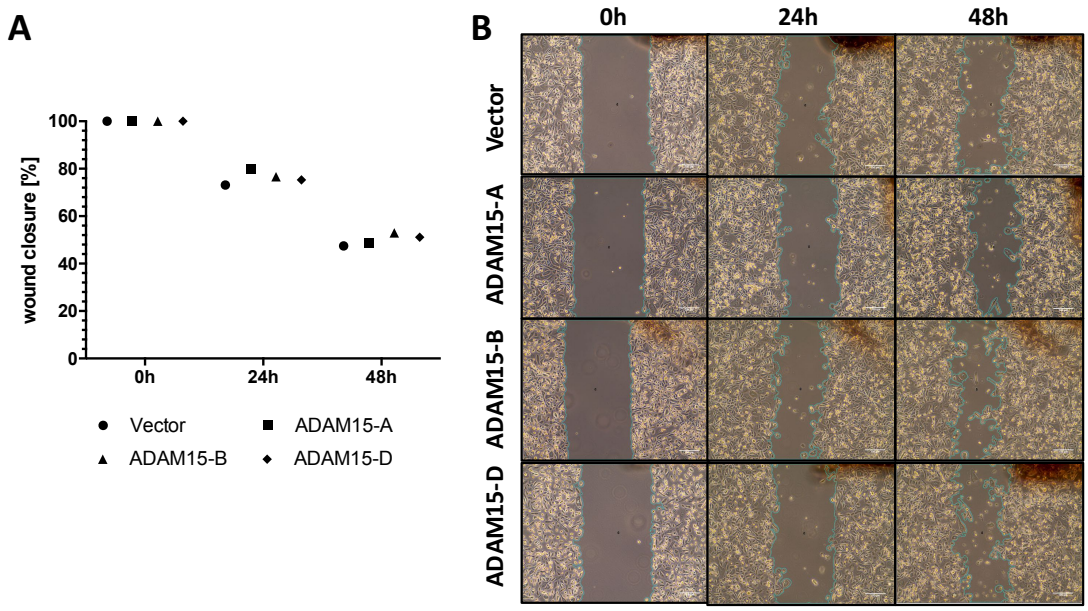

Figure 8.4 Scratch wound assay using PC3 ADAM15 expressing cells.

PC3 ADAM15-A, B and D expressing cells were seeded in 60mm dishes with 1x106 cells/ dish. After 24h incubation in serum free media, 7 scratches were introduced to the monolayer using a white tip (0.5-1μm). Floating cells were removed by 2 consecutive media washes. Pictures were taken using 100x magnification. Cells were fed and pictures were taken after 0, 24 and 48h. (A) Wound closure in % over a time period of 48h. No significant difference between ADAM15-A, B and splice variant D were determined. Wound closure after 48h was almost 50%. However, cells were overgrowing (B). The experiment was repeated twice, as a 100% wound closure could no achieved after 72h, the experiment was terminated. Wound closure in % was analyzed using the ImageJ wound closure tool.

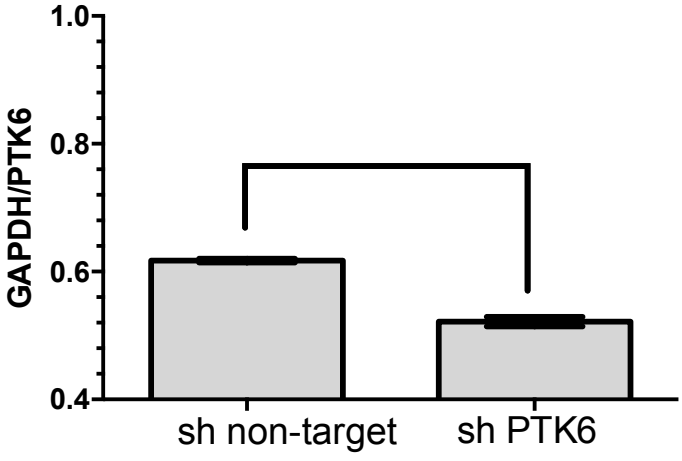

Figure 8.5 qPCR validation of PTK6 knock-down in the PC3 cell line.

From PC3 sh non-target and PC3 shPTK6, RNA was isolated and cDNA was generated by RT-PCR. Using PTK6 specific primer, qPCR was performed. GAPDH was used as endogenous control. Using qPCR, a 20% knockdown of PTK6 was determined, when GAPDH C_t values were divided by PTK6 C_t values.

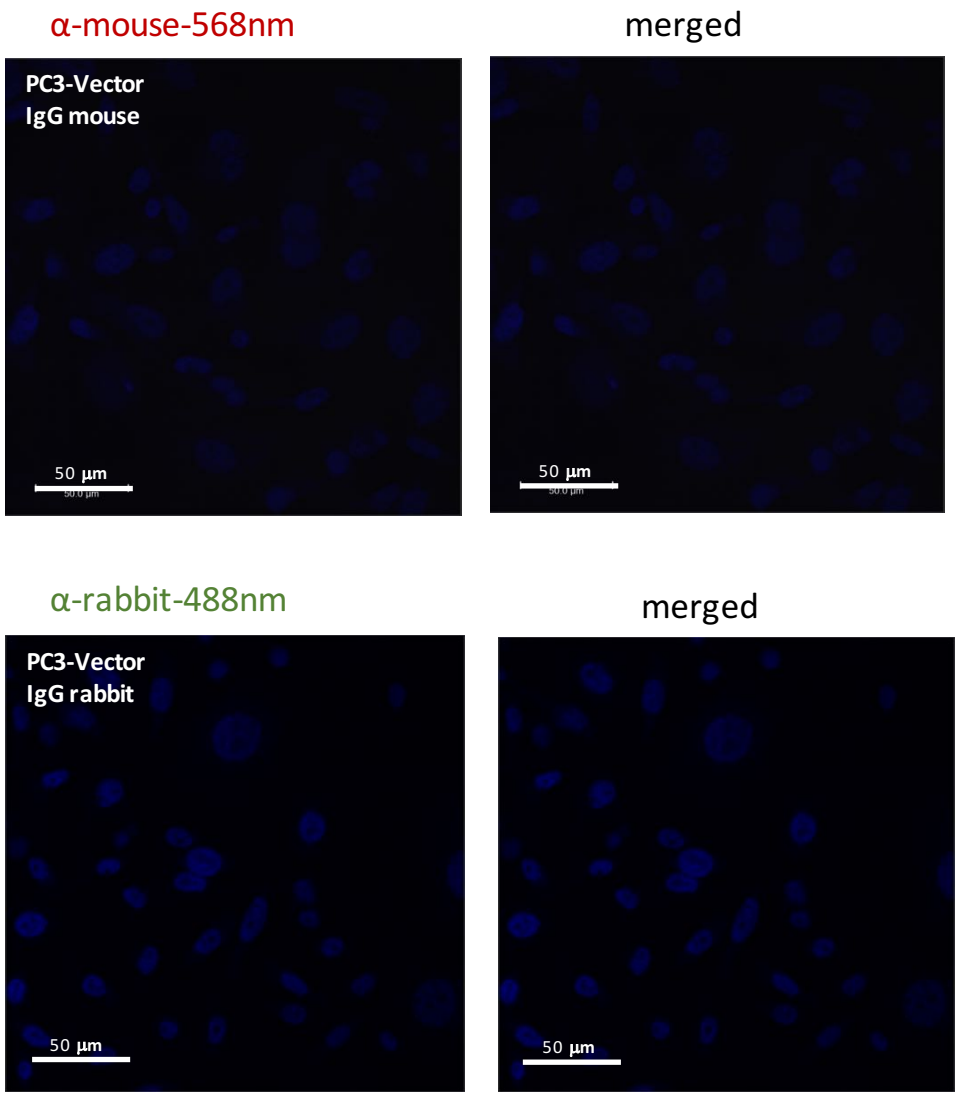

Figure 8.6 Antibody validation.

Prior to the immunohistochemistry experiments, non immune anti-mouse and rabbit antibodies were incubated with PC3 Vector control cells on coverslips O/N at 4°C. Cells were stained using either the secondary Alexa-Fluor-α-mouse-568nm or the Alexa-Flour-α-rabbit. Cells were analyzed using confocal microscopy.

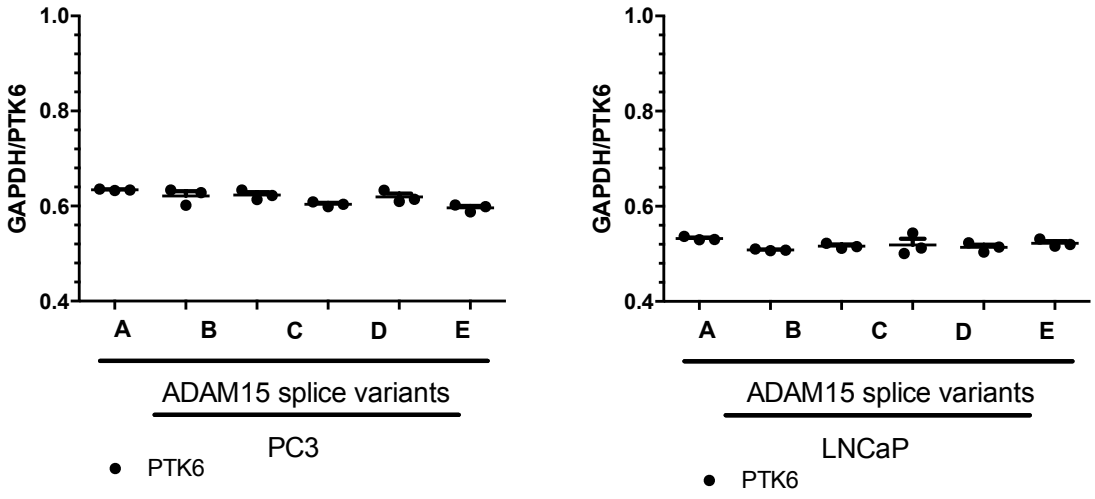

Figure 8.7 PTK6 expression levels in PC3 and LNCaP ADAM15 A-E panels.

qPCR was performed with cDNA generated from extracted RNA from each cell line. GAPDH was used as endogenous control. Using qPCR, PC3 and LNCaP cell panel did not reveal a splice variant specific change in PTK6 expression levels. The PC3 cell panel shows over all a higher PTK6 expression compared to the LNCaP cell panel. GAPDH C_t values were divided by PTK6 C_t values, and plotted for each splice variant.

8.4 Chapter 5

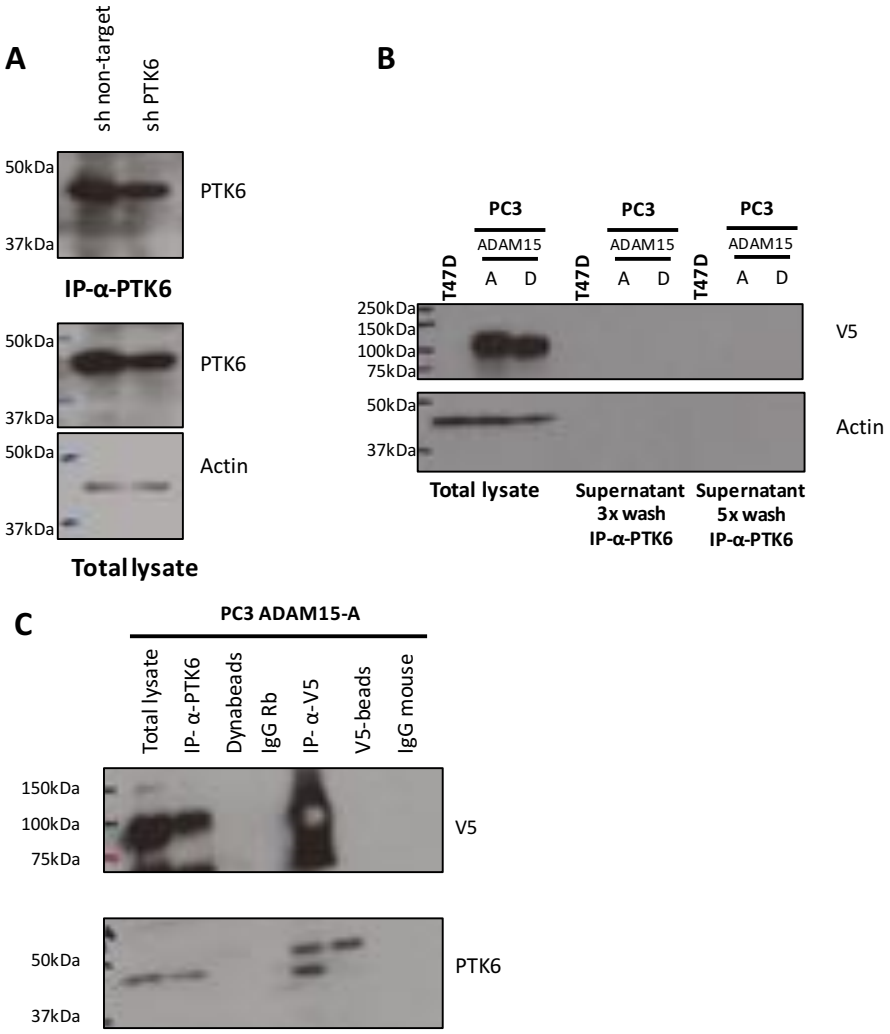

Figure 8.8 PTK6 and V5 antibody validation.

(A) PTK6 antibodies for IP and western blotting were validated using the PC3 shPTK6 cell panel. PTK6-rabbit antibody was used to for IPs with PTK6, western blotting was performed using the PTK6-mouse antibody. (B) Unspecific antibody binding was assessed in IP-supernatants after O/N incubation. ADAM15-A and D PC3 cells were chosen, and as PTK6 positive control, the T47D cell line. Neither PTK6 nor V5 (ADAM15) could be detected in wash-supernatants after the IP. (C) Unspecific binding of antibodies and beads was further assessed by western blotting. Samples were; total lysate, IP-PTK6 and IP-V5, as positive control, Dynabeads, IgG-rabbit antibody, V5-beads and IgG-mouse without cell lysate as negative control. Dynabeads, IgG-mouse and rabbit remained free of unspecific binding. In the V5-bead sample, IgG heavy chains we detectable, but we detected above the 48kDa band for PTK6.

8.5 Chapter 6

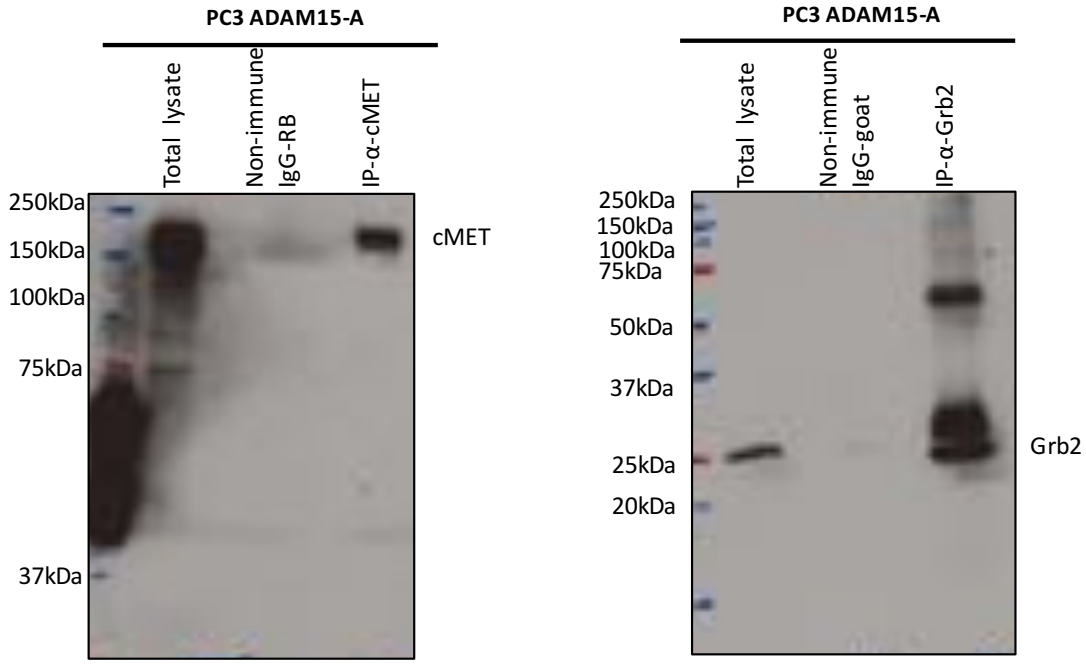

Figure 8.9 cMET and Grb2 antibody validation

PC-3 ADAM15-A expressing cells were used for the cMET and Grb2 IP antibody validation. The positive control was the total lysate and the IP itself. Negative control per IP was chosen as, IgG-rabbit for cMET and IgG-goat for Grb2. Non-immune IgG controls for both IPs were found negative for unspecific binding. Both IPs were found positive for either cMET or Grb2, when probing membranes after western blotting. Grb2 IPs showed unspecific binding below 75kDa and above 25kDa, which did not interfere with any of detected proteins.

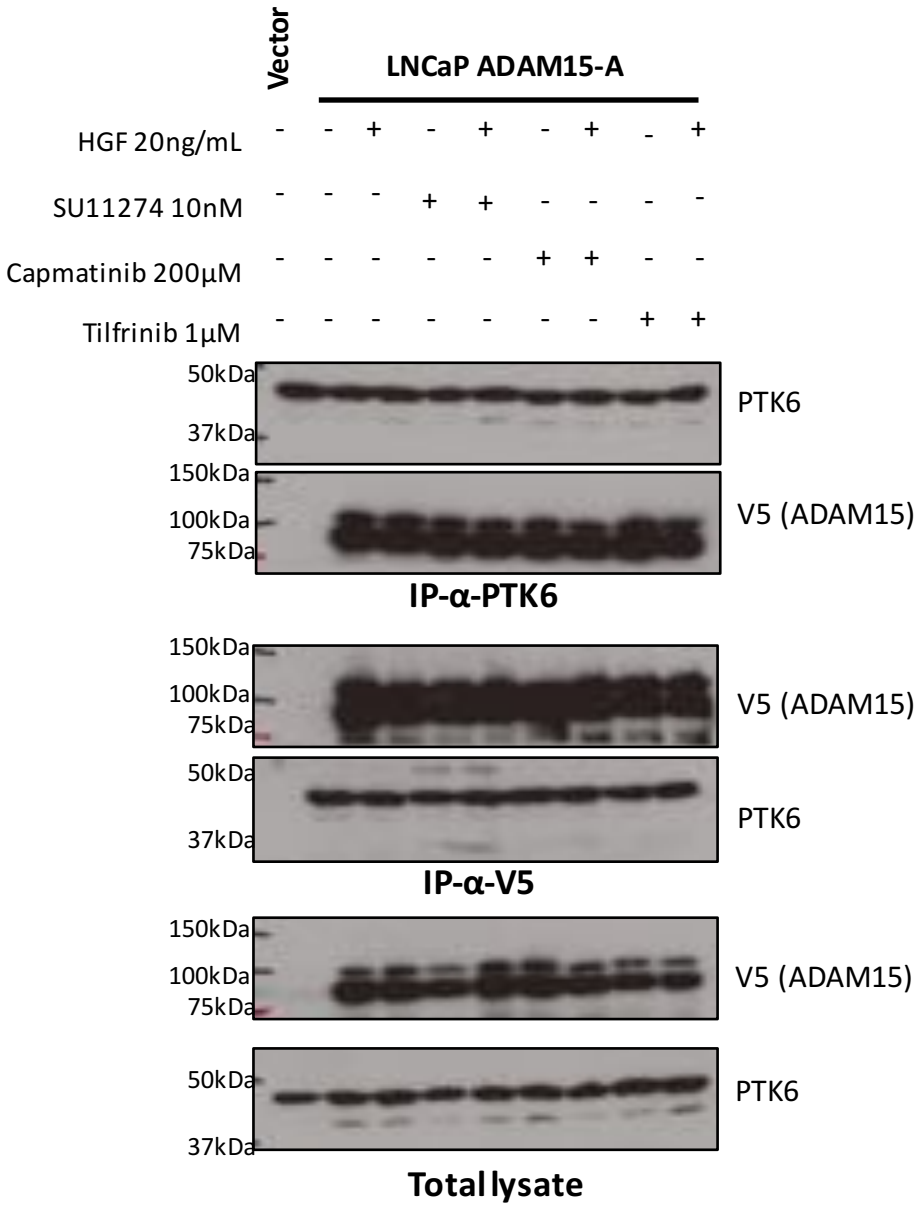

Figure 8.10 No cMET dependent complex interruption of ADAM15 and PTK6 in LNCaP.

LNCaP ADAM15A and vector control cells were treated with the cMET inhibitor SU11274 and Capmatinib and additionally with the PTK6 inhibitor Tilfrinib, to assess a cell line and cMET dependent interaction.

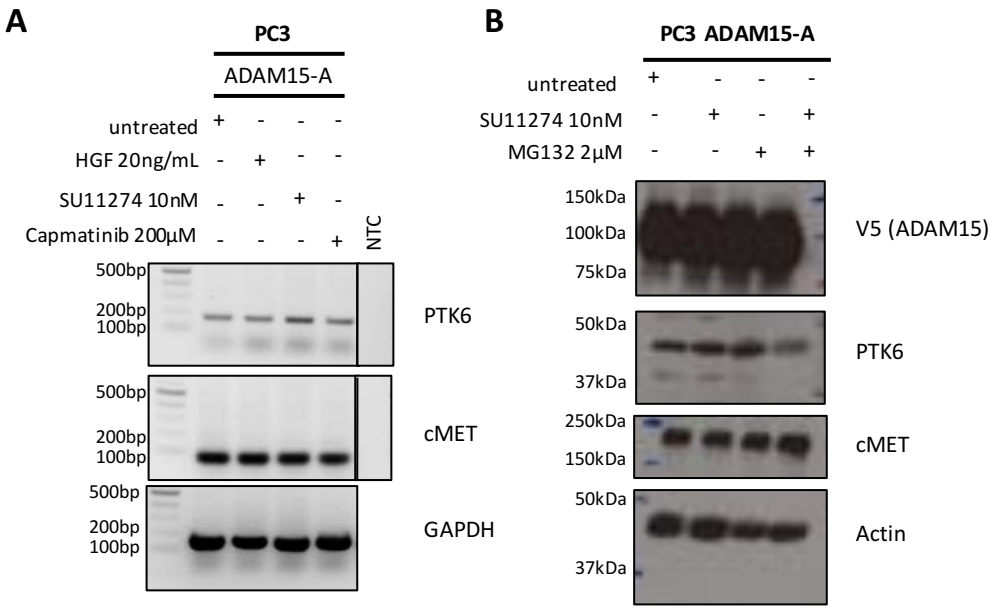

Figure 8.11 cMET or PTK6 protein levels are not affected upon cMET inhibitor treatments.

PC3 ADAM15-A expressing cells were analyzed following cMET inhibitor treatments for changes in expression levels. (A) RNA levels of PC3 ADAM15-A expressing cells were assessed for PTK6 or cMET expression, untreated cells were used as control. GAPDH was used as endogenous control. Cells were treated with either HGF, SU11274 or Capmatinib. PTK6 and cMET expression levels remained unaffected upon treatments. (B) PC3 ADAM15-A expressing cells were treated with SU11274, the proteosomal inhibitor MG132 or a combined treatment. Protein expression levels for ADAM15, PTK6 and cMET remained unaffected by the treatments.

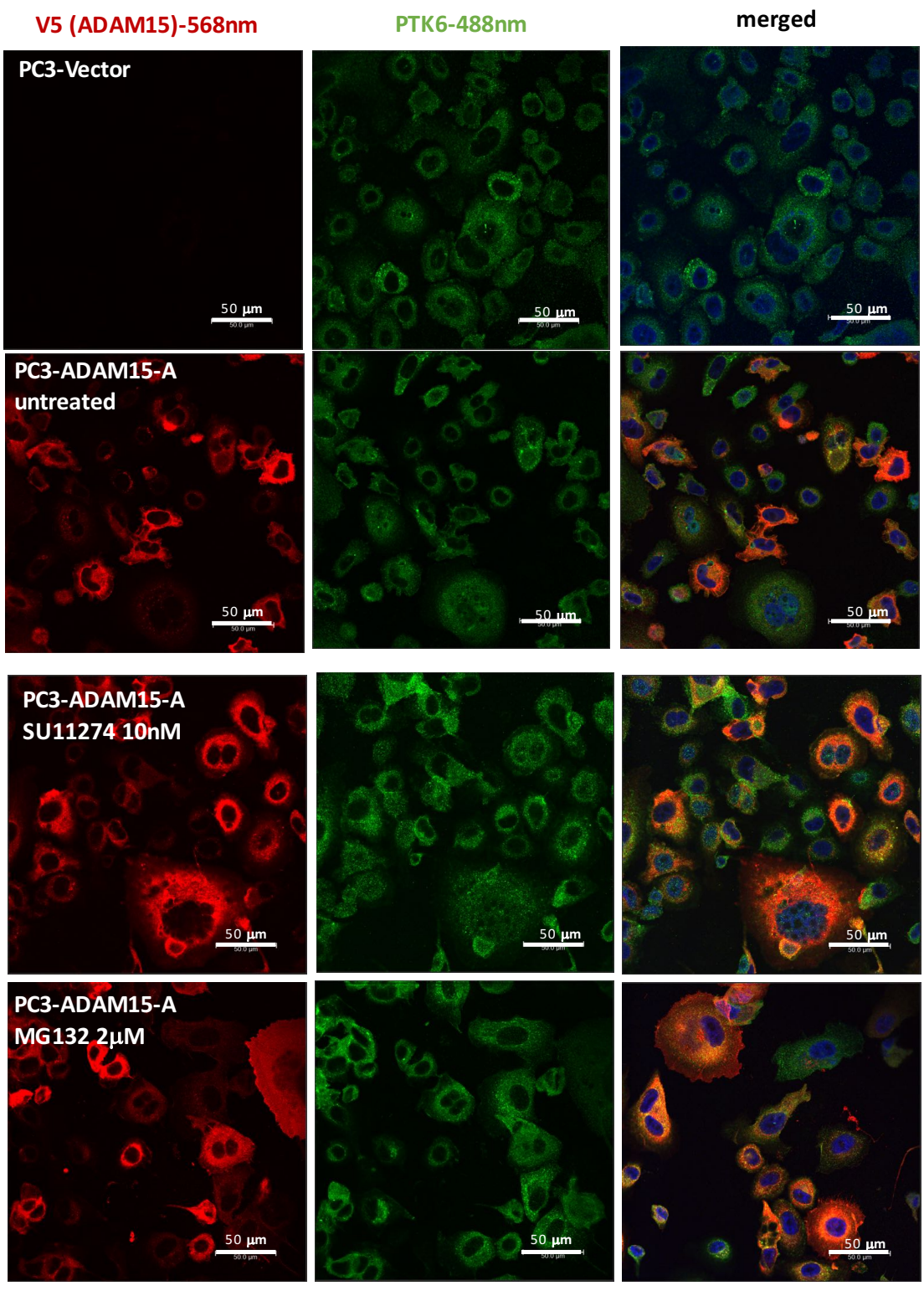
V5 (ADAM15)-568nm
PTK6-488nm
merged
PC3-Vector
PC3-ADAM15-A untreated
PC3-ADAM15-A SU11274 10nM
PC3-ADAM15-A MG132 2µM
50 µm

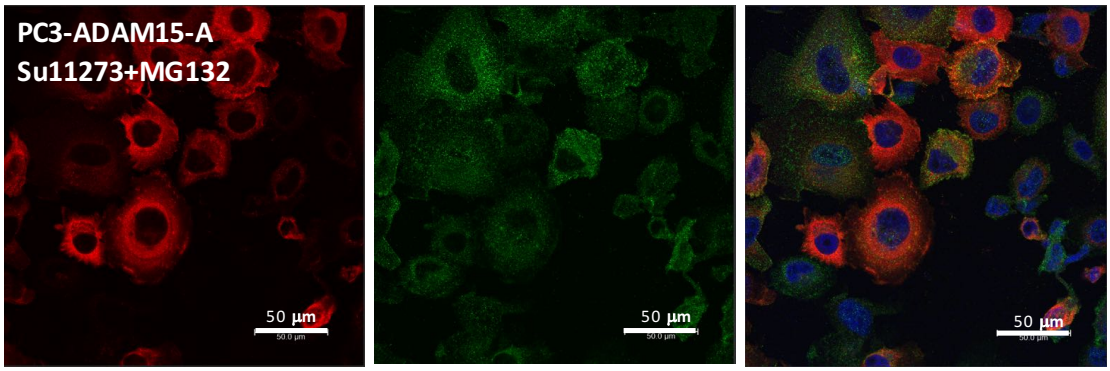

Figure 8.12 Proteosomal inhibitor treatment with PC3 ADAM15-A

PC3 ADAM15-A expressing cells were analyzed following cMET inhibitor treatments for changes in expression levels using confocal microscopy. Cells were treated with either HGF, SU11274, the proteosomal inhibitor MG132 or a combination of both. PTK6 (green) and ADAM15 (red) were detected using the corresponding validated antibodies. No difference in presence of ADAM15 or PTK6 with or without proteosomal inhibitor treatment. The SU11274 treated cells showed a similar weaker staining for PTK6 even in presence of the proteosomal inhibitor, which confirms the western blot and PCR results, however leaves open questions as why cells appear weaker in PTK6 staining upon SU11274 treatment.

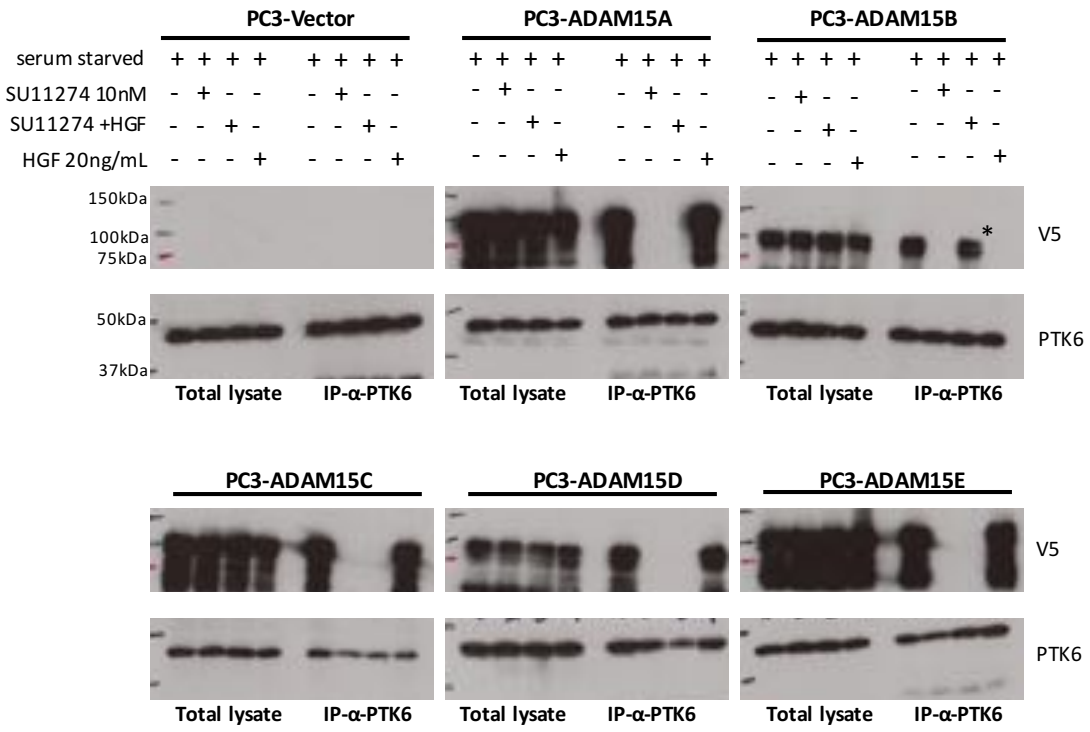

Figure 8.13 cMET dependent ADAM15/PTK6 complex interruption is splice variant independent.

Additionally to PC3 ADAM15A expressing cells, the whole PC3 cell panel was treated with the cMET inhibitor SU11274 in presence or absence of HGF. HGF alone and serum starved cells were used as control. For all ADAM15 splice variants the interruption of the ADAM15/PTK6 complex could be confirmed. The asterisk in ADAM15B expressing cells shows the HGF 20ng/mL treated cells, SU11274+HGF is shown in the right lane next to the asterisk.

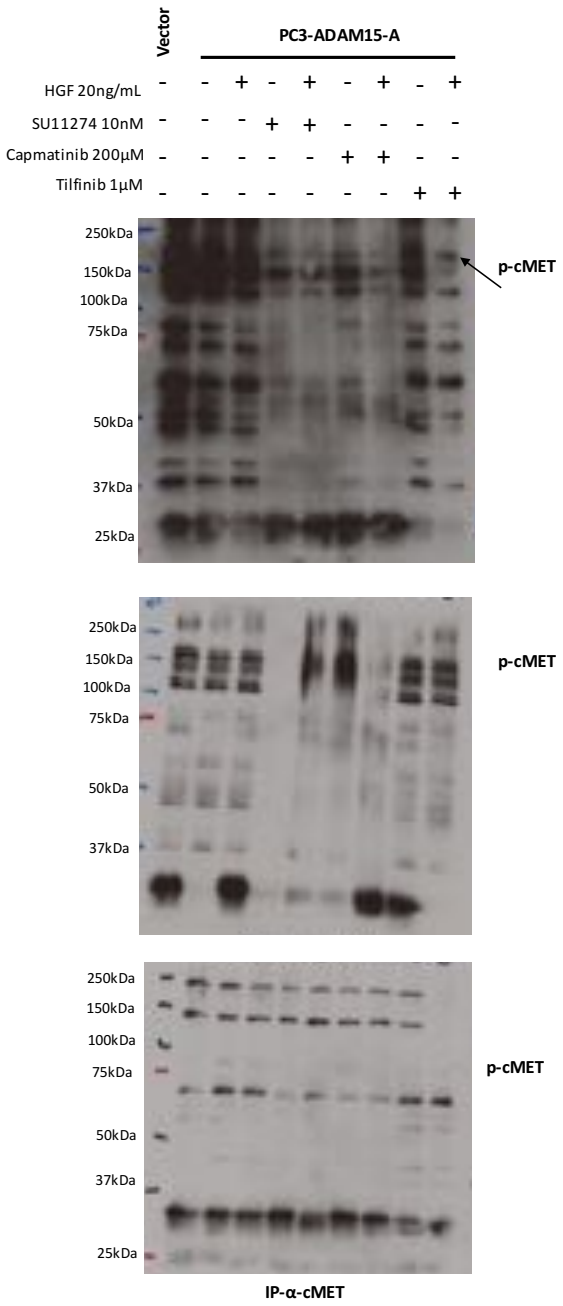

Figure 8.14 PC3 cMET IPs probed for p-cMET

Additionally to cMET, PTK6 and ADAM15, cMET IPs were probed using a p-cMET antibody, raised against the kinase domain of cMET, detecting p-tyrosines 1234 and 1235. The three membranes presented show the three independent repeats of the cMET IP and the corresponding probing for p-cMET.

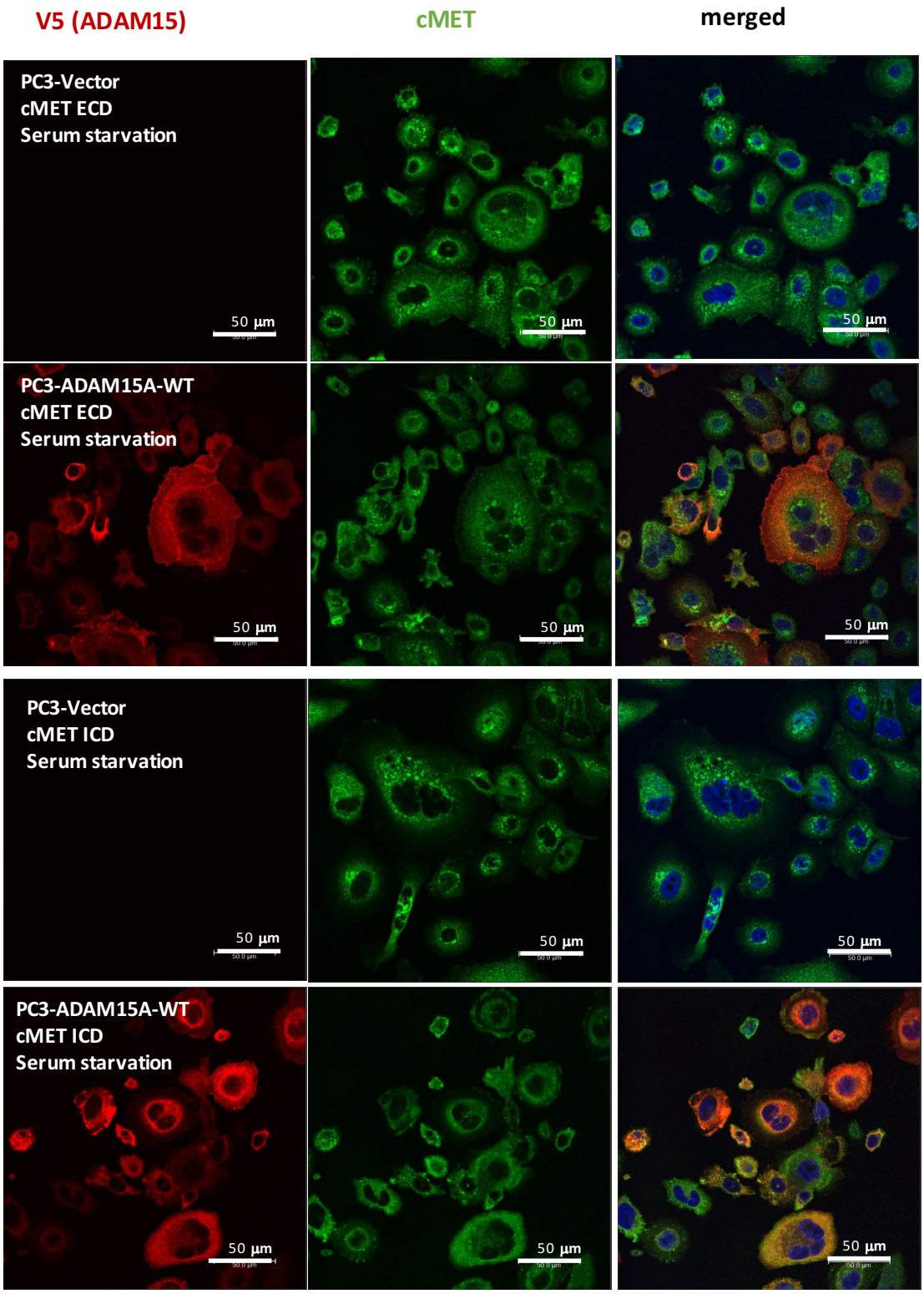

Figure 8.15 cMET ECD and ICD antibody validation

PC3 ADAM15-A expressing cells were used to analysed differences in cMET presence using cMET antibodies detecting either the cMET ECD or ICD.

1. Orgnization, W. H. World cancer factsheet. *World Heal. Organ.* **2012,** 4 (2014).

2. Hanahan, D. & Weinberg, R. A. Hallmarks of cancer: the next generation. *Cell* **144,** 646–74 (2011).

3. Hajdu, S. I., Vadmal, M. & Tang, P. A note from history: Landmarks in history of cancer, part 7. *Cancer* **121,** 2480–2513 (2015).

4. Iglesias-Gato, D. *et al.* The Proteome of Primary Prostate Cancer. *Eur. Urol.* 1–11 (2015).

5. Gordon, T. H. E., Lecture, W., Of, T., Stage, E. & Cancer, P. *History Unequivocally Patients, of*. **111,** (2000).

6. Elo, J. P. & Visakorpi, T. Molecular genetics of prostate cancer. *Ann. Med.* **33,** 130–141 (2001).

7. Balk, S. P. & Knudsen, K. E. AR, the cell cycle, and prostate cancer. *Nucl. Recept. Signal.* **6,** e001 (2008).

8. Humphrey, P. A. Gleason grading and prognostic factors in carcinoma of the prostate. *Mod. Pathol.* **17,** 292–306 (2004).

9. So, A., Gleave, M., Hurtado-Col, A. & Nelson, C. Mechanisms of the development of androgen independence in prostate cancer. *World J. Urol.* **23,** 1–9 (2005).

10. Grönberg, H. Prostate cancer epidemiology. *Lancet (London, England)* **361,** 859–64 (2003).

11. Lawson, D. a & Witte, O. N. Review series Stem cells in prostate cancer initiation and progression. *J. Clin. Invest.* **117,** 2044–2050 (2007).

12. Collins, A. T. & Maitland, N. J. Prostate cancer stem cells. *Eur. J. Cancer* **42,** 1213–1218 (2006).

13. He, Q., Johnston, J., Zeitlinger, J., City, K. & City, K. HHS Public Access. **33,** 395–401 (2015).

14. Lansing, E. Prostate Antigen , a Serine Human Cancer Invasion1. *Clin. Cancer Res.* **1,** 1089–1094 (1995).

15. Shen, M. & Abate-Shen, C. Molecular genetics of prostate cancer: new prospects for old challenges. *Genes Dev.* **24,** 1967–2000 (2010).

16. Mikah, P. *et al.* Dynamic changes of alkaline phosphatase are strongly associated with PSA-decline and predict best clinical benefit earlier than PSA-changes under therapy with abiraterone acetate in bone metastatic castration resistant prostate cancer. *BMC Cancer* **16,** 214 (2016).

17. Cooperberg, M. R., Lubeck, D. P., Meng, M. V., Mehta, S. S. & Carroll, P. R. The changing face of low-risk prostate cancer: Trends in clinical presentation and primary management. *J. Clin. Oncol.* **22,** 2141–2149 (2004).

18. Pentyala, S. *et al.* Prostate cancer markers: An update (Review). *Biomed. Reports* 263–268 (2016). doi:10.3892/br.2016.586

19. Carter, H. B. *et al.* Early detection of prostate cancer: AUA Guideline. *J. Urol.* **190,** 419–26 (2013).

20. Greene, K. L. *et al.* Prostate Specific Antigen Best Practice Statement: 2009 Update. *J. Urol.* **182,** 2232–2241 (2009).

21. Schr??der, F. H. *et al.* Screening and prostate cancer mortality: Results of the European Randomised Study of Screening for Prostate Cancer (ERSPC) at 13 years of follow-up. *Lancet* **384,** 2027–2035 (2014).

22. Epstein, J. I. An Update of the Gleason Grading System. *J. Urol.* **183,** 433–440 (2010).

23. Montironi, R., Mazzucchelli, R., Lopez-Beltran, A., Scarpelli, M. & Cheng, L. The Gleason grading system: Where are we now? *Diagnostic Histopathol.* **17,** 419–427 (2011).

24. Iczkowski, K. A. & Lucia, M. S. Current perspectives on Gleason grading of prostate cancer. *Curr. Urol. Rep.* **12,** 216–222 (2011).

25. Shah, R. B. & Zhou, M. Recent advances in prostate cancer pathology: Gleason grading and beyond. (2016).

26. Montironi, R. *et al.* Original gleason system versus 2005 ISUP modified gleason system: The importance of indicating which system is used in the patient's pathology and clinical reports. *Eur. Urol.* **58,** 369–373 (2010).

27. Epstein, J. I. *et al.* A Contemporary Prostate Cancer Grading System: A Validated Alternative to the Gleason Score. *Eur. Urol.* **69,** 428–435 (2015).

28. Lu, S., Tsai, S. Y. & Tsai, M. Regulation of Androgen-dependent Prostatic Cancer Cell

Growth : Androgen. *Cancer Res.* **57,** 4511–4516 (1997).

29. Zhou, Y., Bolton, E. C. & Jones, J. O. Androgens and androgen receptor signaling in prostate tumorigenesis. *J. Mol. Endocrinol.* **54,** R15–R29 (2015).

30. Stricker, H. J. Luteinizing hormone-releasing hormone antagonists in prostate cancer. *Urology* **58,** 24–27 (2001).

31. Rittmaster, R. S. 5Alpha-Reductase Inhibitors in Benign Prostatic Hyperplasia and Prostate Cancer Risk Reduction. *Best Pract. Res. Clin. Endocrinol. Metab.* **22,** 389–402 (2008).

32. Feldman, B. J. & Feldman, D. The development of androgen-independent prostate cancer. *Nat. Rev. Cancer* **1,** 34–45 (2001).

33. Jariwala, U. *et al.* Identification of novel androgen receptor target genes in prostate cancer. *Mol. Cancer* **6,** 39 (2007).

34. Attar, R. M., Takimoto, C. H. & Gottardis, M. M. Castration-resistant prostate cancer: Locking up the molecular escape routes. *Clin. Cancer Res.* **15,** 3251–3255 (2009).

35. Karantanos, T., Corn, P. G. & Thompson, T. C. Prostate cancer progression after androgen deprivation therapy: mechanisms of castrate resistance and novel therapeutic approaches. *Oncogene* **32,** 5501–11 (2013).

36. Jin, J. K., Dayyani, F. & Gallick, G. E. Steps in prostate cancer progression that lead to bone metastasis. *Int. J. Cancer* **128,** 2545–2561 (2011).

37. Visakorpi, T. *et al.* In vivo amplification of the androgen receptor gene and progression of human prostate cancer. *Nat. Genet.* **9,** 401–406 (1995).

38. Gregory, C. W., Johnson, R. T., Mohler, J. L., French, F. S. & Wilson, E. M. Androgen Receptor Stabilization in Recurrent Prostate Cancer Is Associated with Hypersensitivity to Low Androgen Androgen Receptor Stabilization in Recurrent Prostate Cancer Is Associated with Hypersensitivity to Low Androgen 1. *Cancer Res.* **61,** 2892–2898 (2001).

39. Labrie, F. *et al.* Gonadotropin-releasing hormone agonists in the treatment of prostate cancer. *Endocr. Rev.* **26,** 361–379 (2005).

40. Veldscholte, J. *et al.* The androgen receptor in LNCaP cells contains a mutation in the ligand binding domain which affects steroid binding characteristics and response to

antiandrogens. *J. Steroid Biochem. Mol. Biol.* **41,** 665–669 (1992).

41. Small, E. J. & Srinivas, S. The antiandrogen withdrawal syndrome: Experience in a large cohort of unselected patients with advanced prostate cancer. *Cancer* **76,** 1428–1434 (1995).

42. Signoretti, S. *et al.* Her-2-neu Expression and Progression Toward Androgen Independence in Human Prostate Cancer. *J. Natl. Cancer Inst.* **92,** (2000).

43. Chandrasekar, T., Yang, J. C., Gao, A. C. & Evans, C. P. Mechanisms of resistance in castration-resistant prostate cancer (CRPC). *Transl. Androl. Urol.* **4,** 365–80 (2015).

44. Colombel, M. *et al.* Detection of the apoptosis-suppressing oncoprotein bc1-2 in hormone-refractory human prostate cancers. *Am. J. Pathol.* **143,** 390–400 (1993).

45. Gleave, M. *et al.* Progression to androgen independence is delayed by adjuvant treatment with antisense Bcl-2 oligodeoxynucleotides after castration in the LNCaP prostate tumor model. *Clin. Cancer Res.* **5,** 2891–2898 (1999).

46. Craft, N. *et al.* Evidence for Clonal Outgrowth of Androgen-independent Prostate Cancer Cells from Androgen-dependent Tumors through a Two-Step Process Evidence for Clonal Outgrowth of Androgen-independent Prostate Cancer Cells from Androgen-dependent Tumors through a Two-. *Cancer Res* **59,** 5030–5036 (1999).

47. Maitland, N. J. & Collins, A. T. Prostate cancer stem cells: A new target for therapy. *J. Clin. Oncol.* **26,** 2862–2870 (2008).

48. Cabello, C. M. *et al.* NIH Public Access. **46,** 220–231 (2010).

49. Zhang, C. *et al.* Profiling alternatively spliced mRNA isoforms for prostate cancer classification. *BMC Bioinformatics* **7,** 202 (2006).

50. Li, H. R. *et al.* Two-dimensional transcriptome profiling: Identification of messenger RNA isoform signatures in prostate cancer from archived paraffin-embedded cancer specimens. *Cancer Res.* **66,** 4079–4088 (2006).

51. S. Haile; Sadar, M. Androgen receptor and its splice variants in prostate cancer. **68,** 3971–3981 (2013).

52. Dehm, S. M. & Tindall, D. J. Alternatively spliced androgen receptor variants. *Endocr. Relat. Cancer* **18,** 183–196 (2011).

53. Sette, C. Alternative splicing programs in prostate cancer. *Int. J. Cell Biol.* **2013,** (2013).

54. Dehm, S. M., Schmidt, L. J., Heemers, H. V., Vessella, R. L. & Tindall, D. J. Splicing of a novel androgen receptor exon generates a constitutively active androgen receptor that mediates prostate cancer therapy resistance. *Cancer Res.* **68,** 5469–5477 (2008).

55. Brasso, K. *et al.* Enzalutamide Antitumour Activity Against Metastatic Castration-resistant Prostate Cancer Previously Treated with Docetaxel and Abiraterone: A Multicentre Analysis. *Eur. Urol.* **68,** 317–324 (2015).

56. Stein, M. N., Patel, N., Bershadskiy, A., Sokoloff, A. & Singer, E. a. Androgen synthesis inhibitors in the treatment of castration-resistant prostate cancer. *Asian J. Androl.* **16,** 387–400 (2014).

57. Lin, G. G. & Scott, J. G. Pre-mRNA splicing in disease and therapeutics Ravi. *Trends Mol Med.* **100,** 130–134 (2012).

58. Sharma, N. *et al.* Prostatic tumor cell plasticity involves cooperative interactions of distinct phenotypic subpopulations: Role in vasculogenic mimicry. *Prostate* **50,** 189–201 (2002).

59. Maughan, B. L. & Antonarakis, E. S. Clinical Relevance of Androgen Receptor Splice Variants in Castration-Resistant Prostate Cancer. *Curr. Treat. Options Oncol.* **16,** 57 (2015).

60. Musgrove, E., Caldon, C., Barraclough, J., Stone, A. & Sutherland, R. Cyclin D as a therapeutic target in cancer. *Nat. Rev. Cancer* **11,** 558–72 (2011).

61. Comstock, C. E. S. *et al.* Cyclin D1 splice variants: Polymorphism, risk, and isoform-specific regulation in prostate cancer. *Clin. Cancer Res.* **15,** 5338–5349 (2009).

62. Bielli, P., Busà, R., Paronetto, M. P. & Sette, C. The RNA-binding protein Sam68 is a multifunctional player in human cancer. *Endocr. Relat. Cancer* **18,** (2011).

63. Gomiz-Rüth, F. X. Catalytic domain architecture of metzincin metalloproteases. *J. Biol. Chem.* **284,** 15353–15357 (2009).

64. Stöcker, W. & Bode, W. Structural features of a superfamily of zinc-endopeptidases: the metzincins. *Curr. Opin. Struct. Biol.* **5,** 383–390 (1995).

65. Page-McCaw, A., Ewald, A. J. & Werb, Z. Matrix metalloproteinases and the regulation of tissue. *Nat Rev Mol Cell Biol.* **8,** 221–233 (2007).

66. Murphy, G. The ADAMs: signalling scissors in the tumour microenvironment. *Nat. Rev. Cancer* **8,** 932–941 (2008).

67. Bode, W., Gomis-Rüth, F. X. & Stöckler, W. Astacins, serralysins, snake venom and matrix metalloproteinases exhibit identical zinc-binding environments (HEXXHXXGXXH and Met-turn) and topologies and should be grouped into a common family, the 'metzincins'. *FEBS Lett.* **331,** 134–140 (1993).

68. Seiki, M. Membrane-type matrix metalloproteinases. *APMIS* **107,** 137–43 (1999).

69. Visse, R. & Nagase, H. Matrix metalloproteinases and tissue inhibitors of metalloproteinases: Structure, function, and biochemistry. *Circ. Res.* **92,** 827–839 (2003).

70. Duffy, M. J., McKiernan, E., O'Donovan, N. & McGowan, P. M. Role of ADAMs in cancer formation and progression. *Clin. Cancer Res.* **15,** 1140–1144 (2009).

71. Brocker, C. N., Vasiliou, V. & Nebert, D. W. Evolutionary divergence and functions of the ADAM and ADAMTS gene families. *Hum. Genomics* **4,** 43–55 (2009).

72. Wolfsberg, T. G. *et al.* ADAM, a widely distributed and developmentally regulated gene family encoding membrane proteins with a disintegrin and metalloprotease domain. *Developmental biology* **169,** 378–383 (1995).

73. Blobel Myles, D.G., Primakoff, P., C. P. & White, J. M. Proteolytic processing of a protein involved insperm-egg fusion correlates with acquisition of fertilizationcompetence. *J.Cell.Biol* **111,** 69–77 (1990).

74. Weskamp, G. & Blobel, C. P. A family cellular proteins related of snake venom disintegrins. *Cell Biol.* **91,** 2748–2752 (1994).

75. Powell, R. M., Wicks, J., Holloway, J. W., Holgate, S. T. & Davies, D. E. The splicing and fate of ADAM33 transcripts in primary human airways fibroblasts. *Am. J. Respir. Cell Mol. Biol.* **31,** 13–21 (2004).

76. Gilpin, B. J. *et al.* A novel secreted form of human ADAM 12 (meltrin α) provokes myogenesis in vivo. *J. Biol. Chem.* **273,** 157–166 (1998).

77. Duffy, M. J. *et al.* The ADAMs family of proteases: new biomarkers and therapeutic targets for cancer? *Clin. Proteomics* **8,** 9 (2011).

78. Van Wart, H. E. & Birkedal-Hansen, H. The cysteine switch: a principle of regulation of

metalloproteinase activity with potential applicability to the entire matrix metalloproteinase gene family. *Proc. Natl. Acad. Sci. U. S. A.* **87,** 5578–5582 (1990).

79. Edwards, D. R., Handsley, M. M. & Pennington, C. J. The ADAM metalloproteinases. *Mol. Aspects Med.* **29,** 258–289 (2009).

80. Zhang, X. P., Kamata, T., Yokoyama, K., Puzon-McLaughlin, W. & Takada, Y. Specific interaction of the recombinant disintegrin-like domain of MDC- 15 (Metargidin, ADAM-15) with integrin AvB3. *J. Biol. Chem.* **273,** 7345–7350 (1998).

81. Zhong, J. L. *et al.* Distinct functions of natural ADAM-15 cytoplasmic domain variants in human mammary carcinoma. *Mol. Cancer Res.* **6,** 383–394 (2008).

82. Primakoff, P., Hyatt, H. & Tredick-Kline, J. Identification and purification of a sperm surface protein with a potential role in sperm-egg membrane fusion. *J Cell Biol* **104,** 141–149 (1987).

83. Yuan, R., Primakoff, P. & Myles, D. G. A role for the disintegrin domain of cyritestin, a sperm surface protein belonging to the ADAM family, in mouse sperm-egg plasma membrane adhesion and fusion. *J. Cell Biol.* **137,** 105–112 (1997).

84. Hartmann, D. *et al.* The disintegrin/metalloprotease ADAM 10 is essential for Notch signalling but not for alpha-secretase activity in fibroblasts. *Hum. Mol. Genet.* **11,** 2615–2624 (2002).

85. Jackson, L. F. *et al.* Defective valvulogenesis in HB-EGF and TACE-null mice is associated with aberrant BMP signaling. *EMBO J.* **22,** 2704–2716 (2003).

86. Blobel, C. P. ADAMs: key components in EGFR signalling and development. *Nat. Rev. Mol. Cell Biol.* **6,** 32–43 (2005).

87. Kurisaki, T. *et al.* Phenotypic Analysis of Meltrin α (ADAM12) -Deficient Mice : Involvement of Meltrin α in Adipogenesis and Myogenesis. *Mol Cell Biol.* **23,** 55–61 (2003).

88. Zhou, H.-M. *et al.* Essential role for ADAM19 in cardiovascular morphogenesis. *Mol. Cell. Biol.* **24,** 96–104 (2004).

89. Gomez-Gaviro, M. *et al.* Expression and regulation of the metalloproteinase ADAM-8 during human neutrophil pathophysiological activation and its catalytic activity on L-selectin shedding. *J Immunol* **178,** 8053–8063 (2007).

90. Sagane, K., Ohya, Y., Hasegawa, Y. & Tanaka, I. Metalloproteinase-like, disintegrin-like, cysteine-rich proteins MDC2 and MDC3: novel human cellular disintegrins highly expressed in the brain. *Biochem. J.* **334 (Pt 1,** 93–8 (1998).

91. Sagane, K., Yamazaki, K., Mizui, Y. & Tanaka, I. Cloning and chromosomal mapping of mouse ADAM11 ,. **236,** 79–86 (1999).

92. Dina, O. A. *et al.* Primary afferent second messenger cascades interact with specific integrin subunits in producing inflammatory hyperalgesia. *Pain* **115,** 191–203 (2005).

93. D'Abaco, G. M. *et al.* ADAM22, expressed in normal brain but not in high-grade gliomas, inhibits cellular proliferation via the disintegrin domain. *Neurosurgery* **58,** 179–186 (2006).

94. Gutierrez-Lopez, M. D. *et al.* The sheddase activity of ADAM17/TACE is regulated by the tetraspanin CD9. *Cell. Mol. Life Sci.* **68,** 3275–3292 (2011).

95. Scheller, J., Chalaris, A., Garbers, C. & Rose-John, S. ADAM17: A molecular switch to control inflammation and tissue regeneration. *Trends Immunol.* **32,** 380–387 (2011).

96. Rundhaug, J. E. Matrix Metalloproteinases , Angiogenesis , and Cancer. *Clin. Cancer Res.* **9,** 551–554 (2003).

97. Mochizuki, S. & Okada, Y. ADAMs in cancer cell proliferation and progression. *Cancer Sci.* **98,** 621–628 (2007).

98. Seshacharyulu, P. *et al.* Targeting the EGFR signaling pathway in cancer therapy. *Expert Opin. Ther. Targets* **16,** 15–31 (2013).

99. Wildeboer, D., Naus, S., Amy Sang, Q.-X., Bartsch, J. W. & Pagenstecher, A. Metalloproteinase disintegrins ADAM8 and ADAM19 are highly regulated in human primary brain tumors and their expression levels and activities are associated with invasiveness. *J. Neuropathol. Exp. Neurol.* **65,** 516–527 (2006).

100. Najy, A. J., Day, K. C. & Day, M. L. The ectodomain shedding of E-cadherin by ADAM15 supports ErbB receptor activation. *J. Biol. Chem.* **283,** 18393–18401 (2008).

101. Murphy, G. & Docherty, A. J. P. The Matrix Metalloproteinases and Their Inhibitors. *Am. J. Respir. Cell Mol. Biol.* **7,** 120–125 (1992).

102. McCulloch, D. R., Harvey, M. & Herington, A. C. The expression of the ADAMs proteases in prostate cancer cell lines and their regulation by dihydrotestosterone.

Mol. Cell. Endocrinol. **167,** 11–21 (2000).

103. Arima, T. *et al.* Nuclear translocation of ADAM-10 contributes to the pathogenesis and progression of human prostate cancer. *Cancer Sci.* **98,** 1720–1726 (2007).

104. Fritzsche, F. R. *et al.* ADAM9 Expression is a Significant and Independent Prognostic Marker of PSA Relapse in Prostate Cancer. *Eur. Urol.* **54,** 1097–1108 (2008).

105. Najy, A. J., Day, K. C. & Day, M. L. ADAM15 supports prostate cancer metastasis by modulating tumor cell-endothelial cell interaction. *Cancer Res.* **68,** 1092–1099 (2008).

106. Yagami-Hiromasa, T. *et al.* A metalloprotease-disintegrin participating in myoblast fusion. *Nature* **377,** 652–656 (1995).

107. Weskamp, G., Krätzschmar, J., Reid, M. S. & Blobel, C. P. MDC9, a widely expressed cellular disintegrin containing cytoplasmic SH3 ligand domains. *J. Cell Biol.* **132,** 717–726 (1996).

108. Weskamp, G. *et al.* Mice lacking the metalloprotease-disintegrin MDC9 (ADAM9) have no evident major abnormalities during development or adult life. *Mol. Cell. Biol.* **22,** 1537–1544 (2002).

109. Izumi, Y. *et al.* A metalloprotease-disintegrin, MDC9/meltrin-gamma/ADAM9 and PKC delta are involved in TPA-induced ectodomain shedding of membrane-anchored heparin-binding EGF-like growth factor. *EMBO J.* **17,** 7260–7272 (1998).

110. Mazzocca, A. *et al.* A secreted form of ADAM9 promotes carcinoma invasion through tumor-stromal interactions. *Cancer Res.* **65,** 4728–4738 (2005).

111. Franzke, C. W. *et al.* Transmembrane collagen XVII, an epithelial adhesion protein, is shed from the cell surface by ADAMS. *EMBO J.* **21,** 5026–5035 (2002).

112. Moss, M. L. *et al.* ADAM9 inhibition increases membrane activity of ADAM10 and controls gamma-secretase processing of amyloid precursor protein. *J. Biol. Chem.* **286,** 40443–40451 (2011).

113. Karan, D. *et al.* Expression of ADAMs (a disintegrin and metalloproteases) and TIMP-3 (tissue inhibitor of metalloproteinase-3) in human prostatic adenocarcinomas. *Int. J. Oncol.* **23,** 1365–1371 (2003).

114. Sung, S. Y. *et al.* Oxidative stress induces ADAM9 protein expression in human prostate cancer cells. *Cancer Res* **66,** 9519–9526 (2006).

115. Martin, A. C. B. M., Cardoso, A. C. F., Selistre-de-Araujo, H. S. & Cominetti, M. R. Recombinant disintegrin domain of human ADAM9 inhibits migration and invasion of DU145 prostate tumor cells. *Cell Adhes. Migr.* **9,** 293–299 (2015).

116. Chantry, A., Gregson, N. A. & Glynn, P. A novel metalloproteinase associated with brain myelin membranes. Isolation and characterization. *J. Biol. Chem.* **264,** 21603–21607 (1989).

117. Lammich, S. *et al.* Constitutive and regulated alpha-secretase cleavage of Alzheimer's amyloid precursor protein by a disintegrin metalloprotease. *Proc. Natl. Acad. Sci. U. S. A.* **96,** 3922–3927 (1999).

118. McCulloch, D. R., Akl, P., Samaratunga, H., Herington, A. C. & Odorico, D. M. Expression of the Disintegrin Metalloprotease, ADAM-10, in Prostate Cancer and Its Regulation by Dihydrotestosterone, Insulin-Like Growth Factor I, and Epidermal Growth Factor in the Prostate Cancer Cell Model LNCaP. *Clin. Cancer Res.* **10,** 314–323 (2004).

119. Maretzky, T. *et al.* ADAM10 mediates E-cadherin shedding and regulates epithelial cell-cell adhesion, migration, and beta-catenin translocation. *Proc. Natl. Acad. Sci. U. S. A.* **102,** 9182–9187 (2005).

120. You, B., Shan, Y., Shi, S., Li, X. & You, Y. Effects of ADAM10 upregulation on progression, migration, and prognosis of nasopharyngeal carcinoma. *Cancer Sci.* **106,** 1506–1514 (2015).

121. Kopitz, C. *et al.* Tissue inhibitor of metalloproteinases-1 promotes liver metastasis by induction of hepatocyte growth factor signaling. *Cancer Res.* **67,** 8615–8623 (2007).

122. Borggrefe, T. & Oswald, F. The Notch signaling pathway: Transcriptional regulation at Notch target genes. *Cell. Mol. Life Sci.* **66,** 1631–1646 (2009).

123. Miles A. Miller, Madeleine J. Oudin, Ryan J. Sullivan, Stephanie J. Wang, Aaron S. Meyer, Hyungsoon Im, Dennie T. Frederick, Jenny Tadros, Linda G. Griffith, Hakho Lee, Ralph Weissleder, Keith T. Flaherty, Frank B. Gertler, D. A. L. Reduced Proteolytic Shedding of Receptor Tyrosine Kinases is a Post-Translational Mechanism of Kinase Inhibitor Resistance. *Cancer Discov.* **57,** 742–768 (2015).

124. Düsterhöft, S. *et al.* A disintegrin and metalloprotease 17 dynamic interaction sequence, the sweet tooth for the human interleukin 6 receptor. *J. Biol. Chem.* **289,**

16336–16348 (2014).

125. Mohan, M. J. *et al.* The tumor necrosis factor-alpha converting enzyme (TACE): A unique metalloproteinase with highly defined substrate selectivity. *Biochemistry* **41,** 9462–9469 (2002).

126. Moss, M. L. *et al.* Cloning of a disintegrin metalloproteinase that processes precursor tumour-necrosis factor-alpha. *Nature* **385,** 733–736 (1997).

127. Lin, P. *et al.* ADAM17 regulates prostate cancer cell proliferation through mediating cell cycle progression by EGFR/PI3K/AKT pathway. *Mol. Cell. Biochem.* **359,** 235–243 (2012).

128. Xiao, L. J. *et al.* ADAM17 targets MMP-2 and MMP-9 via EGFR-MEK-ERK pathway activation to promote prostate cancer cell invasion. *Int. J. Oncol.* **40,** 1714–1724 (2012).

129. Miller, M. A., Sullivan, R. J. & Lauffenburger, D. A. Molecular Pathways: Receptor Ectodomain Shedding in Treatment, Resistance, and Monitoring of Cancer. *Clin Cancer Res.* **23,** 623–630 (2016).

130. Rankin, E. & Giaccia, A. The Receptor Tyrosine Kinase AXL in Cancer Progression. *Cancers (Basel).* **8,** 103 (2016).

131. VanSchaeybroeck, S. *et al.* ADAM17-Dependent c-MET-STAT3 Signaling Mediates Resistance to MEK Inhibitors in KRAS Mutant Colorectal Cancer. *Cell Rep.* **7,** 1940–1955 (2014).

132. Burdelski, C. *et al.* Overexpression of the A Disintegrin and Metalloproteinase ADAM15 is linked to a Small but Highly Aggressive Subset of Prostate Cancers. *Neoplasia* **19,** 279–287 (2017).

133. Lum, L. & Blobel, C. P. Metargidin, a Membrane-anchored Metalloprotease-Disintegrin Protein with an RGD Integrin Binding Sequence *. *J. Biol. Chem.* **271,** 4593–4597 (1996).

134. Ortiz, R. M., Kärkkäinen, I. & Huovila, A. P. J. Aberrant alternative exon use and increased copy number of human metalloprotease-disintegrin ADAM15 gene in breast cancer cells. *Genes Chromosom. Cancer* **41,** 366–378 (2004).

135. Kleino, I., Ortiz, R. M. & Huovila, A.-P. J. ADAM15 gene structure and differential

alternative exon use in human tissues. *BMC Mol. Biol.* **8,** 90 (2007).

136. Kratzschmar, J., Lum, L. & Blobel, C. P. Membrane anchored Metalloprotease-Disintegrin Protein with an RGD Integrin Binding Sequence *. 4593–4597 (1996).

137. Loechel, F., Gilpin, B. J., Engvall, E., Albrechtsen, R. & Wewer, U. M. Human ADAM 12 (Meltrin alpha) is an active metalloprotease. *J. Biol. Chem.* **273,** 16993–16997 (1998).

138. Tallant, C., García-Castellanos, R., Baumann, U. & Gomis-Rüth, F. X. On the relevance of the met-turn methionine in metzincins. *J. Biol. Chem.* **285,** 13951–13957 (2010).

139. Lu, D., Scully, M., Kakkar, V. & Lu, X. ADAM-15 disintegrin-like domain structure and function. *Toxins (Basel).* **2,** 2411–2427 (2010).

140. Trochon-Joseph, V. *et al.* Evidence of Antiangiogenic and Antimetastatic Activities of the Recombinant Disintegrin Domain of Metargidin. *Cancer Res.* **64,** 2062–2069 (2004).

141. Stone, A. L., Kroeger, M. & Sang, Q. X. A. Structure-function analysis of the ADAM family of disintegrin-like and metalloproteinase-containing proteins (review). *J. Protein Chem.* **18,** 447–465 (1999).

142. Huovila, A. J., Almeida, E. A. & White, J. M. ADAMs and cell fusion. *Curr. Opin. Cell Biol.* **8,** 692–699 (1996).

143. Wouters, M. a *et al.* Evolution of distinct EGF domains with specific functions. *Protein Sci.* **14,** 1091–103 (2005).

144. Kleino, I., Ortiz, R. M., Yritys, M., Huovila, A. P. J. & Saksela, K. Alternative splicing of ADAM15 regulates its interactions with cellular SH3 proteins. *J. Cell. Biochem.* **108,** 877–885 (2009).

145. Poghosyan, Z. *et al.* Phosphorylation-dependent interactions between ADAM15 cytoplasmic domain and Src family protein-tyrosine kinases. *J. Biol. Chem.* **277,** 4999–5007 (2002).

146. Kärkkäinen, S. *et al.* Identification of preferred protein interactions by phage-display of the human Src homology-3 proteome. *EMBO Rep.* **7,** 186–91 (2006).

147. Chaudhury, A., Chander, P. & Howe, P. H. Heterogeneous nuclear ribonucleoproteins (hnRNPs) in cellular processes: Focus on hnRNP E1's multifunctional regulatory roles. *RNA* **16,** 1449–1462 (2010).

148. Warzecha, C. C., Sato, T. K., Nabet, B., Hogenesch, J. B. & Russ, P. NIH Public Access. **33,** 591–601 (2010).

149. Yasui, A. *et al.* Expression of splice variants of the human ADAM15 gene and strong interaction between the cytoplasmic domain of one variant and Src family proteins Lck and Hck. *Pathobiology* **71,** 185–192 (2004).

150. Kleino, I., Jarviluoma, A., Hepojoki, J., Huovila, A. P. & Saksela, K. Preferred SH3 domain partners of ADAM metalloproteases include shared and ADAM-specific SH3 interactions. *PLoS One* **10,** 1–19 (2015).

151. Fourie, A. M., Coles, F., Moreno, V. & Karlsson, L. Catalytic activity of ADAM8, ADAM15, and MDC-L (ADAM28) on synthetic peptide substrates and in ectodomain cleavage of CD23. *J. Biol. Chem.* **278,** 30469–30477 (2003).

152. Ohtsu, H., Dempsey, P. J. & Eguchi, S. ADAMs as mediators of EGF receptor transactivation by G protein-coupled receptors. *Am. J. Physiol. cell Physiol.* **291,** C1-10 (2006).

153. Martin, J., Eynstone, L. V., Davies, M., Williams, J. D. & Steadman, R. The role of ADAM 15 in glomerular mesangial cell migration. *J. Biol. Chem.* **277,** 33683–33689 (2002).

154. Huissoon, A. P., Emery, P., Bacon, P. A., Gordon, J. & Salmon, M. Increased expression of CD23 in rheumatoid synovitis. *Scand J Rheumatol* **29,** 154–159 (2000).

155. Maretzky, T. *et al.* Characterization of the catalytic activity of the membrane-anchored metalloproteinase ADAM15 in cell-based assays. *Biochem. J.* **420,** 105–113 (2009).

156. Maretzky, T. *et al.* Src stimulates fibroblast growth factor receptor-2 shedding by an ADAM15 splice variant linked to breast cancer. *Cancer Res.* **69,** 4573–4576 (2009).

157. Dong, D. D., Zhou, H. & Li, G. ADAM15 targets MMP9 activity to promote lung cancer cell invasion. *Oncol. Rep.* **34,** 2451–2460 (2015).

158. Schäfer, B., Gschwind, A. & Ullrich, A. Multiple G-protein-coupled receptor signals converge on the epidermal growth factor receptor to promote migration and invasion. *Oncogene* **23,** 991–9 (2004).

159. Hart, S. *et al.* GPCR-induced migration of breast carcinoma cells depends on both EGFR signal transactivation and EGFR-independent pathways. *Biol. Chem.* **386,** 845–855 (2005).

160. Duan, X., Mao, X. & Sun, W. ADAM15 is involved in MICB shedding and mediates the effects of gemcitabine on MICB shedding in PANC-1 pancreatic cancer cells. *Mol. Med. Rep.* **7,** 991–997 (2013).

161. Tousseyn, T. *et al.* ADAM10, the rate-limiting protease of regulated intramembrane proteolysis of notch and other proteins, is processed by ADAMS-9, ADAMS-15, and the gamma-secretase. *J. Biol. Chem.* **284,** 11738–11747 (2009).

162. Hiles, G. L. *et al.* ADAM15 is functionally associated with the metastatic progression of human bladder cancer. *PLoS One* **11,** 1–18 (2016).

163. Ghigna, C., Valacca, C. & Biamonti, G. Alternative Splicing and Tumor Progression. *Curr. Genomics* **9,** 556–570 (2008).

164. Iqbal, N. & Iqbal, N. Imatinib: a breakthrough of targeted therapy in cancer. *Chemother Res Pr.* **2014,** 357027 (2014).

165. Lassila, J. K., Zalatan, J. G. & Herschlag, D. *Biological phosphoryl-Tranfer reactions: understanding mechanism and catlysis*. *Annual Review Biochemistry* **80,** (2012).

166. Robinson, D. R., Wu, Y.-M. & Lin, S.-F. The protein tyrosine kinase family of the human genome. *Oncogene* **19,** 5548–5557 (2000).

167. Maruyama, I. N. Mechanisms of activation of receptor tyrosine kinases: monomers or dimers. *Cells* **3,** 304–30 (2014).

168. Lemmon, M. a & Schlessinger, J. Cell signaling by receptor-tyrosine kinases Mark. *Cell* **141,** 1117–1134 (2011).

169. Burgess, A. W. *et al.* An open-and-shut case? Recent insights into the activation of EGF/ErbB receptors. *Mol. Cell* **12,** 541–552 (2003).

170. Liu, H., Chen, X., Focia, P. J. & He, X. Structural basis for stem cell factor-KIT signaling and activation of class III receptor tyrosine kinases. *EMBO J.* **26,** 891–901 (2007).

171. Stauber, D. J., DiGabriele, A. D. & Hendrickson, W. A. Structural interactions of fibroblast growth factor receptor with its ligands. *Proc. Natl. Acad. Sci. U. S. A.* **97,** 49–54 (2000).

172. Ségaliny, A. I., Tellez-Gabriel, M., Heymann, M. F. & Heymann, D. Receptor tyrosine kinases: Characterisation, mechanism of action and therapeutic interests for bone cancers. *J. Bone Oncol.* **4,** 1–12 (2015).

173. Schlessinger, J. Cell signaling by receptor tyrosine kinases. *Cell* **103,** 211–225 (2000).

174. Hubbard, S. R. & Miller, W. T. Receptor tyrosine kinases: mechanisms of activation and signaling. *Curr. Opin. Cell Biol.* **19,** 117–123 (2007).

175. Hubbard, S. R. Juxtamembrane autoinhibition in receptor tyrosine kinases. *Nat. Rev. Mol. Cell Biol.* **5,** 464–471 (2004).

176. Karamouzis, M. V., Konstantinopoulos, P. A. & Papavassiliou, A. G. Targeting MET as a strategy to overcome crosstalk-related resistance to EGFR inhibitors. *Lancet Oncol.* **10,** 709–717 (2009).

177. Humphrey, P. A. *et al.* Hepatocyte growth factor and its receptor (c-MET) in prostatic carcinoma. *Am. J. Pathol.* **147,** 386–96 (1995).

178. Bottaro, D. P. *et al.* Identification of the hepatocyte growth factor receptor as the c-met proto-oncogene product. *Science* **251,** 802–804 (1991).

179. Giordano, S. *et al.* Biosynthesis of the protein encoded by the c-met proto-oncogene. *Oncogene* **4,** 1383–1388 (1989).

180. Gelsomino, F. *et al.* Targeting the MET gene for the treatment of non-small-cell lung cancer. *Crit. Rev. Oncol. Hematol.* **89,** 284–299 (2014).

181. Nakamura, T., Nawa, K. & Ichihara, A. Partial purification and characterization of hepatocyte growth factor from serum of hepatectomized rats. *Biochem. Biophys. Res. Commun.* **122,** 1450–9 (1984).

182. Weidner, K. M. *et al.* Evidence for the identity of human scatter factor and human hepatocyte growth factor. *Cell Biol.* **88,** 7001–7005 (1991).

183. Nakamura, T. & Mizuno, S. The discovery of Hepatocyte Growth Factor (HGF) and its significance for cell biology, life sciences and clinical medicine. *Proc. Japan Acad. Ser. B Phys. Bol. Sci.* **86,** 588–610 (2010).

184. Shimomura, T. *et al.* Activation of the zymogen of hepatocyte growth factor activator by thrombin. *J. Biol. Chem.* **268,** 22927–22932 (1993).

185. Gherardi, E. *et al.* Structural basis of hepatocyte growth factor/scatter factor and MET signalling. *Proc. Natl. Acad. Sci. U. S. A.* **103,** 4046–51 (2006).

186. Sonnenberg, E., Meyer, D., Weidner, K. M. & Birchmeier, C. Scatter factor/hepatocyte

growth factor and its receptor, the c-met tyrosine kinase, can mediate a signal exchange between mesenchyme and epithelia during mouse development. *J. Cell Biol.* **123,** 223–235 (1993).

187. Stamos, J., Lazarus, R. a, Yao, X., Kirchhofer, D. & Wiesmann, C. Crystal structure of the HGF beta-chain in complex with the Sema domain of the Met receptor. *EMBO J.* **23,** 2325–35 (2004).

188. Blumenschein, G. R., Mills, G. B. & Gonzalez-Angulo, A. M. Targeting the hepatocyte growth factor-cMET axis in cancer therapy. *J. Clin. Oncol.* **30,** 3287–3296 (2012).

189. Faria, C., Smith, C. & Rutka, J. The Role of HGF / c-Met Pathway Signaling in Human Medulloblastoma. *Mol. Targets CNS Tomous* **1,** 641–660 (2011).

190. Pathi, N., Viswanath, S., Pathak, A. & Rathore, A. Receptor tyrosine kinase signaling pathways : a review. **3,** 783–789 (2016).

191. Conrotto, P., Corso, S., Gamberini, S., Comoglio, P. M. & Giordano, S. Interplay between scatter factor receptors and B plexins controls invasive growth. *Oncogene* **23,** 5131–5137 (2004).

192. Trusolino, L., Bertotti, A. & Comoglio, P. M. A signaling adapter function for ??6??4 integrin in the control of HGF-dependent invasive growth. *Cell* **107,** 643–654 (2001).

193. Orian-rousseau, V., Chen, L., Sleeman, J. P., Herrlich, P. & Ponta, H. CD44 is required for two consecutive steps in HGF / c-Met signaling. *Genes Dev.* **16,** 3074–3086 (2002).

194. Puri, N. & Salgia, R. Synergism of EGFR and c-Met pathways, cross-talk and inhibition, in non-small cell lung cancer. *J. Carcinog.* **7,** 9 (2008).

195. Follenzi, A. *et al.* Cross-talk between the proto-oncogenes Met and Ron. *Oncogene* **19,** 3041–3049 (2000).

196. Yeh, C.-Y. *et al.* Transcriptional activation of the Axl and PDGFR-α by c-Met through a ras- and Src-independent mechanism in human bladder cancer. *BMC Cancer* **11,** 139 (2011).

197. Viticchiè, G. & Muller, P. c-Met and Other Cell Surface Molecules: Interaction, Activation and Functional Consequences. *Biomedicines* **3,** 46–70 (2015).

198. Hass, R., Jennek, S., Yang, Y. & Friedrich, K. c-Met expression and activity in urogenital cancers – novel aspects of signal transduction and medical implications. *Cell Commun.*

Signal. **15,** 10 (2017).

199. Birchmeier, C., Birchmeier, W., Gherardi, E. & Vande Woude, G. F. Met, metastasis, motility and more. *Nat. Rev. Mol. Cell Biol.* **4,** 915–925 (2003).

200. Giubellino, A., Burke, T. R. & Bottaro, D. P. Grb2 signaling in cell motility and cancer. *Expert Opin. Ther. Targets* **12,** 1021–33 (2008).

201. Peruzzi, B. & Bottaro, D. P. Targeting the c-Met signaling pathway in cancer. *Clin. Cancer Res.* **12,** 3657–3660 (2006).

202. Bradley, C. A. *et al.* Targeting c-MET in gastrointestinal tumours: rationale, opportunities and challenges. *Nat. Rev. Clin. Oncol.* **14,** 562 (2017).

203. Katz, M., Amit, I. & Yarden, Y. Regulation of MAPKs by growth factors and receptor tyrosine kinases. *Biochim. Biophys. Acta - Mol. Cell Res.* **1773,** 1161–1176 (2007).

204. Yoon, S. & Seger, R. The extracellular signal-regulated kinase: Multiple substrates regulate diverse cellular functions. *Growth Factors* **24,** 21–44 (2006).

205. Gay, B. *et al.* Effect of potent and selective inhibitors of the Grb2 SH2 domain on cell motility. *J. Biol. Chem.* **274,** 23311–23315 (1999).

206. Lock, L. S., Royal, I., Naujokas, M. A. & Park, M. Identification of an atypical Grb2 carboxyl-terminal SH3 domain binding site in Gab docking proteins reveals Grb2-dependent and -independent recruitment of Gab1 to receptor tyorosine kinases. *J. Biol. Chem.* **275,** 31536–31545 (2000).

207. Schaeper, U. *et al.* Coupling of Gab1 to c-Met, Grb2, and Shp2 mediates biological responses. *J. Cell Biol.* **149,** 1419–1432 (2000).

208. Maina, F. *et al.* Uncoupling of Grb2 from the Met receptor in vivo reveals complex roles in muscle development. *Cell* **87,** 531–542 (1996).

209. Goh, L. K. & Sorkin, A. Endocytosis of Receptor Tyrosine Kinases. *Cold Spring Harb. Perspect. Biol.* **5,** 17459–17459 (2013).

210. Kermorgant, S., Zicha, D. & Parker, P. J. Protein kinase C controls microtubule-based traffic but not proteasomal degradation of c-Met. *J. Biol. Chem.* **278,** 28921–28929 (2003).

211. Jeffers, M., Taylor, G. A., Weidner, K. M., Omura, S. & Vande Woude, G. F. Degradation

of the Met tyrosine kinase receptor by the ubiquitin-proteasome pathway. *Mol. Cell. Biol.* **17,** 799–808 (1997).

212. Kermorgant, S. & Parker, P. J. c-Met Signalling: Spatio-Temporal Decisions. *Cell Cycle* **4,** 352–355 (2005).

213. Jeffers, M. *et al.* Activating mutations for the met tyrosine kinase receptor in human cancer. *Proc. Natl. Acad. Sci. U. S. A.* **94,** 11445–11450 (1997).

214. Kanchev, I. & Gregor, M. Original Article ADAM10 / 17-Dependent Release of Soluble c-Met Correlates with Hepatocellular Damage. *Folia Biol. (Praha).* **86,** 76–86 (2013).

215. Trusolino, L., Bertotti, A. & Comoglio, P. M. MET signalling: principles and functions in development, organ regeneration and cancer. *Nat. Rev. Mol. Cell Biol.* **11,** 834–48 (2010).

216. Schmidt, C. *et al.* Scatter factor/hepatocyte growth factor is essential for liver development. *Nature* **373,** 699–702 (1995).

217. Ebens, A. *et al.* Hepatocyte growth factor/scatter factor is an axonal chemoattractant and a neurotrophic factor for spinal motor neurons. *Neuron* **17,** 1157–1172 (1996).

218. Nakamura, T. *et al.* Myocardial protection from ischemia / reperfusion injury by endogenous and exogenous HGF. *J. Clin. Invest.* **106,** 1511–1519 (2000).

219. Tsubouchi, H. *et al.* Levels of the human hepatocyte growth factor in serum of patients with various liver diseases determined by an enzyme-linked immunosorbent assay. *Hepatology* **13,** 1–5 (1991).

220. Galimi, F. *et al.* Hepatocyte growth factor is a regulator of monocyte-macrophage function. *J. Immunol.* **166,** 1241–7 (2001).

221. van der Voort, R. *et al.* Paracrine regulation of germinal center B cell adhesion through the c-met-hepatocyte growth factor/scatter factor pathway. *J. Exp. Med.* **185,** 2121–31 (1997).

222. Baek, J.-H., Birchmeier, C., Zenke, M. & Hieronymus, T. The HGF receptor/Met tyrosine kinase is a key regulator of dendritic cell migration in skin immunity. *J. Immunol.* **189,** 1699–707 (2012).

223. Danilkovitch-miagkova, A. & Zbar, B. Dysregulation of Met receptor tyrosine kinase activity. *J Clin. Invest.* **109,** 863–867 (2002).

224. Cooper, C. S. *et al.* Molecular cloning of a new transforming gene from a chemically transformed human cell line. *Nature* **311,** 29–33 (1984).

225. Liang, T. J., Reid, A. E., Xavier, R., Cardiff, R. D. & Wang, T. C. Transgenic expression of tpr-met oncogene leads to development of mammary hyperplasia and tumors. *J. Clin. Invest.* **97,** 2872–2877 (1996).

226. Soman, N. R., Correa, P., Ruiz, B. A. & Wogan, G. N. The TPR-MET oncogenic rearrangement is present and expressed in human gastric carcinoma and precursor lesions. *Proc. Natl. Acad. Sci. U. S. A.* **88,** 4892–6 (1991).

227. Kitajima, Y., Ide, T., Ohtsuka, T. & Miyazaki, K. Induction of hepatocyte growth factor activator gene expression under hypoxia activates the hepatocyte growth factor/c-Met system via hypoxia inducible factor-1 in pancreatic cancer. *Cancer Sci.* **99,** 1341–1347 (2008).

228. Boccaccio, C., Gaudino, G., Gambarotta, G., Galimi, F. & Comoglio, P. M. Hepatocyte growth factor (HGF) receptor expression is inducible and is part of the delayed-early response to HGF. *J. Biol. Chem.* **269,** 12846–12851 (1994).

229. Sohn, J. *et al.* cMET Activation and EGFR-Directed Therapy Resistance in Triple-Negative Breast Cancer. *J. Cancer* **5,** 745–753 (2014).

230. Scagliotti, G. V., Novello, S. & von Pawel, J. The emerging role of MET/HGF inhibitors in oncology. *Cancer Treat. Rev.* **39,** 793–801 (2013).

231. Dai, Y. & Siemann, D. W. Constitutively active c-Met kinase in PC-3 cells is autocrine-independent and can be blocked by the Met kinase inhibitor BMS-777607. *BMC Cancer* **12,** 198 (2012).

232. Buchanan, I. M. *et al.* Radiosensitization of glioma cells by modulation of Met signalling with the hepatocyte growth factor neutralizing antibody, AMG102. *J. Cell. Mol. Med.* **15,** 1999–2006 (2011).

233. Gordon, M. S. *et al.* Safety, pharmacokinetics, and pharmacodynamics of AMG 102, a fully human hepatocyte growth factor-neutralizing monoclonal antibody, in a first-in-human study of patients with advanced solid tumors. *Clin. Cancer Res.* **16,** 699–710 (2010).

234. Wen, P. Y. *et al.* A phase II study evaluating the efficacy and safety of AMG 102 (rilotumumab) in patients with recurrent glioblastoma. *Neuro. Oncol.* **13,** 437–446

(2011).

235. Hartmut Koeppen, Wei Yu, Jiping Zha, Ajay Pandita, Elicia Penuel, Linda Rangell, Rajiv Raja, Sankar Mohan, Rajesh Patel, Rupal Desai, Ling Fu, An Do, Vaishali Parab, Xiaoling Xia, Tom Januario, Sharianne G. Louie, Ellen Filvaroff, David S, and R. & Yauch, L. Biomarker Analyses from a Placebo-Controlled Phase II Study Evaluating Erlotinib ± Onartuzumab in Advanced Non–Small Cell Lung Cancer: MET Expression Levels Are Predictive of Patient Benefit. *Clin Cancer Res.* **57,** 742–768 (2015).

236. Yu, S. S., Quinn, D. I. & Dorff, T. B. Clinical use of cabozantinib in the treatment of advanced kidney cancer: Efficacy, safety, and patient selection. *Onco. Targets. Ther.* **9,** 5825–5837 (2016).

237. Elisei, R. *et al.* Cabozantinib in progressive medullary thyroid cancer. *J. Clin. Oncol.* **31,** 3639–3646 (2013).

238. Eathiraj, S. *et al.* Discovery of a novel mode of protein kinase inhibition characterized by the mechanism of inhibition of human mesenchymal-epithelial transition factor (c-Met) protein autophosphorylation by ARQ 197. *J. Biol. Chem.* **286,** 20666–20676 (2011).

239. Yap, T. A. *et al.* Phase I trial of a selective c-MET inhibitor ARQ 197 incorporating proof of mechanism pharmacodynamic studies. *J. Clin. Oncol.* **29,** 1271–1279 (2011).

240. Sequist, L. V. *et al.* Randomized phase II study of erlotinib plus tivantinib versus erlotinib plus placebo in previously treated non-small-cell lung cancer. *J. Clin. Oncol.* **29,** 3307–3315 (2011).

241. Maitreyee, K.J., Chen, L., Mudryj, M., Ghosh, P. M. Targeting ErbB3 : the New RTK (id) on the Prostate Cancer Block. *Immunol Endocr Metab Agents Med Chem.* **2,** 1–33 (2011).

242. Arora, a & Scholar, E. M. Role of tyrosine kinase inhibitors in cancer therapy. *J Pharmacol Exp Ther* **315,** 971–979 (2005).

243. Gallick, G. E., Corn, P. G., Zurita, A. J. & Lin, S.-H. Small-molecule protein tyrosine kinase inhibitors for the treatment of metastatic prostate cancer. *Future Med. Chem.* **4,** 107–119 (2012).

244. Horti, J. *et al.* Docetaxel plus Prednisone or Mitoxantrone plus Prednisone for Advanced Prostate Cancer. 1502–1512 (2004).

245. Paller, C. J. & Antonarakis, E. S. Cabazitaxel: A novel second-line treatment for metastatic castration-resistant prostate cancer. *Drug Des. Devel. Ther.* **5,** 117–124 (2011).

246. Urakami, S. *et al.* Combination chemotherapy with paclitaxel, estramustine and carboplatin for hormone refractory prostate cancer. *J. Urol.* **168,** 2444–2450 (2002).

247. Tu, W. H., Zhu, C., Clark, C., Christensen, J. G. & Sun, Z. Efficacy of c-Met inhibitor for advanced prostate cancer. *BMC Cancer* **10,** 556 (2010).

248. Knudsen, B. S. *et al.* High expression of the Met receptor in prostate cancer metastasis to bone. *Urology* **60,** 1113–1117 (2002).

249. Eder, J. P. *et al.* A phase I study of foretinib, a multi-targeted inhibitor of c-Met and vascular endothelial growth factor receptor 2. *Clin. Cancer Res.* **16,** 3507–3516 (2010).

250. Qian, F. *et al.* Inhibition of tumor cell growth, invasion, and metastasis by EXEL-2880 (XL880, GSK1363089), a novel inhibitor of HGF and VEGF receptor tyrosine kinases. *Cancer Res.* **69,** 8009–8016 (2009).

251. Tu, W. H., Zhu, C., Clark, C., Christensen, J. G. & Sun, Z. Efficacy of c-Met inhibitor for advanced prostate cancer. *BMC Cancer* **10,** 556 (2010).

252. Peters, S. & Adjei, A. A. MET: a promising anticancer therapeutic target. *Nat. Rev. Clin. Oncol.* **9,** 314–326 (2012).

253. Barrow-Mcgee, R. & Kermorgant, S. Met endosomal signalling: In the right place, at the right time. *Int. J. Biochem. Cell Biol.* **49,** 69–74 (2014).

254. Paul, M. K. & Mukhopadhyay, A. K. Tyrosine kinase – Role and significance in Cancer. *Int. J. Med. Sci.* **1,** 101–115 (2004).

255. Gocek, E., Moulas, A. N. & Studzinski, G. P. Non-receptor protein tyrosine kinases signaling pathways in normal and cancer cells. *Crit. Rev. Clin. Lab. Sci.* **51,** 125–37 (2014).

256. Rodrigues, G. A. & Park, M. Oncogenic activation of tyrosine kinases. *Curr. Opin. Genet. Dev.* **4,** 15–24 (1994).

257. Simmons, D. L., Levy, D. B., Yannoni, Y. & Erikson, R. L. Identification of a phorbol ester-repressible v-src-inducible gene. *Proc. Natl. Acad. Sci. U. S. A.* **86,** 1178–82 (1989).

258. Parsons, S. J. & Parsons, J. T. Src family kinases, key regulators of signal transduction. *Oncogene* **23,** 7906–7909 (2004).

259. Okada, M., Nada, S., Yamanashi, Y., Yamamoto, T. & Nakagawa, H. CSK: a protein-tyrosine kinase involved in regulation of src family kinases. *J. Biol. Chem.* **266,** 24249–52 (1991).

260. Hamaguchi, I. *et al.* Analysis of CSK Homologous Kinase (CHK / HYL) in Hematopoiesis by Utilizing Gene Knockout Mice 1 related kinases including HYL have been independently reported , and are found to be identical to each other or the mouse / rat counterparts (2-7). CSK ho. *Biochem. Biophys. Res. Commun.* **179,** 172–179 (1996).

261. Serfas, M. S. & Tyner, A. L. Brk, Srm, Frk, and Src42A form a distinct family of intracellular Src-like tyrosine kinases. *Oncol. Res.* **13,** 409–419 (2003).

262. Brauer, P. M. & Tyner, A. L. RAKing in AKT: A tumor suppressor function for the intracellular tyrosine kinase FRK. *Cell Cycle* **8,** 2728–2732 (2009).

263. Zheng, Y. & Tyner, A. L. Context Specific Protein Tyrosine Kinase 6 (PTK6) Signaling in Prostate Cancer. *Eur J Clin Invest* **43,** 397–404 (2013).

264. Goel, R. K. & Lukong, K. E. Tracing the footprints of the breast cancer oncogene BRK-past till present. *Biochim. Biophys. Acta - Rev. Cancer* **1856,** 39–54 (2015).

265. Qiu, H. & Miller, W. T. Role of the Brk SH3 domain in substrate recognition. *Oncogene* **23,** 2216–2223 (2004).

266. Hong, E., Shin, J., Kim, H. I., Lee, S. T. & Lee, W. Solution structure and backbone dynamics of the non-receptor protein-tyrosine kinase-6 Src homology 2 domain. *J. Biol. Chem.* **279,** 29700–29708 (2004).

267. Brauer, P. M. *et al.* The alternative splice variant of protein tyrosine kinase 6 negatively regulates growth and enhances PTK6-mediated inhibition of β-catenin. *PLoS One* **6,** e14789 (2011).

268. Kang, K., Kim, M., Pae, K. & Lee, S. Characterization of the 5P-£anking region of the human PTK6 gene. *Oncogene* **1574,** 365–369 (2002).

269. Vasioukhin, V. & Tyner, a L. A role for the epithelial-cell-specific tyrosine kinase Sik during keratinocyte differentiation. *Proc. Natl. Acad. Sci. U. S. A.* **94,** 14477–82 (1997).

270. Haegebarth, A. *et al.* Protein tyrosine kinase 6 negatively regulates growth and promotes enterocyte differentiation in the small intestine. *Mol. Cell. Biol.* **26,** 4949–57 (2006).

271. Llor, X. *et al.* BRK / Sik Expression in the Gastrointestinal Tract and in Colon Tumors BRK / Sik Expression in the Gastrointestinal Tract and in. *Clin Cancer Res.* **5,** 1767–1777 (1999).

272. Haegebarth, A., Nunez, R. & Tyner, A. L. The intracellular tyrosine kinase Brk sensitizes non-transformed cells to inducers of apoptosis. *Cell Cycle* **4,** 1239–1246 (2005).

273. Derry, J. J., Prins, G. S., Ray, V. & Tyner, A. L. Altered localization and activity of the intracellular tyrosine kinase BRK/Sik in prostate tumor cells. *Oncogene* **22,** 4212–4220 (2003).

274. Petro, B. J., Tan, R. C., Tyner, A. L., Lingen, M. W. & Watanabe, K. Differential expression of the non-receptor tyrosine kinase BRK in oral squamous cell carcinoma and normal oral epithelium. *Oral Oncol.* **40,** 1040–1047 (2004).

275. Peng, M., Ball-Kell, S. M., Franks, R. R., Xie, H. & Tyner, a L. Protein tyrosine kinase 6 regulates mammary gland tumorigenesis in mouse models. *Oncogenesis* **2,** e81 (2013).

276. Nahta, R., Yuan, L. X. H., Zhang, B., Kobayashi, R. & Esteva, F. J. Insulin-like growth factor-I receptor/human epidermal growth factor receptor 2 heterodimerization contributes to trastuzumab resistance of breast cancer cells. *Cancer Res.* **65,** 11118–11128 (2005).

277. Zheng, Y., Peng, M., Wang, Z., Asara, J. M. & Tyner, A. L. Protein tyrosine kinase 6 directly phosphorylates AKT and promotes AKT activation in response to epidermal growth factor. *Mol. Cell. Biol.* **30,** 4280–4292 (2010).

278. Liu, L. *et al.* Identification of STAT3 as a specific substrate of breast tumor kinase. *Oncogene* **25,** 4904–12 (2006).

279. Weaver, A. M. & Silva, C. M. Signal transducer and activator of transcription 5b: a new target of breast tumor kinase/protein tyrosine kinase 6. *Breast Cancer Res.* **9,** R79 (2007).

280. Haegebarth, A. *et al.* The nuclear tyrosine kinase BRK/Sik phosphorylates and inhibits the RNA-binding activities of the Sam68-like mammalian proteins SLM-1 and SLM-2. *J. Biol. Chem.* **279,** 54398–54404 (2004).

281. Zheng, Y. *et al.* PTK6 activation at the membrane regulates epithelial-mesenchymal transition in prostate cancer. *Cancer Res.* **73,** 5426–5437 (2013).

282. Ono, H., Basson, M. D. & Ito, H. PTK6 Promotes Cancer Migration and Invasion in Pancreatic Cancer Cells Dependent on ERK Signaling. *PLoS One* **9,** e96060 (2014).

283. Henry, N. L. & Hayes, D. F. Cancer biomarkers. *Mol. Oncol.* **6,** 140–146 (2012).

284. Frangogiannis, N. G. Biomarkers: Hopes and challenges in the path from discovery to clinical practice. *Transl. Res.* **159,** 197–204 (2012).

285. Oldenhuis, C. N. A. M., Oosting, S. F., Gietema, J. A. & de Vries, E. G. E. Prognostic versus predictive value of biomarkers in oncology. *Eur. J. Cancer* **44,** 946–953 (2008).

286. Prensner, J. R., Rubin, M. A., Wei, J. T. & Chinnaiyan, A. M. Beyond PSA: the next generation of prostate cancer biomarkers. *Sci. Transl. Med.* **4,** 127rv3 (2012).

287. Sieuwerts, A. M. How ADAM-9 and ADAM-11 Differentially From Estrogen Receptor Predict Response to Tamoxifen Treatment in Patients with Recurrent Breast Cancer: a Retrospective Study. *Clin. Cancer Res.* **11,** 7311–7321 (2005).

288. Kuefer, R. *et al.* ADAM15 disintegrin is associated with aggressive prostate and breast cancer disease. *Neoplasia* **8,** 319–29 (2006).

289. Kleino, I., Ortiz, R. M. & Huovila, A.-P. J. ADAM15 gene structure and differential alternative exon use in human tissues. *BMC Mol. Biol.* **8,** 90 (2007).

290. Bustin, S. A. *et al.* The MIQE guidelines:Minimum Information for publication of quantitative real-time PCR experiments. *Clin. Chem.* **55,** 611–622 (2009).

291. Ostrander, J. H., Daniel, A. R. & Lange, C. a. Brk/PTK6 signaling in normal and cancer cell models. *Curr. Opin. Pharmacol.* **10,** 662–669 (2010).

292. Zheng, Y., Asara, J. M. & Tyner, A. L. Protein-tyrosine kinase 6 promotes peripheral adhesion complex formation and cell migration by phosphorylating p130 CRK-associated substrate. *J. Biol. Chem.* **287,** 148–158 (2012).

293. Grose, R. *et al.* The role of fibroblast growth factor receptor 2b in skin homeostasis and cancer development. *EMBO J.* **26,** 1268–1278 (2007).

294. Brauer, P. M. & Tyner, A. L. Building a better understanding of the intracellular tyrosine kinase PTK6 - BRK by BRK. *Biochim. Biophys. Acta - Rev. Cancer* **1806,** 66–73

(2010).

295. Derry, J. J. *et al.* Sik (BRK) phosphorylates Sam68 in the nucleus and negatively regulates its RNA binding ability. *Mol. Cell. Biol.* **20,** 6114–6126 (2000).

296. Castro, N. E. & Lange, C. a. Breast tumor kinase and extracellular signal-regulated kinase 5 mediate Met receptor signaling to cell migration in breast cancer cells. *Breast Cancer Res.* **12,** R60 (2010).

297. Pinglong Xu, Jianming Liu, Masayo Sakaki-Yumoto, and R. D. TACE Activation by MAPK-Mediated Regulation of Cell Surface Dimerization and TIMP3 Association. *Sci Signal* **48,** 1–6 (2014).

298. Deng, W., Cho, S., Su, P.-C., Berger, B. W. & Li, R. Membrane-enabled dimerization of the intrinsically disordered cytoplasmic domain of ADAM10. *Proc. Natl. Acad. Sci. U. S. A.* **111,** 15987–92 (2014).

299. Hastie, C. J., McLauchlan, H. J. & Cohen, P. Assay of protein kinases using radiolabeled ATP: a protocol. *Nat. Protoc.* **1,** 968–71 (2006).

300. Han, Y., Luo, Y., Zhao, J., Li, M. & Jiang, Y. Overexpression of c-Met increases the tumor invasion of human prostate LNCaP cancer cells in vitro and in vivo. *Oncol. Lett.* **8,** 1618–1624 (2014).

301. Organ, S. L. & Tsao, M.-S. An overview of the c-MET signaling pathway. *Ther. Adv. Med. Oncol.* **3,** S7–S19 (2011).

302. Tomizawa, M. *et al.* SU11274 suppresses proliferation and motility of pancreatic cancer cells. *Oncol. Lett.* 1468–1472 (2015).

303. Moran-Jones, K., Brown, L. M. & Samimi, G. INC280, an orally available small molecule inhibitor of c-MET, reduces migration and adhesion in ovarian cancer cell models. *Sci. Rep.* **5,** 11749 (2015).

304. Coxon, A., Rex, K., Meyer, S. & Sun, J. Soluble c-Met receptors inhibit phosphorylation of c-Met and growth of hepatocyte growth factor: c-Met–dependent tumors in animal models. *Mol. cancer …* **8,** 1119–1125 (2009).

305. Schelter, F. *et al.* A disintegrin and metalloproteinase-10 (ADAM-10) mediates DN30 antibody-induced shedding of the met surface receptor. *J. Biol. Chem.* **285,** 26335–26340 (2010).

306. Bardelli, a, Longati, P., Gramaglia, D., Stella, M. C. & Comoglio, P. M. Gab1 coupling to the HGF/Met receptor multifunctional docking site requires binding of Grb2 and correlates with the transforming potential. *Oncogene* **15,** 3103–11 (1997).

307. Wang, X. *et al.* 56 Potent and selective inhibitors of the Met [hepatocyte growth factor/scatter factor (HGF/SF) receptor] tyrosine kinase block HGF/SF-induced tumor cell growth and invasion. *Mol. Cancer Ther.* **2,** 1085–1092 (2003).

308. Han, Y. *et al.* Hepatocyte growth factor increases the invasive potential of PC-3 human prostate cancer cells via an ERK/MAPK and ZEB-1 signaling pathway. *Oncol. Lett.* **11,** 753–759 (2016).

309. Trudel, D., Fradet, Y. & Meyer, F. Significance of MMP-2 Expression in Prostate Cancer : an Immunohistochemical Study. *Cancer Res.* **63,** 8511–8515 (2003).

310. Koon, E. C. *et al.* Effect of a c-Met-specific, ATP-competitive small-molecule inhibitor SU11274 on human ovarian carcinoma cell growth, motility, and invasion. *Int. J. Gynecol. Cancer* **18,** 976–984 (2008).

311. Dornier, E. *et al.* Tspanc8 tetraspanins regulate ADAM10/Kuzbanian trafficking and promote Notch activation in flies and mammals. *J. Cell Biol.* **199,** 481–496 (2012).

312. Jouannet, S. *et al.* TspanC8 tetraspanins differentially regulate the cleavage of ADAM10 substrates, Notch activation and ADAM10 membrane compartmentalization. *Cell. Mol. Life Sci.* **73,** 1895–1915 (2016).

313. Weidner, K. M. *et al.* Interaction between Gab1 and the c-Met receptor tyrosine kinase is responsible for epithelial morphogenesis. *Nature* **384,** 173–176 (1996).

314. Seiden-Long, I. *et al.* Gab1 but not Grb2 mediates tumor progression in Met overexpressing colorectal cancer cells. *Carcinogenesis* **29,** 647–655 (2008).

315. Greene, K. L. *et al.* Exosome release of ADAM15 and the functional implications of human macrophage-derived ADAM15 exosomes. *Biochim. Biophys. Acta* **1796,** 2232–2241 (2009).

316. Maroun, C. R. & Rowlands, T. The Met receptor tyrosine kinase: A key player in oncogenesis and drug resistance. *Pharmacol. Ther.* **142,** 316–338 (2014).

317. Ho-Yen, C. M., Jones, J. L. & Kermorgant, S. The clinical and functional significance of c-Met in breast cancer: a review. *Breast Cancer Res.* **17,** 52 (2015).

318. Etnyre, D. *et al.* Targeting c-Met in melanoma: Mechanism of resistance and efficacy of novel combinatorial inhibitor therapy. *Cancer Biol. Ther.* **15,** 1129–1141 (2014).

319. Xie, T., Dong, B., Yan, Y., Hu, G. & Xu, Y. Association between MMP-2 expression and prostate cancer: A meta-analysis. *Biomed. Reports* 241–245 (2015). doi:10.3892/br.2015.553

320. Chan, P.-C., Sudhakar, J. N., Lai, C.-C. & Chen, H.-C. Differential phosphorylation of the docking protein Gab1 by c-Src and the hepatocyte growth factor receptor regulates different aspects of cell functions. *Oncogene* **29,** 698–710 (2010).

321. Xu, D., Tsai, C. J. & Nussinov, R. Mechanism and evolution of protein dimerization. *Protein Sci.* **7,** 533–44 (1998).